

Evaluation and validation of a novel MST-Radar for studying atmospheric 3D structures

Dissertation
zur
Erlangung des akademischen Grades
Doktor-Ingenieur (Dr.-Ing.)
der Fakultät für Informatik und Elektrotechnik
der Universität Rostock

vorgelegt von
Toralf Renkwitz,
geboren am 06. Mai 1979 in Hagenow,
wohnhaft in Rostock

Datum des Einreichens der Arbeit: 4. April 2014

1. Gutachter: Prof. Dr. Hartmut Ewald,
Universität Rostock
2. Gutachter: Prof. Dr. Markus Rapp,
Ludwig-Maximilians-Universität München
3. Gutachter: Dr. Michael Rietveld,
European Incoherent Scatter Scientific Association

Datum des Einreichens der Arbeit: 4. April 2014
Datum der Verteidigung: 29. Oktober 2014

Abstract

The knowledge of characteristic parameters of a radar as well as of the radiation pattern of its associated antenna array is of fundamental importance for the analysis and comparability of radar observations. Some parameters can be measured directly at the radar, while in particular the parameters characterizing the radiation pattern of the antenna array typically need to be derived indirectly as the array is already deployed and its aperture is too large to be measured in a dedicated measuring chamber. Furthermore, the phase distribution of the individual subarrays needs to be known to properly combine them in phase forming larger subarrays as well as for the profitable application of interferometric methods. The combination of subarray groups with imperfect phases quickly result in the deterioration of the radiation pattern.

Thus, the main focus of this thesis is the evaluation and estimation of these demanded parameters and thus to apply dedicated calibration methods to ensure optimal performance of the radar and the analysis of the data collected with this radar. For this purpose passive and active experiments were performed along with measurements directly at the radar hardware, which are examined in detail. The passive observation of cosmic radio sources allows the estimation of beam pointing accuracy, beam width and antenna gain as well as of the absolute phases of the individual receiver subarray combinations. The comparison of these observations with an accurate radio astronomy reference map revealed high similarity. Active experiments, observing the Earth's moon, artificial satellites, meteors and a sounding rocket payload refine these findings. These results are compared to dedicated most accurate simulations of the radiation pattern and showed an excellent agreement.

Kurzfassung

Die Kenntnis der charakteristischen Eigenschaften eines Radarsystems und des zugehörigen Antennenarrays sind von größter Bedeutung für die Auswertung und Vergleichbarkeit von Radarbeobachtungen. Einige dieser Parameter können direkt am Radarsystem gemessen werden, während dies für das Strahlungsdiagramm oft nur begrenzt möglich ist. Für die optimale Kombinierung von kleinen Antennengruppen zu größeren Gruppen und deren interferometrische Nutzung ist die Kenntnis der jeweiligen Phasenlagen erforderlich. Die Kombinierung der Gruppen mit fehlerhaften Phasen führt zu einer Modifikation des Strahlungsdiagramms, z.B. zu einer Verbreiterung oder einer falschen Positionierung der Hauptstrahlkeule oder zur Veränderung der Nebenzipfel in Position und Intensität, was deutlichen Einfluss auf die Qualität der Radarmessungen hat.

In dieser Arbeit werden daher Methoden zur Bestimmung der wichtigsten Eigenschaften des untersuchten Radars und dessen Antennenarrays beschrieben und angewendet. Dabei kommen sowohl passive als auch aktive Experimente und Messungen direkt am Radar zum Einsatz. Die Beobachtung von kosmischen Radioquellen erlaubt die Bestimmung der Strahlpositionierung und -breite, der Phasenlage der jeweiligen Antennengruppen, sowie eine Abschätzung des Antennengewinns. Der Vergleich dieser Beobachtungen mit einer genauen radioastronomischen Referenzkarte zeigte sehr gute Übereinstimmungen. Diese Experimente werden durch aktive Radarexperimente ergänzt, bei denen der Mond, künstliche Satelliten, Meteore und die Nutzlast einer instrumentierten Höhenforschungsrakete als Radarziele genutzt werden, um das Strahlungsdiagramm zu validieren. Die Ergebnisse werden jeweils mit genauen Simulationen des Strahlungsdiagrammes verglichen, wobei eine sehr gute Übereinstimmung gefunden wurde.

Contents

1	Introduction	1
2	Earth's atmosphere and radar measurements therein	5
2.1	Earth's atmosphere	6
2.2	Radar observations in the atmosphere	7
2.3	Examples of atmospheric phenomena observed by radar at high latitudes	9
3	The Middle Atmosphere Alomar Radar System	12
3.1	The design of the Middle Atmosphere Alomar Radar System (MAARSY)	13
3.2	The MAARSY array element	18
3.3	The polarization upgrade of MAARSY	20
3.4	Simulations of the radiation pattern of MAARSY using NEC	23
3.5	Array performance of MAARSY	26
3.6	Special beam forming - simultaneous multi-beam meteor observations	28
3.7	Improved side lobe suppression by the use of amplitude taper	30
3.8	Summary	32
4	Passive experiments to estimate the radiation pattern	33
4.1	Sky noise - cosmic radio emission in the VHF range: Origin and observation requirements	34
4.2	Phase calibration methods applicable to MAARSY	37
4.2.1	Absolute phase calibration of MAARSY by the observations of cosmic radio sources	38
4.2.2	Automatic hardware phase and amplitude calibration measurements	42
4.2.3	Comparison of the hardware phase test and radio source phase calibration	43
4.2.4	The influence of combining subarrays with inaccurate phase conditions	45
4.2.5	The correlation of the individual receiver groups	45
4.3	Observations of cosmic radio emissions with MAARSY	47
4.3.1	Observations September 2012 - May 2013	47
4.3.2	Observations May to September 2013	51
4.3.3	Observations September to November 2013	53
4.4	Comparison of observations with the Global Sky temperature Model (GSM)	55
4.5	Expansion of the sky noise scan	61
4.6	Antenna array gain estimation by observing cosmic radio sources	63
4.6.1	Methodology of the antenna gain estimation by the aid of cosmic radio source observations	64
4.6.2	Results of the gain estimation method using cosmic radio sources	65

Contents

4.7	Geophysical applications of sky noise observations	68
4.7.1	Observation of scintillation events	68
4.7.2	D-region ionizations	72
4.8	Summary	75
5	Active experiments to estimate the radiation pattern	76
5.1	Measurements in the near electric field	78
5.2	Moon experiment	80
5.3	Satellite observations	82
5.4	Approximation of the radiation pattern with the aid of meteor head echo observations	84
5.5	Observations during the WADIS rocket campaign	86
5.6	Summary	90
6	Conclusions and outlook	91
Appendix A	The analysis of NEC simulated radiation pattern	97
A.1	Numerical Electromagnetic Code - Method of Moments	98
A.2	Quality of a radiation pattern	98
A.3	Antenna pattern modifications due to variations or component failures	100
A.4	Comparison of a simple pattern model to NEC	103
Appendix B	Radar hardware performance measurements	106
B.1	Measurements of MAARSY's array elements	107
B.2	Measurements of coaxial feeding cables	107
B.3	Linearity and dynamic range measurements	108
B.4	Estimation of the receiver noise figure of MAARSY	112
B.5	MAARSY bandwidth measurements	116
Appendix C	Passive observations with MAARSY	118
C.1	Results of the Phase calibration attempts	119
C.2	Detection of radio sources by the use of correlation phases	122
C.3	Additional tables and figures related to the sky noise observations performed with MAARSY	123
Appendix D	Airborne near field measurements	126
D.1	Sampling the transmission pattern of MAARSY	127
	List of Acronyms, Abbreviations and Symbols	144
	List of Tables and Figures	147
	List of own publications and presentations	158
	Thesen	161

Chapter 1 Introduction

Chapter 1 Introduction

The Middle Atmosphere Alomar Radar System (MAARSY, see Figure 1.1) is a large aperture high power radar designed for studies of phenomena in the mesosphere, stratosphere and troposphere. Radars that perform observations in these three altitude ranges are typically abbreviated as MST-radars. The construction of the radar with its active phased array antenna has been started in 2009 on the polar North-Norwegian island Andøya (69.3°N, 16.04°E) by the Leibniz-Institute of Atmospheric Physics e.V. at the University of Rostock (IAP). Its design, especially the flexible beam forming and steering capability, makes it a powerful instrument to perform observations with high angular and temporal resolution. In particular, this versatile radar aims for the investigation of the 3-dimensional structure and their temporal evolution of radar phenomena in the mesosphere like the Polar Mesospheric Summer and Winter echoes (PMSE and PMWE). Additionally, wave parameters derived from the analysis of the observed wind structure and the wave dynamics are of particular interest. Especially the latter represents the interconnection to other atmospheric heights and regions, i.e., these waves are one of the main coupling mechanisms in the atmosphere. Observations of PMSE and PMWE are generally performed with radars in the VHF range. Even though these radar echoes partially reach strong intensities and appear horizontally widely spread at higher latitudes, a powerful and flexible radar is needed not only to monitor, but to investigate these phenomena in detail. For this purpose a phased antenna array is used to focus the power of the transmitter and thus the radiation of the radar to specific directions. At the same time phased arrays permit rapid beam swinging within a defined volume. This arrangement typically requires more modules for transmission and reception than e.g. radars using parabolic dish antennas of equivalent size, and thus also necessitates significant calibration and validation efforts. However, phased arrays easily outperform classical parabolic dish antenna radars in terms of beam forming and pointing flexibility, cancellation of interfering signals and especially imaging methods. The latter is actually favorably applied to smaller antenna array groups, allowing the observation of a larger target area than at the best angular resolution of the total antenna. Depending on the specific targets and their properties, especially their distance and horizontal speed, the flexible selection of



Figure 1.1 Photograph of the MAARSY site, showing on the left the MAARSY antenna array, accompanied by the ALWIN64 antenna array on the right.

subarray groups is mandatory for optimal monitoring performance.

For the investigation of the 3D structure of mesospheric phenomena as well as their originating processes and dynamics, highly resolved measurements in time and space are needed. This incorporates the flexible definition of beam pointing positions with good isolation to adjacent regions and rapid beam swinging on e.g. pulse-to-pulse basis. The discrimination of the targets' horizontal structure for near-vertical pointing directions is limited by the angular resolution of the radar system. The pulse length, coding and sampling frequency, however, defines the range resolution. For larger off-boresight pointing, both the angular resolution, defined by the antenna array size, and the range resolution soon extend over various nearby altitudes. To limit this effect the effective antenna array size should be as large as possible, while for the analysis the actual beam direction and width need to be known. Thus, MAARSY allows observations within the middle atmosphere with high volume resolution (basic resolution: conic section of approximately 2.6 km radius x 50 m height without applying interferometric methods at an altitude of 85 km) as well as temporal resolution with a sampling frequency of e.g. 1 kHz and above.

The knowledge of the present radiation pattern used for the individual radar experiments is essential for both the planning of these experiments and the analysis of the radar raw and pre-analyzed data. Fundamental radar parameters like transmitted power, pulse width as well as gain and beam width of the antenna array need to be known for the calculation of e.g. the radar cross-section or volume reflectivity (which is defined as the scattering cross-section per radar volume). The use of e.g. volume reflectivity facilitates the comparison of individual calibrated radar measurements characterizing the prominent scattering target within the observed volume. Some of these parameters can directly be measured on-site at the radar, while others can be derived and estimated remotely with dedicated radar experiments.

Even when assuming that a radar has been built with optimum precision, integrated and superposed phase or time delays of the involved components may reach significant orders to impair the radiation pattern. This may result in either pointing the main beam off its nominal position or deteriorate the pattern by deformation or derogation of the side lobes in position and intensity.

Furthermore, even though the individual antenna and the entire array have been simulated thoroughly with the well accepted Numerical Electromagnetic Code package (NEC), some parameters within the array and its surrounding area can hardly be simulated. Therefore an extensive evaluation of the performance of both the antenna array and the radar hardware need to be performed.

Some of the required parameters can be measured directly at the radar hardware, like the output power of the individual transceiver modules or the actual pulse width. Other parameters need to be derived indirectly, like the shape and the width of the beam and the pointing accuracy. Smaller arrays, especially at higher frequencies are typically evaluated in dedicated anechoic measuring chambers. However, due to the size of the MAARSY array with a diameter of approximately 90 m this option is not feasible and thus other methods need to be applied.

The absolute phase distributions of the individual subarray receiver phases are inherently important for the combination of these groups to form larger subarrays, or their use for interferometric methods. This method is also important for continuing quality control as damages to e.g. the antennas and feeding coaxial cables may be seen remotely.

Chapter 1 Introduction

Therefore, the major aim of this thesis is the estimation and validation of the radiation pattern of the MAARSY antenna array and its receiver characteristics. Therein, the major key points are the quantification of

- the beam shape and pointing accuracy,
- the beam width and gain of the antenna array,
- the intensity and influence of the side lobes,
- the phase distribution and stability of the individual receiver subarray groups and
- the sensitivity and dynamic range of the radar.

To address these goals, this thesis is structured as follows: Chapter 2 gives an introduction to the Earth's lower and middle atmosphere and a brief summary of corresponding measurement techniques, followed by a dedicated section about radar measurements of the respective altitude regions. Subsequently, the two radar phenomena Polar Mesosphere Summer and Winter Echoes are introduced, which represent major targets for mesospheric observations with MAARSY. This introduction is augmented by the presentation of the typical observation strategy using multiple beam positions within a scan experiment to investigate these phenomena.

Chapter 3 gives a detailed introduction to the MAARSY radar, focussing on the receiving part of the radar and its antenna array and the system design. These points clearly mark the high observational flexibility and performance, which necessitates thorough and careful calibration processes. Furthermore, simulations of the radiation pattern, which are to be verified in the remainder of this thesis are presented in this chapter.

In Chapter 4 passive methods for the estimation and validation of MAARSY's radiation pattern are presented. This in first place is done by the observation of emissions emanating from two distinct cosmic radio sources. Doing so, the absolute phases of various receivers and their associated subarray groups are derived, as well as the beam pointing accuracy, the beam width and gain of the largest subarray as well as the entire antenna array are estimated for the receive part of the radar. Furthermore, the scan experiments observing the diffuse radio background allow the generation of intensity maps for this specific radar system. These maps can be compared to a highly resolved reference radio astronomy map to verify both the radiation pattern (especially the beam pointing) and sensitivity of the radar. Additionally, as a geophysical application of these passive observations, the use of MAARSY as a narrow beam imaging riometer is presented. In these experiments spatially localized cosmic noise absorption events have been observed, which permit the characterization of the D-region electron density.

Chapter 5 presents experiments where MAARSY has been actively operated as a radar to verify the radiation intensity distribution, beam pointing accuracy and partially the shape of the two-way radiation pattern. Here, emphasis is laid on the side lobes' distribution and intensity. Initially, the near electric field intensity is pointwise measured and compared to simulations, accompanied by the presentation of an airborne experiment to sample the radiation pattern directly. To attack the beam pointing accuracy and side lobe evaluation various targets from significantly different distances to the radar like the Earth's moon, artificial satellites, meteors and a rocket payload are used to corroborate the findings of the passive experiments.

Finally, the major results of this thesis are presented in Chapter 6 along with an outlook on future work.

Chapter 2 Earth's atmosphere and radar measurements therein

This chapter presents a brief introduction to the Earth's atmosphere, focussing on the lower and middle atmosphere. The relevant characteristics of the individual regions as well as the main instruments that are generally used to perform observations of the particular physical parameters in this broad altitude range are introduced. Subsequently, the principle and cause of radar echoes from the lower and middle atmosphere are given, accompanied by the presentation of two prominent radar echoes, which are in the primary focus of the operation of MAARSY.

2.1 Earth's atmosphere

Mean temperature and electron density profiles for high latitudes (69°N) for summer and winter conditions derived from the International Reference Ionosphere model IRI-2000 (see *Bilitza*, 2001) are shown in Figure 2.1. The actual profiles vary depending on the exact geographic and magnetic position, the time of the day, the day of year, the solar cycle and dynamic circulations within the atmosphere.

The individual atmospheric regions are partially called differently depending on their reference to parameters like temperature and electron content.

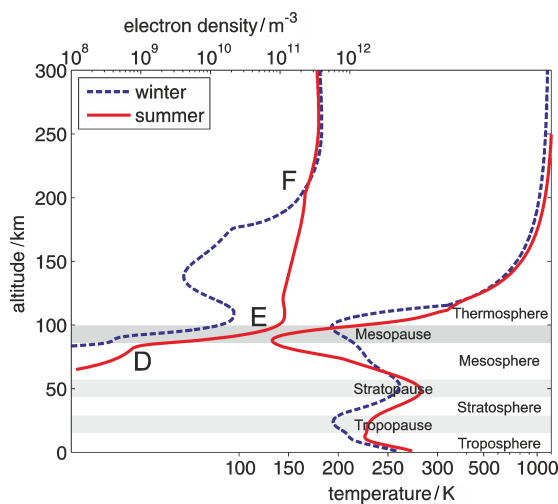


Figure 2.1 Temperature profiles (upper left) and electron density profiles (lower right) for high latitudes (69°N) derived from IRI model (see *Bilitza*, 2001) for summer (red) and winter (blue) conditions. Taken from *Li* (2011).

limited in the observation time for the specific altitudes, like in the case of rockets. Balloons typically ascend from ground and are drifted by the background air flow. Quasi-stationary observations with balloons are only possible for few days under special conditions, when the horizontal background flow is almost negligible, e.g. during the seasonal transition times in Northern Scandinavia.

In contrast, remote sensing, however, allows measurements, where in-situ observations are either too expensive, spatially resolved multi-point measurements are needed or rather continuous observations shall be performed. Observations from satellites e.g. allow global measurements, however the height coverage and spatial resolution may vary significantly as

The electron density maximizes within the so-called F-region of the ionosphere around 250 km altitude, although secondary maxima may also be apparent in the D- and E-region between 60 and 120 km.

The atmospheric layers are defined according to the gradient of the temperature profile: the troposphere, stratosphere, mesosphere, thermosphere. These layers are separated by regions where the temperature gradient reverses sign, the so called tropo-, strato- and mesopause.

Observations of e.g. temperature, pressure and wind can be performed depending on the actual altitude in-situ by airplanes, balloons and rockets. In-situ observations typically only sample the atmosphere within a very small area, which allows spatially highly resolved measurements, however fluctuations of larger scales are typically not seen. Furthermore in-situ observations are often very

well as the temporal resolution of identical observation points (1.5 h at best or up to several days, depending on the satellite orbit). Localized observations with lidar (light detection and ranging) systems e.g. allow highly resolved measurements, where, however, only few systems allow observations during daylight. Nevertheless, very narrow beams can be generated due to the wavelength in the nm-range, allowing observations within a comparably small volume. However, ground based lidars depend on cloud-free conditions in the troposphere (free line of sight). In contrast, the benefit of radars (radio detection and ranging) below a frequency of a few GHz is their weather immunity, which allows continuous observations with a given beam width, determined by the used frequency and effective aperture of the antenna, at one or more pointing directions.

2.2 Radar observations in the atmosphere

Reflection, refraction or scattering of a radar pulse off the atmosphere requires variations in the radio refractive index n (e.g. Bragg-condition in case of volume scattering). In general, the refractive index is defined as

$$n = \frac{c}{v}, \quad (2.1)$$

where c is the speed of light and v the velocity of the electromagnetic wave in the medium. The refractive index for the ionosphere can be written as:

$$n = \sqrt{1 - \frac{\omega_p^2}{\omega_o^2}}, \quad (2.2)$$

with the wavelength of the operating frequency ω_o and the plasma frequency ω_p . The latter is given by:

$$\omega_p = \sqrt{\frac{n_e e^2}{\epsilon_r \epsilon_0 m_e}} \approx 18\pi \sqrt{n_e}, \quad (2.3)$$

where n_e is the number density of electrons per m^3 , e and m_e are the electric charge and mass of an electron and ϵ_r and ϵ_0 are the relative permittivity and the permittivity of the vacuum. The simplified relationship for the radio refractive index can be written as:

$$n - 1 = \frac{0.373 \cdot e}{T^2} + \frac{77.6 \cdot 10^{-6} Pa}{T} - \frac{40.3 n_e}{f_0^2}, \quad (2.4)$$

where e (in mb) is the partial pressure of water vapor, P_a (in mb) is the total atmospheric pressure, T (in K) is the absolute temperature and f_0 is the operating frequency (see *Balsley and Gage*, 1980). This is equivalent to the dry and wet air approximations of the latest ITU reference (*ITU*, 2012). The first two terms relate to the neutral atmosphere, while the third term describes the contribution of the free electrons content in the ionosphere. The contribution of the three terms are individually depicted in Figure 2.2 for realistic scales, while the N_e/f^2 term is calculated for the frequencies 53 MHz and 3 MHz respectively. With the increase of the electron density in the D-region, caused by ionization due to incident radiation of the sun, backscatter is received at mesosphere heights with a MF radar (≈ 3 MHz), see

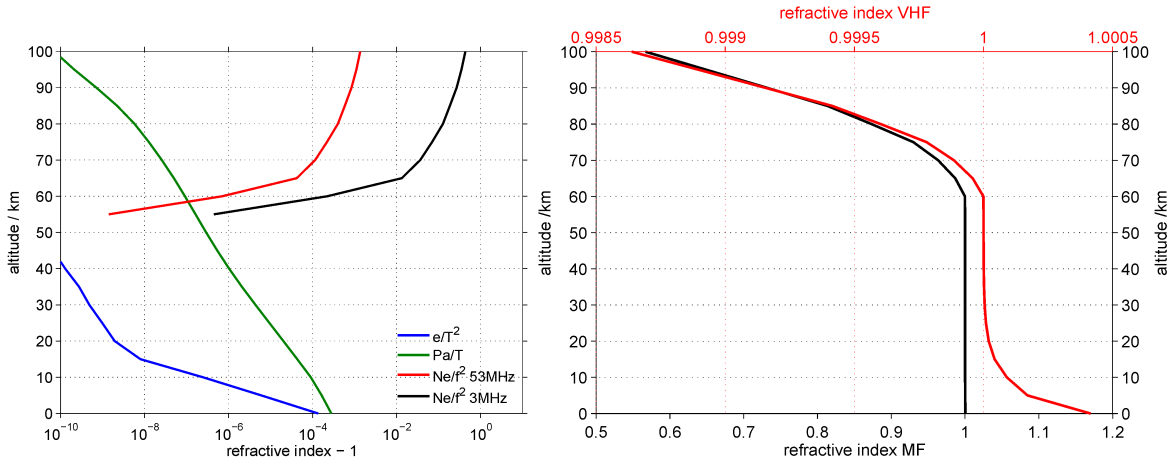


Figure 2.2 Left: Individual terms of the radio refractive index (Equation 2.4) for 53 MHz (red) and 3 MHz (black) and the corresponding total refractive index for both frequencies in respect to their individual colored abscissa (right panel).

black line in the left panel of Figure 2.2. The contribution of the ionization and thus electron density in the ionosphere for 3 MHz supersedes 53 MHz, where the lower frequency allows almost continuous observations in time for the altitude range of 80 to 100 km. However, due to the mandatory size of the antenna array the angular resolution of radars operated at around 3 MHz is inferior to a radar as it is investigated in this thesis.

In the troposphere turbulent radar echoes can be detected due to the variations of total pressure and water vapor partial pressure by a 50 MHz radar.

In the mesosphere the contribution of the electron density supersedes the contribution by pressure and water vapor by orders of magnitude. This allows the detection of radar echoes, provided that coherent structures at the appropriate scale need to be present. From the lower stratosphere to the lower mesosphere these requirements are usually not fulfilled (unless, for the latter, significant ionization is created for example by a solar proton event) and thus, no radar echoes from this part of the atmosphere are detected. The typical altitudes covered by radars operated on various frequencies are marked schematically in Figure 2.3.

The mesosphere offers a variety of phenomena that can be observed with a radar at lower VHF frequencies. Two mesospheric phenomena, related to turbulence, enabling VHF radar echoes in the middle and higher latitudes are introduced in the following section.

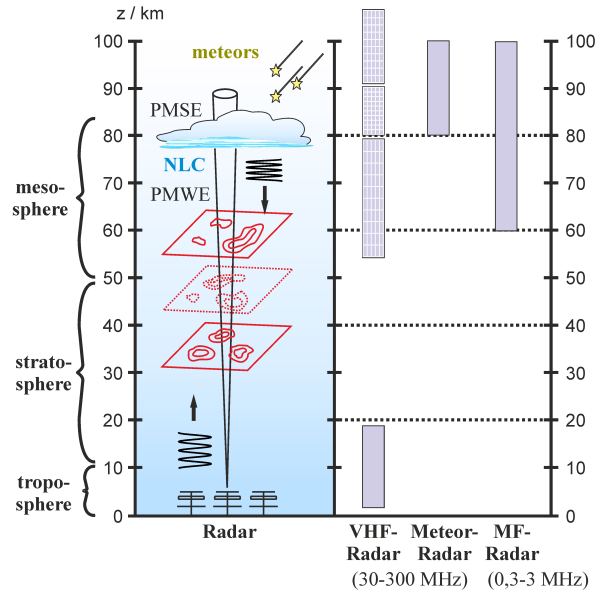


Figure 2.3 Sketch of typical height coverage of atmospheric radars using coherent scattering. The shaded areas mark the altitude range, from where the specific radars do not continuously receive backscatter.

2.3 Examples of atmospheric phenomena observed by radar at high latitudes

Additionally, radar echoes can also be caused by Fresnel reflection or partial reflection, which is produced by stable horizontal layers with a large gradient of the refractive index (see e.g. *Röttger, 1980; Rapp et al., 2011a*). Mainly observed in the mid-latitudes are sporadic echoes from the E-region (see e.g. *Haldoupis, 2011*), as well as magnetic field aligned irregularities in the E- and F-region (e.g. *Yamamoto et al., 1991; Otsuka et al., 2012*).

As an example, meteors, that enter and ablate in the Earth's atmosphere leave an ionization trail, which drifts with the background wind and can be detected with rather small radar systems.

Radar measurements permit to determine the strength of the echo, its phase and spectral distribution, which depend on the specific target, the scatter process and the movement of the target. The width of the received spectrum gives an indication on the generation process, e.g. turbulence, while the center of the spectrum might be shifted due to the Doppler effect by the relative motion of the target and thus its line of sight velocity. Standard parameters that can be determined with radars in the MST-region are winds, wave parameters, and turbulence.

The strength of the radar echo depends on the radar characteristics and the reflectivity or scattering cross-section of the target. The incident power P_r can be calculated by the modified Friis transmission equation (*Friis, 1946; Hocking, 1985; Hocking and Röttger, 1997*).

$$P_r = \frac{P_t G_t G_r \lambda^2 e \theta_{[1/2]}^2 \eta c \tau}{128 \pi^2 2 \ln 2 r^2}, \quad (2.5)$$

where P_t is the transmitted power, G_r and G_t are the gain of the receiving and transmitting antenna, $\theta_{[1/2]}^2$ is the half-power half-width of the beam, λ is the wavelength, c is the speed of light, τ is the effective pulse width, r is the distance to the target and η is the volume reflectivity, which is related to turbulence. Alternatively to volume reflectivity, the classical radar cross-section σ can be used as follows (see e.g. *Johnson, 1993; Skolnik, 2008*).

$$P_r = \frac{P_t G_t G_r \lambda^2 \sigma}{(4\pi)^3 r^4}. \quad (2.6)$$

Both equations show that radar measurements can be used for quantitative studies of the scattering cross-section or reflectivity, which in turn depends on the structure of the atmosphere. This, however, requires precise knowledge of the radar system parameters such that a precise characterization of these parameters is of utmost importance.

2.3 Examples of atmospheric phenomena observed by radar at high latitudes

In case of MAARSY, a primary scientific focus is on two phenomena known as PMSE and PMWE. These are now shortly introduced.

Polar Mesospheric Summer Echoes (PMSE) are radar echoes that occur in the altitude range of 80-90 km at latitudes typically above approximately 55° (first seen and reported by e.g. *Czechowsky et al., 1979; Ecklund and Balsley, 1981*). The primary necessary prerequisite for this phenomenon is the presence of charged ice particles that form in the cold summer mesopause (≈ 130 K, see *Lübken, 1999*). These very low temperatures are caused by a mean vertical upwelling over the summer pole and thus adiabatic cooling (see e.g. *Garcia and*

Solomon, 1985; *Becker*, 2004). The driving mechanism of this flow is the momentum deposition by the breaking of gravity waves, which are named due to their restoring force, i.e., the Earth's gravity, which leads to buoyancy effects in a stably stratified atmosphere. The presence of gravity waves can be seen as periodic oscillations of the atmospheric variables like density, temperature and wind.

The presence of the charged ice particles reduces the diffusivity of free electrons and thus allows electron density fluctuations at the radar Bragg scale ($\lambda_B = \lambda/2$) due to neutral air turbulence. Without the presence of ice particles these structures would be destroyed by molecular diffusion (see *Rapp and Lübken*, 2004). These ice particles of nm-size can also be visually observed as so-called noctilucent clouds (NLC) by naked eye after dusk, when the sun still illuminates these altitudes, or actively by lidar-systems (see e.g. *Baumgarten et al.*, 2008).

In the northern hemisphere, the PMSE are seen in the altitude range of 80 to 90 km, where ice supersaturation exists (see e.g., *Lübken et al.*, 2002). A statistical analysis of the occurrence rate of PMSE at MAARSY's location for a full solar cycle is given by *Latteck and Bremer* (2013). An investigation of the microphysical parameters of PMSE is presented, e.g., in *Li et al.* (2010), analyzing observations at approximately 50 MHz and 500 MHz. A comprehensive summary of mesospheric radar echoes and the importance of charged aerosols is given in *Rapp et al.* (2012) for a broad frequency range.

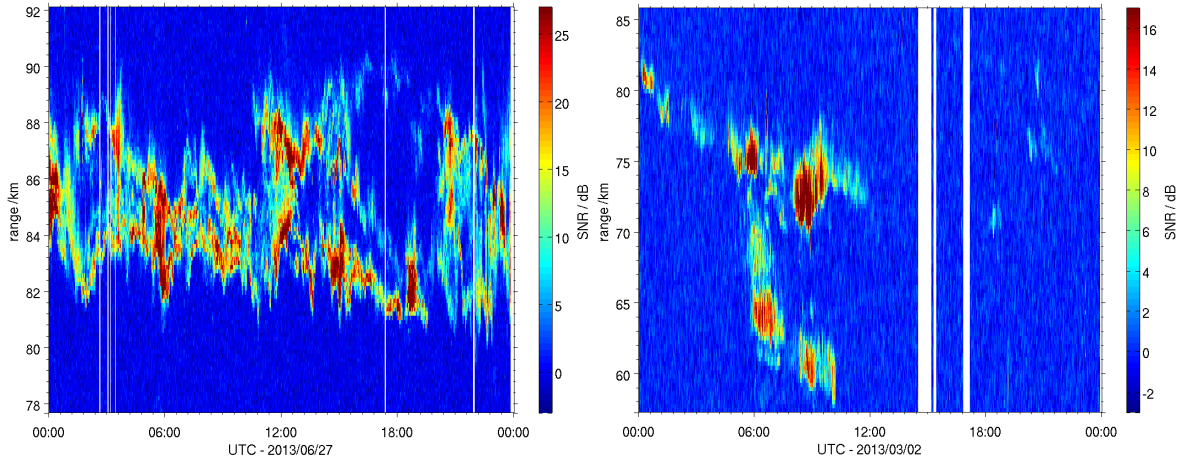
An example of PMSE observed with MAARSY is depicted in Figure 2.4(a), showing a high variability of the intensity and shape of the individual structures. A sketch of 97 quasi-simultaneously beam directions used in the PMSE campaign 2011 is depicted in Figure 2.5(a), see *Latteck et al.* (2012) for further information regarding this experiment. An example of detected signal-to-noise ratio (SNR) with this arrangement is shown in Figure 2.5(b). For the appropriate analysis and the combination of the data obtained from the individual beam directions to derive a comprehensive picture of the observations, the beam pointing directions and the shape of the radiation pattern need to be known. Results of the first spatially highly resolved observations of PMSE performed with MAARSY have been analyzed and presented recently in *Stober et al.* (2013a).

Polar Mesospheric Winter Echoes (PMWE) are a phenomenon mainly observed in the autumn to spring period, typically maximizing in winter in the altitude range from 50 km to 85 km at both, northern and southern latitudes (e.g. *Czechowsky et al.*, 1979; *Ecklund and Balsley*, 1981; *Czechowsky et al.*, 1989, for the northern and *Morris et al.* (2011) for the southern hemisphere). More recent observations confirm a relation to the geomagnetic activity, particle precipitation, cosmic noise absorption events and enhanced electron densities at these heights (see, e.g. *Zeller et al.*, 2006; *Lübken et al.*, 2007).

Lübken et al. (2006) showed that the presence of turbulence may quantitatively explain the observed echoes for an observation frequency of about 53 MHz, however observations performed by EISCAT at 224 MHz cannot be explained by pure turbulence (see e.g. *Strelnikova and Rapp*, 2013). Further mechanisms like the effect of charged aerosols (here: meteoric smoke particles) presumably have to play a role in combination with the neutral air turbulence, which necessitates further investigations. The first three-dimensional observations of PMWE were conducted with MAARSY and presented in *Rapp et al.* (2011b). An example of a PMWE event observed with MAARSY is depicted in Figure 2.4(b).

Besides the application of absolute power and range calibration, Figures 2.4(a) and 2.4(b) already incorporate also cosmic radio sources calibration including phase calibration methods. These two calibration methods are described in detail in Chapter 4.

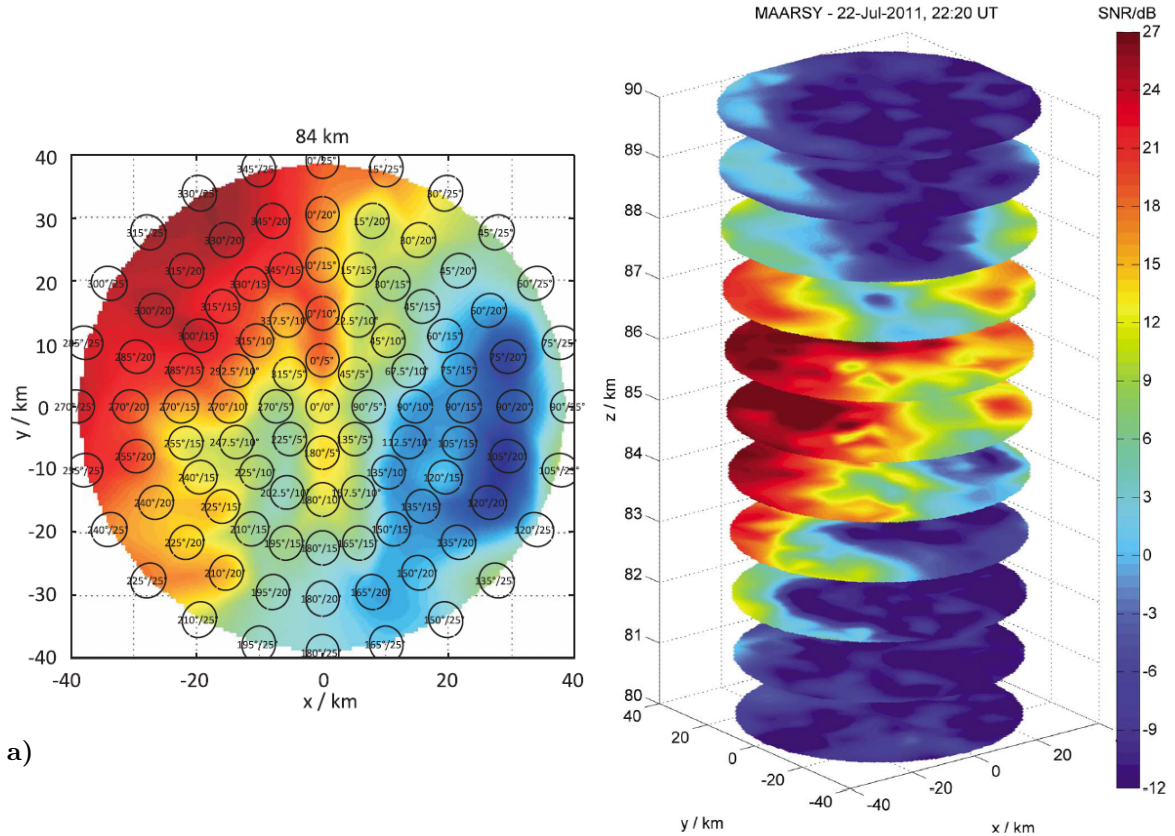
2.3 Examples of atmospheric phenomena observed by radar at high latitudes



a)

b)

Figure 2.4 Range-Time-Intensity plots of a) Polar Mesospheric Summer Echoes and b) Polar Mesospheric Winter Echoes observed with MAARSY, zenith beam. Note the differing range interval of approximately 78 to 92 km in a) and 57 to 86 km in b).



a)

b)

Figure 2.5 a) Sketch of the 97 beam positions used in the PMSE campaign 2011, projected for 84 km altitude. b) Signal to noise ratio for an observation of PMSE on 2011/07/22 depicted for 1 km altitude resolution, derived from 97 quasi-simultaneous beam direction. Taken from *Latteck et al. (2012)*.

Chapter 3 The Middle Atmosphere Alomar Radar System - system design and simulations of the radiation pattern

3.1 The design of the Middle Atmosphere Alomar Radar System (MAARSY)

This chapter introduces the MAARSY radar in general, the overall motivation for its construction, its design and abilities as well as its flexibility in terms of the experiment definition and e.g. the beam steering and receiver group selection. A brief technical description of the receiving system of this radar is given, reasoning the necessity of the calibration efforts, which are described in this thesis work. Furthermore, the lately performed conversion from linear to circular polarization is described and motivated. Subsequently, simulations for single beam pointing as well as examples of more sophisticated broad beam or multiple beams, generated simultaneously, are presented including the analysis of the radiation pattern properties. Furthermore, the feasible implementation of amplitude tapering for transmission is envisaged, which would ultimately improve the unambiguity of the radar observations. The system description of MAARSY, first results of its operation as well as some of the results presented here have already been published in *Latteck et al.* (2012), which was co-authored by the author of this thesis.

3.1 The design of the Middle Atmosphere Alomar Radar System (MAARSY)

In 2011 the Leibniz-Institute of Atmospheric Physics in Kühlungsborn (IAP) completed the installation of the Middle Atmosphere Alomar Radar System (MAARSY) on the North-Norwegian island Andøya. MAARSY allows classical beam swinging operation as well as experiments with simultaneous multiple beams and the use of interferometric applications for improved studies of the Arctic atmosphere from the troposphere up to the lower thermosphere with high spatio-temporal resolution. Especially the troposphere can be observed continuously (see Section 2.2), which allows to derive the 3-D wind field and its temporal evolution from e.g. 1 km altitude to the tropopause (typically 9 to 11 km height for the geographic latitude of MAARSY). However, the major focus of the IAP and thus also of MAARSY are observations within the mesosphere and the coupling processes to the adjacent altitude regions.

The predecessor of MAARSY was the ALWIN (ALomar WIND) VHF radar, which was built and put into operation in 1998. ALWIN was a classical Doppler beam steering radar with a phased antenna array of 144 4-element Yagi antennas (see Figure 3.1). The design and specifications are described by *Latteck et al.* (1999). This radar consisted of basically six channels for both the receiver and transmitter part and individual antenna subarrays. With this configuration beam steering to five different directions without the generation of grating lobes was possible. The individual receiver channels are typically combined with appropriate phases to form an identical narrow beam on reception. With this method the radial velocities of the scattering targets are derived from the Doppler shift of the incident signal. This method is called Doppler Beam Swinging (DBS, see *Woodman and Guillen* (1974) and references therein). The horizontal wind field is computed from the radial velocities of at least three, typically five, different directions with one vertical and four orthogonal beams. Complementarily, the Space Antenna technique (SA) was used (see e.g. *Briggs*, 1984; *Vincent et al.*, 1987; *Doviak et al.*, 1996; *Holloway et al.*, 1997), generally using the total array for transmission, forming a pencil beam. The signals of the six available antenna subarrays are analyzed by the Full Correlation Analysis (FCA) to derive the horizontal wind field. This radar was operated almost continuously for ten years, allowing new insights into e.g. the formation, occurrence rate and strength of the Polar Mesospheric Summer Echoes (PMSE) and Polar Mesospheric Winter Echoes (PMWE).



Figure 3.1 Photograph of the former ALWIN radar. The container in the left housed the radar equipment, while a part of the 144 4-element Yagi array is shown on the right.

The vertical resolution of typically 300 m, defined by the pulse width, could be improved by Frequency Domain Interferometry (FDI, see e.g. *Kudeki and Stitt, 1987; Palmer et al., 1990; Franke et al., 1992*) by the use of multiple frequencies and analyzing the phase differences of the individual frequencies within one range gate.

However, the main limitation of the ALWIN system was its beam steering capability connected to its radiation pattern at off-vertical directions and the data acquisition. The major drawback in terms of atmospheric science was ALWIN's inability to investigate the horizontal structure of the observed targets due to the limited amount of beam positions. For this purpose flexible beam steering and a better angular resolution were needed, accompanied by improvements on flexible experiment configurations, subarray selection, pulse coding and sensitivity.

These demands were the guideline for the design of the ALWIN successor, finally named Middle Atmosphere Alomar Radar SYstem (MAARSY).

MAARSY is a monostatic radar with an active phased array antenna as used with modern MST radars and employed by the MU radar in the early 1980s for the first time (*Fukao et al., 1980; Kato et al., 1984; Fukao et al., 1985a,b*), later for the Equatorial Atmospheric Radar (EAR, see *Fukao et al., 2003*) and more recently for the PANSY radar at the Antarctic Syowa station (under construction, see *Sato et al., 2011*). The operational frequency of MAARSY is 53.5 MHz and the maximum peak power is approximately 800 kW. The nearly circular antenna array with a diameter of approximately 90 m corresponding to an aperture of $\approx 6300 \text{ m}^2$ results in a symmetric antenna radiation pattern. This antenna array facilitates the generation of a pencil beam with a width of minimum 3.6° , a gain of 33.4 dBi and a side lobe suppression of approximately 17.5 dB.

The radar hardware, namely e.g. transceiver modules for each individual antenna, synchronization, reference, control and monitor units, the generation of the local oscillator signal and pulse forming are housed in six containers surrounding the antenna array. This distributed structure allows the limitation of the necessary length of coaxial cables feeding the antennas

3.1 The design of the Middle Atmosphere Alomar Radar System (MAARSY)

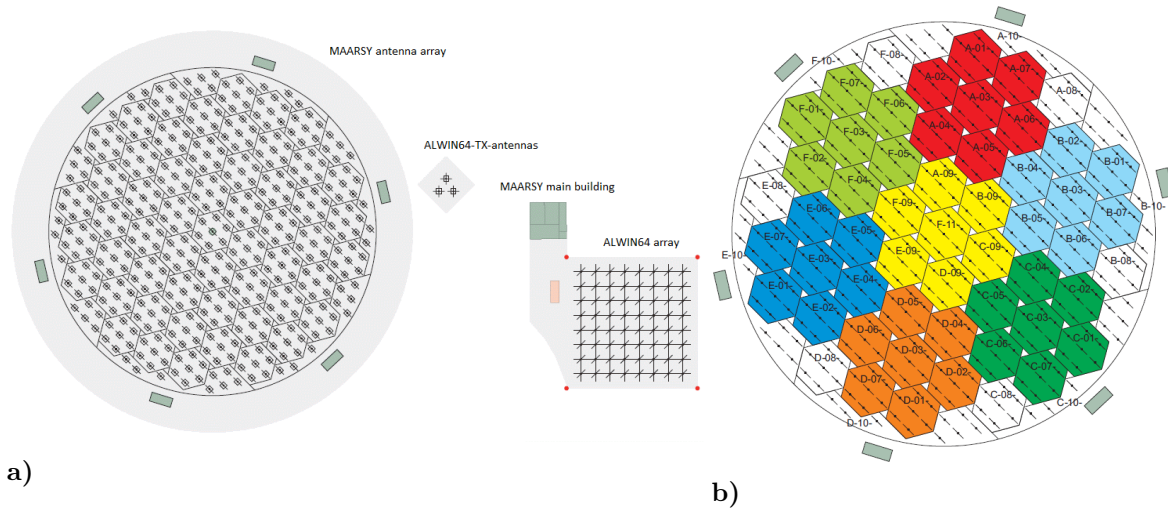


Figure 3.2 a) Sketch of the VHF radar site MAARSY, left the 433 element MAARSY array, accompanied by the ALWIN64 array, three individual ALWIN64 transmit antennas and the main building. b) Drawing of the total antenna array MAARSY, colored groups form seven Anemones named MAARSY343, the entire antenna array is called MAARSY433 in this work. Taken from *Latteck et al. (2012)*

and therefore signal losses for both transmission and reception and also costs. However, this distributed hardware inherently requires considerable efforts to synchronize the six containers reliably. The size of the antenna array was defined by the available space at the position of the former ALWIN radar, where the availability of infrastructure and support by the Andøya Rocket Range (ARR) prevailed the option of acquiring a new site for the radar. Various array characteristics have been studied and evaluated in a concept study for a planned EISCAT3D-radar (*Renkowitz, 2008*), whose results also contributed to the design of MAARSY. Thus, the array architecture was changed from a squared grid structure like it was used for ALWIN to an equilateral grid structure, allowing increased beam steering capability and a different shape of subarrays. The available space for the antenna array and the projected beam steering capability to at least 30° off-vertical resulted in an antenna spacing of approximately 0.71λ wavelength, which equals 4 m. The circumference of the antenna array should have a circular shape other than the squared shape of ALWIN, which affects the shape of side lobes and their suppression. The sketch of the antenna array composed of 433 elements is shown in Figures 3.2(a) and 3.2(b) accompanied by the dedicated antenna and subarray identifier.

The smallest subarray groups, which can be seen in see Figure 3.2(b), were defined to be composed of seven antennas. One antenna in the center and six surrounding antennas form a hexagonal shape, leading to its given name Hexagon. Even though every single antenna is connected to its designated transceiver module, on reception the output of a Hexagon subarray is combined on the intermediate frequency (IF). This configuration allows the flexible beam steering of all antennas for transmission and reception, but limiting the amount of individual receiver channels.

Combining seven Hexagons forms a subarray group of 49 antennas, named Anemone, corresponding to the similar shape of the anemone flower. Combining seven Anemones incorporates an array of 343 elements, named MAARSY343, which is mainly used and analyzed

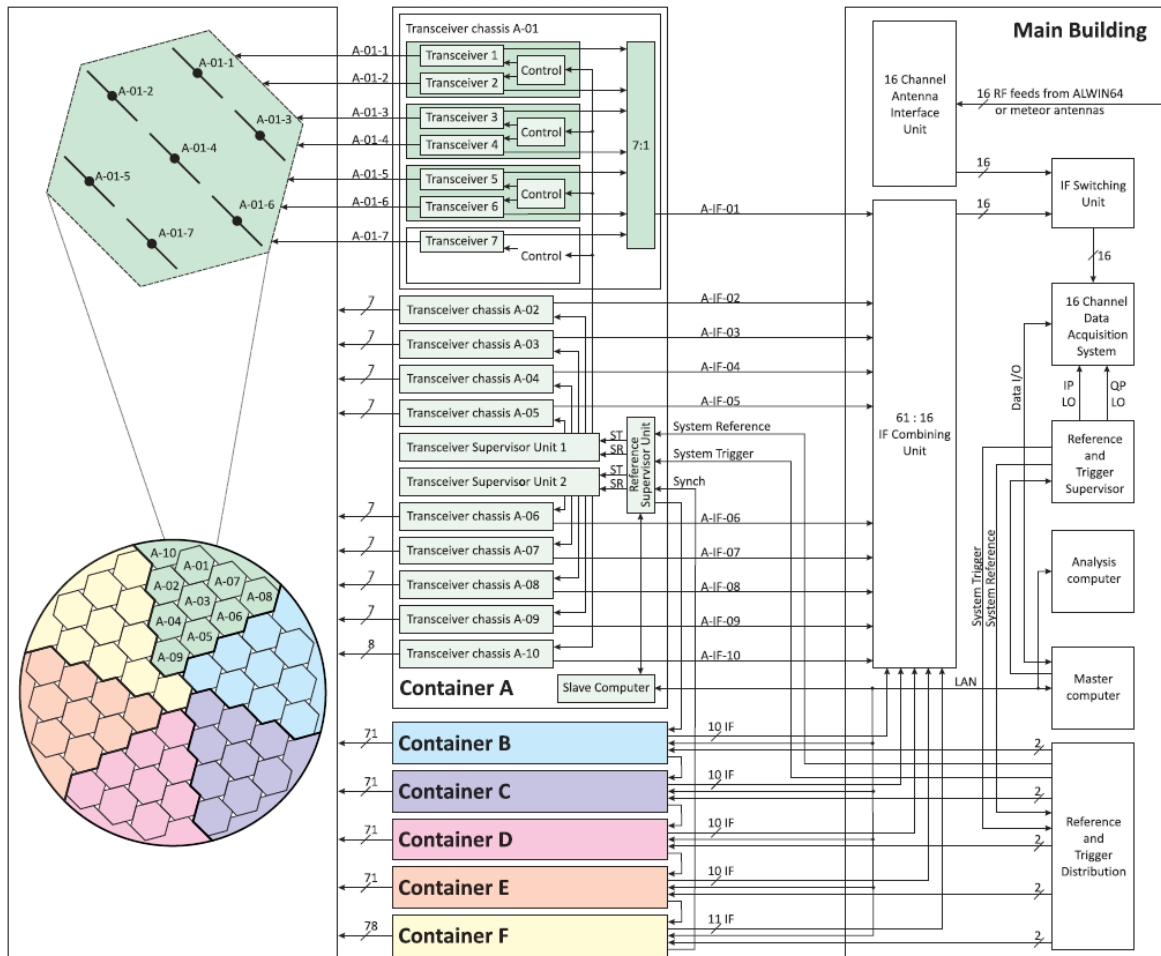


Figure 3.3 Block diagram of the MAARSY system, taken from *Latteck et al.* (2012). The left column shows the antenna array with magnified Hexagon subgroup, connected to its dedicated transceiver modules and subsequent Hexagon combiner, placed in the containers surrounding the array (middle column). In total 61 individual IF signals are connected to the combining and switching units in the main building, where the user selected groups are finally feeding the baseband receivers. For transmission, the individual signals are generated in the transceivers, triggered and disciplined by appropriate trigger and reference signals from the main building.

thoroughly in this thesis.

The usage of the entire array will be marked by MAARSY433, respectively.

Not included in the Anemones are the Hexagons "8", which are located almost at the circumference of the array, but still have a regular Hexagon shape. The antennas placed directly at the rim of the array could not be used to form an equivalent Hexagon structure, but six patches each composed of eight scattered antennas are combined to form the groups named "10". Even though, these subarray groups are not incorporated in the Anemones, they are of importance to the combination of the entire antenna array (MAARSY433) and their individual use for interferometric purpose. In total 55 regular Hexagon IF channels plus six scattered groups ("10") are transferred to the main building at the MAARSY site, where

3.1 The design of the Middle Atmosphere Alomar Radar System (MAARSY)

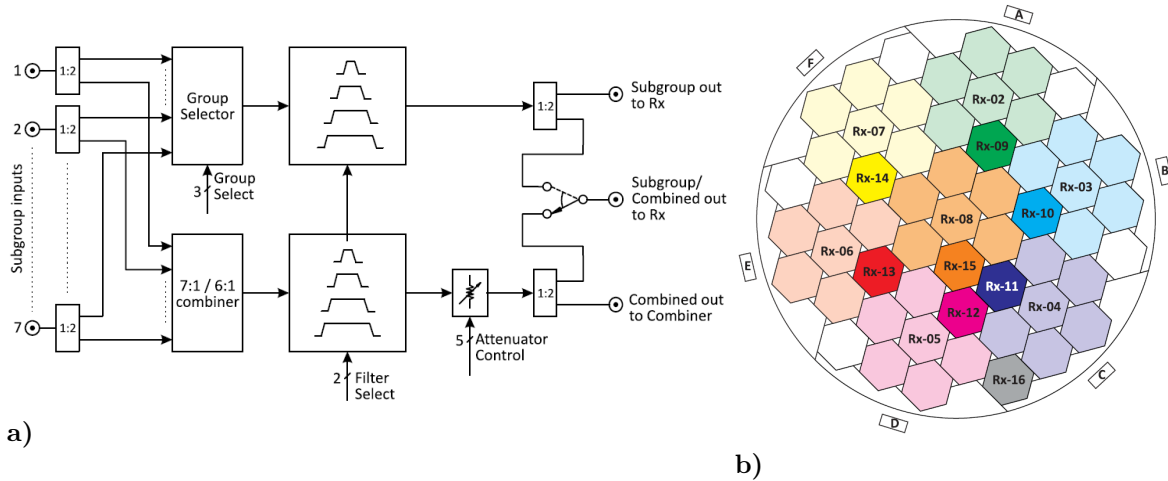


Figure 3.4 a) Sketch of MAARSY’s IF switching and combining unit (IFSCU), taken from *Latteck et al. (2012)*. b) Selection of different array subgroups, RX-01 for the total MAARSY433 array, RX-02 to RX-08 seven Anemones, RX-09 to RX-16 eight Hexagons.

they are connected to the IF receivers.

The final nomenclature of the array antennas is depicted in Figure 3.2(b), which was defined to be named in the systematic ”container”-”Hexagon”-”antenna no.”, e.g. B-06-3.

The block diagram of the MAARSY system with its main components is depicted in Figure 3.3. The receiver was initially limited to eight channels, but quickly expanded to a system with 16 individual channels for both the in-phase and quadrature components (I/Q) of the complex signal. Therefore, a selection of subarray groups can only be connected to the available 16 receiver channels. To enlarge the flexibility a switching and combining unit a) forms the Anemone signals, b) splits the Hexagon inputs to allow c) the user defined selection of either the combined Anemone or an individual Hexagon signal onto the dedicated receiver channels, complemented by four user selectable filters (see upper right part of Figure 3.3 and Figure 3.4(a) for more details). The amount of selectable subarray groups facilitates the flexibility of experiment configurations and thus MAARSY’s prospects.

Besides the individual subarray groups, a hardware combined signal of the entire antenna array is available on one of the 16 channels, incorporating the theoretical maximum gain and minimum beam width. Just this channel may be used for the classical DBS method. Besides this hardware combined MAARSY433, the individual Anemones and Hexagons or external antennas can be connected to the receiver. Contrary to the hardware combined MAARSY433, MAARSY343 is combined in software, where the signals of the seven Anemones are integrated with proper phase settings. MAARSY343 is the largest subarray of MAARSY that is generally available besides the hardware combined MAARSY433.

For a typical experiment, the signals of the hardware combined total array, the seven Anemones, and eight Hexagons were configured and sampled. Such a configuration and selection of different receiver groups is indicated in Figure 3.4(b). The subarray groups may be selected depending on the needs of the particular experiment, e.g. beam width, gain, base line length between the individual groups for the analysis by interferometric means.

This receiver architecture was expanded by additional 16 full receivers (53.5 MHz down to IF, named Antenna Interface Unit) to allow the usage of antennas outside the MAARSY antenna array, e.g. dedicated meteor reception antennas, or the ALWIN64 array. The co-

located ALWIN64 array is a remnant of the earlier ALWIN radar, which has been used to bridge the time between the decommissioning of ALWIN and the first operation of MAARSY. This array of 64 4-element Yagi antennas has e.g. also been used to observe cosmic radio emissions (*Renkowitz et al.*, 2011).

All MAARSY transmitter modules permit the definition of multiple amplitude and phase settings of their output signal for each experiment individually, which facilitates versatile beam forming and pointing. To increase the reliability and stability of the radar, various parameters are continuously monitored like the output power and temperature of the transmitters and their power supplies as well as the reflected power from the corresponding antenna. This monitoring system is not only of importance for quality control (e.g. monitoring the output power and impedance match of the antennas), but also to prevent damages to the components due to total failures of e.g. the air conditioning system or antennas and their feeding cables.

The first radar hardware was integrated in the beginning of 2010 and subsequently expanded to full operation with the entire antenna array and their transceiver modules in 2011. During this time and afterwards several improvements and updates have been implemented enriching the functionality of the system and increasing its ruggedness. For example, the improvement of the receiver dynamic range was one major issue, which is also documented in this thesis (see Section B.3).

3.2 The MAARSY array element

The individual MAARSY antenna has been designed under several requirements. The antennas within the array should not be fixed by ropes anymore, as it was done for ALWIN, but self-supporting. Following this and due to some mechanical issues that have been encountered in the past with ALWIN at the Atlantic shore, it was agreed to increase the robustness of the antenna by thickening the elements, which at the same time slightly increases its available bandwidth around the operating frequency. The antenna array element should be limited to a rather short 3-element Yagi antenna to minimize the gain loss for off-vertical beam pointing, which is dependent on the half-power beam width of the individual array element. The use of short pulses in the order of $0.33\mu s$ ($\hat{=}$ 50 m range resolution) requires a bandwidth of at least 3.5 MHz, what needs to be provided by the antenna. Considering the usage of FDI (multiple nearby frequencies) and the necessary reserve, the total planned bandwidth should be in the order of 5 MHz, what coincides with the allowance by the Norwegian regulatory authorities for this radar. The designed 3-element Yagi antenna is composed of a folded dipole of 20 mm diameter tubes and 30 mm diameter tubes for director and reflector. The impedance of the design is in the proximity of 200Ω , which is transformed to 50Ω impedance of the coaxial cables by a half-wavelength balun (converts the balanced signal of the antenna to the unbalanced coaxial cable). The director and reflector elements are electroconductive and friction-locked mounted to the antenna mast to ensure mechanical sturdiness. Due to the length of the elements up to 3 m and availability of weather-proof casings, in which the balun and the connection to the dipoles are housed, a width of 12 cm for the mast was decided. However, the proximity of the antenna elements to the massive mast and the electroconductive mounting leads to a significant influence on the electro-magnetic design of the antenna and the so-called boom-correction (see e.g. *Viezbicke*, 1976) needs to be applied. The boom-correction represented by lengthening of the elements was calculated to be in the order of half the mast diameter, which was confirmed by the prototypes built

3.2 The MAARSY array element

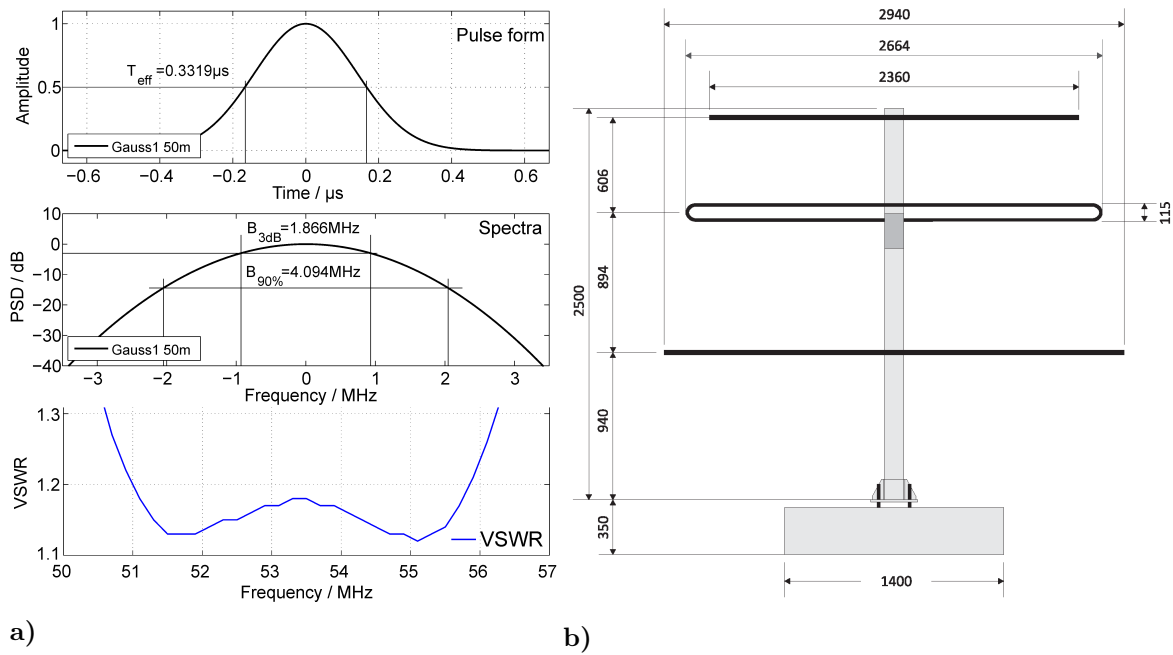


Figure 3.5 a) Shape and frequency width of a $0.33 \mu\text{s}$ pulse accompanied by the simulated band width of the MAARSY antenna in form of a voltage standing wave ratio (VSWR). b) Drawing of the MAARSY array element. Taken from *Latteck et al. (2012)*.

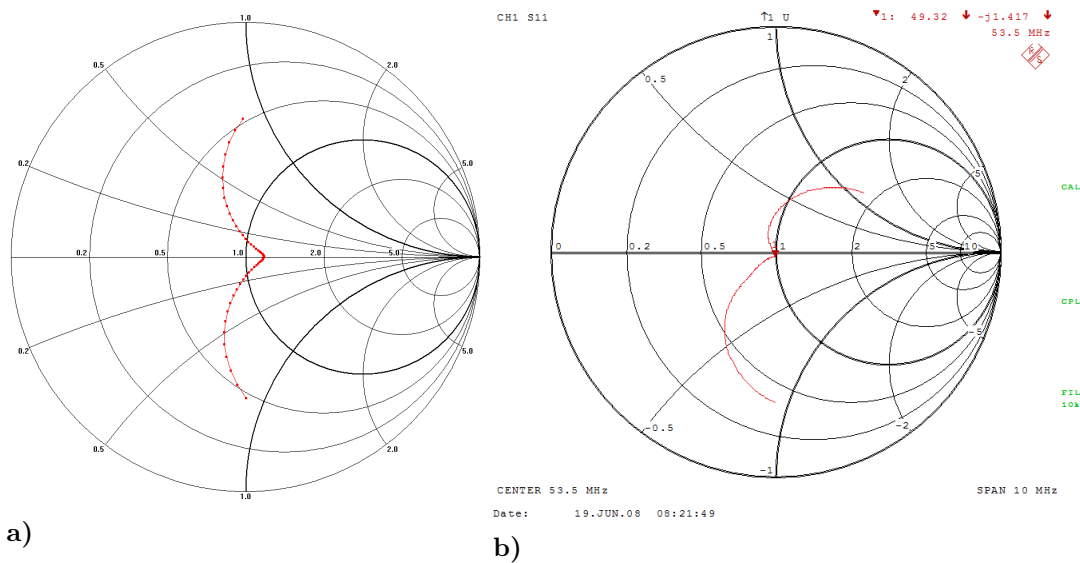


Figure 3.6 a) Simulated impedance of the MAARSY antenna depicted in a Smith-chart and b) measured impedance of the prototype antenna.

by IAP personnel.

The proposed design and layout have been evaluated by a structural engineer, demanding a sufficient foundation of the individual antennas to safely withstand the harsh winds at the Atlantic coast.

The final arrangement of the individual antenna of which the total array has been built in

the summer of 2009 is depicted in Figure 3.5(b). The simulated and measured impedance of an individual MAARSY antenna is depicted in the Figures 3.6(a) and 3.6(b) respectively, which agree pretty accurately. The approximately 10° rotation of the curve is introduced by the feeding cable within the dipole-box from the connector socket to the dipole/balun. Reference measurements of the MAARSY array elements are shown in the Appendix in Section B.1, corroborating the properties of the prototype and the simulations.

The properties of the coaxial cables connecting the transceiver modules with the antennas as well as the coaxial cables delivering the combined intermediate frequency (IF) signals of the subarray Hexagon groups to the IF to baseband receiver in the main house were examined before their installation at the radar. The measured characteristics are presented in the Section B.2 in the Appendix.

3.3 The polarization upgrade of MAARSY

After completing the radar hardware, the MAARSY antenna array was subject to a polarization upgrade, which was motivated by various points. First of all, the successful use of only one linear polarization requires the undisturbed propagation of the transmitted linearly polarized wave to the target, followed by a 180° reflection at the target and undisturbed return path. However, depending on the specific target the linearly polarized wave might be modified and thus receiving both perpendicular linear polarizations would be needed to detect the entire energy. Equation 3.1 describes the polarization efficiency ϵ_p , or polarization loss for two linearly polarized waves by the dot product of the unit polarization vectors of the incident wave \mathbf{p}_i at the reference polarization \mathbf{p}_r (see e.g. *Johnson, 1993; Balanis, 2005; Kraus, 1997*, for further information)

$$\epsilon_p = |\mathbf{p}_i \cdot \mathbf{p}_r^*|^2 = \cos^2 \psi. \quad (3.1)$$

The polarization of an electromagnetic wave is defined with the orientation of the electric field \mathbf{E} as follows:

$$\mathbf{p} = \frac{\mathbf{E}}{E} \quad (3.2)$$

The wave polarization can also be expressed with the components

$$\mathbf{p} = \frac{E_y}{E_x} = -\frac{H_x}{H_y}, \quad (3.3)$$

where the z-component is oriented with the direction of the wave-normal (see e.g. *Budden, 1961*).

The relation of general polarization states is shown in Figure 3.7 (referring to Equation 3.1), where the left panel depicts the angular dependency of an incident linearly polarized wave received with an antenna of linear polarization, clearly marking the theoretically perfect decoupling for orthogonal geometry. The right panel shows the inherent loss of signal intensity received by a circularly polarized antenna for an incident signal of elliptical polarization. The axial ratio describes the power distribution of both orthogonal planes of the propagating elliptically polarized wave, where 1 forms a perfectly circular and 0 linear polarization. Thus, as an extreme case, only half of the power from an incident linearly polarized wave is received with a circularly polarized antenna and vice versa.

3.3 The polarization upgrade of MAARSY

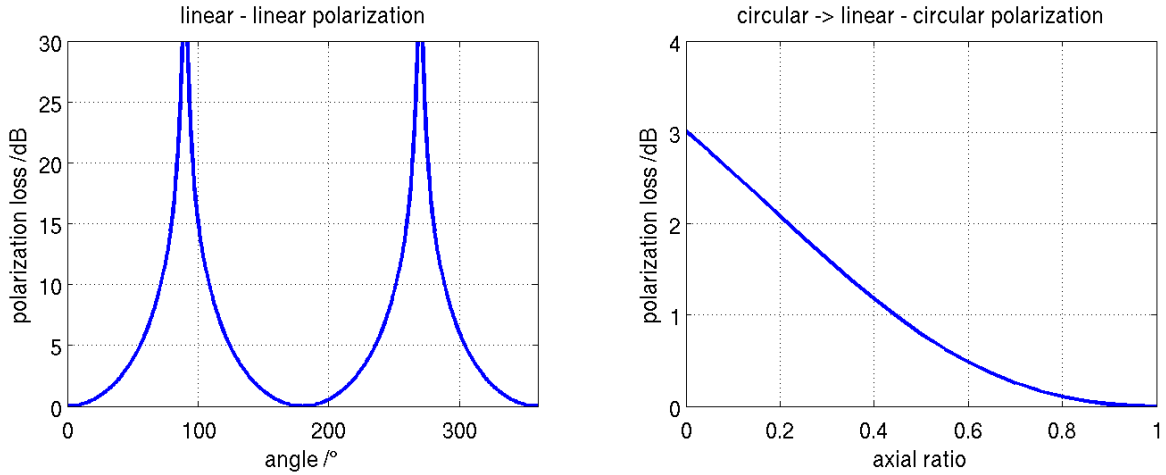


Figure 3.7 The left panel depicts the angular dependency of an incident linearly polarized wave received with a linearly polarized antenna. The right panel shows the inherent loss of an elliptically polarized wave received with a circularly polarized antenna.

The motivation for the polarization upgrade is the Faraday effect, which causes a rotation of the polarization plane of a propagating wave. The Faraday effect is linearly proportional to the magnetic field strength along the direction of propagation. The linear polarization can be expressed as the sum of two circular polarizations with opposite sense. Due to the propagation of the wave through a magnetized plasma with different real parts of refractive indices the phase difference of the two circular wave components is modified and thus the orientation of the resulting linearly polarized wave. This polarization modification reaches altitudes as low as 90 km at the polar latitude of MAARSY as the magnetic field vector is normally oriented at approximately 12.3° zenith angle and 185.3° azimuth (see e.g. *IAGA et al.*, 2010; *Chau et al.*, 2013a).

Furthermore, off-vertical beam steering results in superposition of the transmit signal of the antenna itself and the coupled signal of the adjacent antennas. This coupled energy is traveling to the transceiver modules and is "falsely" detected as return power of the own transmit signal, making it appear as if the antenna had a high Voltage Standing Wave Ratio (defining the impedance match to the system). A high VSWR typically indicates a poorly matched antenna and thus is e.g. treated as non-functional leading to switching-off of the connected power amplifier. This subsequently manifests in two ways, a) the transmit energy is lost in the total transmit power due to the missing power amplifier and b) the radiation pattern is likely distorted as the regular equilateral grid structure of the array is corrupted. Depending on the explicit beam pointing direction in some experiments up to ten percent and more of the power amplifiers were switched off due to VSWR alarm, leading to a power loss of 0.5 dB and likely disturbed suppression of side lobes. It was found that circularly polarized antennas are not as strongly influenced by active coupling as linear polarized antennas in the array are. This is mainly caused by their more uniform radiation pattern and thus coupling to the adjacent antennas.

To generate circular polarization both perpendicular planes have to be fed with orthogonal signals, where the sense of the 90° phase difference defines the direction of rotation.

A dedicated polarization unit was built for MAARSY, which incorporates the switching of

Chapter 3 The Middle Atmosphere Alomar Radar System

period	MAARSY433	MAARSY343	circularly polarized subarrays
until Aug. 2012	linear	linear	none
Sept. 2012 - May 2013	mainly linear	mainly linear	M, B-08
May 2013 - Sept. 2013	mixed	circular	A - M, B-08
since Sept. 2013	circular	circular	all

Table 3.1 Individual periods of MAARSY's conversion from linear to circular polarization.

the rotational sense for receive (right hand) and transmit (left hand), which is mounted directly at the antenna masts.

The first subarray groups of MAARSY were converted to circular polarization in September 2012, namely the middle Anemone M and the Hexagon B-08. In May 2013 the remaining six Anemones were converted, completing MAARSY343, followed by the antennas at the circumference of the array, modified in September 2013. Table 3.1 summarizes the individual periods of MAARSY's polarization conversion.

3.4 Simulations of the radiation pattern of MAARSY using NEC

Simulations of the antenna array radiation pattern in this thesis are performed using Numerical Electromagnetic Code in the version 4.1. NEC is a user-oriented software package developed by the Lawrence Livermore National Laboratory. The purpose of NEC is the analysis of the electromagnetic response of antennas and e.g. their mutual interaction and with their environment.

NEC is based on a Method of Moments (MoM) code for analyzing the interaction of electromagnetic waves emitted from the individual parts of the antenna structure and defined incident waves. Within NEC arbitrary conducting structures, formed by wires and subdivided in segments, may be modeled. The individual wires or wire patches are typically defined in Cartesian coordinate system, while the output is often requested in spherical coordinates as depicted in Figure 3.8. The point P can thus be defined by the zenith angle θ and the azimuth angle ϕ , which is oriented oppositely to the commonly used geographic direction. The code bases on the numeric solution of the integral equations for both, the electric field for thin wires and the magnetic field of conducting surfaces. The defined antenna structures in the models can be excited by e.g. voltage sources as it is done for the MAARSY antenna array in reality.

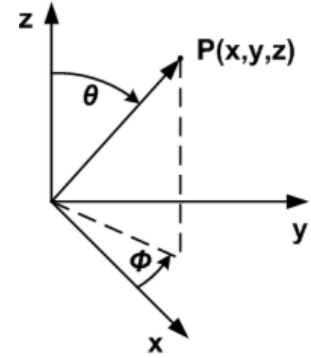


Figure 3.8 Coordinate system used for the NEC simulations.

The output data of NEC contains current distributions, impedances, power input, dissipation, efficiency and radiation patterns with gain or cross-section. The applicability of NEC for the simulations of VHF antenna arrays and thorough use have al-

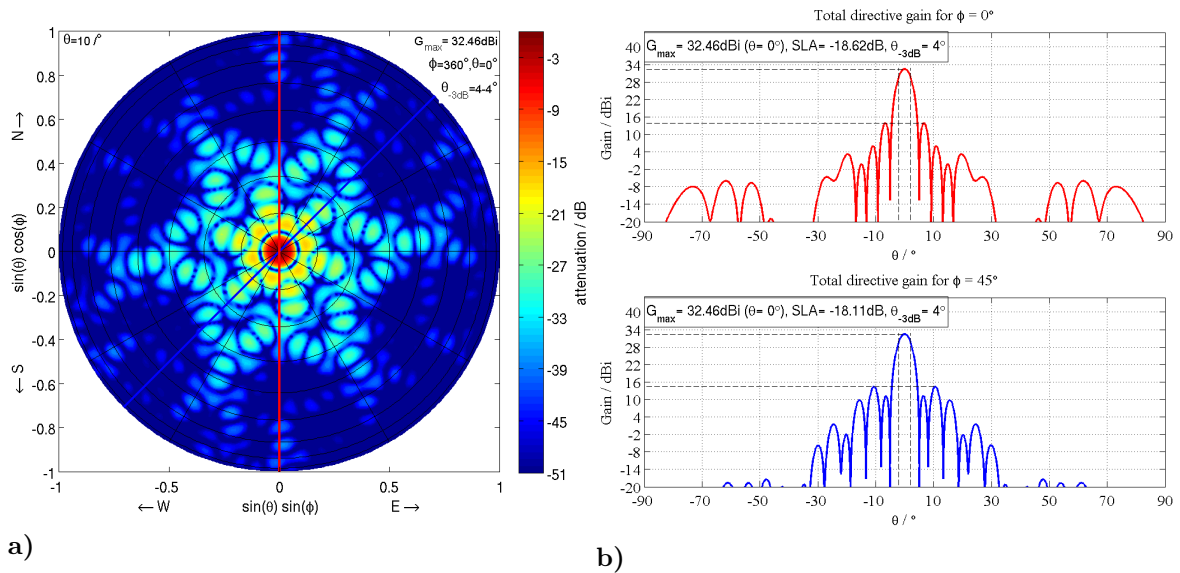


Figure 3.9 a) Computed radiation pattern of MAARSY343, formed by seven Anemone subarray groups, pointing vertical in top-view overlaid by colored lines indicating the cross-sections depicted in b) along $\phi = 0^\circ$ and 45° .

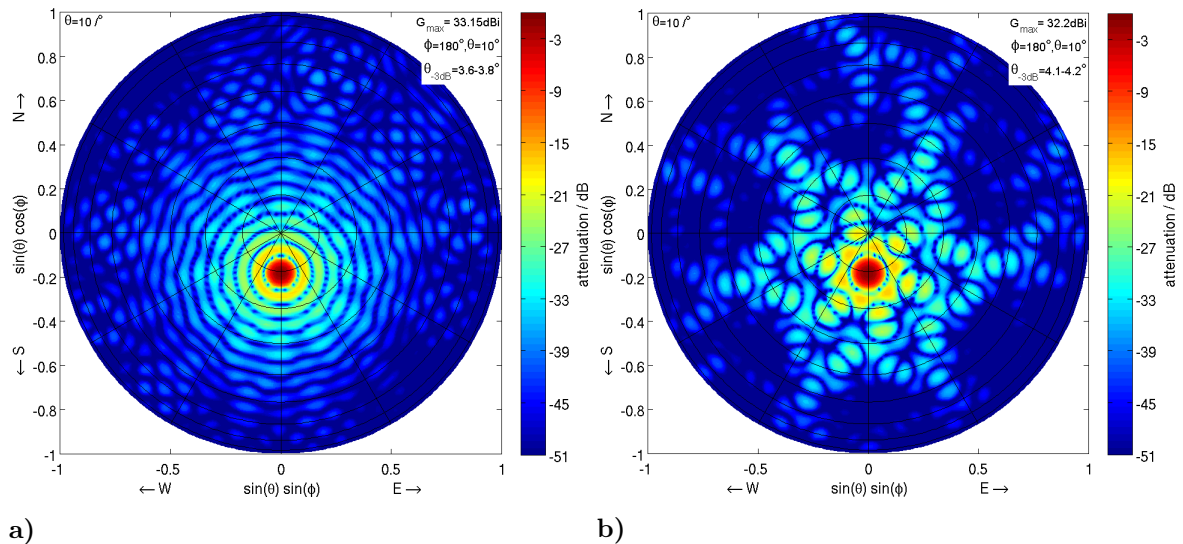


Figure 3.10 Computed radiation pattern of **a)** MAARSY433 and **b)** MAARSY343 pointing to $\phi = 180^\circ$, $\theta = 10.5^\circ$, depicted in top-view.

ready been described in *Renkwitz* (2008). The radiation pattern cross-sections are typically computed with a resolution of 0.1° , where for the surface and top-view plots typically 1° is used. The radiation pattern of MAARSY433 and MAARSY343 for boresight pointing are depicted in Figures 3.9(a) to 3.9(b) respectively. Figures 3.10(a) and 3.10(b) show the radiation pattern of MAARSY433 and MAARSY343 for $\theta = 10.5^\circ$ off-vertical pointing. The shown radiation pattern are characterized by generally symmetric structure, and a suppression of the side lobe in the order of at least 17 dB. A detailed direct comparison of the radiation pattern of MAARSY433 with MAARSY343 is shown in Figure 3.11(a) for vertical and 3.11(b) for two off-vertical beam pointing directions. In these pattern, the generally clean pattern is conserved also for high beam pointing close to 30° off-zenith. The beam pointing positions of $\phi = 180^\circ$, $\theta = 10.5^\circ$ and $\theta = 28.5^\circ$ are of particular importance for this thesis as cosmic radio sources are observed at these off-vertical angles to verify the properties of the actual radiation pattern.

Subsequently, the performance of the MAARSY antenna array is evaluated for both the hardware combined MAARSY433 and the software combined MAARSY343. The main focus here is the beam steering flexibility and the purity of the radiation pattern for the perfectly fed antenna array.

A more sophisticated investigation of radiation pattern performance, comparing the main lobe to all side lobes is presented in the Appendix in Section A.2 for MAARSY and other atmospheric VHF radar systems.

In Section A.3 of the Appendix, the modification of MAARSY's radiation pattern caused by amplitude and phase errors as well as failures of individual transceiver module and antenna combinations are presented. This allows to estimate the impact of variations or failures to the radiation pattern's properties for the specific experiments performed with the radar.

3.4 Simulations of the radiation pattern of MAARSY using NEC

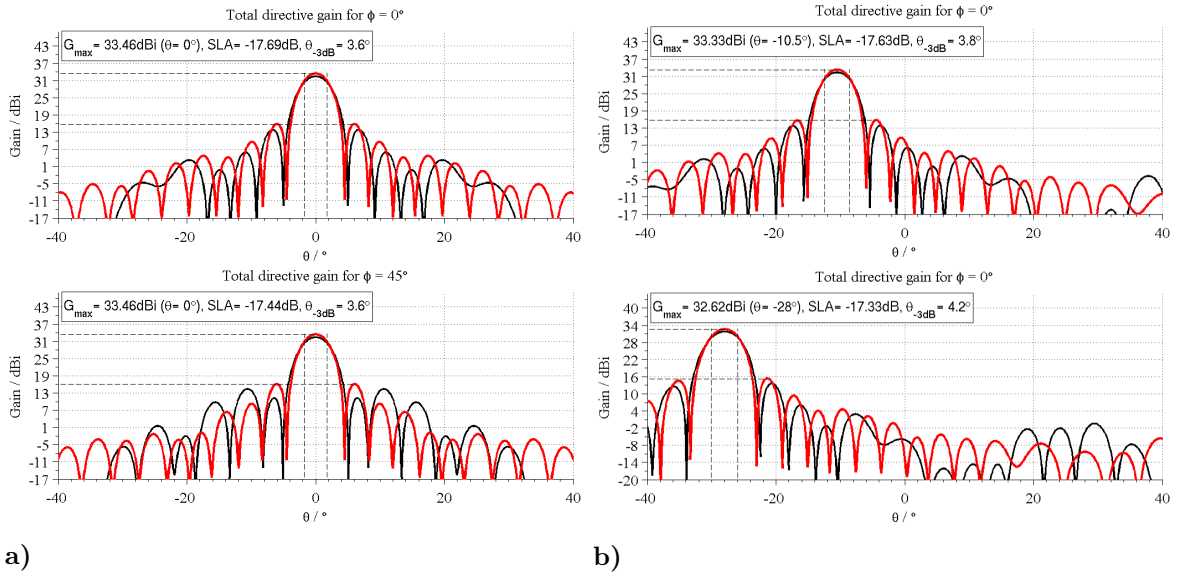


Figure 3.11 a) Computed radiation pattern of the hardware combined MAARSY433 (red) and the software combined MAARSY343 (black) pointing vertical for two cross-sections $\phi = 0^\circ$ and 45° . b) Comparison of MAARSY433 (red) and MAARSY343 (black) pointing to $\phi = 180^\circ$, $\theta = 10.5^\circ$ and $\theta = 28^\circ$.

(sub)array	gain	θ_{-3dB}	1st side lobe	1st null	2nd side lobe		
Hexagon	15.5 dBi	30.7°	55.0°	-21.2 dB	40.2°	-	-
Anemone	23.9 dBi	11.0°	18.5°	-15.9 dB	13.4°	30.6°	-35.4 dB
MAARSY343	32.4 dBi	4.0°	6.6°	-16.2 dB	5.0°	11.1°	-24.2 dB
MAARSY433	33.4 dBi	3.6°	6.0°	-17.4 dB	4.5°	10.1°	-24.5 dB

Table 3.2 Simulated gain, beam width, the position and suppression of the 1st and 2nd side lobe and position of the 1st null in MAARSY's radiation pattern for unity amplitude distribution and boresight pointing.

3.5 Array performance of MAARSY

The radiation pattern of almost all real directional antennas is composed of a wanted main lobe and unwanted side lobes, separated by nulls. Typically, for focussing antennas, the main objective in designing an antenna or arrays of antennas is to concentrate the most intensity in the main lobe and thus minimize the level of side lobes. Side lobes pick up additional noise and arise the likelihood for interferences to and from other systems that operate on the same frequency.

To characterize a radiation pattern the gain of the antenna, the beam width and the position and intensity of the first and second side lobes as well as the position of the first null are typically used. The main characteristics for the two largest arrays available for MAARSY (MAARSY433 and MAARSY343) and the subarrays Hexagon and Anemone are shown in Table 3.2.

The angular beam width of the main lobe of an antenna array depends on the maximum distance of the antenna elements (L) with respect to the wavelength (λ),

$$\theta_{-3dB} = \arcsin \left(0.886 \cdot \frac{\lambda}{L} \right), \quad (3.4)$$

where the array does not need to be filled mandatorily (see e.g. *Mailloux*, 1994). This is valid for simple array elements, like dipoles or short Yagi antennas with a boom length significantly smaller than the wavelength. However, the gain, the side and grating lobes are highly influenced by the amount and spatial distribution of antennas within an array. The intensity of side lobes is affected by e.g. a) the distance between the array elements and b) the shape of the circumference of the array. For MAARSY a completely filled array with 0.71λ equilateral spacing between the array elements has been chosen as a compromise of various factors. This configuration ensures a symmetrical antenna pattern, a beam steering capability down to $\theta = 30^\circ$ and mainly uniform subarray antenna groups (Anemone, Hexagon).

MAARSY433 uses the total antenna array, generating a pencil beam of minimum beam width ($\theta_{-3dB} = 3.6^\circ$) and good side lobe suppression (> 17.5 dB) - see Figure 3.11(a). These properties are independent of the azimuth pointing direction, however, the off-zenith pointing angle affects the beam width as the effective area varies. This beam broadening can be computed by Equation 3.5, where θ_{3b} describes the resulting beam width for a beam with the boresight width θ_{-3dB} steered to θ_s .

$$\theta_{3b} = \theta_{-3dB} / \cos \theta_s \quad (3.5)$$

Another form of undesired radiation pattern disturbances are grating lobes, which are only generated for off-boresight pointing of an antenna array. The generation and the position of grating lobes depend on the distances between the individually fed array elements (independent phase) that are placed on a regular grid structure and the specific pointing direction. Grating lobes are generally only generated in real space for element distances greater than 0.5λ , where the individual phases are unambiguous. The occurrence of grating lobes is calculated by

$$\pi \frac{d}{\lambda} [\sin \theta_g - \sin \theta_0] = \pm n\pi, \quad (3.6)$$

where θ_g and θ_0 are the zenith angles of grating and main lobe respectively (see e.g. *Mailloux*, 1994).

3.5 Array performance of MAARSY

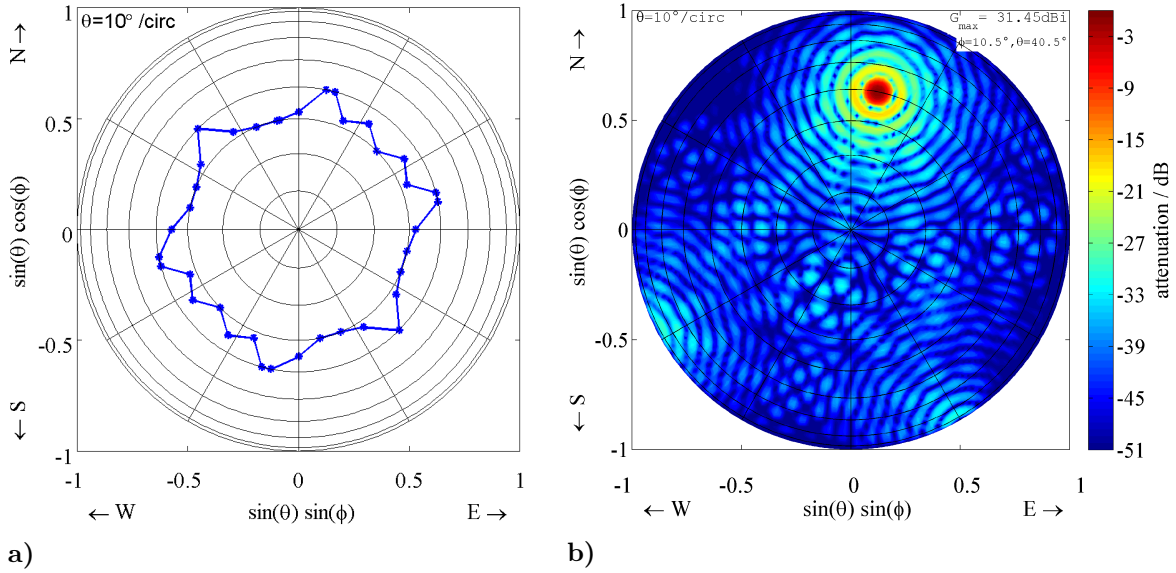


Figure 3.12 a) Sketch of the maximum zenith beam pointing angle for the linearly polarized MAARSY avoiding the generation of grating lobes derived from simulations. b) Exemplary radiation pattern in top-view of the total MAARSY array pointing to $\phi = 11^\circ, \theta = 40^\circ$. For this large off-vertical pointing no direct grating lobes are seen, however their side lobes are already generated into south-eastern and south-western directions.

As mentioned before, the MAARSY antennas are placed on an equilateral grid with a spacing of 0.71λ . For this array structure the grating-lobe-free beam pointing area is depicted in Figure 3.12(a). The maximum grating-lobe-free off-zenith pointing varies between approximately 30 to 40 degrees, depending on the actual azimuth direction. An example for high off-zenith beam pointing of MAARSY is shown in Figure 3.12(b), where the main beam is pointed towards $\phi = 11^\circ, \theta = 40^\circ$, while no direct grating lobe of the main beam is generated. However, side lobes of two grating lobes can already be seen in south-western and south-eastern directions.

The detailed analysis of the radiation pattern quality of MAARSY and other MST radars is presented in the Appendix in Section A.2.

3.6 Special beam forming - simultaneous multi-beam meteor observations

For classical radar applications the total antenna array is used to form a narrow pencil beam, combining all antennas with appropriate phases to steer the main beam to a specific direction. However, for some experiments with an atmospheric radar it might be advantageous to illuminate a larger area of the sky. As an example, the observation of specular meteors ablating in the mesosphere is typically performed by the use of a single antenna on transmission and five individual antennas, used as interferometer, for reception (see Figure 3.13 and *Jones et al.*, 1998). Such simple configurations allow the detection of meteors and the unambiguous estimation of their positions relative to the radar and their trajectories. Similar observations performed with MAARSY could possibly provide very high count rates of meteors given the large total output power of the radar.

For the detection of such meteor plasma trails the radar wave needs to intercept the meteors trajectory perpendicular to maximize the return power (see Figure 3.13). At the same time the effective collecting area in the mesosphere increases for off-zenith beam pointing, where the likelihood of a meteor detection to zenith is very low due to the possible trajectories. Thus, the transmitted signal needs to be pointed to off-zenith angles covering a large area in the mesosphere.

For this purpose various NEC simulations were carried out with different subarray groups and dedicated phasing. The aim was to use as many antenna array elements as possible to form a broad beam. Part of this study is described in the diploma thesis of *Gancarz* (2010). The configuration with the most promising radiation pattern is composed of twelve individual subarrays in the circumference of the MAARSY array (see Figure 3.14(a)). Each subarray forms a beam at $\theta = 25^\circ$ resulting in an almost donut-like contour (Figure 3.14(b)), using 55% of the total array and thus of the available output power.

In another attempt, the MAARSY antenna array was split into six subarrays, namely the six outer Anemones A to F, individually generating a beam spot. As the middle Anemone is not used in this configuration, 68% of the total MAARSY antenna array are used.

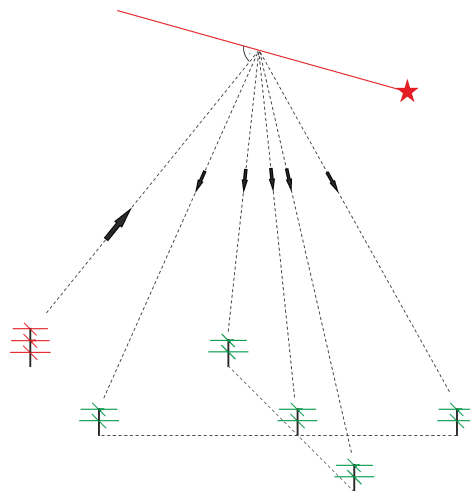


Figure 3.13 Schematic of a classical All-Sky Interferometric Meteor Radar (SkiYmet) configuration.

3.6 Special beam forming - simultaneous multi-beam meteor observations

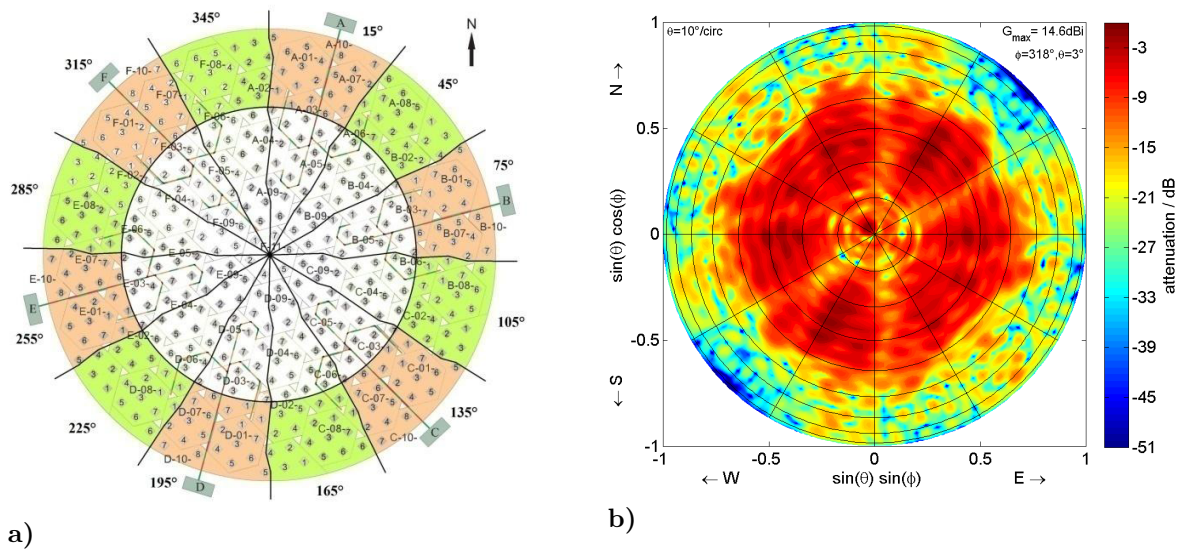


Figure 3.14 a) Sketch of the MAARSY antenna array, divided into 12 approximately equal slices, of which the colored antennas are used to form individual beams at $\theta = 25^\circ$, taken from *Gancarz (2010)*. b) Simulation of the radiation pattern generated by the configuration marked in a).

The simulated radiation pattern is depicted in Figure 3.15(a), where the individual beam spots are pronounced.

On September 22nd to 23rd 2012 this configuration was applied for approximately 12 hours to observe meteors with MAARSY, where for transmission the MAARSY antenna array was run in the above described configuration with six individual beams. For reception a classical meteor interferometer consisting of five antennas was used. The angular appearance of detected meteors is depicted in Figure 3.15(b), where each individual point describes the detected location for one meteor. The increased count rate near the simulated beam spots underlines the good agreement to the simulated radiation pattern. It has to be noted, that this plot allows a qualitative view as the detection of a meteor highly depends on its signal-to-noise ratio (SNR), and thus velocity, specific trajectory and likely composition. Some events outside the beam spots might be favored due to large SNR than weaker events inside the beam spots.

The likelihood to detect meteors at high off-zenith angles is generally greater due to the possible geometries compared to zenith-near directions. The detection of meteors with this configuration describes a) good angular coverage of the receiving interferometer antennas and b) the presence of side lobes that illuminate that far off-zenith angles. However, especially the latter is also suggested by the simulation (Figure 3.15(a)), showing a level of partially 20 dB below the maximum intensity at zenith angles greater than 60° . The missing meteor detections above 60° zenith angle at southern to south-western directions are caused by the nearby hill Andhue (≈ 300 m height and distance to MAARSY).

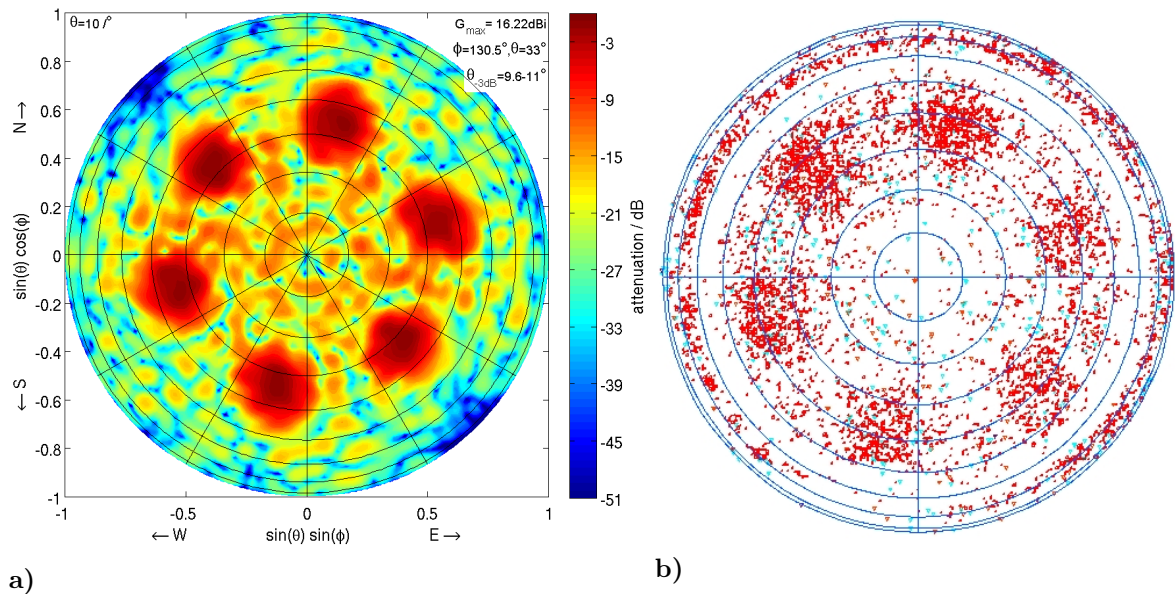


Figure 3.15 a) Simulated radiation pattern of MAARSY using 6 Anemones A-F, each forming an individual beam. b) Angular distribution of observed meteors for the six simultaneous beam directions. The orientation of the axes are identical to a). Consistent with earlier figures, each ring overlaying both plots denotes a zenith angle distance of 10° .

3.7 Improved side lobe suppression by the use of amplitude taper

Even though the side lobes in MAARSY's radiation pattern are already well attenuated, for specific experiments an even better attenuation might be advantageous. For this purpose amplitude taper is typically used in various radar applications. The benefit of damping the side lobes intensity is at the expense of lowering the total output power and broadening the main beam. Depending on the desired side lobe attenuation, beam broadening and accepted power loss various taper functions can be used, like cosine, triangular or even step functions. Table 3.3 depicts some theoretical values taken from *Mailloux* (1994) and *Balanis* (2005) for uniform illumination of the antenna array and two examples for a radial decrease of amplitude. In the table, λ is the wavelength, D the maximum distance of the active antennas within the antenna array and r is the ratio of the actual distance d of the array element from the center and the radius of the array ($r = 2d/D$). Amplitude taper is currently only feasible for MAARSY on the transmission path, as for reception the limitations in the amount of receiver channels do not allow any performance improvements. The beauty of amplitude taper is its impact on the total radiation pattern, thus all side lobes, not only the first most intense, are affected. This significantly decreases the noise pickup by the side lobes and thus improves the overall main lobe vs. side lobe relation.

For transmission, Figure 3.16(a) shows an example for the MAARSY343 array aiming for at least 10 dB improvement of side lobe attenuation (see e.g. Figure 3.9(a) for comparison to unity amplitude). The taper function used for this configuration equals $(1 - r)^2$, resulting in a beam broadening of approximately 1° and an effective usage of only 1/3 of the total output power (-4.78 dB). The resulting total radiation pattern in comparison to MAARSY343 with equal phase and amplitude is depicted in Figure 3.17. This configuration is highly

3.7 Improved side lobe suppression by the use of amplitude taper

amplitude distribution	θ_{-3dB} [°]	θ_{FN} [°]	side lobe level [dB]	gain factor
$f(r) = 1$	$58.9 \frac{\lambda}{D}$	$69.8 \frac{\lambda}{D}$	17.6 dB	1
$f(r) = (1 - r)$	$72.7 \frac{\lambda}{D}$	$93.6 \frac{\lambda}{D}$	24.6 dB	0.75
$f(r) = (1 - r)^2$	$84.3 \frac{\lambda}{D}$	$116.2 \frac{\lambda}{D}$	30.6 dB	0.56

Table 3.3 Examples of amplitude taper for a circular-aperture antenna array (Balanis, 2005; Mailloux, 1994). θ_{-3dB} and θ_{FN} are the half-power beam width and the position of the first null in the pattern.

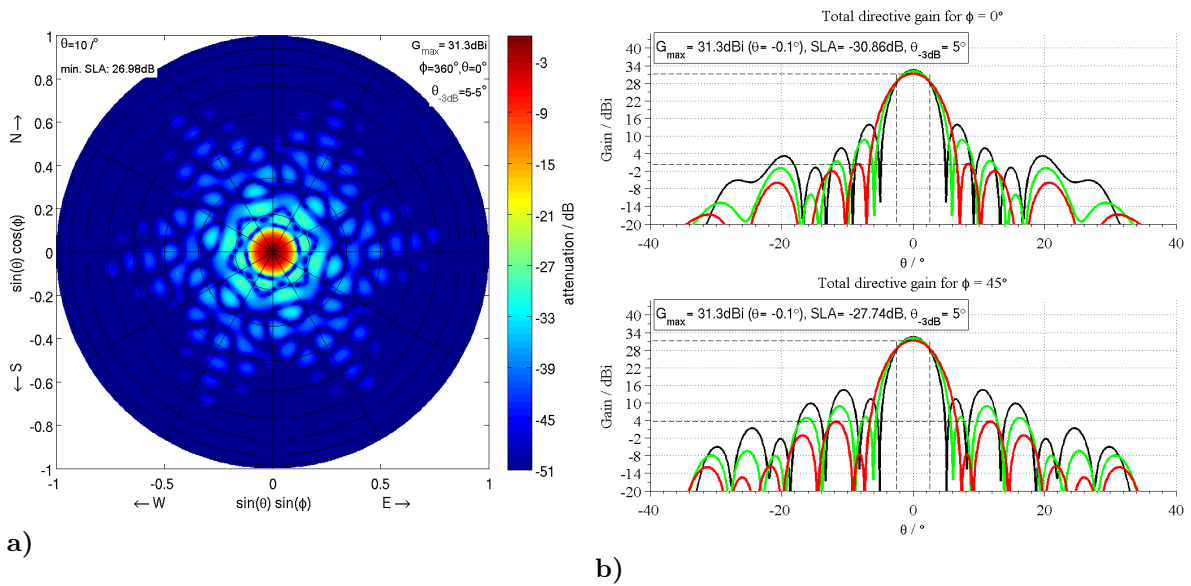


Figure 3.16 a) Simulated radiation pattern in top view of MAARSY343 applying amplitude taper. b) Radiation pattern of MAARSY343 for unity illumination (black), amplitude taper with a $(1-r)$ taper function (green) and $(1 - r)^2$ (red) as used in a).

recommended for special experiments in which the impact of side lobes shall be reduced to its absolute minimum, e.g. for studying the spatial distribution of PMSE signatures. PMSE are often observed with high SNR even in large off-zenith directions, which may impair observations if poorly attenuated side lobes point to these targets.

As a compromise a $(1 - r)$ taper function (marked in green in Figure 3.16(b)) may be used, which facilitates about 5 dB additional side lobe suppression at 53% total output power and 0.6° beam broadening.

Additionally, for slightly improved side lobe attenuation (≈ 2.5 dB on the first side lobes) a raised cosine taper function (e.g. $\cos(\frac{\pi}{2}r)$ with $r = 2d/D$ as introduced above) could be used where only 25% of the total output power would be unused, resulting in a moderate beam broadening of only 0.4° .

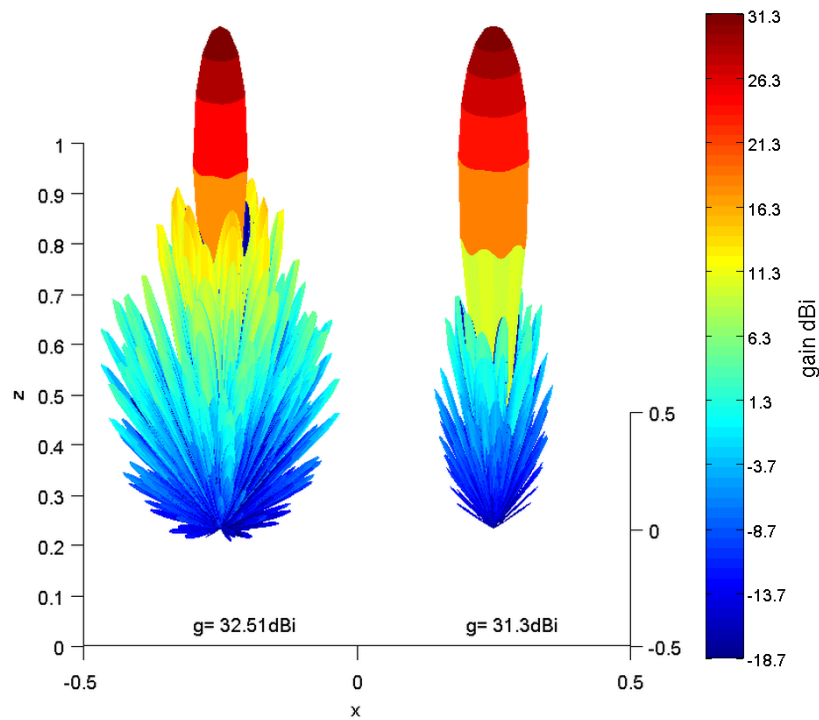


Figure 3.17 Comparison of MAARSY343 with uniform phase and amplitude (left) and incorporating amplitude taper to reduce the side lobe level by additional 10 dB (right).

3.8 Summary

This chapter introduced the Middle Atmosphere Alomar Radar System (MAARSY) with main focus on the receiving system and the antenna array. For this purpose the general setup of MAARSY has been presented and the importance of an accurate calibration is pointed out to achieve and preserve the best performance of the system.

Since MAARSY's general full functionality, the antenna array was converted from linear polarization to circular polarization. The major aim of this upgrade of the antenna array's polarization was e.g. to avoid signal losses due to Faraday rotation events within the ionosphere.

Subsequently a selection of the thorough simulations of the MAARSY antenna array performed to characterize its radiation pattern are presented, which also underlines the earlier given specifications. In particular, the minimum beam width of 3.6° , the side lobe suppression of better than 17 dB and the beam steering range without generating grating lobes (30° to partially 40° zenith angle) are of most interest. Furthermore, it was demonstrated that MAARSY is capable of forming multiple beams simultaneously, which was verified by observations of specular meteors. In this experiment MAARSY was generating six individual beam spots on transmission, while for reception an all sky interferometer was used. For the positions of the individual beam spots, an increased amount of meteors was detected.

Finally, the application of using amplitude taper has been proposed and results of appendant simulations were presented, which allow the enhanced suppression of the radiation pattern side lobes.

Chapter 4 Passive experiments to estimate the radiation pattern

This chapter presents passive methods that have been used to evaluate the radiation pattern of MAARSY. This in first place is the verification of the beam pointing, the estimation of the beam width and side lobe suppression.

Contrary to small antennas, which may be examined in detail in dedicated anechoic measurement chambers, the MAARSY array can not be tested directly that easily because of its size. Thus, incident broadband noise power emanating from distant cosmic radio sources is used to obtain information about the radiation pattern. For these experiments MAARSY was typically operated on reception only. On some occasions the data was also extracted from active experiments to demonstrate the feasibility of combined experiments to improve the temporal resolution of all experiments performed with this radar within a sequence.

In the beginning of this chapter a brief introduction to observations of cosmic radio emissions at VHF frequencies is given. Section 4.2 describes the methodology to derive absolute receiver phases of MAARSY's subarray groups. These phases are inherently important for the optimal combination of the individual subarrays and their use for interferometric observations. The subsequent Section 4.3 presents MAARSY observations of cosmic radio emissions, which focus on the estimation of beam pointing accuracy and the estimation of the beam width. These observations are compared to an accurate reference model approving the quality of the radiation pattern in general and details. These observations and the results of the analysis have already been partially published in *Renkwitz et al. (2011)* and *Renkwitz et al. (2012)*. Furthermore, the observations of cosmic radio emissions are used to estimate the gain of MAARSY's antenna array to complement the earlier characterizations of the radiation pattern. Additionally, simultaneous observations of a distinct cosmic radio source by MAARSY and another receiving station are presented in Section 4.7.1. This experiment is motivated by frequently seen severe fluctuations of the intensities of the radio sources. Furthermore, as a byproduct of the thorough observations of the cosmic radio sources, the geophysical application of MAARSY as a riometer is demonstrated in a case study. This is of special interest, as with these observations the D-region ionization level can be quantified.

4.1 Sky noise - cosmic radio emission in the VHF range: Origin and observation requirements

The operating frequency of MAARSY in the lower VHF range (very high frequency, typically summarizing the frequency range of 30 to 300 MHz) is characterized by strong cosmic radio emissions of both distinct and diffuse sources. The main source of cosmic radiation in this frequency range is non-thermal synchrotron radiation (see e.g. *Priese, 1964*; *Kuz'min, 1966*; *Kraus, 1986*). This radiation is emitted due to the acceleration of relativistic electrons within the presence of magnetic fields. The electrons spiral around the magnetic field lines resulting in radiation, while its frequency is related to the velocity of the electrons and strength of the magnetic fields and thus, the width of the spiral. These emissions are often radiated by e.g. supernova remnants and radio galaxies, and do not depend on the physical temperature of the source. Contrary, thermal radiation is modeled as blackbody radiation, which is typically emitted by stars and interstellar heated dust grains. Radio emissions in the VHF region were first observed by *Jansky (1933)* and have since been a subject of research covering larger and larger frequency ranges.

The subsequently described absolute phase calibration and the later presented angularly resolved sky noise observations were performed within the linear range of the MAARSY receiver as can be seen in Figure 4.1(a), indicated by the horizontal marks. The determination

4.1 Sky noise - cosmic radio emission in the VHF range: Origin and observation requirements

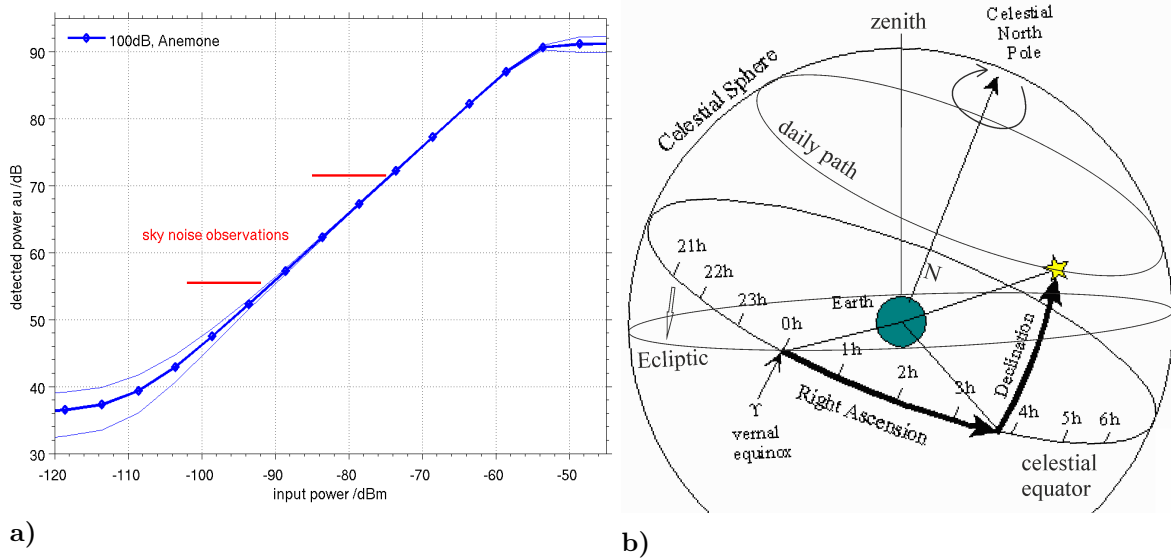


Figure 4.1 a) Linearity and dynamic range of the MAARSY receiver for the gain setting used in the sky noise and phase calibration observations. b) Celestial coordinate system, zenith is marked for an observation position of $\approx 69^\circ\text{N}$.¹

of the total dynamic range and its linear part of the receiver are examined and presented in detail in the Appendix in Section B.3. This is of particular interest as for MAARSY the gain of the receiving system can be adjusted at the transceiver modules and the IF-receivers. The systematic relative standard deviation of the power detected by the receiver for this power level region can be estimated to 1-3% (see reference measurements in Figure B.3(b)).

To successfully detect the entire dynamic range of the incident intensities of the cosmic radio sources, the noise figure of the total receiving system has to be significantly below the minimum intensity of the external signal which is to be observed, e.g. the observed radio sources. The noise figure of the receiving system has been examined for various gain and band width settings in Section B.4. This analysis revealed, that the gain settings modify both the dynamic range and the noise figure of the total receiving system. Typically, the lowest noise figure and the maximum dynamic range are desired, which however sometimes oppose each other. As an outcome of thorough evaluation of the receiving system (Section B.3 and following) the available dynamic range was found to be deficient for many active experiments, which is evident as the cosmic emissions already use 10 to 20 dB of the dynamic range. This is depicted in Figure 4.1(a), where the typical dynamic range of the sky noise experiments is marked. Active experiments with strong back scatter, e.g. PMSE and meteor head echo observations, often require another 40 dB. Thus, the Signal Processor Units were modified, reducing their gain aiming for the increase of available dynamic range from initially partially less than 40 dB to about 70 dB without sacrificing the noise figure significantly. See Section B.3 in the Appendix for more details.

In the following, the natural cosmic radio emissions (often abbreviated by sky noise) are used to evaluate the radiation pattern of MAARSY as the positions of the individual major sources are well known from radio astronomical observations. This allows us to compare the detected incident power per beam pointing direction with the position and intensity of the

¹Figure 4.1(b) is modified from the original figure of National Oceanic & Atmospheric Administration, Solar Calculator Glossary - <http://www.esrl.noaa.gov/gmd/grad/solcalc/celsphere.gif>

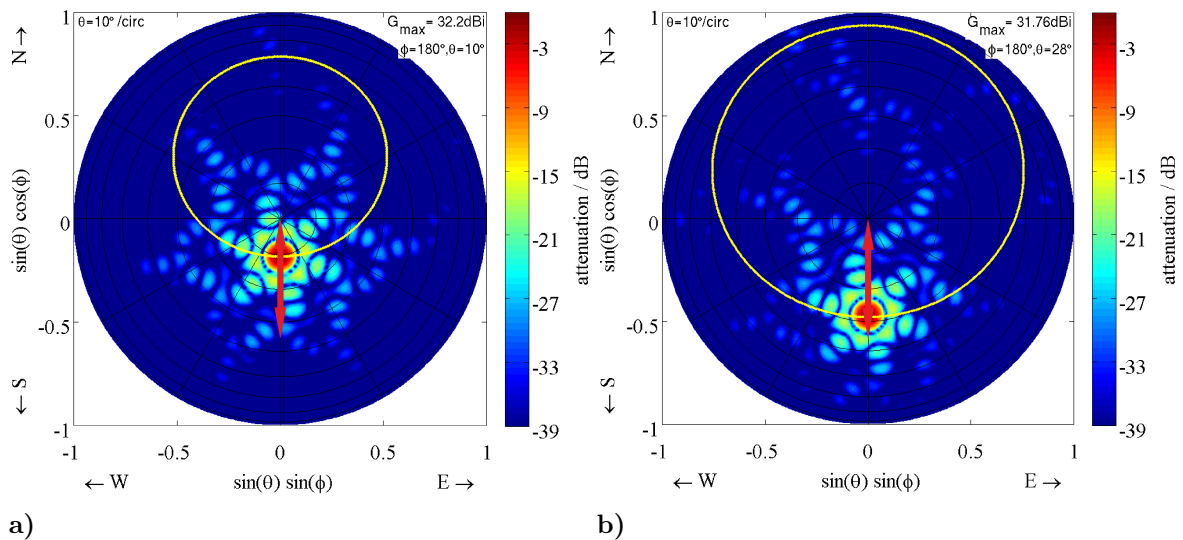


Figure 4.2 a) Radiation pattern in top-view of the software combined MAARSY343 pointing to $\phi = 180^\circ, \theta = 10.5^\circ$ and b) to $\phi = 180^\circ, \theta = 28.5^\circ$. Both figures are overlaid with the trajectory of Cassiopeia A (in a)) and Cygnus A (in b)), respectively, as well as a red arrow indicating the typically performed scan from $\theta = 0 - 34^\circ$.

known sources.

The position of the cosmic radio sources are generally defined in the celestial coordinate system (see Figure 4.1(b)). For vertical observations the geographic latitude l_{geo} equals the declination δ , while for off-vertical observations along the north-south direction the zenith angle (θ_B , oriented positive northwards) has to be considered (Equation 4.1).

$$\delta = l_{geo} + \theta_B \quad (4.1)$$

Due to the polar latitude of MAARSY (69.3°N), observations of southern directions are privileged. This is caused by the positions of the radio sources and the Milky Way, which have their upper culmination south of MAARSY. In northern directions the sources typically have too low elevation angles above the horizon to observe them with MAARSY. Thus, in almost all dedicated sky noise experiments MAARSY has been operated in a scan mode, where in southern directions multiple off-zenith beam directions were sampled. This systematic is depicted for the use of MAARSY343 in the Figures 4.2(a) and 4.2(b) for the two major radio sources Cassiopeia A and Cygnus A at radio frequencies around 50 MHz. Generally, the observed distinct radio sources are recognized by the increase of detected power for the corresponding time and beam pointing direction. Alternatively, the method which is used for the absolute phase calibration presented in Section 4.2 was reversely used to identify the presence of a distinct radio source, even though it is not explicitly visible in the detected power. This has been successfully tested for the case of the Tycho supernova remnant, which is presented in the Appendix in Section C.2.

A detailed overview of cosmic radio sources that may be observed with MAARSY and their location is presented in the Appendix in Table C.3.

4.2 Phase calibration methods applicable to MAARSY

Typically, several methods are used to calibrate a radar for various technical parameters. In *Latteck et al. (2007)* and *Latteck et al. (2008)* the so called delay line and noise source calibration are described. The delay line calibration allows the range calibration of a radar using an ultrasonic delay device. In this method, a fraction of the radar's transmit signal is attenuated, passed through a dedicated delay line and fed into the antenna port of the radar's receiver. With the knowledge of the inherent time delay of the delay line the signal should be detected at a specific range. Any deviation of the detected to the nominal range has to be corrected in the radar controller. The accuracy of this method depends on the transmitted pulse length and range sampling resolution. Furthermore, by applying this method the gain of the observed receiver channels can be measured, knowing all losses in the setup. By varying the path attenuation from the transmitter to the receiver this method also allows the evaluation of linearity and dynamic range.

Furthermore, a calibration factor can be derived, converting the detected power in arbitrary units to absolute power. This can be combined with the above described method, if the absolute output power of the transmitter and all losses in the measurement path are known. Depending on the specific configuration of the experiments dedicated calibration factors have to be derived.

Another method is the so called noise calibration, where typically a wideband noise source of known intensity is fed into the receiver. This method allows us to estimate the sensitivity of the receiving system and its dynamic range and linearity if enough output power of the noise source is available. The noise calibration is in principle consistent with the method described before, but in this case the transmitter is inactive and thus the likelihood of signal leakage or other interferences from the transmitter to the receiver are excluded.

To gain information on the individual receiver phases, typically a common signal of known amplitude and phase is fed into the receiver channels. Comparing the phase of the injected signal to the signal present at the A/D-converter reveals the individual phase shifts along the receiver path. **The knowledge of the individual receiver phases is mandatory for a) the optimal combination of subarray groups to form a larger group in software as well as b) for the interferometric use of the individual subarray groups.** The usage of wrong phase information leads to faulty estimation of e.g. angle of arrival, while the imperfect combination of antenna groups with differing phase likely leads to a deviation in the beam pointing and a deterioration of the radiation pattern. The latter is subjected in the Appendix in Section A.3.

However, none of the described methods delivers information about the total receiver system, where also the external antenna cables and the individual antennas belong to. *Woodman (1971)* and *Palmer et al. (1996)* e.g. described a method to derive receiver phases of VHF radars observing the cosmic radio sources Hydra and Cygnus A respectively. In the case of MAARSY, *Chau et al. (2013b)*, co-authored by the author of this thesis) performed the first absolute phase calibrations for the MAARSY radar by observing the cosmic radio source Cassiopeia A.

4.2.1 Absolute phase calibration of MAARSY by the observations of cosmic radio sources

The MAARSY receiving system is currently comprised of 16 individual I/Q receiver channels. The individual receiver channels can be connected to different antenna groups within the MAARSY antenna array or additional external antennas like the meteor interferometer or the ALWIN64 array. This complexity does not simplify the calibration procedure, but the regular observation of radio sources facilitates the receiver phase estimation of the used channels and thus also uncovers short term fluctuations or system failures which would not immediately be seen in standard maintenance calibrations, typically performed rarely per year.

Therefore, phase calibration observations of cosmic radio sources like Cassiopeia A (CasA) or Cygnus A (CygA) have been performed whenever feasible since July 2012.

By now an optimal experiment configuration for MAARSY has been found, with which the individual phases for all subarray groups are derived reliably (see Table 4.1). This experiment incorporates five different beam directions pointing to the trajectory of CasA. Within a limited angular window around the radio source (typically 10-15°) the cross correlation phases with respect to a reference receiver are calculated as well as the geometrically determined phase distribution for the array elements pointing to the radio source for every time step of the observation. The offset phase Ψ_{offs} is calculated as the subtraction of the calculated beam pointing phase Ψ_c (see e.g. Section A.4) and the received cross-correlation phase Ψ_r for the individual subarray group pairs, e.g. Anemone A to E.

$$\Psi_{offs}^{(A,E)} = rem(\Psi_c^{(A,E)} - \Psi_r^{(A,E)}, 2\pi) \quad (4.2)$$

Where $rem(\dots, 2\pi)$ denotes the remainder to 2π after division to wrap the phases between 0 and 2π . For all times during the passage of the radio source the derived offset phase should be fairly constant. The standard deviations of those resulting offset phases are used as an indicator of the quality in the subsequent processing. To reference the derived offset phase of the various beam pointing directions to vertical (system phase Ψ_{sys}), the median of the offset phase is corrected by the apparent beam pointing phase.

$$\Psi_{sys}^{(A,E)} = \Psi_{offs}^{(A,E)} - \Psi_c^{(A,E)} \quad (4.3)$$

Data with significantly enhanced deviation to the total median phase are rejected in the final processing. This method allows the suppression of doubtful data, caused by interferences or geomagnetic disturbances, but inherently leads to data gaps for individual receiver channels. However, besides the mentioned method, no pre-selection of the individual daily data is needed or performed.

Figure 4.3 depicts an example of the phase calibration process for a single pass of Cassiopeia A into south-eastern direction of MAARSY on 2013/04/29. Shown are the calculated (green)

observation bandwidth	$B_{BB}=0.5, B_{IF}=1$ MHz				
pulse repetition frequency	525 Hz and 1000 Hz				
beam pointing direction					
azimuth ϕ	90°	135°	180°	225°	270°
zenith angle θ	23.9°	13°	10.5°	13°	23.9°

Table 4.1 Parameters of the absolute phase calibration experiment for MAARSY.

4.2 Phase calibration methods applicable to MAARSY

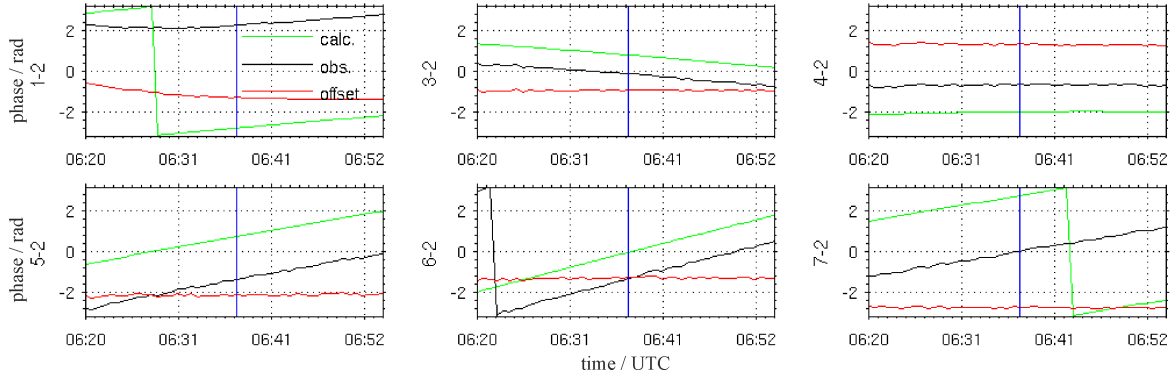


Figure 4.3 Example of a phase calibration experiment for one passage of Cassiopeia A through MAARSY’s main beam on 2013/04/29. Shown are the calculated (green), the observed (black) and their difference (red) phases for the antenna groups 433 (1), Anemones B (3) to F (7) in reference to Anemone A (2).

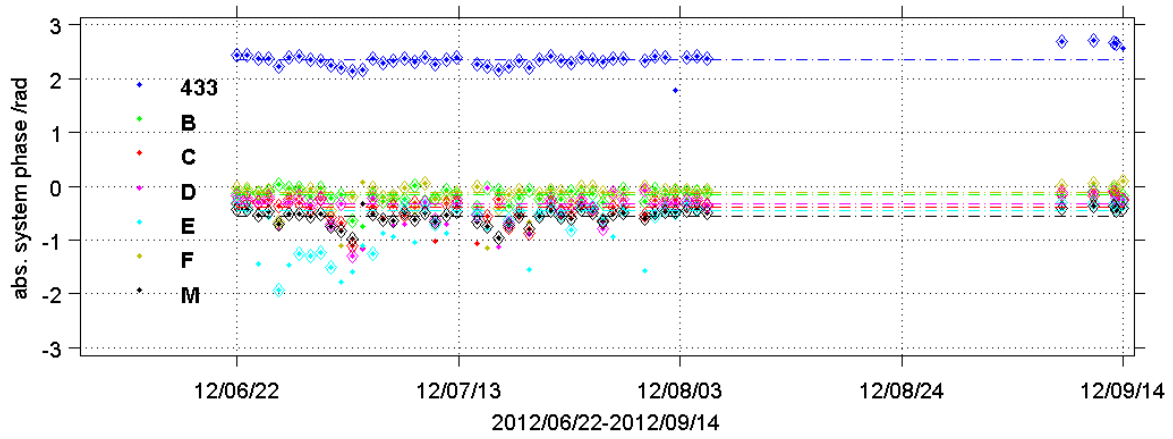


Figure 4.4 Results of the phase measurements using Cassiopeia A for the 433 and the Anemone receivers A to F in reference to Anemone A for the period before September 2012. The broken horizontal lines mark the median phase of the respective receiver. Phases marked with a diamond symbol are used for the further analysis.

and observed (black) phases as well as their difference (red). This example is exceptionally good, marked by undisturbed atmospheric conditions and thus shows very smooth curves. Generally, it has to be noted that the Hexagons provide about 8.5dB less gain than the Anemones (see e.g. Table 3.2 as reference). Therefore, CasA’s signature is broader and less intense, which might increase the variance of the estimated phases. Additionally, due to the wider beam width the received signal of the observed source may be impaired by other distinct or diffuse radio sources. Figures 4.4 and 4.5 show the derived phases for the period, when MAARSY was still linearly polarized. In general stable phases with typically small variations for the Anemones and also the Hexagons are found for these observations covering three months ($< 15^\circ$). However, until the beginning of July 2013 the phases of container E appear to be suspicious. These initial observations, performed in summer 2012, are explicitly valuable as after that time the first period in MAARSY’s conversion from linear to circular

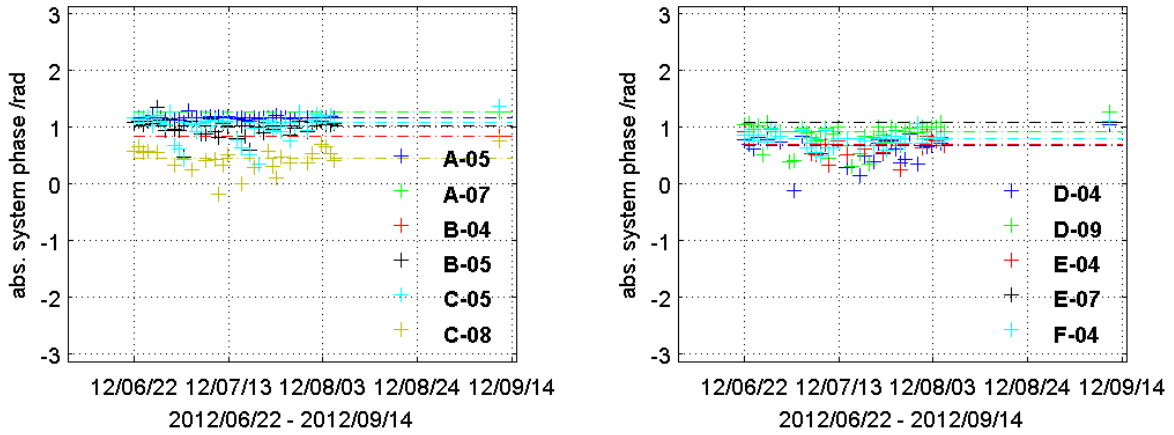


Figure 4.5 Results of the phase measurements using Cassiopeia A for 11 Hexagons for the period before September 2012. Both panels show the derived phases of the individual receivers in reference to Anemone A. The broken horizontal lines mark the median phase of the respective receiver.

polarization started. During the first step of this upgrade, the middle Anemone M and the Hexagon B-08 were converted to circular polarization. This allowed us to study apparent effects by modifying the polarization, while the remaining linear antenna groups were used as reference. The derived phases of the observed receiver subarray combinations for the period of September 2012 to April 2013 are depicted for the Anemones in Figure 4.6 and for the Hexagons in Figure C.1 in the Appendix. The change of polarization of the Anemone M was immediately seen in the phase observations, as this Anemone jumped 86° off its earlier phase (see e.g. Table C.2 in the Appendix for an overview of all antenna groups and periods). The variances are comparable to the earlier periods.

In May 2013 the next period of polarization upgrade was started, the remaining Anemones A to F were converted, accompanied by a phase jump of these antenna groups in the same

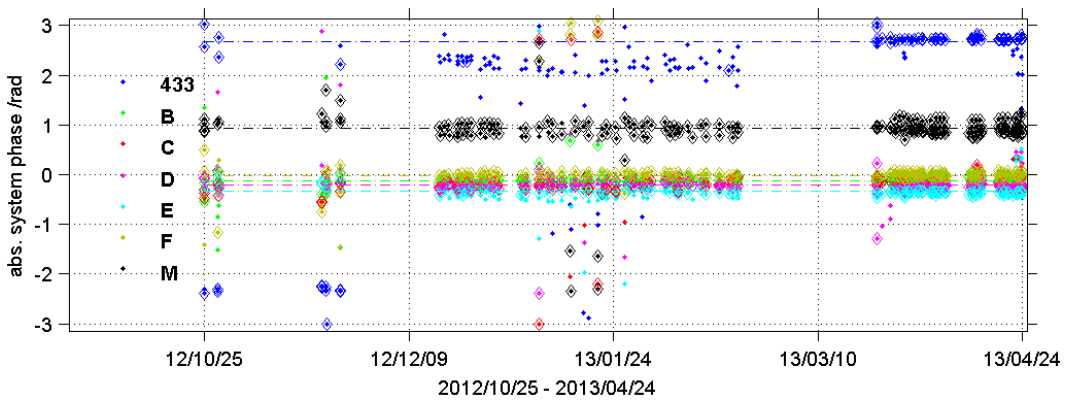


Figure 4.6 Phase distribution and variation of the phase measurements observing Cassiopeia A for the 433 and Anemone receiver. Period: Sept. 2012 - May 2013. Phases marked by a diamond are used in the subsequent analysis. Note, the Anemone M is approximately 75° separated from the Anemones A-F due to its circular polarization.

4.2 Phase calibration methods applicable to MAARSY

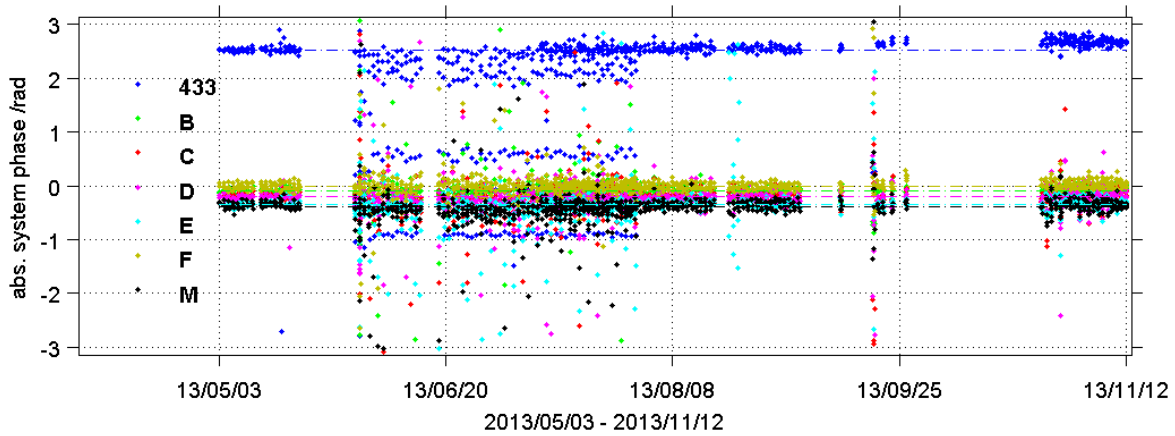


Figure 4.7 Observed phases for MAARSY433 and the Anemone receiver including data from active mesospheric experiments in June and July. Increased variability and spurious phases for the hardware combined MAARSY433 channel are found, the Anemones remain reliable.

order as Anemone M before. Thus, all Anemone phases are now again close to each other in the same phase region as they have similar polarization. The standard deviation of the derived phases for the Anemones and Hexagons are typically in the order of 8° and 10° respectively, which is equivalent to the earlier period.

In September 2013 the remaining antenna groups at the circumference of the MAARSY array were converted to circular polarization. These antenna groups are typically not used in the specific radar experiments besides for the hardware combined MAARSY433. Only the Hexagon C-08 is regularly used and thus is observed in the phase calibration. The derived phases for the periods May to September 2013 and the time afterwards are depicted in the Figures C.2 and C.3.

During summer 2013 no dedicated passive phase calibration experiments were conducted due to the importance of PMSE observations. Therefore, data from active mesospheric scanning experiments were extracted from range gates free of other prominent signals and used for phase calibration. The results of this analysis are shown in Figure 4.7, which are generally characterized by similar median values, besides the MAARSY433 array. Especially for the latter increased standard deviation compared to the exclusive passive observations was found. This increased uncertainty is likely caused by imperfect selection of range gates, extraction of meteor events or other contamination. An advanced analysis algorithm should be able to cope with these circumstances. Another approach is the use of "quiet" range gates within the stratosphere, which however, occasionally might still be contaminated by range aliased scatter of e.g. satellites.

The results of all phase observations until November 2013 are presented in a summarized form in Table C.2.

4.2.2 Automatic hardware phase and amplitude calibration measurements

Since September 28th 2013 the MAARSY radar automatically performs a phase and amplitude test for all receiving channels. These tests include all available designated subarray group combinations and are performed once per day. The only receiver groups that are not included in this test are the six scattered outer groups (A-10 to F-10) and the receivers of the additional antenna interface unit. This antenna interface unit allows the use of antenna groups, that are not incorporated in the MAARSY433 antenna array, e.g. the meteor interferometer antennas. Nevertheless, 63 receiver channels for all Hexagons that are e.g. combined to the MAARSY343 are available and can be analyzed in terms of reliability, standard deviation and thus also abnormal behavior. For these amplitude and phase tests a reference signal is injected into the front-ends of all receivers, passing through the entire receiving chain, including mixer, filter and amplifier stages down to the baseband A/D-converter.

In Figure 4.8(a) the deviation of the median values for the phase and the amplitude measurements are depicted. In the phase measurements the receiver group no. 58 (Hexagon C-04) appeared to have a $+3^\circ$ phase offset to the median for about 10 days right at the beginning of these measurements. Since October 10th the phase of that receiver group appears to be pretty stable around the median value. Until now, the reason of this phase jump cannot be found as unfortunately during that time no phase calibration experiments, using a cosmic radio source, have been performed with MAARSY.

Interestingly, besides the mentioned phase jump of receiver C-04 the typical standard deviation of the measured phases of all receivers are in the order of only 0.5° (see Figure 4.8(b)). This can be considered as pretty stable, having in mind the large number of involved stages within the receiving chain.

The standard deviation of the amplitudes is remarkably good as well, with generally below 0.2 dB for all receiver groups. This variation is in good agreement with the hardware measurements performed at the MAARSY receivers, where about 1.5-2%, equivalent to 0.2 dB, are seen (see Figure B.3(b) in the Appendix). The apparent outlier is the group no. 8,

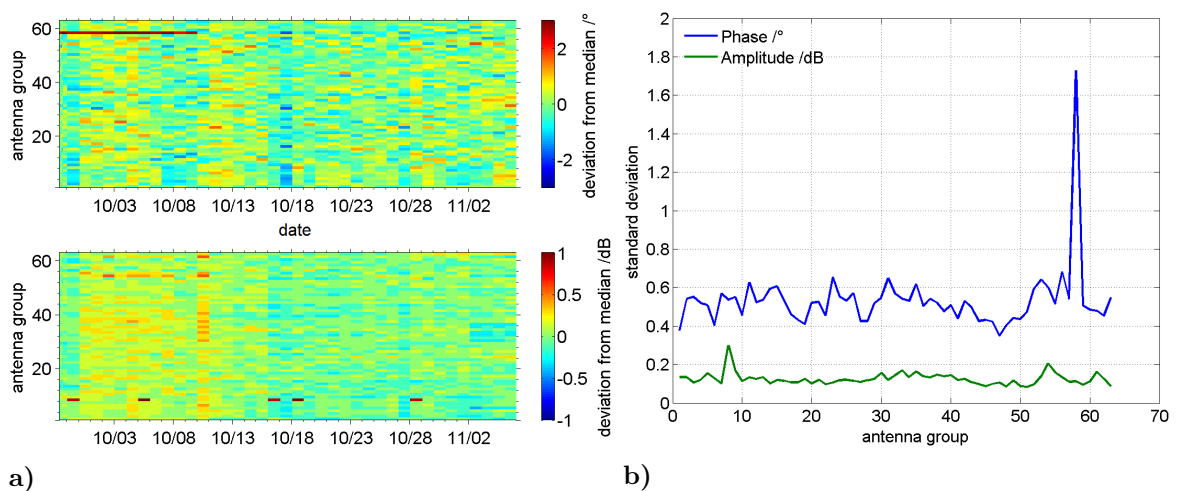


Figure 4.8 a) Phase and amplitude deviation from the median for 63 antenna group and receiver combinations, derived from the hardware phase test. b) Standard deviation of the amplitude and phase measurements in a).

which is the Anemone M. However, this Anemone in the center of the array is distributed over all six containers located at the array periphery housing the receivers. Any random gain fluctuations of the six containers superpose and thus, may result in greater standard deviations than all the other channels, where the receivers are concentrated only within a single container. Interestingly, the Anemone M is not peculiar in the phase deviations, which can be seen as an indicator for a good phase synchronization of the distributed hardware in all six containers.

4.2.3 Comparison of the hardware phase test and radio source phase calibration

In this section the absolute phase data collected by observing the cosmic radio source Cassiopeia A and the hardware phase test automatically performed nowadays once per day are compared.

For the period of September 2012 to April 2013 the data of only one hardware phase test was available. The deviation of the hardware phase test from phases estimated from the radio source observations is shown in Table 4.2. It has to be recalled, that at this period the center Anemone M and the Hexagon B-08 were already circularly polarized, while the rest of the array possessed linear polarization. The median of the linearly polarized Anemones is approximately -9.1° relative to Anemone A, while the standard deviation is 8.5° . The phase of the circularly polarized Anemone M has an offset of 67.8° to the median of the linearly polarized Anemones.

The deviation of the Hexagons to the median's phases appears to be in similar order, while A-01 has a remarkably large offset. The deviation's median of the Hexagons is about 14.7° and the standard deviation 13.3° . The offset of the circularly polarized Hexagon D-09 to the median of the linearly polarized Hexagons consistently equals (66.2°) the beforehand found offset for the Anemones with linear and circular polarization. The automatic hardware phase test measurements, performed daily since the end of September 2013, enable to compare the phases derived from the radio source observations and the hardware phase test on a daily basis and also the long term stability.

In the left panel of Figure 4.9(a) the daily variation between the two methods is shown for the days, when both methods were applied. The receiver groups are sorted as follows: the hardware combined MAARSY433, the Anemones A to M succeeded by 15 Hexagon channels (see a detailed list in the Appendix, Table C.1). The median values of these common day measurements and their standard deviation are depicted in the right panel. Notably, the median phases of both measurements differ by up to 20° , while the standard deviation of these differences are in the order of up to 5° , but typically around 2.5° .

ant. group	433	A	B	C	D	E	F	M
phase dev. /°	-5.33	0	-8.38	-9.85	-21.12	-16.80	-0.31	58.73
ant. group	A-01	A-05	A-08	B-01	B-05	C-01	C-05	C-06
phase dev. /°	44.89	14.30	-8.43	27.69	16.59	16.39	12.37	15.45
ant. group	C-08	D-01	D-02	D-09	E-01	E-05	F-01	F-05
phase dev. /°	-8.67	12.00	2.03	79.43	20.85	10.13	23.11	14.68

Table 4.2 Comparison of hardware phase test and cosmic radio source calibration for the period Sept. 2012 to May 2013.

As the temporal data overlap of both methods is still rather poor, the median values of all available data for both methods are compared, disregarding the specific day they were determined. This is to prevent a possible contamination within the earlier presented common day data. Figure 4.9(b) shows the median and standard deviation of all available data of the hardware phase tests and the phases obtained from the radio source observations. The result is almost similar to that of the common time data and therefore a contamination of the data seems to be unlikely.

Since we gained the information of the absolute system phases of MAARSY and the median deviation to the daily hardware phase test, it is possible to reduce the number of exclusive phase calibration experiment runs in favor of the temporal resolution of other experiments. However, the combination of these passive phase calibration experiments with other active experiments is advantageous as long as e.g. "quiet" range gates are used. This would allow continuing monitoring of the absolute phases and comparison with the daily hardware phase test without donating additional observation time.

Another problem of only relying on the daily hardware phase tests is, that failures of external components, like the antennas and their feeding coaxial cable or transceiver input cannot be discovered. Especially defects in the decoupling capacitors placed directly at the coaxial socket or the traces to these capacitors on the printed circuit board of the transceiver modules have been discovered occasionally. These defects may appear due to thermal or mechanical stress to the boards and sockets. Therefore, whenever applicable, an absolute phase calibration experiment should be performed, as only these experiments include the entire receiving path.

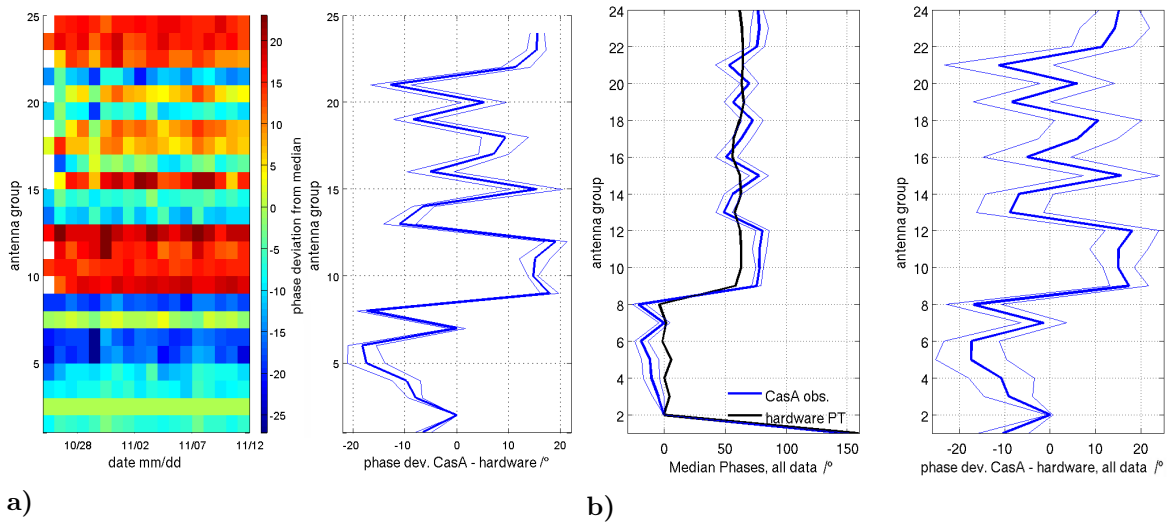


Figure 4.9 a) Deviation of the antenna and receiver phases determined by radio source observations and the hardware phase tests since May 2013 (left) and the median of all common day observations (right). b) Median phases of all existent radio source phase calibration and hardware phase test data since May 2013, regardless of the specific day of the observations (left). The resulting phase deviations between the two methods (right). All phases are referenced to Anemone A (antenna group 2).

4.2.4 The influence of combining subarrays with inaccurate phase conditions

The knowledge of the individual antenna group phases inversely allows the simulation of the resulting radiation pattern for the case, where no phase correction is applied. The radiation pattern for poorly combined array groups is shown in top view in Figure 4.10(a), while the comparison to the phase-corrected combined MAARSY343 is depicted in Figure 4.10(b) for two cross-sections. The main beam seems to be slightly deformed in combination with an apparent pointing aberration in the order of $\theta = 0.5^\circ$ and a deterioration of side lobe suppression by at least 4 dB. These findings are also directly applicable to the hardware combined MAARSY433, with which the largest deviations have been seen in the passive cosmic noise observations during the polarization upgrade periods. During these periods the inherent phase offsets of the individual subarray groups were superimposed with the polarization mixture introducing additional distortions to the antenna pattern, resulting in significantly deteriorated performance of MAARSY433.

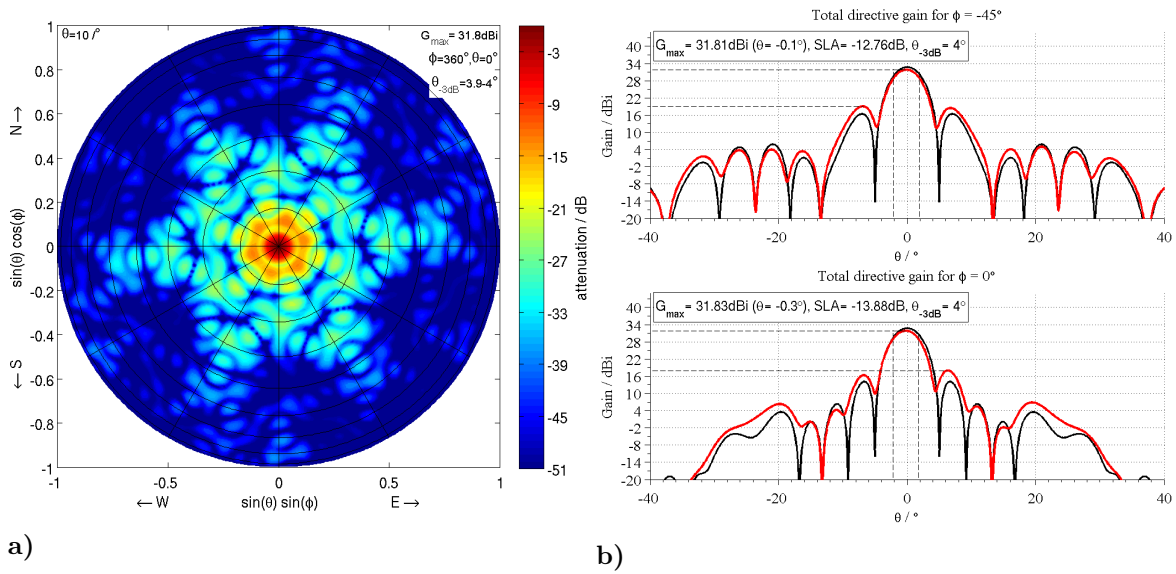


Figure 4.10 a) Simulated radiation pattern of MAARSY343 in top view without phase correction. b) Comparison of the ideally combined MAARSY343 (black) and without phase correction (red) for two cross-sections $\phi = -45^\circ$ and 0° .

4.2.5 The correlation of the individual receiver groups

In the previous sections the cross-correlation between individual receiver groups was used to derive the system phases. Here, the magnitude of the cross-correlation amplitudes are used to indicate the similarity between the signals of the individual receiver groups and thus likely to detect enhanced crosstalk between the individual channels. This question is obvious as all signals from the Hexagon subarray groups are split for the purpose of either sampling a Hexagon individually or to combine Hexagons to form larger subarray groups by hardware combiners, ultimately forming the entire array (MAARSY433).

For this purpose the magnitude of the cross-correlation is weighted with the autocorrelation of the compared receiver groups to derive a relative measure between 0 and 1, equivalent to no

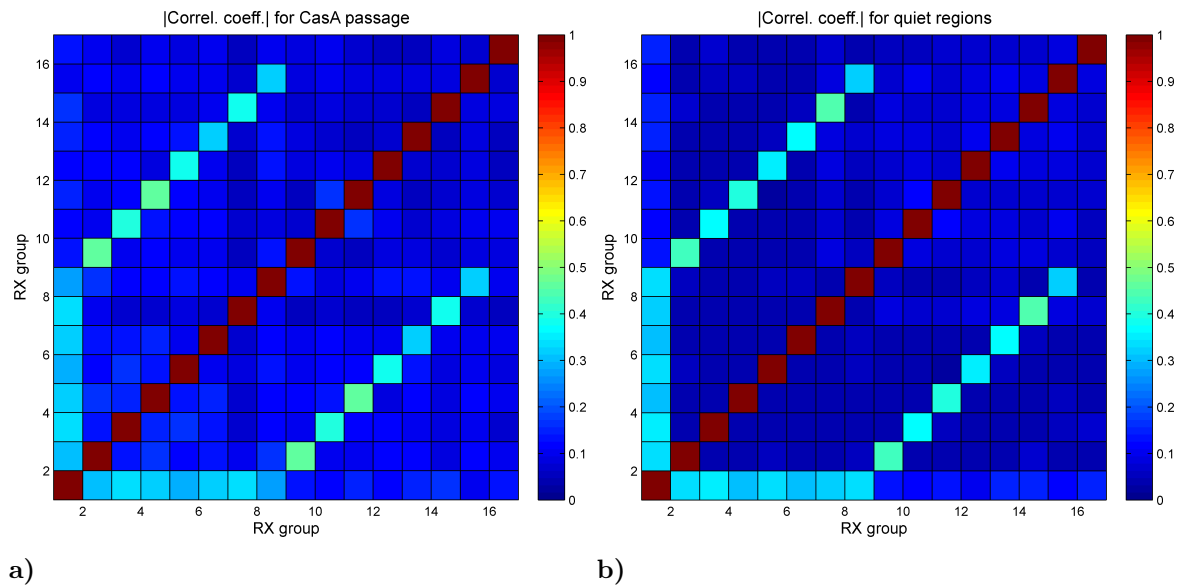


Figure 4.11 Magnitude of cross-correlation of all 16 receiver channels for times of a Casiopeia A passage (a) and for beam pointing to "quiet" regions (b). 1: MAARSY433, 2-8: Anemones A-M, 9-16: Hexagons A-05, B-05, C-04, D-04, E-04, F-05, C-09, B-08.

and high similarity. Figure 4.11(a) shows the resulting magnitude of correlation amplitudes for the combination of 16 receiver and array group combinations for the passage of CasA on 2013/09/27. Consistently to the described method of power scaling, the resulting autocorrelation of all receiver channels equals 1. High correlations are found for 1 (MAARSY433) and the Anemones (2-8) as well as for the Anemones and Hexagons (9-15) belonging to the individual Anemones. B-08 (16) is only part of MAARSY433, but not of any Anemone, thus no enhanced correlation is found for the latter. For the remaining combinations a mean magnitude of 0.2 is found, which appears to be greater than anticipated. Therefore, the same correlations are shown in Figure 4.11(b) for a time, when MAARSY is pointing towards a "quiet" region in the sky. The increased values during the passage of CasA are caused by the reception of the coherent emissions of CasA, other than the less intense incoherent signals of the diffuse background for the case in Figure 4.11(b). Therefore, this analysis should be performed for beam pointing directions off the dominant cosmic radio sources.

The derived magnitudes for MAARSY433 to the Anemones are equivalent to -7 dB (0.45), which approximately agrees with the amount of antennas 49 to 433 (-9.5 dB) considering the amount of involved combiners to generate the hardware combined MAARSY433. The correlations of Anemones to Hexagons, which are part of the Anemone, account for -7 dB (0.45) compared to theoretically -8.5 dB. The correlation of Anemones to Hexagons, that are not included in the Anemones as well as Hexagons to Hexagons, show approximately -25 dB (0.06). Here, the correlation of Anemones to Hexagons is less than it is for Hexagons to Hexagons, where the likely reason is the combined beam width of the subarrays and thus increased likelihood to have a coherent radio source within the combined beam width (10.4° to 21.5° combined beam width).

In general, no suspicious correlations were found, the observed discrepancies are likely caused by crosstalk in the combiners and between the individual receiver channels as well as differing gains of the individual subarray receiver combinations that are combined.

4.3 Observations of cosmic radio emissions with MAARSY

In the earlier section the phase distribution of the individual subarray groups are derived by the observation of distinct cosmic radio sources, primarily Cassiopeia A. These phases are important for the interferometric use of subarray groups and their combination in software to form a larger array and thus generate a radiation pattern with a narrow beam and increased gain with best performance. If not marked otherwise, the latter is subsequently applied for forming MAARSY343 by the integration of seven Anemone signals with appropriate phases. The objectives of the subsequent sections are the estimation of beam pointing accuracy, beam width and if possible the intensity of the inherent side lobes.

4.3.1 Observations September 2012 - May 2013

In September 2012 the upgrade of MAARSY from linear to circular polarization was started aiming for opposite sense of rotation for transmission and reception. The main reason was the planned immunity to Faraday rotation with its typical onset at heights above 90 km (see e.g. *Chau et al.*, 2013a).

For the period of September 2012 to May 2013 the MAARSY antenna array was mainly linearly polarized, but the center Anemone M and the Hexagon group B-08 were already circularly polarized. Considering simulations, the radiation pattern was likely distorted for both MAARSY343 and MAARSY433 due to the different polarizations existent within the same antenna array. This deterioration of the radiation pattern, especially the side lobe attenuation, leads to decreased detectable dynamic range of the incident cosmic noise as the "quiet" portions of the sky are spoiled by the side lobe pick up and therefore eventually increased the detected total incident noise.

Nevertheless, these observations were very valuable as this period offered geomagnetic stable and rather undisturbed conditions. This can especially be seen in the observations of November 28th to 29th (see Figure 4.12), where almost no fluctuations in the intensities of

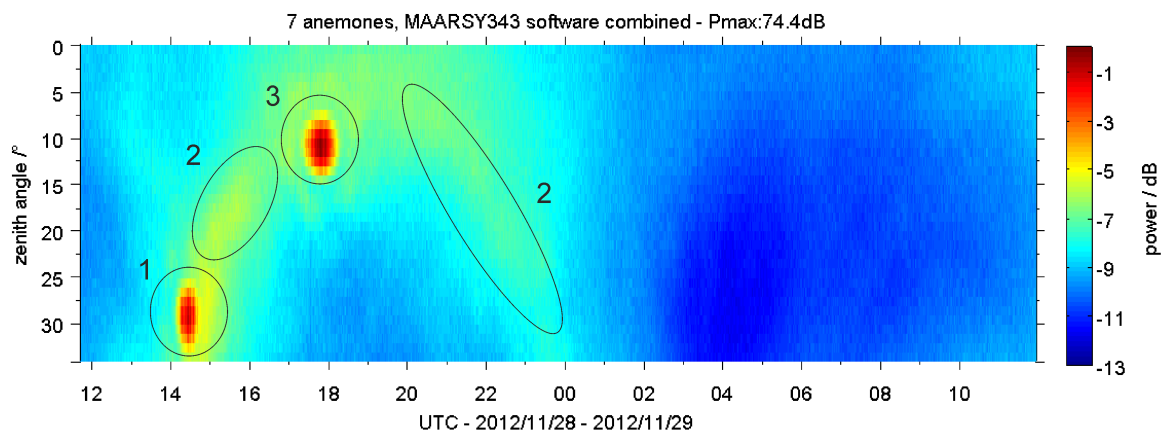


Figure 4.12 Detected incident relative power (P_{max} is depicted in the title) in arbitrary units for a sky noise scan on 28th-29th of November 2012 for the software combined MAARSY343. The highlighted individual sources are Cygnus A (1), the Milky Way (2) and Cassiopeia A (3).

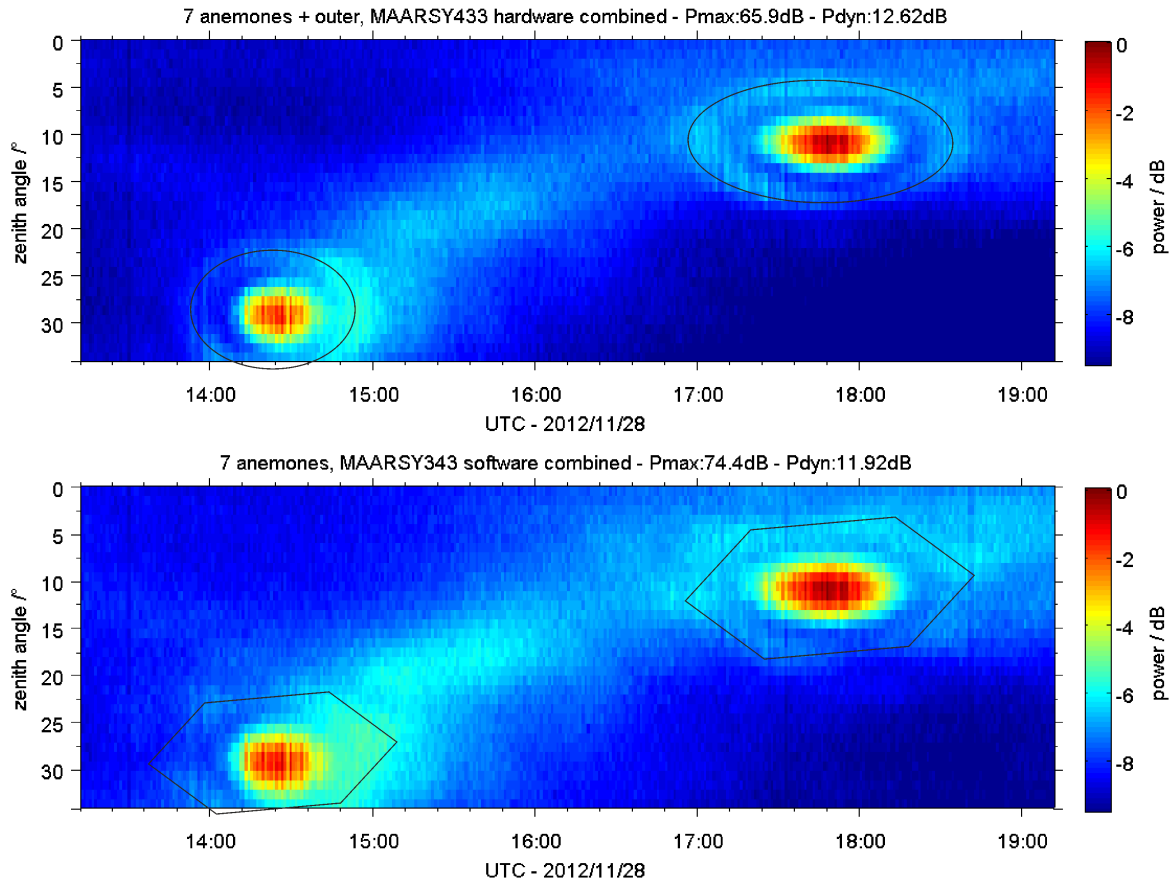


Figure 4.13 Zoom of the detected incident relative power for a sky noise scan performed on 28th of November 2012 for MAARSY433 and the software combined MAARSY343. The black ellipses and hexagons mark the visible side lobes in the detected intensities.

Cassiopeia A and Cygnus A are visible. At the time of observation the K-indices² were derived to be 1-2 and 0-1 respectively (see *Tromsø Geophysical Observatory*, 2014; *GFZ Helmholtz Centre Potsdam*, 2014), which underlines "quiet ionospheric day" characteristics. Especially November 28th was the third quietest day of the month.

For both MAARSY433 and MAARSY343 the first side lobe can be observed regularly, e.g. in Figure 4.13 from November 28th/29th, where the detected intensities around the two sources are magnified. The first side lobe can easily be identified around the culmination of Cassiopeia A ($\approx 17:50$ UTC) and Cygnus A ($\approx 14:20$ UTC). The side lobes can be found at an angular distance of six to seven degrees off the maximum intensity for MAARSY433 and MAARSY343 respectively, which is in good agreement to the simulation of the radiation pattern with NEC (see Figure 4.2(a) and Table 3.2). The reason for the discontinuity of the detected side lobe intensity in the power plot is the actual beam pointing at a given time. The maximum intensity of the side lobe power occurs when the main beam and the side lobes are pointed towards signal sources, e.g. CasA and the Milky Way. In the case of CasA this is valid for almost all directions, besides the pointing of 18:00 UTC, 17° zenith

²K-index quantifies the 3 hour instability of the horizontal component of the Earth's magnetic field, quasi-logarithmic local index, see e.g. *Bartels et al.* (1939)

angle. At this specific time and beam pointing only a fraction of the first side lobe points to CasA, while the rest of the first side lobe and the main lobe are pointing towards less intense regions in the sky. The same is valid for Cygnus A, where the side lobes are pronounced at times at and after the culmination where the superposition of the radiation of Cygnus A and the Galaxy dominates.

Another interesting aspect of seeing the side lobes in the observations is their actual shape. For the MAARSY433 the side lobes appear to form a ring, while it is a hexagon shape for MAARSY343 (see Figure 4.13). This is consistent to the simulations with NEC, which have been shown in Section 3.4, also depicted in Figure 4.2(a) and 4.2(b). However, it is not possible to judge the detected power of the seen side lobe and directly assign this to the side lobe attenuation of the radiation pattern. For this purpose a model with the exact geometry and intensity of the various sources contributing to the detected power needs to be used. The beam pointing analysis and beam width estimation of this two-day observation from 28th to 29th November 2012 were presented in *Renkowitz et al. (2013a)*.

For the further analysis, the data set of this period was averaged for all observations of selected "quiet" days, where only little or no fluctuation of the incident intensities and small a_p ³ and K_p ⁴ indices have been found. This procedure decreases the uncertainty of the individual measurements and has been compiled for the periods of identical antenna array properties. For a given temporal resolution, typically 1 min, the median values of all data sets per beam pointing direction and sidereal time (LST) are calculated, which improves the reliability and robustness as interferences and minor power fluctuations due to scintillation or absorption events are suppressed.

The marked need for such a selection and filtering process can be seen in Figure 4.14(a), where five individual beam directions were used to observe CasA on its trajectory ($\phi = 90^\circ$,

³ a_p planetary a-index : 3-hourly average, scaled from K-index.

⁴ K_p 3-hourly planetary K-index, see corresponding footnote on page 48.

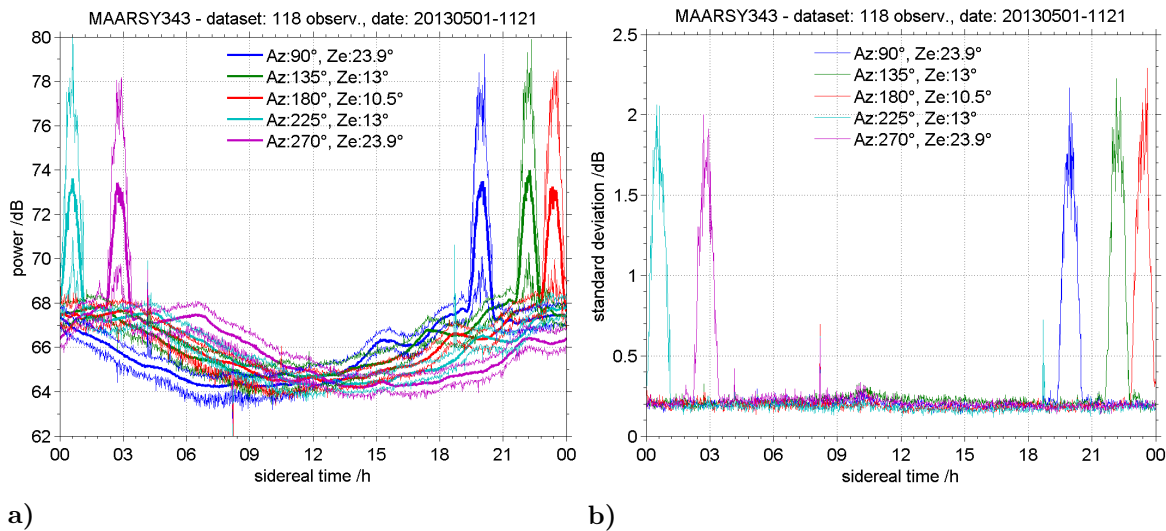


Figure 4.14 a) Incident power for five individual beam pointing directions intended to observe the passage of Cassiopeia A between May and November 2013. Bold lines depict the median enclosed by the absolute minima and maxima. b) Standard deviation for the same observations.

135°, 180°, 225°, 270°). Depicted are the unmodified median values enclosed by the absolute minima and maxima per sidereal time for measurements of the period May to July 2013. At times of high ionospheric disturbances, the incident power of the radio sources may vary by ± 4 dB. In Figure 4.14(b) it can be seen that for the diffuse incident power outside of CasA the standard deviation is constant and related to the measurement error defined by the total system. The standard deviation of 0.2 dB is in agreement with the hardware measurements, see Section B.3 and Figure B.3(b) in the Appendix, where 0.2 dB accord to 1-2% relative standard deviation.

The composites of the individual periods are subsequently analyzed for beam pointing accuracy, beam width estimation and the evaluation of side lobes.

Figure 4.15 presents the analysis of the incident sky noise power for the passage of CasA for the period of October 2012 to April 2013. The deviation of the beam pointing from the simulated direction is estimated by analyzing the incident noise power from the zenithal scans. The zenithal pointing deviation for this data was thus estimated to be less than 0.5°. The beam pointing accuracy for azimuth is analyzed by two methods, a) the temporal deviation of the detected maximum to the predicted time (23:23:45 LST) and b) the angular deviation. For this purpose, in method a) the time series for the beam direction of maximum intensity is convolved with a sum of two Gaussian functions of appropriate width matching the width of the observed source and its proximity to the Milky Way. An example is depicted in the Appendix in Figure C.5. The lag of the best overlap (least squares fit) describes the time of CasA's passage, which can be compared to the predicted time. This methodology has been described in *Renkowitz et al. (2012)*. For method b) the intensities of CasA for beam pointing directions of $\Delta\phi = -1^\circ, 0^\circ$ and $+1^\circ$ in reference to its culmination point are simulated for the used radiation pattern. The estimated time of passage described in method a) is depicted in the lower right panel of Figure 4.15 by a black vertical line, while the simulated pattern and their corresponding midpoints are marked in red, blue and green. The simulations in this case are based on the assumption of a single point-like source at the described pointing direction, which is applicable for MAARSY's angular resolution.

The beam width estimation is also performed in two methods, a) directly from the scan along the off-zenith angles at the maximum incident power and b) from the detected intensity along the sidereal time for the off-zenith angle of maximum power. The beam width for b) is then calculated from the times of detected half-power t_{3dB} related to the time of 1° rotation of Earth t_{er} and the declination of the observed radio source δ_{rs} .

$$\theta_3 = t_{3dB} \cdot \frac{360^\circ}{t_{er}} \cdot \cos \delta_{rs} \quad (4.4)$$

This analysis allows the estimation of the beam width in two cross-sections through the beam. It has to be noted, that both cross-sections are only identical for boresight pointing, unity amplitude and phase distribution for a very symmetric antenna array like MAARSY. For off-boresight pointing the beam width along the direction of beam tilting increases as the effective area is reduced (see Equation 3.5 on page 26).

For the example shown in Figure 4.15 the beam width has been estimated to be in the order of 4.8° and thus about 0.6° wider than simulated for MAARSY343 for the observation of CasA. This broadening is caused by the proximity of the individual sources to the Milky Way and will later be examined in detail.

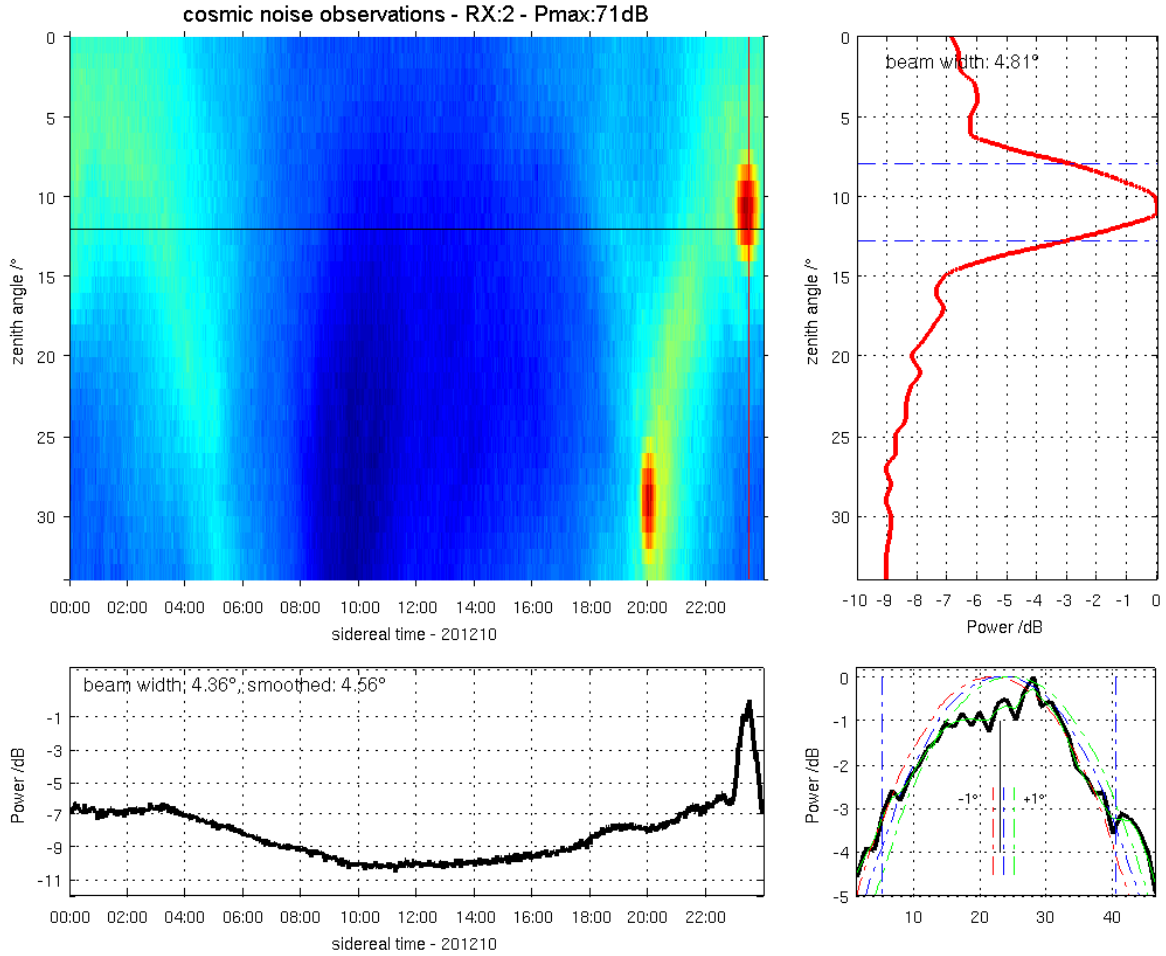


Figure 4.15 Analysis of the incident sky noise power for the period of Sept. 2012 to April 2013 received with MAARSY343. The left upper panel depicts the total incident noise power of the composite for a complete sidereal day for beam pointing directions zenith to 34° off-zenith. The upper right and lower left panel depict the cross-sections through CasA. The distribution of power for both planes is analyzed for beam pointing accuracy and beam width, where the latter is denoted in the panels. The lower right panel presents a zoom to the temporal cross-section through CasA. Overlaid are the simulated intensities of CasA for beam pointings in red, blue and green for $\Delta\phi = -1^\circ, 0^\circ$ and $+1^\circ$ in reference to its culmination point. The black vertical line indicates the estimated time of passage from the observation. The broken vertical blue lines mark the estimated 3 dB points.

4.3.2 Observations May to September 2013

In May 2013 all Anemone antenna groups of MAARSY were transformed to circular polarization, which facilitates the forming of the MAARSY343 receive beam with equal polarization. Besides other experiments during this period, MAARSY has also been used for exclusive passive sky noise observations to evaluate the potential change in the detected cosmic radio sources' signatures due to the new polarization.

In the simulations, MAARSY343's radiation pattern improved as all elements of that array

period	MAARSY433	MAARSY343
- Sept. 2012	33.46 <i>dBi</i> , 3.6°, -17.4 <i>db</i>	32.46 <i>dBi</i> , 4.0°, -16.3 <i>db</i>
Sept. 2012 - May 2013	33.24 <i>dBi</i> , 3.6°, -15.3 <i>db</i>	32.18 <i>dBi</i> , 4.0°, -15.8 <i>db</i>
May 2013 - Sept. 2013	33.07 <i>dBi</i> , 3.8°, -17.6 <i>db</i>	32.5 <i>dBi</i> , 4.0°, -18.1 <i>db</i>
Sept. 2013 -	33.5 <i>dBi</i> , 3.6°, -17.5 <i>db</i>	32.5 <i>dBi</i> , 4.0°, -18.1 <i>db</i>

Table 4.3 Characteristics of the simulated radiation pattern of MAARSY for the individual periods. Listed are the gain, the beam width, minimum side lobe attenuation

are now consistently circular. The gain of the array returned approximately to that of the fully linear version, the beam width is unchanged, while the side lobe attenuation seems to be improved to the earlier period. Simulations of MAARSY433 with the polarization of this period, however, predict a deterioration of the radiation pattern (see Table 4.3) due to the mixed polarization used within the same antenna array - circular polarization from MAARSY343 and the Hexagon B-08 and linear polarization from the remaining antennas. The beam width of the main beam apparently increases by 0.2°, the gain drops by marginally 0.15 dB, while the attenuation of the strongest side lobe is improved to 16.3 dB. Especially the latter is rather doubtful as the subsequent analysis indicates an increased pick up of incident noise power.

The incident noise power as well as the beam pointing and width analysis for CasA during the mentioned period for MAARSY343 is depicted in Figure 4.16. The estimated beam position and width of MAARSY343 and the dynamic of incident power for this period seems to be comparable to the earlier period. In general, this period appears to be slightly noisier as the contours of the individual sources and the Milky Way are slightly diffuse. However, the different time of the year and thus the zenith distance of the sun, geomagnetic activity and different amount of observational data have to be considered.

The largest discrepancy is the actual amount of the median filtered maximum incident power, which seems to have dropped by 1.5 dB since the conversion to circular polarization. In the earlier periods CasA was the dominating radio source in the sky, not considering the drop of antenna gain for the different zenith angle pointing directions. Since circular polarization is used, the intensities of CasA and CygA dropped by 1.5 dB and 1.1 dB respectively, while CygA is now superseding CasA by +0.2 dB as the major radio source for MAARSY.

From various observations and studies it is known that CasA emits linear polarization from almost everywhere on its supernova shell, but with varying intensity and spectral index (see e.g. *Boland et al.*, 1966; *Downs and Thomson*, 1972; *Mayer and Hollinger*, 1968, for observations at higher frequencies and *Taylor et al.* (2012) for VHF observations). Thus, a mixture of many linearly polarized waves, but different tilt angle, is received, where the strength received by orthogonal linear antennas is approximately identical. The shape of the Milky Way and the remaining diffuse background radiation appears to be unchanged, while their detected power is damped by approximately the same order.

Theoretically, the intensity of a single linear wave will be damped by 3 dB when received with a circularly polarized antenna compared to a linear antenna perfectly matched to the tilt angle (see Figure 3.7 on page 21). A potential source for additional attenuation, namely the polarization box combining the two linear antennas, could be excluded as reference measurements indicate only about 0.1 dB attenuation.

Concordantly, the beam width of MAARSY433 for this period appears to be increased by approximately 0.7° (see Figure C.6 in the Appendix), the dynamic range of detected

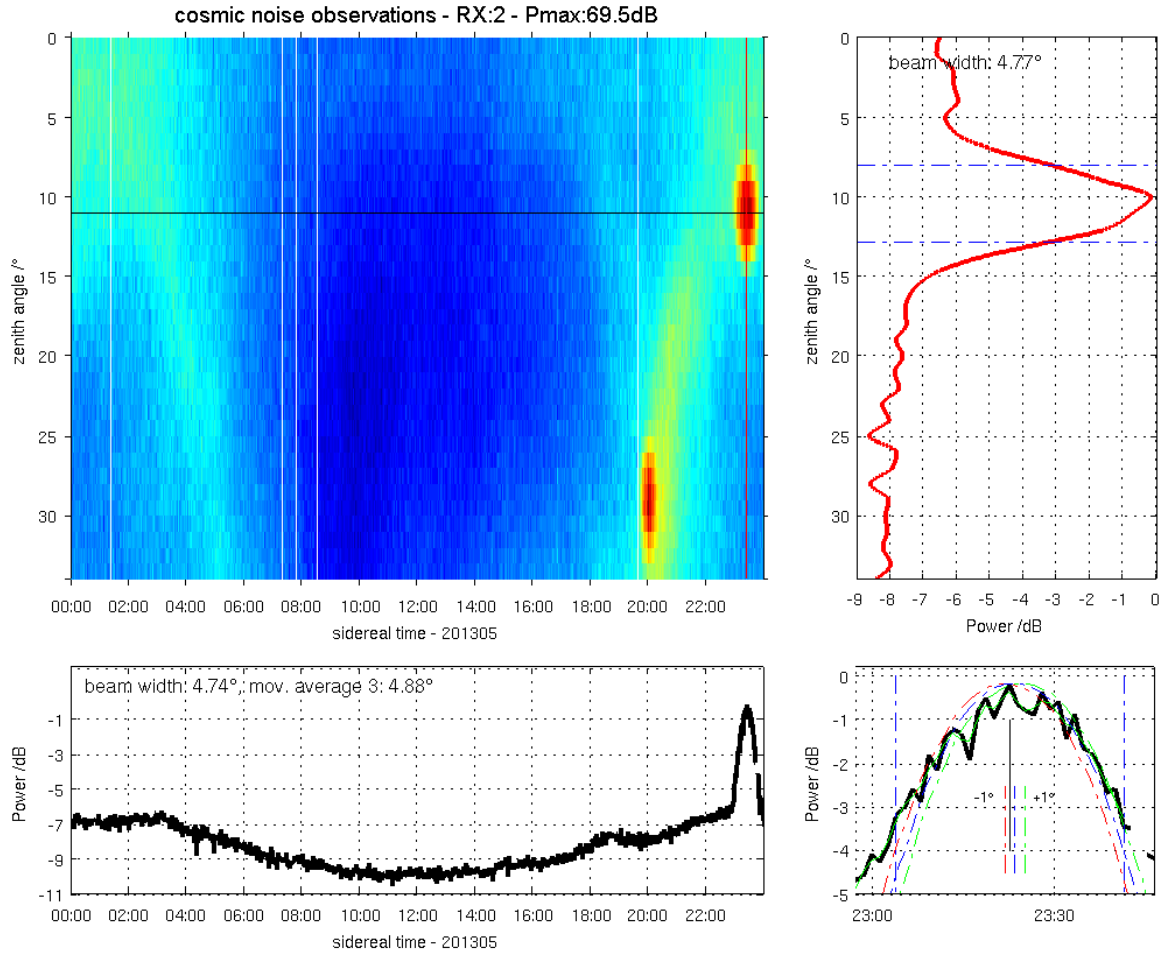


Figure 4.16 Analysis of the incident sky noise power for the period of May to September 2013 received with MAARSY343. A detailed description of the individual panels is given in Figure 4.15 and in the accompanied text.

noise power dropped by 2.25 dB while the maximum intensity dropped by 2.6 dB. Assuming 1.5 dB polarization loss as estimated for MAARSY343, the maximum detected intensity for MAARSY433 lacks 1.1 dB. As at the same time the dynamic is also significantly reduced, the reason can only be found in the radiation pattern in terms of broadened beam width, deteriorated side lobe attenuation and likely reduced gain of the total array. This is partially also indicated in the simulations of MAARSY433’s radiation pattern for this period (see Table 4.3).

4.3.3 Observations September to November 2013

The last step in the polarization upgrade of MAARSY’s antenna array was taken in September 2013 when all of the remaining antennas were converted to circular polarization. It was anticipated to see restored quality in the MAARSY433 observations, while for MAARSY343 they should be equal to the prior period. Unfortunately, this period is characterized by frequent and intense fluctuations of the detected power. Therefore, the data can only be

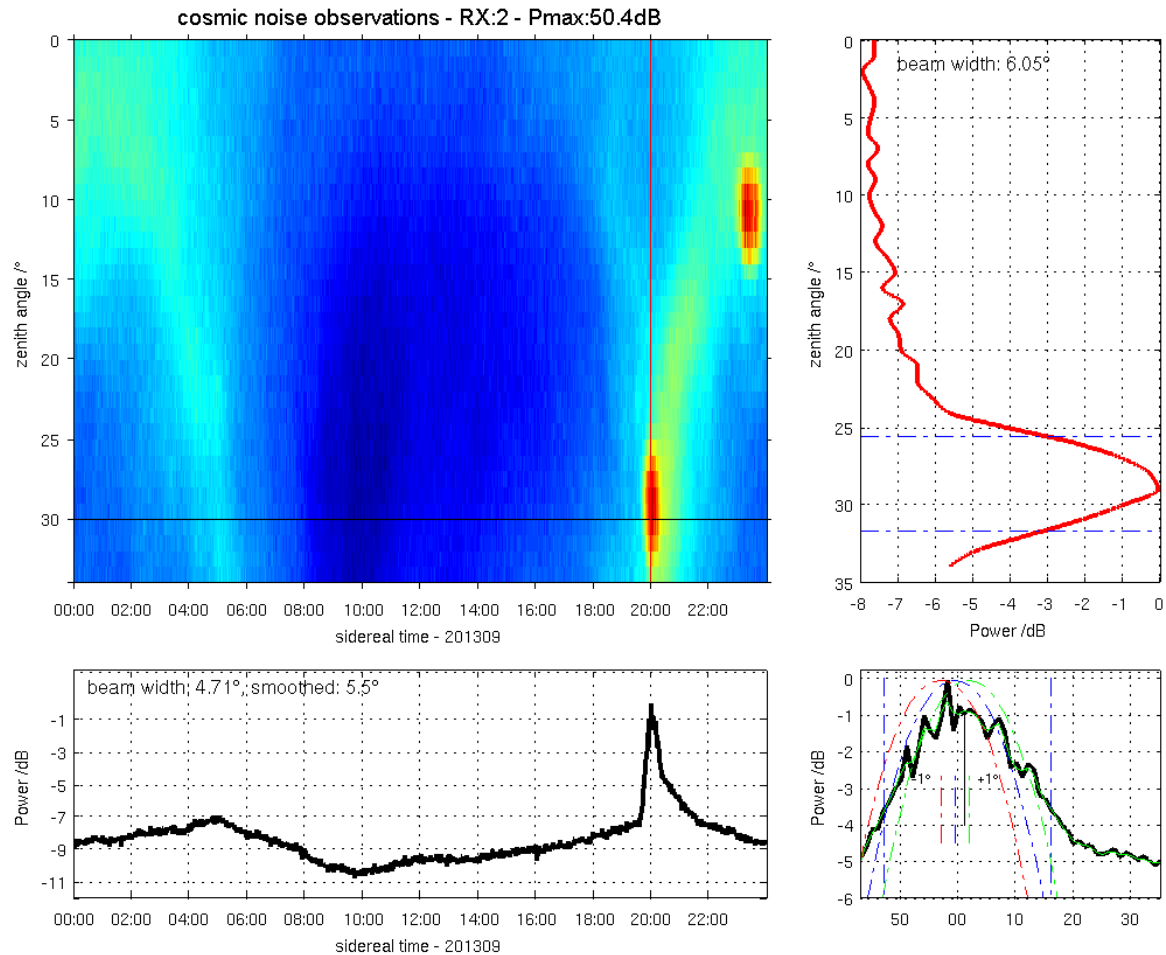


Figure 4.17 Analysis of the incident power of Cygnus A for the period starting in September 2013 received with the circularly polarized MAARSY343. Descriptions of the individual panels are given in Figure 4.15 and in the accompanied text.

analyzed for either rather unreliable single days or a composite of all existing data of that period, where both are still marked by intense fluctuations.

The beam pointing appears unchanged, while the estimated beam widths for both MAARSY433 and MAARSY343 are enlarged for CasA. The reason for this apparently imprecise estimate can be found in the shape of the individual and the averaged passages of CasA, caused by the high variability of and also during the individual days. Even though the estimated beam width observing CygA for MAARSY433 for the averaged data is larger than for the earlier period, but still plausible and in the order of the simulations for both azimuth and zenith. The analysis of the software combined MAARSY343 beam is depicted in Figure 4.17. The estimated beam width along the zenithal scan appears too large, which is likely caused by the flattening of the curve around CygA due to averaging of the highly variable data. The findings for this period underline the necessity to analyze undisturbed days or the use of a median filtered data series of sufficient length. To derive more accurate and reliable estimates additional observations are needed, with at least a few days of undisturbed conditions.

4.4 Comparison of observations with the Global Sky temperature Model (GSM)

Interestingly, the estimated deviation of nominal beam pointing for CygA is slightly conflicting the same method applied for CasA. The reason of this apparently flawed estimation is the proximity of both sources to the galaxy. For all periods the same approximate offsets to the predicted positions of both sources were observed, $\approx -0.5^\circ$ for CasA due to the chronological earlier "arrival" of the Milky Way and $\approx +0.5^\circ$ for CygA due to its opposite location in respect to the Milky Way. An influence of the zenith pointing angle on the azimuth pointing precision, which has to be systematic, can not be reasonably distinguished and is thus neglected. Therefore, the likely true deviation has to be within that range, presumably corresponding very well to the intended and simulated pointing direction.

Another complication for the analysis of these cosmic noise observations and the evaluation of the radar's performance is caused by the modification of the Signal Processor Units (SPU), performed during a maintenance visit of IAP and Genesis staff (see Section B.3). The aim of these modifications was the improvement of MAARSY's total dynamic range, by decreasing gain at the SPUs and thus also limiting the noise contribution of that stage to the total noise figure. The gain of the SPUs have been reduced by 25 dB, which was confirmed later on by the standard delay line calibration method. However, the 25 dB reduction could only be found using the widest filter widths selectable for the intermediate frequency (IF) and baseband (BB). Concordantly, the averaged sky noise observations with MAARSY343 starting in September 2013 (Figure C.7 in the Appendix) show a reduction of detected power by about 19.7 dB for the maximum power (CygA) and about 18.5 dB for the "quiet" regions of the sky, resulting in 10.1 dB dynamic range. Using MAARSY433 a decrease in power by 17.8 dB for the maximum detected power and 19.2 dB for the minimum intensities could be found. These observations were conducted similar to those of the earlier periods with the same experiment configuration, e.g. the same filter settings ($B_{eff}=1.24$ MHz), which is just less than half of the maximum available bandwidth. The reason of this discrepancy is presumably dependent on the filter settings and has to be evaluated carefully during the next maintenance visits.

Interestingly, the dynamic range of the incident sky noise detected with MAARSY433 supersedes MAARSY343 for the now completely transformed array, which agrees with the simulations of the radiation pattern and underlines the pattern improvements of MAARSY433 since it applies uniform polarization.

4.4 Comparison of observations with the Global Sky temperature Model (GSM)

In this section the comparison of the averaged time series for a sidereal day to a global sky model is presented. The method has already been applied and published in *Renkowitz et al. (2012)* and *Renkowitz et al. (2013a)*. Surveys of cosmic noise radiation have been performed by several radio astronomers in the last seven decades. The first systematic survey was performed by *Reber (1940)*, who discovered the inverse relation of observation frequency and power density of these emissions, where he therefore suspected a non-thermal radiation process. One of the first extensive surveys has been presented by *Haslam et al. (1974)*, *Haslam et al. (1981)* and *Haslam et al. (1982)* for a frequency of 408 MHz, which is still used as an all sky reference nowadays. On even higher frequencies e.g. *Reich et al. (1997)* undertook detailed studies of cosmic noise emissions at approximately 1.4 GHz. For lower frequencies the earlier cosmic sky noise surveys e.g. *Cane (1978)* are based on observations with a 11° wide beam, which is considerably large compared to MAARSY. The map of this survey

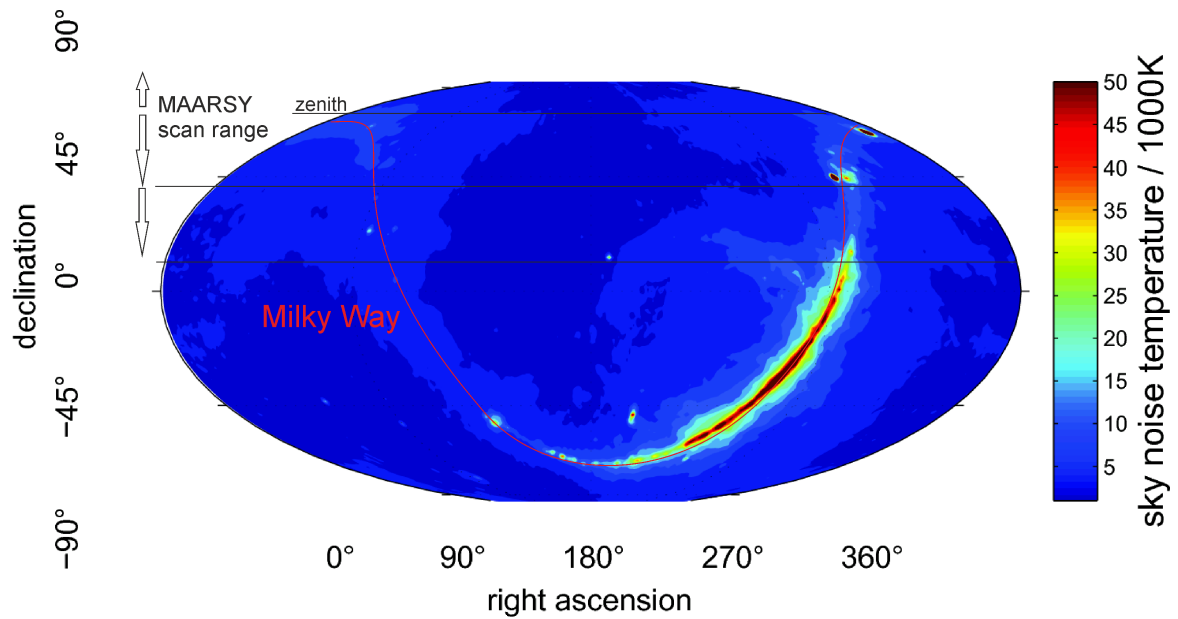


Figure 4.18 GSM simulated intensities emanating from distinct and diffuse cosmic radio sources for 1° resolution at the frequency of 53.5 MHz transformed to Mollweide projection in celestial coordinates. The red line indicates the Milky Way, the horizontal lines mark the MAARSY zenith position and the typical (30°) and the extended (60°) scan range. Modified after *Renkwitz et al.* (2012).

appears smoothed due to the larger beam width and does not show the dynamic range. However, there have been e.g. narrow beam studies at 22 MHz by *Roger et al.* (1999). Every of these studies implies valuable information for further comparisons, while the difference in the observation frequency has to be considered. Recently, *de Oliveira-Costa et al.* (2008) derived the Global Sky temperature Model (GSM), which allows to create temperature references for any user defined frequency in the range from 10 MHz to 100 GHz and sky pointing direction. The model is based on the merging of the eleven most accurate sky noise surveys. At our frequency of interest, this results in a GSM with significantly increased resolution. The accuracy of the temperatures of the GSM is given as $\leq 10\%$ depending on the frequency and sky region. For our observation frequency the GSM is highly dependent on the 45 MHz surveys of *Maeda et al.* (1999), which have been performed with the MU radar for the northern declinations and on *Roger et al.* (1999) using the 22 MHz DRAO radio telescope⁵. The angular resolution and beam width in both surveys are better than the beam width we used for the observations with MAARSY. The fine structure in the GSM relies on observations performed on higher frequencies. Hence, the model data offers an appropriate angular resolution for further comparisons. A similar approach has been used by *Stober et al.* (2011) for the calibration of meteor radars. Applying this technique, we may gain additional information about the radiation pattern of the radar. The sky noise temperatures derived from the GSM⁶ (see Figure 4.18) with its native resolution are interpolated to the resolution of

⁵Dominion Radio Astrophysical Observatory, Canada

⁶As a co-author Dr. G. Stober (IAP) contributed to earlier publications (e.g. *Renkwitz et al.*, 2012, 2013a) and the here presented analysis with the computation of the GSM model data.

4.4 Comparison of observations with the Global Sky temperature Model (GSM)

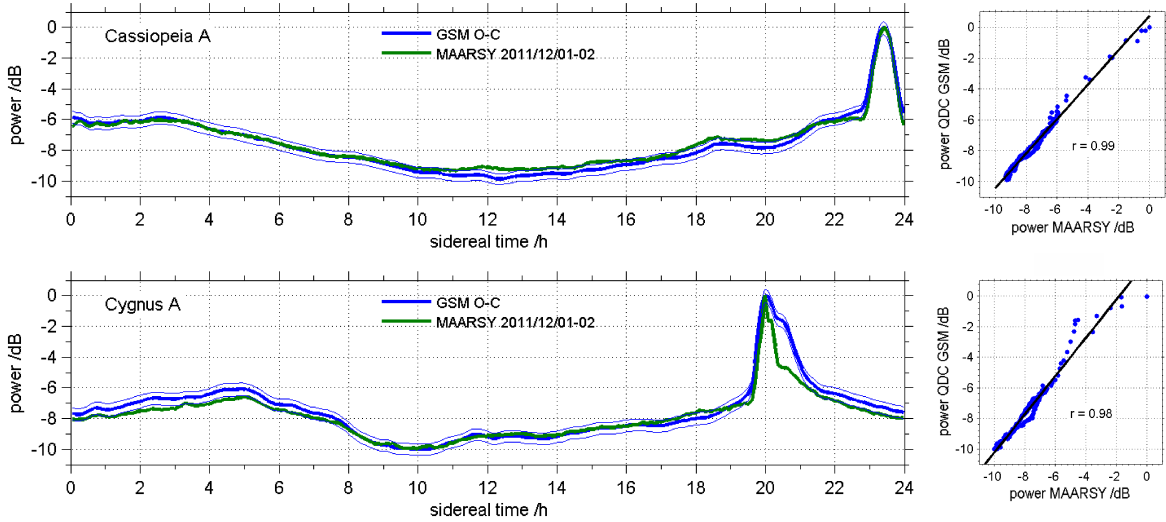


Figure 4.19 Left: Comparison of the observed intensities during December 2011 with the GSM temperature model for two beam directions pointing to Cassiopeia A and Cygnus A. Right: Correlograms of both comparisons highlight the similarity of observations and the model data. Modified after *Renkwitz et al. (2012)*.

the simulated radiation pattern. The GSM data is convolved with the simulated radiation pattern to derive realistic temperature profiles. Included are the losses in the coaxial cables to the antennas and the typical noise figure of the receiver front ends (see Sections B.2 and B.4 for a detailed discussion).

The first analysis results for fixed off-zenith beam pointing through the culmination of CasA and CygA were presented in *Renkwitz et al. (2012)*, where a very good agreement was already found (see Figure 4.19). Subsequently, two-dimensional results including maps of both observations and GSM simulations were shown in *Renkwitz et al. (2013a)* for the total scan range of $\theta = 0 - 34^\circ$.

The earlier experiments were mainly restricted to the use of either the full hardware combined MAARSY433 or the software combined MAARSY343, generated from the integration of the seven Anemone signals (A to M) with appropriate phasing. The only exception was an observation on a campaign basis where also the outer antenna groups Hexagons '8' and the scattered groups '10' were connected to separate receiver channels, which allowed us to form MAARSY433 in software (e.g. *Renkwitz et al., 2013b*). In the data of this experiment an increase of incident power for the distinct radio sources Cassiopeia A and Cygnus A and a decrease of power around the "cold" part of the sky resulting in approximately 1 dB more dynamic range of incident power was found. This confirmed the obvious assumption of the impact of the radiation pattern on the detection of galactic radio emissions, where both the distinct sources and the "quiet" part of the sky provide valuable information. Continuous comparisons of observations and the GSM data facilitated the understanding of the sensitivity to the detected cosmic noise emissions due to changes in the antenna array.

The computed GSM model for the period of May to September 2013 is depicted in Figure 4.20 which resembles the observations performed with MAARSY. The deviation is presented in the bottom panel, where main deviations can be seen around zenith and areas around $\theta = 30^\circ$. The intensity of cosmic radio sources like supernova remnants experiences a frequency dependent intrinsic fading rate of 0.5-1% year⁻¹ (see e.g. *Bridle, 1967; Agafonov,*

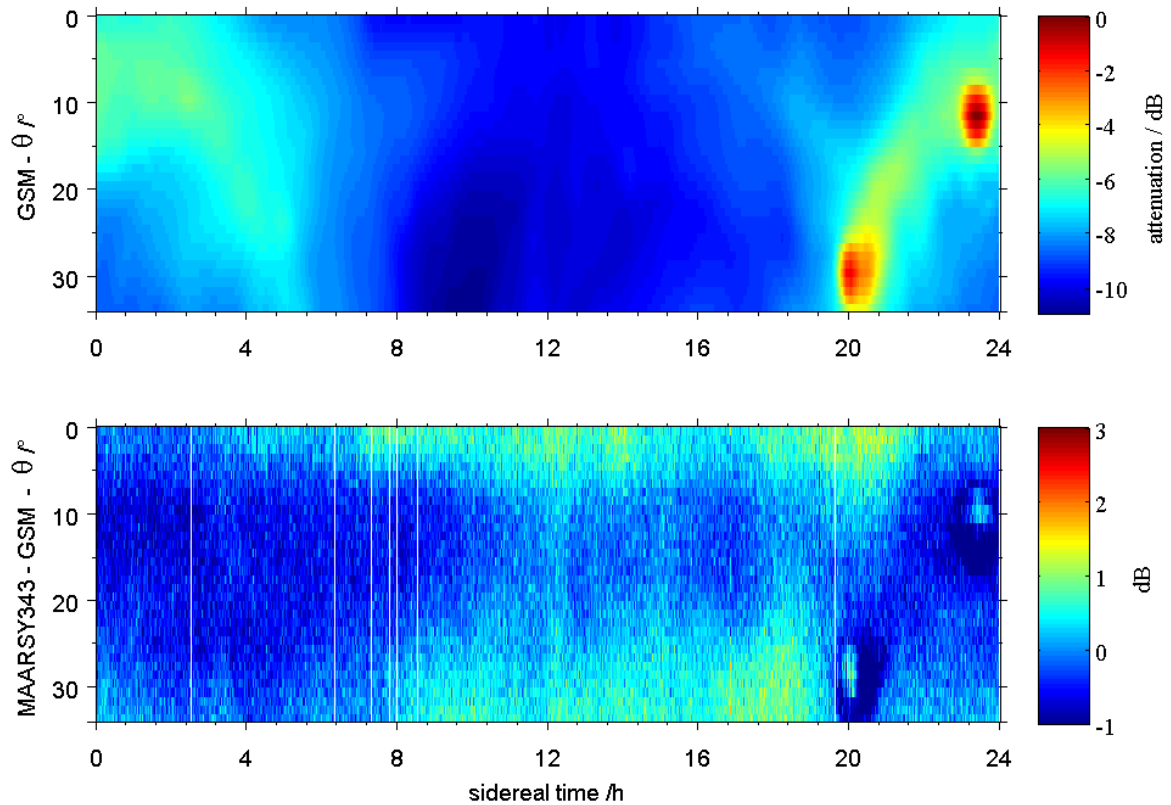


Figure 4.20 Top: Incident power originating from distinct and diffuse cosmic radio sources from modeled GSM data convolved with the simulated complete MAARSY343 radiation pattern. Bottom: Deviation of the observations (composite May to September 2013, previously depicted in Figure 4.16) and GSM model data.

1996; Riahi, 2002; Vinyajkin and Razin, 2004; Helmboldt and Kassim, 2009). As the secular decrease of the supernova remnant CasA is pretty accurately resolved in the GSM no additional amendment is needed. This can be seen from the simulated GSM temperatures for CasA and the reference source CygA ($T_{CasA}/T_{CygA} = 1.137$), considering the simulated gain loss pointing to higher off-boresight directions ($g_{CasA}/g_{CygA} = 1.174$) the relative intensity CasA/CygA in the GSM equals 0.968. For comparison, a factor of approximately 0.97 is seen in recent preliminary LOFAR⁷ measurements (Yatawatta, 2008). This is supported by the VLSS⁸ database (*VLSS Remote Sensing Division*, 2014), which considering the secular decrease of CasA finally results in a relative intensity CasA/CygA of 0.99.

Concordantly, for all observations within the mentioned periods of MAARSY the beam pointing accuracy was satisfactorily, however, the estimated beam widths appeared to be at least 0.5° larger than simulated. The source of this broadening was assumed to be additional noise pick up due to the presence of the side lobes. To verify this, the simulated radiation pattern used for the comparisons with the GSM described above was modified by removing MAARSY's main beam. The convolution of this radiation pattern with the GSM represents the incident noise power which is unintentionally picked up with all side lobes (see Figure

⁷LOFAR: LOw Frequency ARray for radio astronomy, built by ASTRON, Netherlands

⁸VLSS: Very Large Array Low frequency Sky Survey, the VLA is operated by the National Radio Astronomy Observatory, see Helmboldt *et al.* (2008) and Cohen *et al.* (2007) for more details.

4.4 Comparison of observations with the Global Sky temperature Model (GSM)

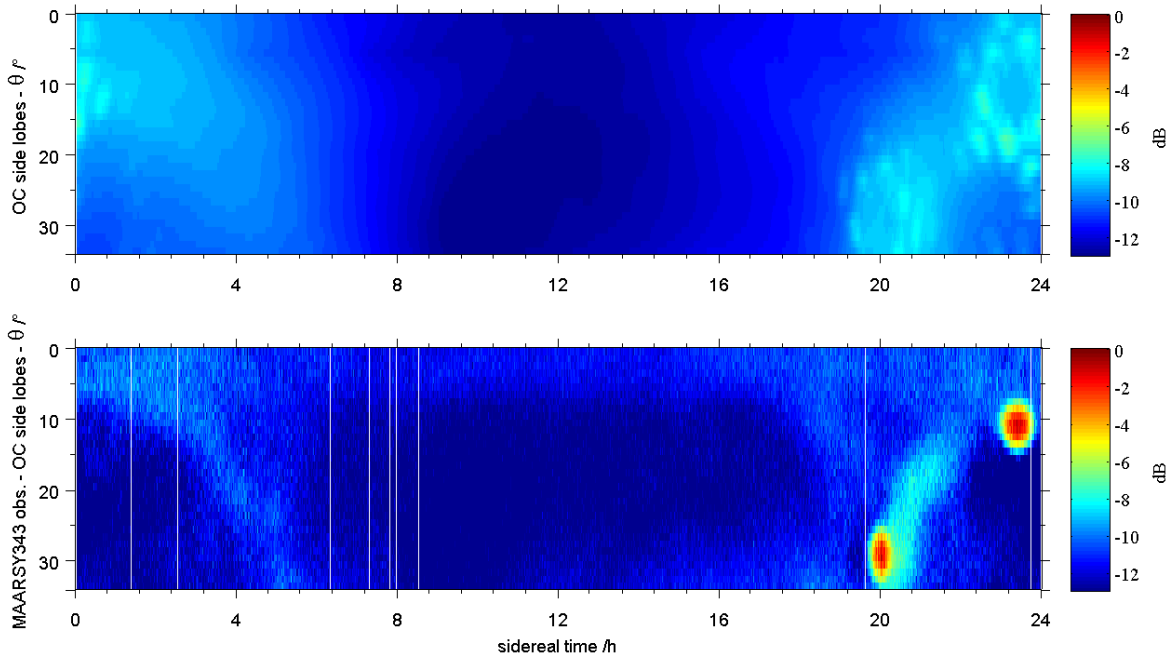


Figure 4.21 Top: Modeled GSM sky noise data convolved with the simulated side-lobe-only MAARSY343 radiation pattern. Bottom: Observation data (composite May to Sept. 2013) subtracted by the above shown side lobe pick up.

period	MAARSY433		MAARSY343		MAARSY343 w/o SL	
	Cas A	Cyg A	Cas A	Cyg A	Cas A	Cyg A
simulated width	3.8°	4.2°	4.2°	4.6°	4.2°	4.6°
Sept. 2012 - May 2013	4.28°	4.86°	4.90°	5.56°	4.46°	4.77°
w/o scintillations	4.46°	4.86°	4.77°	5.56°	4.37°	4.72°
May 2013 - Sept. 2013	5.21°	6.45°	5.12°	6.49°	4.59°	5.65°
w/o scintillations	5.17°	6.40°	4.68°	4.77°	4.15°	4.11°
Sept. 2013 -	4.55°	4.99°	4.85°	6.05°	4.46°	4.53°
w/o scintillations	4.68°	5.21°	4.99°	5.83°	4.55°	5.17°

Table 4.4 Results of the analysis of the galactic radio emissions estimating the beam width for beam pointing to Cassiopeia A and Cygnus A with MAARSY433, MAARSY343 and the side lobe cleaned MAARSY343 sorted for the observation periods with and without ionospheric scintillations.

4.21). The typical shape of the side lobes of MAARSY343 can be recognized. The intensity of this figure is referenced to the maximum intensity of the GSM model with the complete MAARSY343 pattern. To derive the incident noise power collected only by the main lobe, the side-lobe-only reference is subtracted from the earlier analyzed observations. The analysis of these "corrected" data sets reveals beam widths which are in better agreement to the simulated radiation pattern (see Figure 4.22). The results of this re-analysis is presented in Table 4.4, highlighting the significance of the side lobes for radio astronomical experiments.

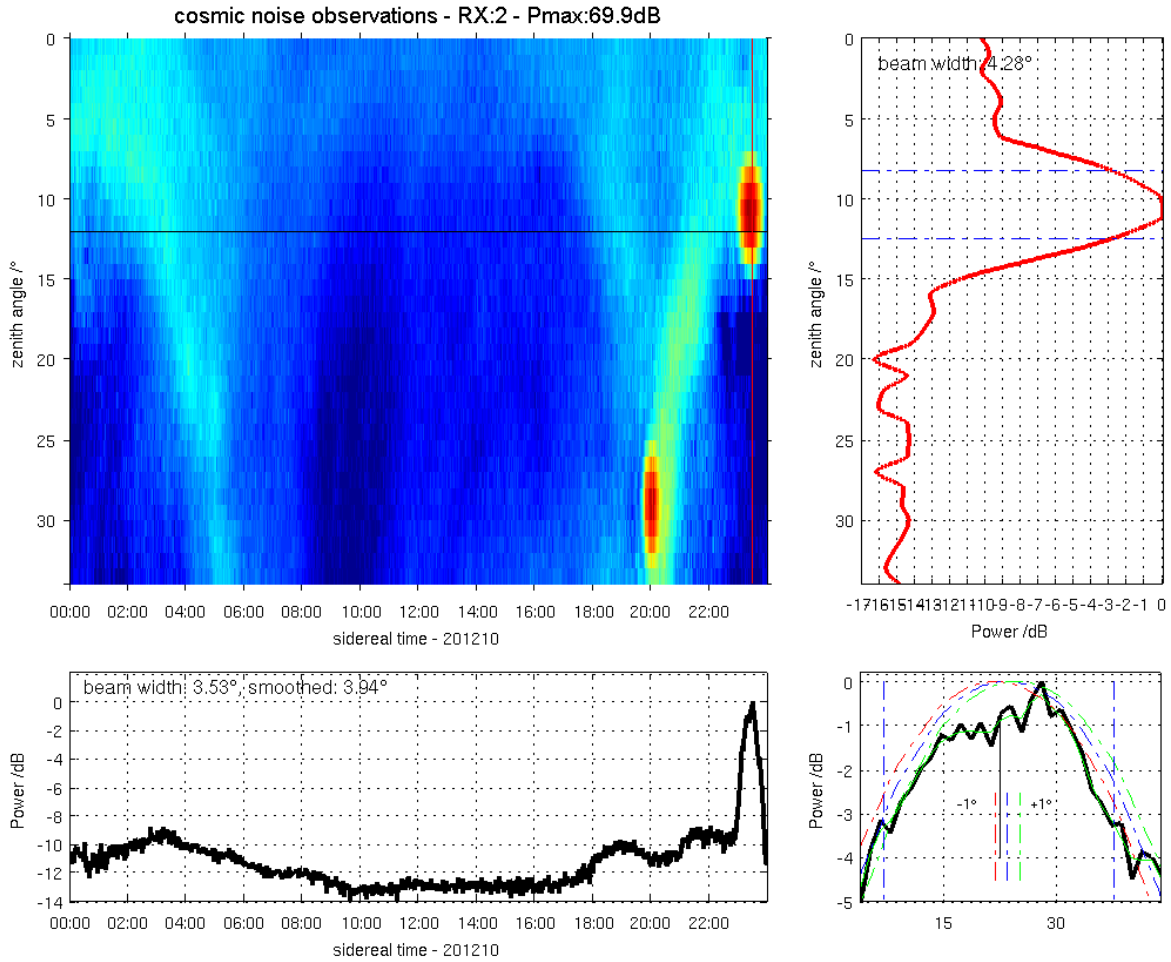


Figure 4.22 Analysis of the data from Sept. 2012 to April 2013 (shown in Figure 4.15), but subtracted by the simulated side lobe pick up. The estimated beam width of this side-lobe-free pattern is now in good agreement with the simulations (4° to 4.2° for both planes).

It is clearly evident, that the direct use of the detected radio source intensities leads to an overestimation of the beam width. After the subtraction of the simulated pick up of all side lobes from the data, the estimation of the beam width appears much more reasonable. However, the influence of the detected radio sources' intensity fluctuations, modulated by ionospheric scintillation and absorption events, is remarkable. Here, only the selection of apparently quiet days and the continuing observation of the sources offer reliable estimations. A similar attempt has been tried convolving the GSM data with only the main beam, where cleaned signatures of the individual radio sources without side lobes could be seen. However, the GSM simulation with the side-lobe-only pattern clearly marks directly the inherent quality of the antenna array used for the observations.

4.5 Expansion of the sky noise scan

Encouraged by the observations during the earlier described experiments an additional experiment was performed expanding the cosmic emissions observation scan from $\theta = 0^\circ$ to 60° off zenith. Despite the inherent generation of grating lobes at these high off-zenith angles, such an experiment may provide valuable information. With the presence of grating lobes additional power may be received originating from the grating lobes pointing directions. At the same time the gain of the main beam is decreasing as the integral power from all directions is constant, no matter how many lobes are generated or to which direction they are pointing to. Thus, the detected incident power may be highly affected by the grating lobes, as soon as their pointing directions are co-located with any radio sources within the observed frequency spectrum. The composite of both experiments is presented in Figure 4.23. Here, a general increase of power towards lower declinations ($\leq 30^\circ$), which is likely caused by additional noise pick up of the now appearing grating lobes, can be seen. With the expanded scan range the continuation of the Milky Way, the radio sources Taurus A (supernova remnant at $\approx 05:30$ LST and $\theta = 48^\circ$, $\delta = 21^\circ$) and the nebula 3C400 (at $\approx 19:30$ LST and $\theta = 55^\circ$, $\delta = 14^\circ$) can be identified. Additionally, increased intensity can be seen around the position of the radio galaxy Virgo A at 12:35 LST and $\theta = 57^\circ$, $\delta = 12^\circ$ and the North Polar Spur.

The detection of these additional radio sources underlines the potential of large off-zenith angle observations, even though the generation of grating lobes has to be carefully considered.

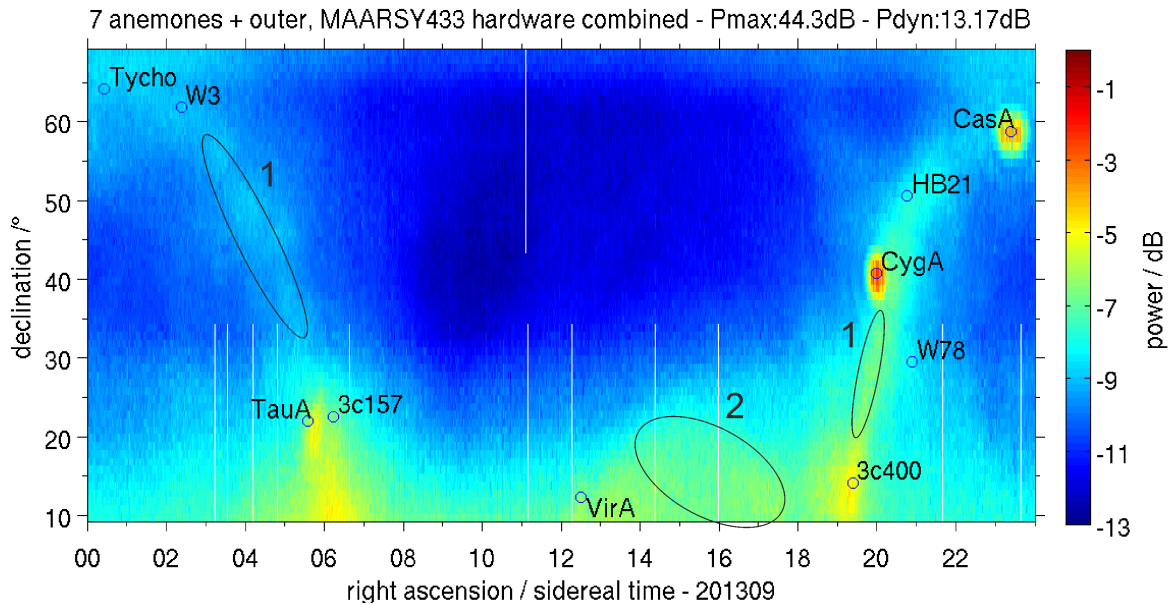


Figure 4.23 Composite of cosmic noise scans ($\phi = 180^\circ$, $\theta = 0 - 60^\circ$) covering a declination range of $9.3 - 69.3^\circ$. The individual radio sources dominating on the observation frequency are marked according their position and can be found in the Appendix in Table C.3. The increased intensity extending along most of the individual radio sources marked by (1) originate from the Milky Way, as well as (2) which is the North Polar Spur.

These observations were subsequently compared with the GSM including the simulated radiation pattern, where a reasonably good agreement was found (see Figure 4.24). The side lobe subtracted intensities for the entire scan $\theta = 0^\circ$ to 60° and 1 min resolution are shown in Figure 4.25. The signature of the Milky Way, the North Polar Spur (12-18 sidereal time, $\theta = 50 - 60^\circ$) and the other distinct sources are now slightly more pronounced compared to the direct observations using the full radiation pattern in Figure 4.23 as well increased dynamic range of the detected intensities.

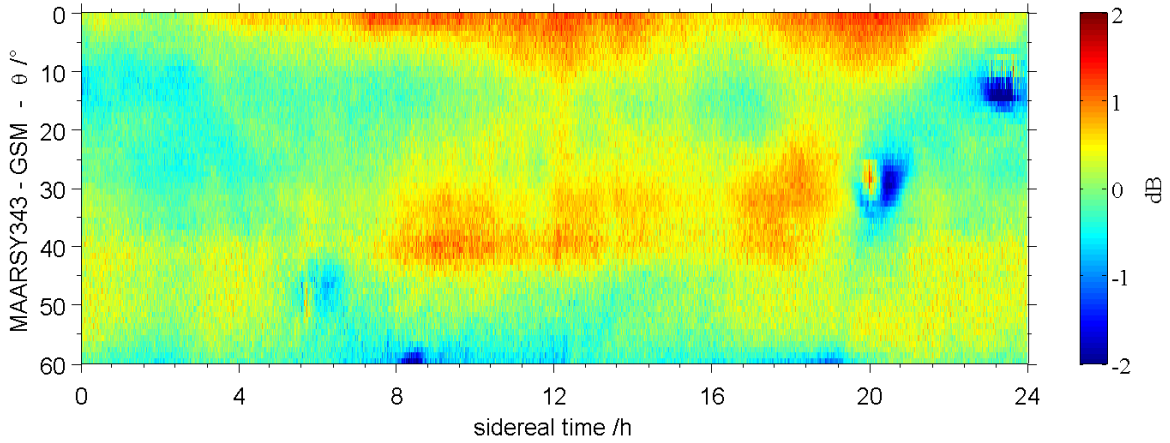


Figure 4.24 Deviation of observation with MAARSY343 for September to November 2013 for the zenith scan range of $0^\circ - 60^\circ$ (see Figure 4.23) and GSM reference model data.

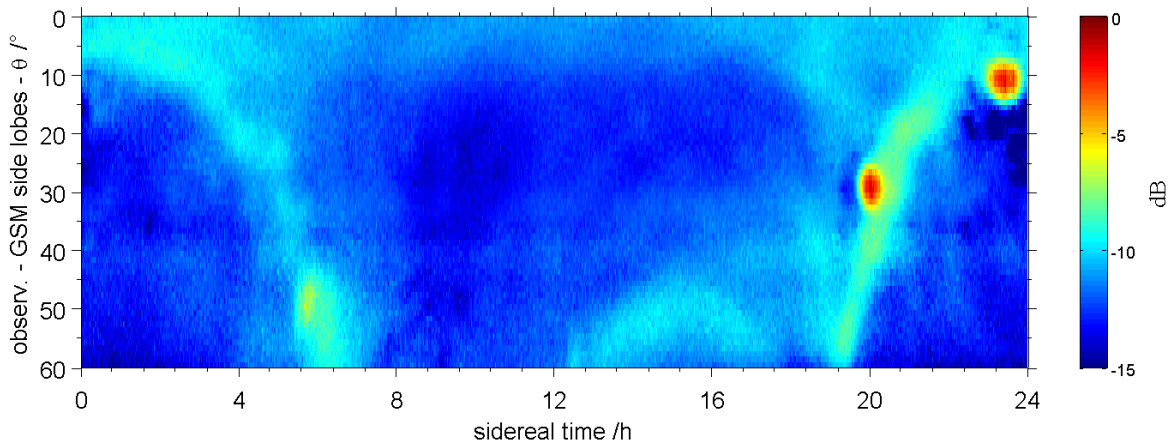


Figure 4.25 Detected intensities for the scan range $\theta = 0^\circ$ to 60° with subtracted side lobes pick up (similar to Figure 4.22) for the period September to November 2013. Compare to Figure 4.23.

4.6 Antenna array gain estimation by observing cosmic radio sources

In this section a method is presented which allows the estimation of the effective gain of the antenna array used to observe cosmic radio sources. The most prominent radio sources at the center frequency of MAARSY (53.5 MHz) are the supernova remnant Cassiopeia A and the radio galaxy Cygnus A. The gain estimation method highly depends on the absolute flux densities of the observed sources at the observing frequency and the knowledge of the appropriate calibration factor and all losses, which are not included in the calibration factor, e.g. losses in the antenna feeding network and reflection at the antenna array.

The calibration factor relates the power detected by the radar in arbitrary units to either power or equivalent temperature in units of W or K respectively. The calibration factor used here is derived in two ways, namely a) by the use of the Global Sky temperature Model (GSM) by *de Oliveira-Costa et al.* (2008) and the accurate simulation of the radiation pattern composing c_{GSM} , and b) by the calibration factor c_{RX} derived from measurements with a broadband signal source of known intensity (see Figure B.8 in Section B.4, page 115).

As pointed out before, the knowledge of the sensitivity of the receiving system is essential and thus all components of the receiving chain have to be evaluated. In Section B.4 in the Appendix the noise figure of the MAARSY receiver has been determined, where a broadband noise source of known intensity is compared to the detected power. All losses existent in front of the calibrated receiver are directly convertible to a noise figure of the individual stage and deteriorate the overall noise figure of the system. The total system noise figure can be calculated as described in Equation 4.5, where NF_{RX} is the already measured noise figure of the MAARSY receiver and a_{losses} are losses in front of the receiver and thus not included in NF_{RX} , e.g. the loss of the antenna feeding network in dB (see Section B.2), the mismatch loss of the antenna in dB or any other additional losses. The impedance mismatch power loss is shown in the Appendix in Figure A.3 (page 102).

$$NF_{sys} = NF_{RX} + \sum a_{losses} \quad (4.5)$$

A serious source of concern for the accuracy of these gain estimations are the absolute flux densities for the observed sources Cassiopeia A and Cygnus A. While both sources have been thoroughly studied in the last six decades, a reliable flux density for approximately 50 MHz is not really existent. Recently, radio astronomers rediscovered the lower VHF frequencies and below for studies. One of the reasons to observe on lower frequencies is the spectrum of the individual sources, where non-thermal synchrotron radiation typically maximizes at frequencies around 10-20 MHz as well as the observation of the red-shifted emission spectra of the expanding universe. With the commissioning of e.g. LOFAR⁹ (*de Vos et al.*, 2009), LWA¹⁰ (*Ellingson et al.*, 2013), VLA¹¹ (*Kassim et al.*, 2007), SKA¹² (*Hall et al.*, 2008) and other VHF radio observatories the gap of the last 40 years is going to be filled. Recently, first preliminary estimations of Cygnus A flux densities observed with LOFAR were published (*McKean et al.*, 2011; *McKean*, 2011, 2013). Also, a relative Cassiopeia A flux density could be estimated by *Yatawatta* (2008). A second valuable and reliable source is the online

⁹LOw Frequency ARray for Radio astronomy, built by ASTRON, Netherlands

¹⁰Long Wavelength Array, New Mexico/USA

¹¹Very Large Array, New Mexico/USA

¹²Square Kilometre Array, Australia, New Zealand, South Africa

database of *VLSS Remote Sensing Division* (2014) referring to *Helmboldt et al.* (2008), *Cohen et al.* (2007), *Baars et al.* (1977) and *Kühr et al.* (1981). This database allows the search for various natural radio sources and corresponding flux density estimation for a user specified frequency by interpolation and model fit. However, the given values are not corrected for the secular decrease of supernova remnants like Cassiopeia A. *Vinyajkin and Razin* (2004) published their analysis of the Cassiopeia A fading rate for 155 MHz.

Therefore, the observations of Cygnus A are very useful, even though this radio source does not reach an elevation of more than 61.5° , which is generally just within the normal beam pointing cone of MAARSY and is thus already subject to significant drop of antenna array gain. Nevertheless Cygnus A offers a constant flux density and due to its distance of approximately 600 million light-years it can easily be treated as a point source for the angular resolution of MAARSY, even though the source is split into two separate jets (see e.g. *Lazio et al.*, 2006).

The following methodology is in principle identical to the experiments described by *Kuz'min* (1966) and *Priese* (1964).

4.6.1 Methodology of the antenna gain estimation by the aid of cosmic radio source observations

As introduced previously, the calibration factor for the used receiving system and the losses that are not included in the calibration factor need to be known. The first calibration factor used here is derived from the Global Sky temperature Model by *de Oliveira-Costa et al.* (2008). This method has already been used in Section 4.4 for the comparison with the angularly resolved observations. The GSM allows the generation of Quiet Day Curves (QDC) for the specified antenna pattern and receiving system (noise figure, losses). Due to $P = k_B T B$ the equivalent temperatures from the GSM are then compared to the detected incident noise power from the distinct radio sources and the diffuse background to derive the calibration factor c_{GSM} (see Figure C.8 in the Appendix on page 125).

The data set used here is identical to the one discussed in Section 4.3. The detected incident maximum noise power is converted to the equivalent temperature, where both are the sum of the internal and external noise power or equivalent noise temperature.

$$T_e = P_{max} \cdot c_{GSM} \quad (4.6)$$

Alternatively, the calibration factor c_{RX} is used, which was derived from comparisons to a solid state noise source of known intensity.

$$T_e = P_{max} \cdot \frac{c_{RX}}{N_{CI}} \quad (4.7)$$

The calibration factor c_{RX} used here is interpolated by the derived calibration factors for two bandwidths settings (see Sections B.4 and B.5). N_{CI} is the number of coherent integrations used in the observations.

The system noise figure is also converted to equivalent noise temperature as given by Equation 4.8 and subtracted from T_e , which should now only describe the equivalent temperature of noise power collected by the antenna array (T_{source}), presumably emanating from the actually observed distinct radio source.

$$T_{source} = T_e - 290(10^{N_{Fsys}/10} - 1) \quad (4.8)$$

4.6 Antenna array gain estimation by observing cosmic radio sources

observation bandwidth	1.24 MHz
c_{RX} until Sept. 2013	$1.61 \cdot 10^{-3} K/du^2 \pm 3\%$
c_{RX} since Sept. 2013	$1.79 \cdot 10^{-1} K/du^2 \pm 3\%$
N_{CI}	8
c_{GSM} until Sept. 2013	$1.89 \cdot 10^{-3} K/du^2 \pm 10\%$
c_{GSM} since Sept. 2013	$1.56 \cdot 10^{-1} K/du^2 \pm 10\%$
T_{sys} until May 2013	775 K $\pm 2\%$
T_{sys} since May 2013	800 K $\pm 2\%$
S_ν CasA	18111 Jy
S_ν CygA	19065 Jy

Table 4.5 Calibration factor c_{RX} and c_{GSM} for MAARSY343 (including the observational bandwidth), the system temperature for the individual periods and the flux density of the individual sources used for the gain estimation for Cassiopeia A and Cygnus A. For the calibration factors du represents the detected power in digitizer units, the absolute value of the digitized in-phase and quadrature components.

The effective antenna aperture for the incident flux intensity is calculated by Equation 4.9, where k_b is the Boltzmann's constant and S_ν is the radiation flux density of the radio source. The gain of the antenna array can then be calculated by Equation 4.10.

$$A_{eff} = T_{source} \cdot k_b / S_\nu \quad (4.9)$$

$$g = \frac{4\pi \cdot A_{eff}}{\lambda^2} \quad (4.10)$$

The results of these calculations for both sources Cassiopeia A and Cygnus A are subsequently presented and summarized in Table 4.6 for the two main periods September 2012 to April 2013, May 2013 to September 2013 and the preliminary results for observations since September 2013.

4.6.2 Results of the gain estimation method using cosmic radio sources

The constants used in the gain estimation calculations are given in Table 4.5 for the individual periods. The results of the calculations for both sources Cassiopeia A and Cygnus A are presented in Table 4.6 for the two main periods September 2012 to April 2013 and May 2013 to September 2013. During the first period the MAARSY array was still mainly linearly polarized and therefore only collected approximately half of the incident intensity, therefore S_ν has been accordingly set in the calculation. For the second period the MAARSY343 array was completely converted to circular polarization involving both orthogonal planes and thus the total flux density was used in the calculations.

The repeatedly detected averaged power values for the passages of CasA and CygA are rather high, which lead to high equivalent source temperatures and thus estimated gain.

For the second period the detected power for both sources decreased by 1-2 dB, which in combination with the supposed full flux densities of the sources leads to an estimated gain for the antenna array clearly below the simulated radiation pattern (-2.35 to -3.55 dB). A likely reason is the polarization of the radio sources and the Faraday rotation while the wave is traveling through the ionosphere. The observations imply that the incident polarization of the radio sources is not equal to the receiving polarization of MAARSY. Especially interesting is the differing drop of detected incident power of both sources from the first to

the second period. During the second period CygA's intensity consistently supersedes CasA, which underlines the assumption of polarization effects affecting the observations of both sources radiation. The emissions of CygA appear to match better to MAARSY's polarization than CasA's.

period	CasA	CasA, removed side lobes	CygA	CygA, removed side lobes
Sept. 2012 - May 2013				
direct, c_{RX}				
P_{in}/dB	71.0	69.9	70.6	69.2
T_{source}/K	18161	14418	16495	12156
g_{obs}/dBi	33.46	32.45	32.82	31.49
g_{sim}/dBi	32.4	32.4	31.7	31.7
$\Delta g/dB$	1.06	0.05	1.12	-0.21
GSM cal. c_{GSM}				
T_{source}/K	22263	17862	20304	15203
g_{obs}/dBi	34.19	33.19	33.55	32.23
$\Delta g/dB$	1.79	0.79	1.85	0.53
May - Sept. 2013				
direct, c_{RX}				
P_{in}/dB	69.3	68.1	69.5	68.3
T_{source}/K	12802	10038	13406	10511
g_{obs}/dBi	28.65	27.51	28.64	27.50
g_{sim}/dBi	32.2	32.2	31.6	31.6
$\Delta g/dB$	-3.55	-4.69	-3.00	-4.14
GSM cal., c_{GSM}				
T_{source}/K	14022	10923	14848	11474
g_{obs}/dBi	29.32	28.24	29.35	28.23
$\Delta g/dB$	-3.08	-4.16	-2.35	-3.47
Sept. - Nov. 2013				
direct, c_{RX}				
P_{in}/dB	50.0	48.9	50.0	49.2
T_{source}/K	13718	10550	14699	11305
g_{obs}/dBi	28.97	27.74	29.06	27.85
g_{sim}/dBi	32.2	32.2	31.6	31.6
$\Delta g/dB$	-3.23	-4.46	-2.54	-3.75
GSM cal., c_{GSM}				
T_{source}/K	14823	11494	15883	12316
g_{obs}/dBi	29.32	28.15	29.42	28.24
$\Delta g/dB$	-3.08	-4.25	-2.28	-3.46

Table 4.6 Gain estimation for MAARSY343 by observing cosmic radio sources for the three periods a) Sept. 2012 to May 2013, b) May 2013 to Sept. 2013 and the preliminary results for c) the time since Sept. 2013. The columns CasA and CygA refer to observations of the radio sources Cassiopeia A and Cygnus A, respectively. Δg depicts the deviation to the simulated gain of the antenna array.

4.6 Antenna array gain estimation by observing cosmic radio sources

For the first period, the estimated gain exceeds the simulated radiation pattern, which underlines the additional noise power pick up besides the intended discrete radio sources. Every single side lobe of the radiation pattern collects noise power, where the integral of all side lobes may reach significant orders. This is unfortunately the case for MAARSY, where the first two side lobes are pointed towards additional sources during the observations of CasA and CygA, due to their proximity to the Milky Way. The first two side lobe rings of MAARSY are generated at $6-7^\circ$ and approximately $10-11^\circ$. This offset to the main beam results in large overlap portions around the two radio sources with the Milky Way, "contaminating" the measurements of the distinct sources.

The overestimation of array gain clearly demanded a detailed evaluation of the pattern side lobes. Therefore, similar to the attempts in Section 4.4, the simulated radiation pattern of MAARSY has been modified to cut out the main beam. This side-lobe-only pattern was convolved with the GSM data to quantify the impact of the side lobes in the observations. This side lobe pick up was then subtracted from the earlier GSM-model and the observation data, concordantly resulting in a larger dynamic range of the incident noise power and a reduction of incident power for the distinct radio sources by approximately 1.2 dB.

Applying this technique for the first period, the estimated gain for both radio sources agrees well with the gain of the simulated radiation pattern for both calibration factor methods. The result for the calibration factor obtained from hardware measurements appears to match the simulated gain of the antenna array better. The estimated gain for the GSM calibration using c_{GSM} is about 0.7 dB larger, however the uncertainty of the GSM (10%) is significantly larger than for the other method. The estimated gain for the subsequent periods drops accordingly with the side lobe rejection, which does not impair the earlier findings of polarization selectivity. The results for September to November 2013 are preliminary as there is no reliable calibration factor available yet, since the gain modification of the Signal Processor Units. Thus, the calibration factor was approximated according to the detected incident noise of that period as no further changes to MAARSY343 were done. However, the GSM calibration indicates equivalent results, which supports the estimation of the calibration factor c_{RX} . Nevertheless, the estimated gain of MAARSY343 for partial or complete circular polarization is likely systematically flawed due to the favored circular polarization compared to the generally linear polarization of the radio sources.

The individual availability of both orthogonal linear polarization planes would allow a significant improvement in the observations of the natural radio sources. Such a configuration would facilitate the formation any polarization on demand during the subsequent analysis, like both orientations of linear and circular polarization. .

The presence of the side lobes and their impact were known previously, but the quantity of the influence was rather astonishing as the side lobes are attenuated by approximately 15 dB and better.

4.7 Geophysical applications of sky noise observations

In the subsequent sections two examples of geophysical applications of sky noise observations are presented. In the previous sections of this chapter composite intensity maps of the individual MAARSY periods were used to estimate the characteristics of the radiation pattern. Here, these maps are compared to observations of an individual day and are analyzed to derive background information of the D- and F-region ionization. This is of special interest, as these information can also be derived in combination with active radar experiments and hence do not deteriorate the temporal or angular resolution of these experiments.

4.7.1 Observation of scintillation events

Within several experiments observing cosmic radio sources like e.g. CasA, strong fluctuations in power were often recognized. On geomagnetic quiet days, only very little deviations of the expected gaussian-like shape were seen during the passage of the sources through MAARSY's main beam. However on some days, the intensity received with MAARSY may rapidly vary by ± 4 dB. The reason for these fluctuations is assumed to be a mixture of ionospheric scintillations (inhomogeneities in the electron content within the F-region, see e.g. *Weiler, 2000; Rao, 2003*), absorption events in the D-region and potentially events outside the Earth's atmosphere stimulated by the solar wind (typically at frequencies below 50 MHz, see e.g. *Rickett and Coles, 2000*).

First thoroughly studies of ionospheric scintillations were performed by e.g. *Aarons (1973), Crane (1974)* and *Whitney and Basu (1977)* for the VHF range due to encountered signal fading events on satellite up- and downlinks. These events could be related to the individual geomagnetic position, variances in the refractive index on the propagation path in the ionosphere due to irregularities in the electron density, influencing both, amplitude and phase of the propagating signal. The propagating wave experiences scattering and diffraction processes, where the wave is spread, split and likely subsequently superposed with the indi-

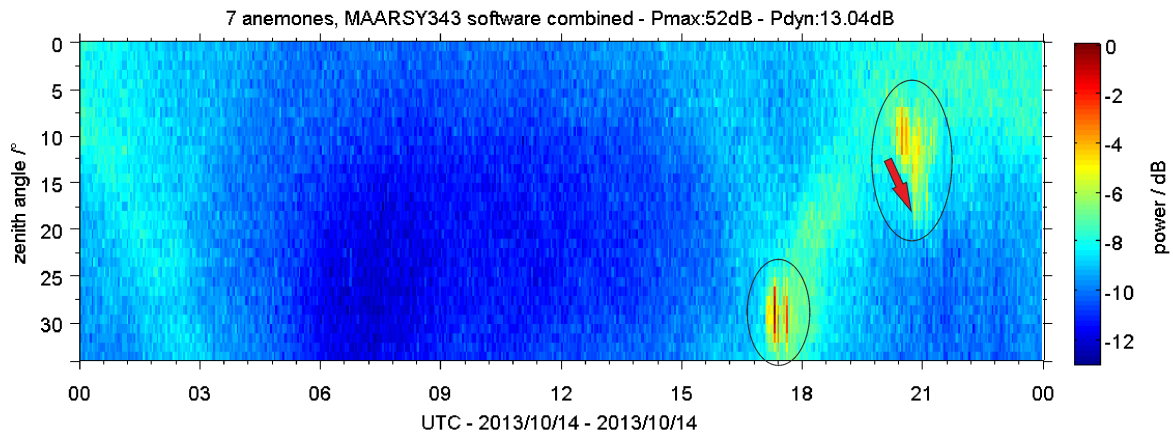


Figure 4.26 Incident noise power for the standard sky noise zenith scan from 0° to 34° on 2013/10/14. The individual sources CasA ($\approx 20:40$ UTC) and CygA ($\approx 17:20$ UTC) show extremely high fluctuations in power (ellipses), while the intensity originating from CasA also seems to change its angle of arrival by about 3° during the passage through the beam (red arrow). See Figure 4.23 on page 61 as reference for rather undisturbed conditions.

4.7 Geophysical applications of sky noise observations

vidual phases of all components. The amplitudes of signals originating from distinct sources received on Earth may thus fluctuate significantly and even appear to suddenly arrive from a different direction, see e.g. the MAARSY observations in the case of CasA on 2013/10/14 at approximately 20:50 UTC in Figure 4.26 marked by a red arrow.

A review of 50 years of scintillation studies has been given by *Aarons* (1997), while the dependency on the solar cycle has also been examined by *Basu et al.* (1988). In recent years ionospheric scintillations are still of interest for both VHF, see e.g. *Banola et al.* (2005) and *Visessiri et al.* (2004), and for microwave frequencies e.g. on the propagating signals of global satellite navigation systems, see e.g. *Béniguel et al.* (2009) and especially for high latitudes *Jiao et al.* (2013).

Simultaneous observations of a common radio source by MAARSY and another independent station in the same frequency range would help to exclude a possible source for the observed power variations within the MAARSY system. For this purpose Dr. McKay-Bukowski from Sodankylä Geophysical Observatory (SGO) kindly offered to provide data for 53.5 MHz taken by the Kilpisjärvi Atmospheric Imaging Receiver Array (KAIRA), which is located near Kilpisjärvi in Northern Finland ($69^{\circ}4.25\text{N}$, $20^{\circ}45.72\text{E}$, ≈ 200 km east of MAARSY).

The applicability of KAIRA measurements for comparison is illustrated in the Figures 4.27(a) to 4.28(b), where first the intensity distribution for quiet conditions is shown as reference, succeeded by three plots of highly variable intensities detected on 2013/12/25 marking disturbed ionospheric conditions. The detected intensities fluctuated in time scales of seconds (see references in the above paragraphs), which let the sources flicker in the observations. This underlines the earlier reasoning to either refuse the data during these disturbed times (as for the generation of the composite maps presented earlier in the thesis) or carefully applying e.g. a median filter. In total, the observations of MAARSY and KAIRA for four

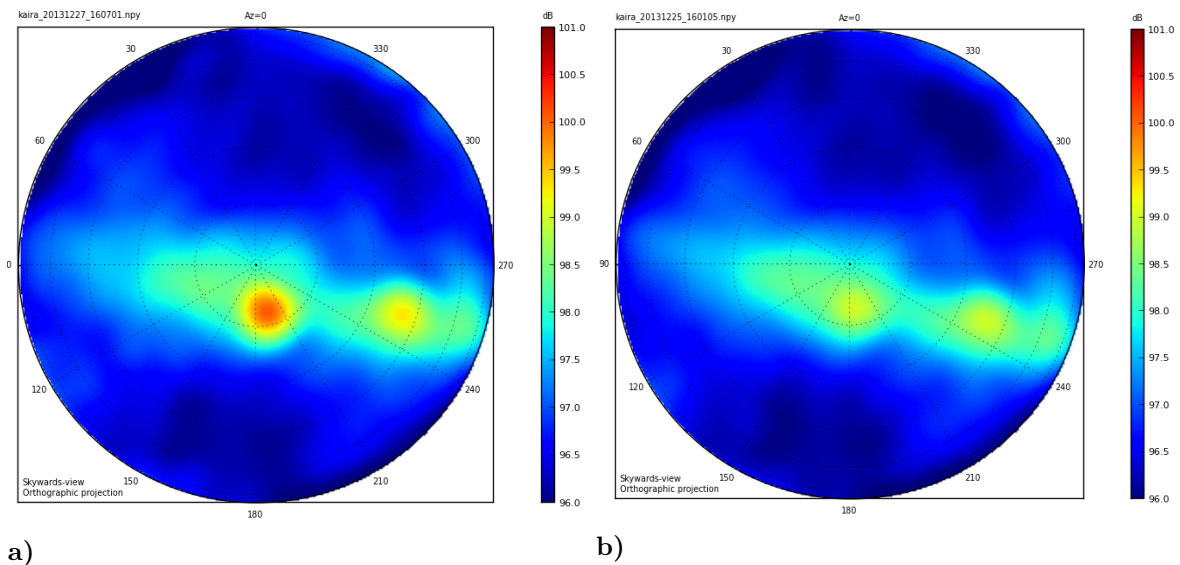


Figure 4.27 All-sky snapshots of the angular distribution of incident cosmic radio emissions received by KAIRA on **a)** 2013/12/27 for quiet conditions with CasA close to zenith ($\phi = 185^{\circ}$, $\theta = 11^{\circ}$) and CygA ($\phi = 250^{\circ}$, $\theta = 40^{\circ}$) at an equivalent sidereal time as in the subsequent figures. **b)** shows the onset of a scintillation event, where CasA's intensity is damped, for 2013/12/25 at 16:01:05 UTC. The green contour intensity originates from the Milky Way. Courtesy of Dr. McKay-Bukowski, SGO.

Chapter 4 Passive experiments to estimate the radiation pattern

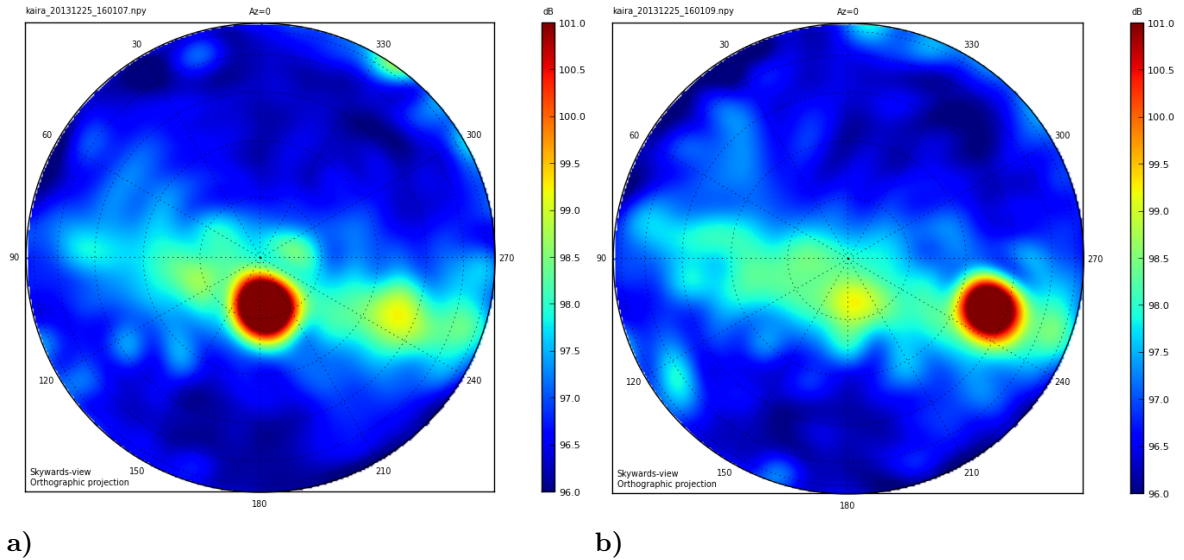


Figure 4.28 All-sky snapshots of the angular distribution of incident cosmic radio emissions received by KAIRA on 2013/12/25 at a) 16:01:07 UTC and b) 16:01:09 UTC. Note, Figures 4.27(b) to 4.28(b) are separated by 2 s each. Courtesy of Dr. McKay-Bukowski, SGO.

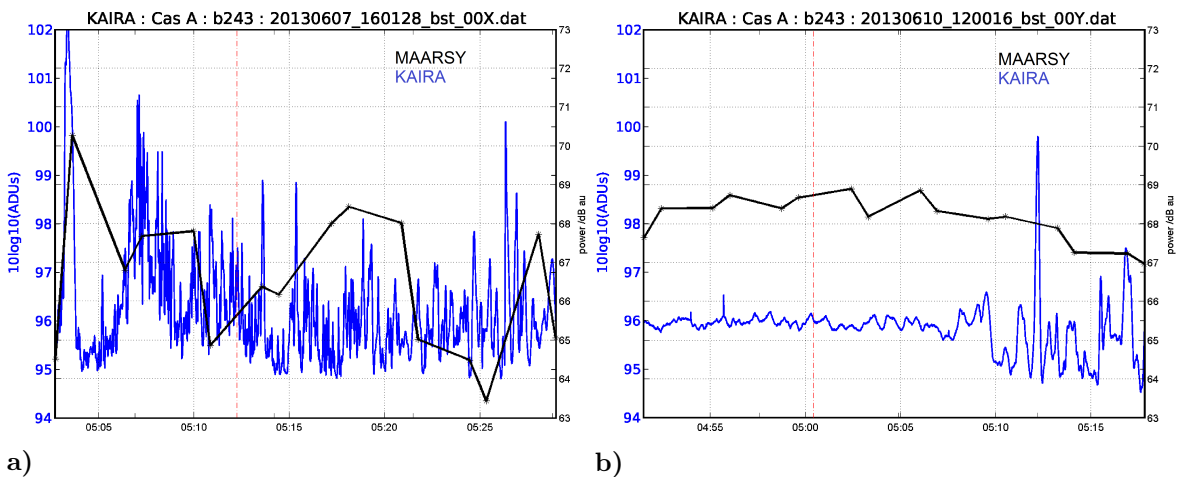


Figure 4.29 a) Incident power of Cassiopeia A observed with KAIRA (blue, left axis) and MAARSY (black, right axis) on 2013/06/08 at $\approx 05:12$ UTC. The red broken vertical line marks the time of the culmination of CasA. The detected power emanating from CasA vary significantly for both stations, indicating disturbed ionospheric conditions, while b) depicts mainly quiet conditions for both stations as detected on 2013/06/11 at $\approx 05:01$ UTC. Note, KAIRA tracks CasA and thus, a flat line is assumed for quiet conditions, while for the MAARSY observations CasA drifts through the main beam.

different days at times near the upper culmination of CasA are subsequently compared. It has to be noted, that these experiments were not planned initially and are just analyzed on the basis of already existing data. The data from KAIRA emanates from an experiment in which the position of CasA was tracked, while for MAARSY the data is taken from different experiments with a beam pointing direction of $\phi = 180^\circ$ and $\theta \approx 10^\circ$ observing the drift of

4.7 Geophysical applications of sky noise observations

CasA through MAARSY's beam as at these days no distinct sky noise experiment was performed. Nevertheless this comparison already thoroughly confirms the earlier assumptions. In the Figures 4.29(a) and 4.29(b) the detected power of CasA is depicted for the station KAIRA (blue) and MAARSY (black). The detected power of CasA around its culmination (red vertical line) at the days May 9th, June 8th and June 13th is highly variable. On June 11th the detected power appears to be rather flat for KAIRA (until approximately 05:08 UTC) due to tracking of the source, while for MAARSY the expected slight increase of power up to the culmination and descending afterwards can be seen. This day was exceptionally quiet in terms of geomagnetic activity. The nearby magnetometers did not show any disturbances in the Earth's magnetic field and both, the locally and planetary geomagnetic indices were remarkably low. For the same days the data of the ionosonde located near Tromsø¹³ (69°35N, 19°13.2E) was analyzed and for the same "disturbed" days (2013/05/09, 2013/06/08 and 2013/06/13) indicators of Spread-F could be found, which is also caused by inhomogeneities in the F-region (see Figures 4.30(a) and 4.30(b)).

Therefore, it can be stated, the power fluctuation effects seen frequently by MAARSY on extra-terrestrial radio sources, were also seen simultaneously by an independent system and are hence not generated internally by MAARSY. For detailed continuing investigation of scintillation effects, specific dedicated experiments need to be arranged for both systems. Furthermore, this topic opens a new research area for MAARSY, where the drift of these F-region electron density irregularities producing ionospheric scintillation events can be observed with interferometric means (see e.g. *Basu et al.*, 1996, 1998; *Xu et al.*, 2009; *Tiwari et al.*, 2012).

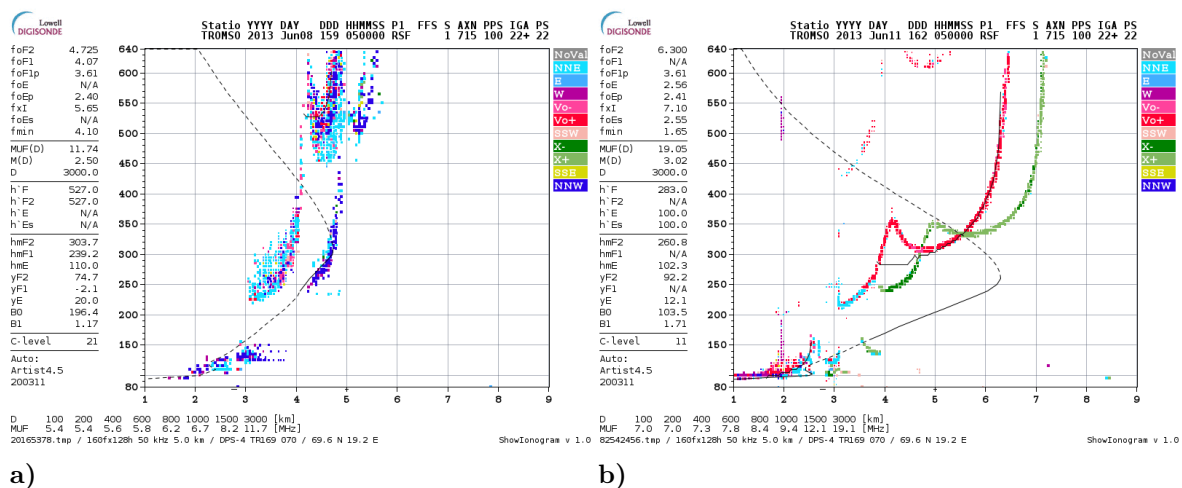


Figure 4.30 Ionograms derived from observations of the ionosonde in Tromsø, show in **a)** distortion events called Spread-F on 2013/06/08, while the profiles in **b)** describe a quiet F-region on 2013/06/11.

¹³Ionosonde data are provided by the Tromsø Geophysical Observatory at the University of Tromsø/Norway and are obtained through the Lowell Digital Ionogram Database (DIDBase, <http://ulcar.uml.edu/DIDBase/>). Reinisch, B. W., and I. A. Galkin, Global ionospheric radio observatory (GIRO), Earth, Planets, and Space, 63, 377-381, doi:10.5047/eps.2011.03.001, 2011

4.7.2 D-region ionizations

In this section the use of MAARSY as a narrow beam imaging riometer is presented, which finally may allow the estimation of D-region ionization for every beam pointing direction. A riometer measures the incident noise power received from galactic radio sources and its damping caused by its propagation through the D-region of the ionosphere. It is well known from the magneto-ionic theory (see e.g. *Budden, 1961*) that this damping occurs as a consequence of collisions between free electrons and neutrals and hence maximizes at altitudes between about 80 km to 90 km. The actual state of this absorption layer may vary in height and intensity depending on solar and geomagnetic activity (see e.g. *Friedrich et al., 2002; Harrich et al., 2003; del Pozo et al., 2002*). Additionally, the precipitation of highly energetic particles may lead to localized enhanced ionization and electron densities of significant order, see e.g. *Singer et al. (2011)* and *Chau et al. (2013a)*.

By creating averaged and if necessary additionally filtered Quiet Day Curves (QDC) for the individual beam directions, which were observed in the sky noise experiments, the key point for the analysis of diurnal data has been established. The detected intensity of the diffuse cosmic radio emissions of a single day were compared to a QDC, typically generated from at least ten quiet and interference-free days.

Figure 4.31 shows the incident noise power from 2013/06/07 observed with MARSY343 (similar events were also prominent on the following day), where the major radio sources show large fluctuations and decreased intensities of the diffuse radiation sources can be seen. This explicitly high absorption event is compared with the averaged QDC of the appropriate period (May to August 2013) and depicted in Figure 4.32. In the upper panel the angularly resolved deviation from the QDC is shown, while the median of all beam directions is shown in the bottom panel. The big red/brown spots are the distinct radio sources Cassiopeia A and Cygnus A, marked by high fluctuations in power presumably due to ionospheric scintillation effects. Besides these major sources the incident power originates from the Milky Way, minor distinct sources and the diffuse background. These sources thus do not prone to scintillation effects and the detected deviations are mainly caused by damping due to absorption events in the D-region. Remarkably high absorption events can be seen at around 21 h, 01 h,

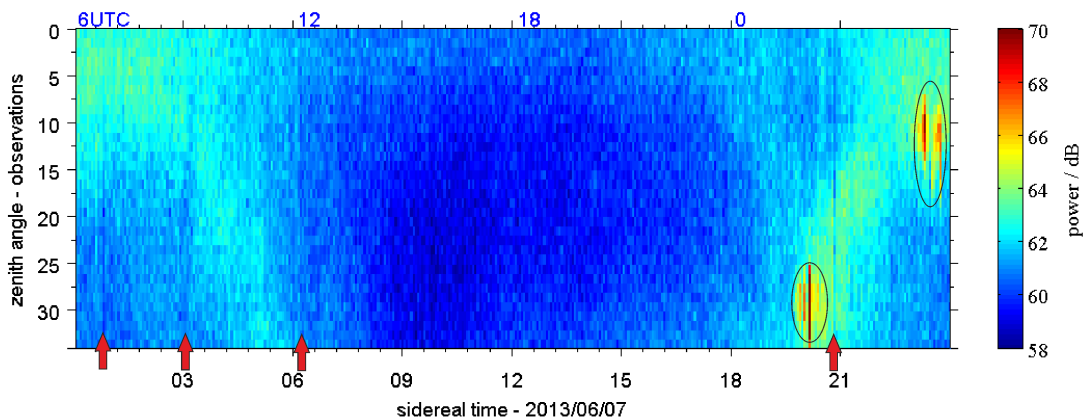


Figure 4.31 Incident noise power detected on 2013/06/07, marked by intense fluctuations of the individual sources (black ellipses) and damping events of the diffuse background (red arrows). See Figure 4.23 on page 61 as reference for rather undisturbed conditions.

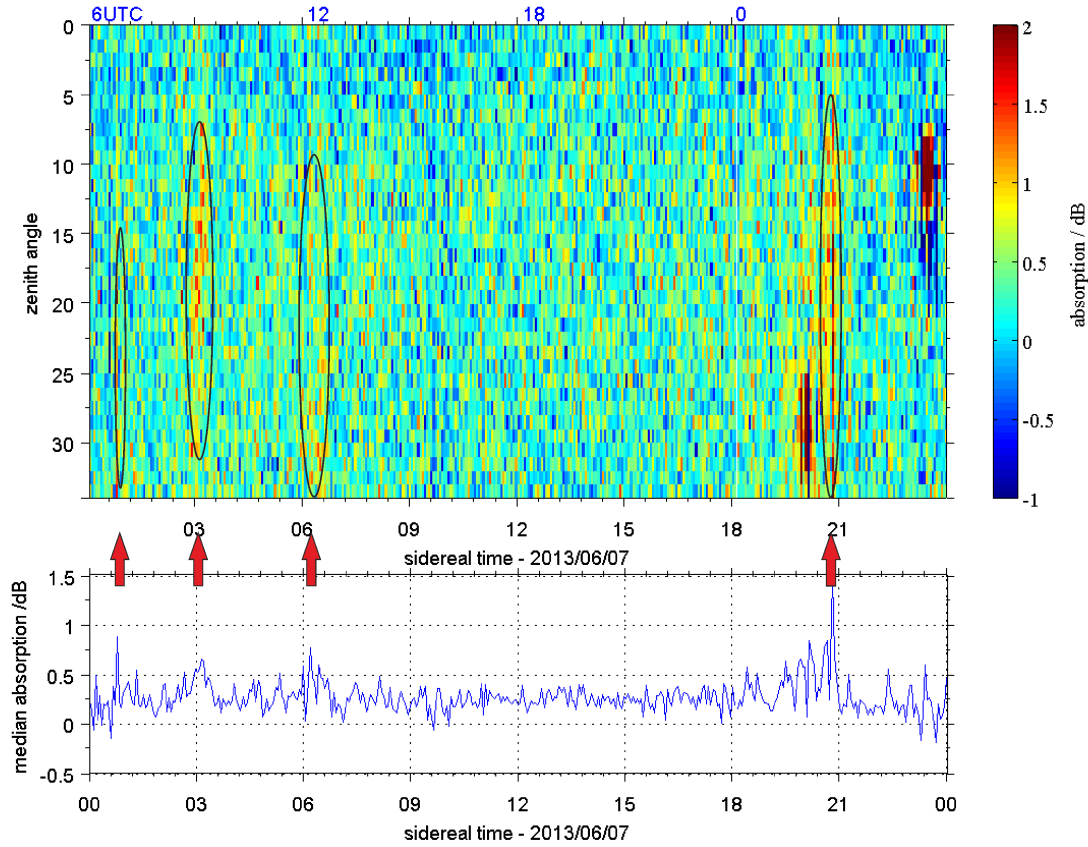


Figure 4.32 The upper panel depicts the angularly and temporally resolved deviation of the observations from 2013/06/07 to the appropriate QDC of the same period. The lower panel represents the median of all beam pointing direction for one sampling period of time. The arrows and ellipses mark the major absorption events.

03 h and 06 h sidereal time, mainly detected at larger off-zenith angles ($5\text{-}35^\circ$). These angularly localized absorption events can be interpreted as patches of enhanced electron densities with horizontal extension along the north-south direction of 10 km to 50 km, based on the observed $5\text{-}35^\circ$ zenith angle and the assumed height of 85 km. Measurements performed on 3.17 MHz with the Saura-MF radar, which is located just 30 km south of MAARSY, indicate increased electron densities for the time of the observed absorption events, see Figure 4.33. These electron densities are derived with the differential absorption (DAE) and differential phase (DPE) technique (see *Singer et al.*, 2005, and references therein). This figure shows the median of hourly electron densities profiles for 2013/06/07 at 02, 06, 08, 12 UTC, complemented by a "reference" night and noon profile of an apparently undisturbed day 2013/06/11 (agrees in principle with the mean profiles in *Singer et al.*, 2011). Additionally, one hourly night profile of 2013/06/07 20 UTC is shown, where the electron densities almost reverted to the normal state. To generate these profiles, data with too low or negative (non-physical) values were rejected as well as data where DAE and DPE differ significantly (by more than a factor of two). The data is subsequently median filtered for one to three hours to generate a reliable profile. No further averaging or smoothing has been applied for Figure 4.33. Even though the profiles of 2013/06/07 are hourly medians, for the times

when absorption events were simultaneously observed with MAARSY, the electron densities appear to be significantly increased compared to a "quiet" day profile. During these events, the maximum received power from the Saura-MF radar and thus also the general electron density in the D-region descends in altitude. The Saura-MF radar may typically only derive electron densities up to 2000 cm^{-3} and thus limiting the height coverage to approximately 70 km at times of strong ionization of the lower D-region.

A generally high global geomagnetic activity can be seen for the night of June 6th and 7th in the data available from *GFZ Helmholtz Centre Potsdam* (2014), indicating a K_p index of 5 to 6, representing one of the most intense distortions in June 2013. Additionally, for the same night a maximum K-index of $K = 7$ has been derived for both Tromsø (69.66°N , 18.94°E) and Dombås (62.07°N , 9.13°E) indicating a severe geomagnetic disturbance (see *Tromsø Geophysical Observatory*, 2014). At the same time the magnetometers on Andøya, Tromsø and Dønna (66.12°N , 12.49°E) detected variations of the magnetic field in amplitude (up to $\pm 1000 \text{ nT}$) and orientation off normal. However, the magnetometers placed north of Andøya indicated weaker disturbances (up to $\pm 700 \text{ nT}$), which could indicate an activity center primarily south of Andøya.

Thus, it could be demonstrated that MAARSY can be used as an imaging riometer to derive background information of the D-region ionization. This is of particular interest if it is derived as a byproduct of active scan experiments, which might e.g. help to understand the generation of Polar Mesospheric Winter Echoes and other phenomena. Furthermore these riometer observations of MAARSY may be used to support and strengthen the electron density estimations of the Saura-MF radar.

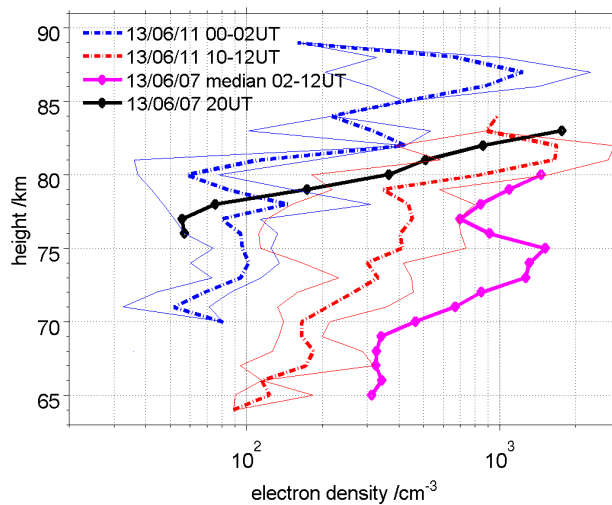


Figure 4.33 Estimated electron densities for 2013/06/07 derived with the Saura-MF radar accompanied by two profiles from 2013/06/11 as reference for quiet night/day conditions and the variability during these hours marked by thin lines of according color. The magenta profile depicts the median for the 2013/06/07 2, 6, 8, 12 UTC hourly profiles. The black profile for 20 UTC underlines the ongoing reversion to the quiet profile.

4.8 Summary

In this chapter passive experiments were presented, which were conducted to derive information about the receiving radiation pattern of the MAARSY antenna array.

First of all, Cassiopeia A was used to derive absolute phases for the MAARSY antenna array and various subarrays. Here, reasonable small phase deviations of the individual subarrays were found (typically $< 10^\circ$). The offset of the cosmic radio source phase calibration to an automatic daily hardware phase test is derived, where the latter does not include the antennas and their feeding cables to the transceiver modules. The standard deviation of the receivers amplitudes could be estimated to 0.2 dB , which agrees well with measurements conducted at the receiving system. Furthermore, no suspicious crosstalk of independent receiver antenna array combinations was found in their correlations.

Two distinct cosmic radio sources (Cassiopeia A and Cygnus A) and the diffuse background as well as the Milky Way were used to estimate the beam pointing accuracy, beam width, approximate side lobe suppression and gain of the antenna array. For the reliable analysis, quiet atmospheric conditions needed to be selected. Thus, composite maps of the detected cosmic radiation for the scan experiments were generated for each period of the polarization conversion from linear to circular. The time of the passage of the distinct radio sources through the individual beam pointing directions of MAARSY was compared to simulations. With this, the beam pointing accuracy could be derived to be better than 1° . The observations were furthermore compared to a Global Sky temperature Model which revealed a high congruence. The width of the main beam was verified for both distinct radio sources ($+0.1^\circ$). The prerequisite for this was the subtraction of the modeled intensities, that are collected by the side lobes, from the observations. Doing so, in reverse, the overall intensity of the side lobes used for the model can be assumed to be appropriate and thus the side lobe attenuation is approximately as simulated.

The detected intensities of the distinct radio sources and the diffuse background consistently decreased during the conversion from linear to circular polarization. The current sense of MAARSY's circular polarization does not coincide perfectly with the incident polarization of the sources, resulting in $\approx 1.5 \text{ dB}$ polarization loss.

With the detected intensities and the appropriate calibration factor the gain of the used antenna array can be estimated for the individual periods of the polarization conversion. While the estimated gain for the linear polarization agrees well with the simulations, it deviates for the mixed and purely circular polarization.

Finally, geophysical applications of the passive experiments were shown. Contrary to the findings observing the diffuse cosmic radio background, significant variations ($\pm 4 \text{ dB}$) were often seen for the distinct radio sources, predominantly caused by ionospheric scintillation and absorption events. To eliminate the source of these fluctuations within MAARSY, simultaneous observations of Cassiopeia A were performed with MAARSY and KAIRA. Even though the stations are separated by 200 km, for four days an equivalent behavior of the detected intensities was found, for both geophysical quiet and disturbed conditions.

Finally, an example was shown, where the earlier derived composite map was compared to the detected intensities of an geophysical highly disturbed day. Strong absorption events (up to 1.5 dB) of the incident cosmic emissions could be shown for times of high ionization. Thus, the feasibility of using MAARSY as an imaging riometer to detect local electron density enhancements could be demonstrated as well as the estimation of the horizontal extent of these patches. In the future it is planned to combine these observations with active scan experiments and can thus be performed regularly to derive D-region background information.

Chapter 5 Active experiments to estimate the radiation pattern

In the prior chapter passive experiments were described, which only provided information about the receiving system. However, with the observations of cosmic radio sources the beam pointing accuracy could already be estimated to be better than one degree for both azimuth and zenith angle as well as finding the beam width to be in good agreement with the simulations. Furthermore, the gain of the antenna array could be estimated for the individual periods for different polarizations.

Complementary to this, information about the transmitting part of the radar have to be gained by either reflecting or scattering off natural or artificial targets or sampling the radiated intensity directly. Only the latter facilitates to gather information of the transmit radiation pattern exclusively, while the other attempts constitute the superposition of both, the radiation pattern on reception and transmission.

For full calibration of the radar targets with known properties like cross-section need to be available within the nominal beam pointing cone. Within the last years, e.g. no calibration sphere satellite of adequate dimensions for the operation frequency of MAARSY was available, which would be significantly beneficial. Thus, other means need to be used. The following sections describe active experiments, which aim for the evaluation of the radiation pattern properties like beam pointing accuracy, beam width and side lobe attenuation to corroborate the findings of the passive experiments.

The first section presents near electric field measurements performed in the proximity of the antenna array or inside. Corresponding simulations are shown, which show good agreement with the measurements of the transmission pattern at ground level. To corroborate this comparison it was planned to perform equivalent measurements of the transmission pattern in greater distance, preferably in the far field. For this purpose a measurement setup, which in principle consists of a receiver, severe filtering, a power detector and an acquisition system, was placed underneath a helicopter. The idea of this experiment was to fly over the operating radar and to measure the radar's intensity directly. The setup including the experiment description and results is presented in detail in the Appendix in Section D.1. Unfortunately, this experiment provided only limited insight for the evaluation of the radiation pattern. The reasons for this were technical issues and the rather low altitude in which the radiation pattern was sampled and is thus severely spoiled by intense reflection and scattering off the co-located hills and the sea, and possibly also interference by other systems. Subsequently active experiments are presented which allow the evaluation of the two-way radiation pattern, which however can be referred to the one-way pattern of the radar. For this purpose, targets like the Earth's moon, satellites, meteors and a payload of an atmospheric sounding rocket are used.



Figure 5.1 Experimental setup during lift-off aiming for the direct sampling of the MAARSY radiation pattern in Dec. 2012.

5.1 Measurements in the near electric field

Since the installation of the first transceiver modules in three Anemones ('A', 'B' and 'M') near electric field measurements have been conducted occasionally. The measurements were evaluated by comparison to NEC simulations and analytical estimates of the radial decrease of intensity.

Near electric field measurements around the antenna array have been performed e.g. in November 2011, which are subsequently compared to two-dimensional model simulations. The simulated field strength is depicted in Figure 5.2(a), where the individual positions of the measurements are marked by red asterisks. Each measurement was obtained with a calibrated NBM-520 meter and EF-0391 E-field probe manufactured by NARDA, using 6 min averaging, for a typical experiment sequence consisting of tropospheric and mesospheric sounding experiments with up to 5 kHz pulse repetition frequency and maximum 5% duty cycle. The comparison of the measurements with the pointwise interpolated simulation is shown in Figure 5.2(b). For all measured intensities (blue) and values above 1 V/m (black) the least-squares fit is shown, which appears to be rather equivalent. This actually indicates that the detected lower intensities are likely originating from the radar and are not caused by the background noise. Additional measurements at the greater distances did show values of less than 0.5 V/m, which is at the background noise level and are thus not compared. The slope of approximately 0.14 is primarily caused by the duty cycle of the radar and the pulse form and width.

Additionally, during a maintenance stay in February 2013 the near electric field was measured for a special selection of transmit antennas to emulate a potential configuration of the planned successor of the IAP OSWIN radar in Kühlungsborn. For this purpose only 19 Hexagons (133 antennas) of MAARSY's antenna array were transmitting with approximately 1 kW peak.

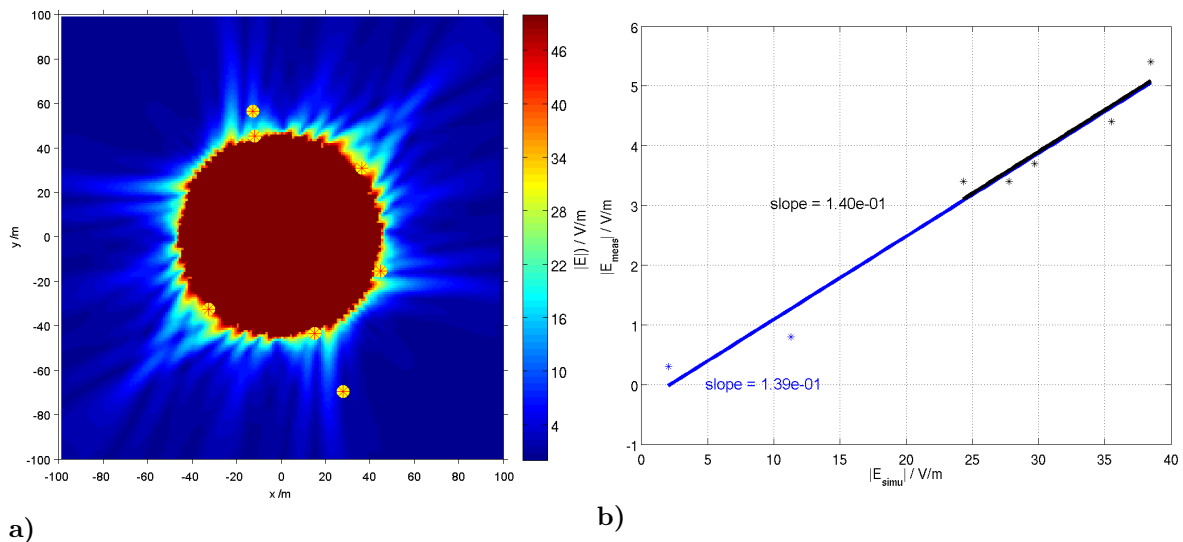


Figure 5.2 a) Simulated two-dimensional intensity of the electric near field in the proximity of MAARSY. The red asterisks above yellow circles mark the individual measurement positions used for the comparison to the model. b) Comparison of the simulated intensities to the measured field strengths including least-squares fit for all values (blue) and measured intensities above 1 V/m (black).

5.1 Measurements in the near electric field

The near electric field strength was measured with a field probe on specific positions within and outside the MAARSY antenna array. The exact positions for the measurements were chosen in the middle of adjacent antennas in the approximate height of the dipoles. At the time of these measurements the ground of the antenna array was covered by approximately 30 cm of snow, while the antenna elements were mainly free of snow.

Figure 5.3(a) shows the simulated near electric field strength emitted by MAARSY, when the antenna array was mixed polarized. Here, the existent polarization mixture can be seen in the simulated intensities as both planes of the crossed antennas are fed. Furthermore, there can be seen intensity enhancements at the antennas, which are not actively used as well as some angularly enhancements outside of the entire antenna array. Thus, the passive antennas couple with the antennas actively fed and re-emit the energy, which is not terminated by the passive transceiver modules.

In Figure 5.3(b) the simulated and measured intensities of the near electric field are depicted accompanied by an analytical estimate of the radial decrease of intensity. The two curves are separated by about 17 dB, which corresponds to the factor of 0.14 already seen in Figure 5.2(b). In the measurements a peak within the circular part of the antenna array was detected, which is not seen in the simulation. This could potentially indicate the reason for the argued deviations from the simulated far field radiation pattern for the same period of the polarization upgrade. In the respective passive experiments e.g. a slightly enlarged beam width was estimated (see Section 4.3.1). The circumference of the active antennas and partially the complete array can be seen. Interestingly, the decay in the measurements commences a few meters away from the center, which might indicate a stronger coupling of the antennas than simulated.

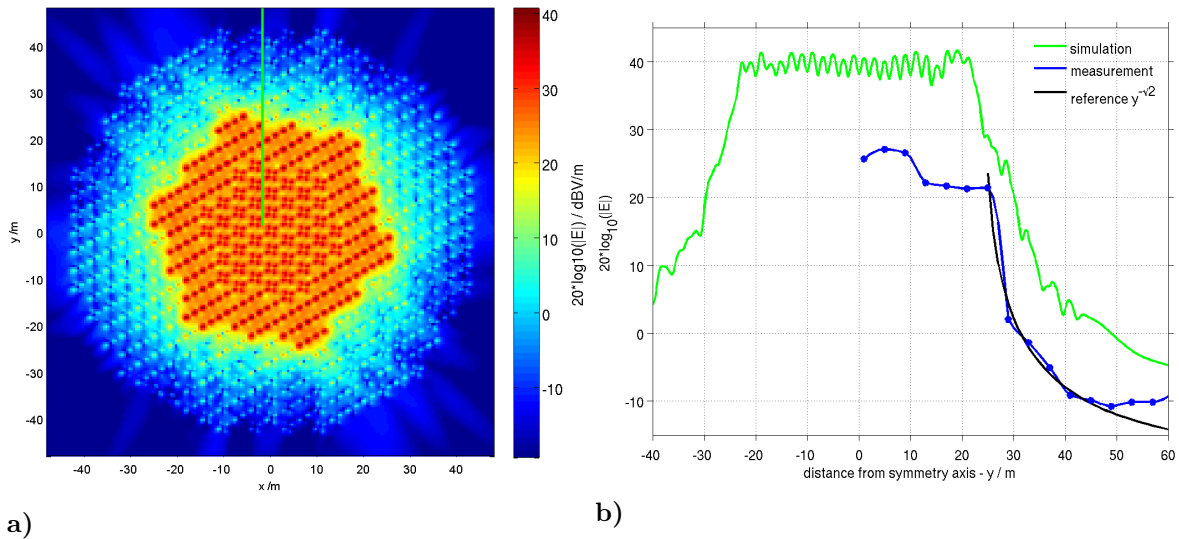


Figure 5.3 a) Simulated, scaled near electric field strength of MAARSY for $z=1.8$ m and 1 kW peak power per transceiver module. The green line marks the path of the measurements. b) Comparison of simulated and measured near electric field strength accompanied by an analytical radial decrease of the intensity.

5.2 Moon experiment

One of the natural targets with significant size and availability is the Earth's moon. The major drawback of this target is its low declination, which results in low elevation angles at polar latitudes. During February 2012 the moon was still reaching an elevation of 42 degrees, which is the maximum for the next years at the polar position of MAARSY due to the precession of the moon. The feasibility of this experiment can be proven by calculating the resulting path loss and the signal-to-noise ratio considering the radar parameters (see Table 5.1) with the radar equation (see Equation 5.1, which was already shown on page 9). The effective output power P_t is the product of the peak output power, coaxial losses and the duty cycle (5%).

$$P_r = \frac{P_t G_t G_r \lambda^2 \sigma}{(4\pi)^3 r^4}. \quad (5.1)$$

The radar cross-section is calculated by

$$\sigma = \pi r_m^2 g\rho, \quad (5.2)$$

where $g\rho$ are given by e.g. (*Senior et al.*, 1962; *Evans and Pettengill*, 1963a,b; *Giraud*, 1965) to 0.074 ± 0.01 . This leads finally to

$$\begin{aligned} SNR(dB) = & 103.4 - 40 \cdot \log_{10}(d) - 20 \cdot \log_{10}(f) + 10 \cdot \log_{10}(\sigma) \\ & + 10 \cdot \log_{10}(P_t) + g_c - 10 \cdot \log_{10}(B \cdot 10^{(NF/10)}), \end{aligned} \quad (5.3)$$

where the first term is derived from $10\log_{10}((4\pi)^3/c^2)$ and the conversion factors using MHz and km instead of Hz and m respectively. The latter term in this equation describes the noise generated by the receiver for the given noise figure NF and bandwidth B .

Doing so, 9.75 dB signal-to-noise ratio is calculated, which should easily allow the detection of the moon.

During this experiment the full antenna array was used to transmit a $50\mu s$ long pulse equivalent to approximately 7.2 km range, while for reception the software combined MAARSY343 was used. Similar to the beforehand described cosmic noise experiments we performed a scan in zenithal directions while pointing southwards to see the passage of the moon. At these high off-zenith beam pointing angles (up to 50°) grating lobes are inherently generated, which in this experiment were pointing to about 70° and 335° azimuth. These grating lobes should not inflict with other targets, but they pick up additional noise for the receiver. Potential targets like satellites may be rejected due to their apparent Doppler velocity. The

frequency, f	53.5 MHz
effective output power, P_t	30 kW
combined antenna gain, g_c	62 dBi
noise figure, NF	4 dB
bandwidth, B	0.5 MHz
distance Earth-moon, d	384350 km
moon radius, r_m	1739 km
radar cross-section, σ	$7 \cdot 10^{11} m^2$

Table 5.1 Radar and geometry parameters of the moon experiment.

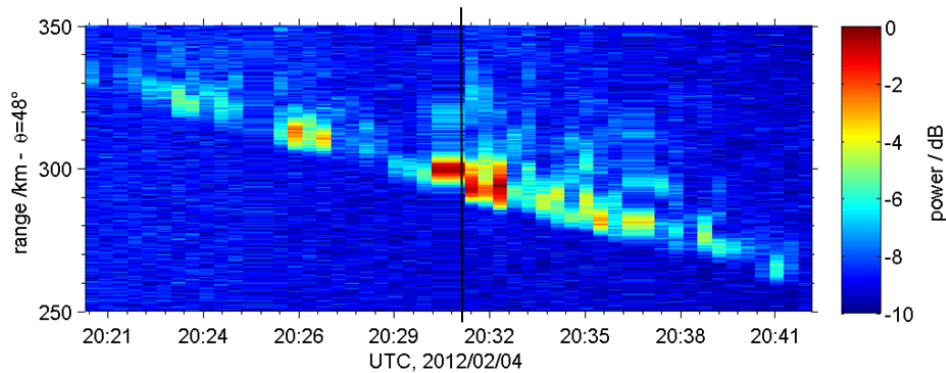


Figure 5.4 Received backscatter from the moon during an experiment on 2012/02/04. The approach of the moon, its calculated time of passage (black vertical line) and high fluctuation of incident power can be seen. The depicted range is aliased due to the high pulse repetition frequency to provide sufficient duty cycle and thus integrated radiated power for this experiment. Modified after *Renkwitz et al.* (2012).

backscatter signal of the moon was found at the predicted time and zenith angle as shown in Figure 5.4. The maximum detected power above noise is in the order of 10 dB, which is in very good agreement with the calculation above. Due to the pulse repetition frequency used in this experiment the range is aliased, but the source of the received signal can be identified by analyzing the slope. The estimation of the approach speed is approximately 205 km/h, while 202 km/h were simulated for this specific observation time.

The detected moon echo is characterized by high variations in power which may be related to Faraday rotation and scintillation and/or absorption effects (see e.g. *Chau et al.*, 2013a) as the radar signal travels along a considerable long path through the ionosphere, pointing 48° off-zenith. At the time of this experiment the geomagnetic indices showed disturbances and the surrounding magnetometer indicated variations of ± 200 nT of the magnetic field components (see *Tromsø Geophysical Observatory*, 2014). During this experiment MAARSY was exclusively linearly polarized for both transmission and reception, which results in power drops for deviating polarizations angles (see Figure 3.7 on page 21). Additionally, scintillation events modulating both amplitude and phase of the signal on both ways through the ionosphere may lead to imperfect combination of the Anemone antenna groups while forming both MAARSY433 and MAARSY343. Thus, a reliable estimation of the antenna array gain from the Equation 5.3 is not feasible and is thus not pursued. The signatures received with both arrays appear to be equal, which indicates disturbed ionospheric conditions rather than MAARSY internal fluctuations.

Considering the beforehand limitations we could also estimate the beam pointing error for this experiment to be in the order of two degrees in azimuth ($d\phi = +2^\circ$) and less than 1 degree for the zenith angle ($d\theta = -0.7^\circ$). These findings are in approximate agreement with earlier experiments observing the radio source Taurus A, which is connected to the Crab nebula and was successfully detected at about the same zenith angle (*Renkwitz et al.*, 2012). The first signal was detected at approximately 20:18 UTC, when the moon was at $\phi = 176.0^\circ$ and $\theta = 49.0^\circ$ which coincides with the onset of the main beam. As no signal was received earlier, no specific estimation of the suppression of the first side lobe can be given, besides on the basis of maximum received SNR from the moon during this experiment, accounting

for better than 5 dB for the one-way pattern. The same holds for the time after the passage of the moon through the radar beam. The beam width can only roughly be estimated due to the severe power fluctuation limiting the estimate to less than 6° .

5.3 Satellite observations

Contrary to the previously described experiment, where grating lobes were generated while pointing at large off-vertical beam directions to detect the moons backscatter, in this section active experiments observing the passage of satellites within MAARSY's regular beam pointing cone are presented. The aim of these experiments was to verify MAARSY's beam pointing accuracy and to gain information about the side lobe attenuation.

For this purpose the satellites GRACE and ENVISAT were chosen, as these have high inclination orbits and represent significantly large targets due to their dimensions of 3.1 x 1.9 m and 26 x 10 m respectively. Figure 5.5 shows the range-time-intensity plots for one passage of the two GRACE satellites almost overhead of MAARSY. In total, five beam directions with 5° to 25° zenith angle were used in the experiment, sampling the range of 445 km to 500 km on pulse to pulse basis. Due to a pulse length of approximately 7 km strong backscatter from the two GRACE satellites was received for all five beam directions. The time of passage through the individual radar beams and the detected range are in good agreement with simulations of the orbital trajectory of both satellites.

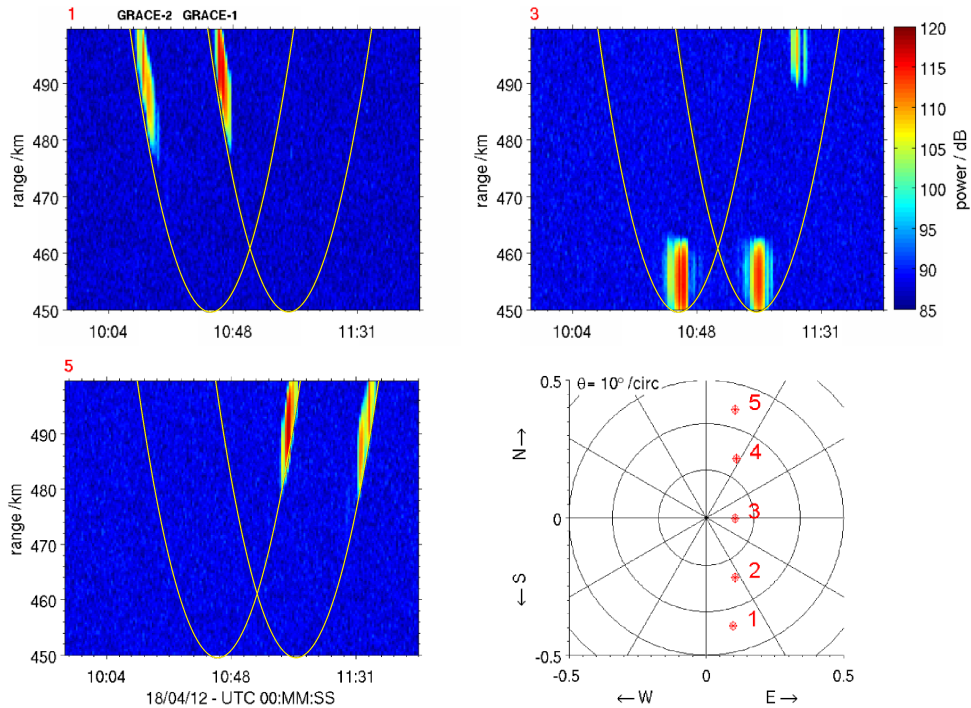


Figure 5.5 Observations of the GRACE satellites for three selected beam directions. The beam positions according to the orbital trajectory of the satellites are depicted in the lower right panel. The yellow lines mark the orbital trajectory of the satellites. Modified after *Renkwitz et al. (2012)*.

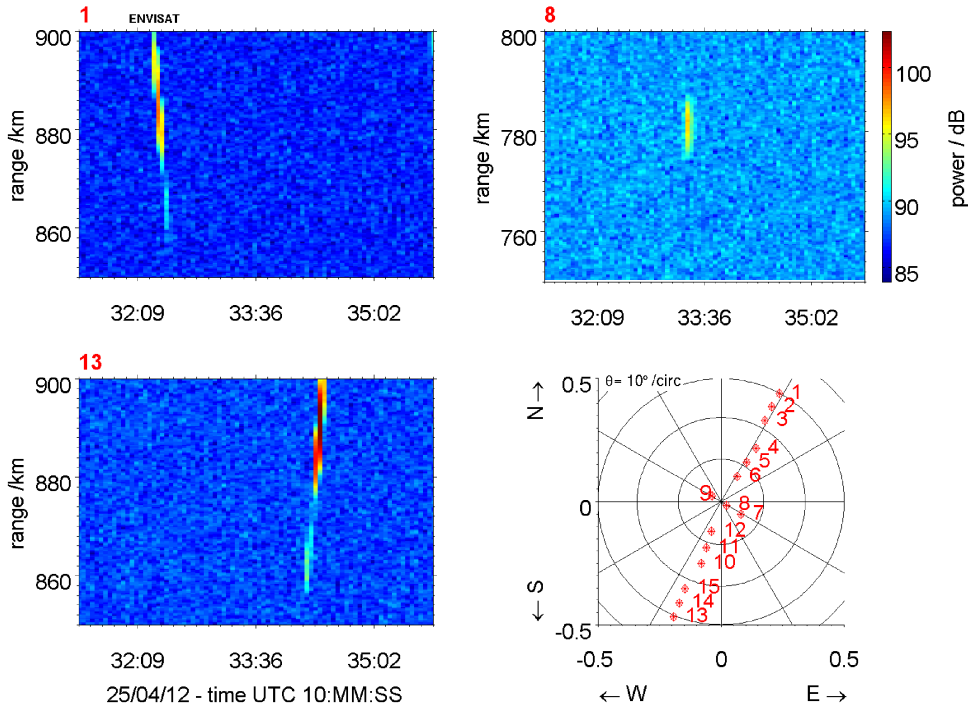


Figure 5.6 Observations of the ENVISAT satellite for three selected beam directions. The beam positions according to the trajectory of the satellites are depicted in the lower right panel. Taken from *Renkowitz et al.* (2012).

The side lobe attenuation can be estimated from beam no. 3 to be around 20 dB, which is about 10 dB less than anticipated for the two-way pattern. This implies either variable cross-sections of the satellite for the individual relative positions around this beam direction or an imperfect radiation pattern of MAARSY. However, in other beam directions no explicit side lobes can be distinguished. Significant variations in the detected power level are seen e.g. for GRACE-2 in Beam 1 ($\approx 11:45$ UTC) and for GRACE-1 in Beam 5 ($\approx 11:45$ UTC), which indicate varying cross-sections of the satellite.

Subsequently, MAARSY was used to detect ENVISAT, which is one of the largest known targets passing MAARSY's coverage. In this experiment 15 radar beam positions were defined, of which 13 were pointing directly to the trajectory of ENVISAT and two beams were displaced by four degrees. At the latter two pointing directions, the first side lobe of MAARSY should point to the trajectory of the satellite in case of significant beam pointing aberration. Doing so, we might get information of the side lobe attenuation and the mis-pointing of the radar beam. In Figure 5.6 three examples of the passage of ENVISAT through MAARSY's radar beam are depicted.

Alike the previously described experiment observing the GRACE satellites, we received backscatter from ENVISAT in all 13 beam positions that were pointing at the trajectory. However, we were not able to detect any signal in the radar beams marked with no. 7 and 9, both separated by 4° adjacent to beam no. 8. The detected intensities, however, show high variability between the individual beam directions placed on the orbital trajectory of this satellite. Especially beam no. 8 shows significantly lower power than e.g. beam no. 1 and 13. This is presumably caused by the shape and exact orientation of the satellite's surface and especially its large solar panels in relation to MAARSY, implying that the radar waves

were reflected rather than scattered off the target.

The side lobe attenuation may be estimated from the signatures in e.g. beam 1 and 13. Doing so, about 20 dB maximum side lobe attenuation were found, which is in agreement with the experiment observing the GRACE satellites. This implies an imperfect amplitude and phase distribution for MAARSY during the time of the satellite experiments, which however apparently did not significantly modify the beam pointing. Unfortunately it was not possible to verify the beam pointing accuracy in detail, since ENVISAT has been out of control since the 8th of April 2012 (see *European Space Agency*, 2012). However it appeared to be still on the predicted orbit, which is also proven by our observation performed four days after the loss of communication with the satellite. The variation of backscatter seen in our data may be caused by the unpredictable orientation of the spacecraft and thus varying radar cross-section. Furthermore, plenty of other backscatter signals were detected, which are likely related to other spacecrafts or debris. Some of these signals also may have been received via side lobes from explicitly large targets, which complicates the assignment to specific spacecrafts.

With these two satellite experiments we were able to verify our beam pointing on 18 individual positions for up to 30° zenith angle. This is especially valuable as due to the polar position of MAARSY passive observations of galactic radio emissions are generally restricted to southern directions. An estimate for the side lobe attenuation could be given (>10 dB), indicating imperfect pattern during the time of the satellite experiments. The beam width could not be derived accurately, due to the intense power fluctuations likely caused by varying cross-sections of the targets. However, the beam width can be estimated to be smaller than 6°.

Finally, it has to be noted that both the moon and the satellite experiments were performed under the assumption of perfectly phased Anemone signals, however, for this stage of MAARSY phase calibrations were not yet applied. Thus, the software combined MAARSY343 radiation pattern was likely inferior to the ideally phased simulated pattern (see e.g. Figure 4.11 and corresponding comments).

5.4 Approximation of the radiation pattern with the aid of meteor head echo observations

The idea of this experiment is the experimental evaluation of the radiation pattern by the use of the signal-to-noise ratios of meteor head echoes (MHE). Meteors entering the Earth's atmosphere typically ablate in the altitude range of 70 to 120 km. High-power large-aperture radars like MAARSY are able to scatter off the plasma formed in front of the meteor, not just from the specular meteor trail (see e.g. *Pellinen-Wannberg and Wannberg*, 1994; *Janches et al.*, 2000). The meteors travel, depending on their source and trajectory, with about 11-76 km/s partially covering large portions in the sky. By interferometric means the position of the observed meteor head echo for every single sample can be calculated (see e.g. *Sato et al.*, 2000; *Chau and Woodman*, 2004; *Pellinen-Wannberg*, 2005; *Dyrud and Janches*, 2008; *Chau et al.*, 2009; *Kero et al.*, 2012) and for measurements with MAARSY (see e.g. *Stober et al.*, 2013b; *Schult et al.*, 2013). Each detected meteor head echo event can be described by its signal-to-noise ratio (SNR) and its associated point on the trajectory. The use of meteor head echoes to perform phase calibration of the antenna and receiving system of atmospheric radars was described e.g. by *Chau et al.* (2008). The pointwise comparison of the MHEs intensity with the radiation pattern of MAARSY has been evaluated by *Chau et al.* (2013b).

5.4 Approximation of the radiation pattern with the aid of meteor head echo observations

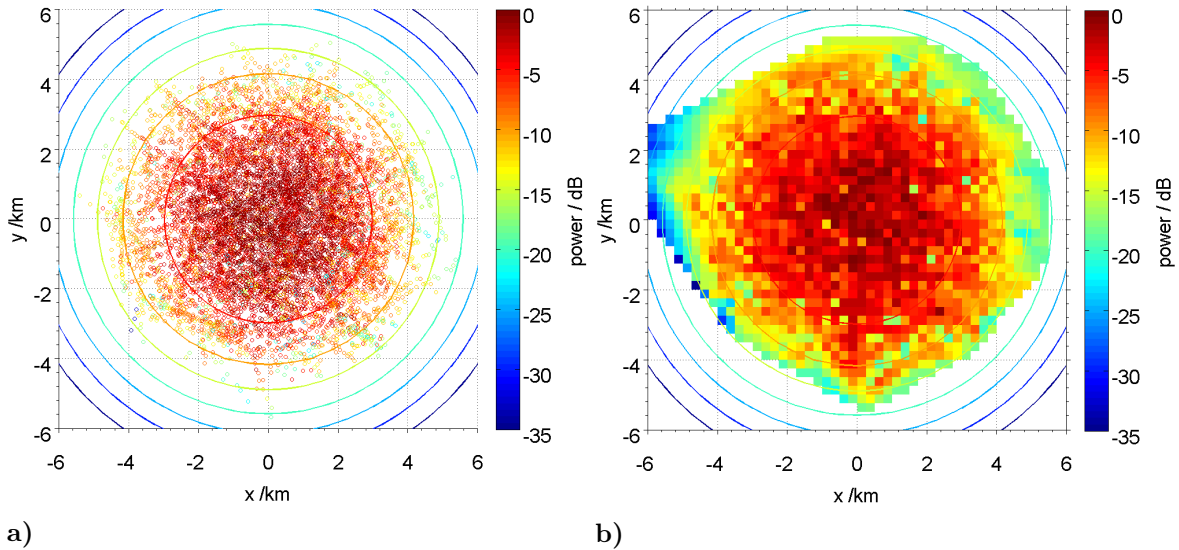


Figure 5.7 a) Overlay of 700 meteor head echo trajectories observed during the Geminids meteor shower 2012, b) smoothed and interpolated from a). The colored circles represent the pattern approximation which was used to normalize the individual trajectories.

The intention of this experiment is the use of as many MHE observations as possible to derive a SNR distribution in order to image the radiation pattern of the main lobe.

The intensity of a MHE's signal-to-noise ratio highly depends on its specific entry velocity and angle of arrival to the Earth's atmosphere and the meteor's chemical composition. Thus, different MHE events cannot be compared directly as their properties may be severely different. For further analysis of the MHE events, every trajectory¹ was normalized by its maximum to a simple radiation pattern of gaussian shape and appropriate width, which systematically neglects the appearance of side lobes. However, the intention of this experiment is to demonstrate a potential way to estimate the radiation pattern within the main lobe. Note, that many of the meteors travel through large portions of the radiation pattern revealing signatures of nulls and sidelobes.

The overlay of approximately 700 trajectories and their normalized signal to noise ratios are depicted in Figure 5.7(a) and the corresponding smoothed appearance in Figure 5.7(b). There is an evident general agreement to the radiation pattern, albeit, due to the prior restrictions there is still a quite high variability within adjacent pointing directions. Therefore, the pointing accuracy can only be roughly estimated to be better than 2° for the zenith angle. With the aforesaid restrictions, the beam width was estimated to be around 5° or smaller. Admittedly, the suppression of the first side lobes cannot be estimated due to the methodology applied in this experiment.

The main systematic problem of this method is the preconditioning with a radiation pattern assumption to which the trajectories are normalized. A better way without imposing a radiation pattern is a purely statistical approach, where only the occurrence frequency of trajectories (or their center) per direction is evaluated. This method certainly needs more observation time than the method presented here, whereas, it is free of any radiation pattern assumptions.

¹The analysis of the individual meteor head echo observations was performed by Carsten Schult (IAP).

5.5 Observations during the WADIS rocket campaign

Around June 27th 2013 the WADIS sounding rocket campaign (WAVE propagation and DISSipation in the middle atmosphere) was conducted at the Andøya Rocket Range close to MAARSY, where several meteorological and an instrumented rocket were launched. At the same time various ground based radar, lidar and balloon facilities were contributing. MAARSY was the leading radar facility to detect and observe PMSE with multiple beam directions to facilitate information on potentially favorable launch conditions and detailed information about the PMSE structure during the flight. For this purpose MAARSY was operated with a specific experiment configuration observing 16 different beam directions along the predicted rocket trajectory.

Besides the initial objectives of the scan configuration, the analysis of the radar data set turned out to contain strong backscatter from the rocket, the payload and likely the rockets nose cone, due to the dimensions of the complete rocket (see Figure 5.8). As the beam directions were predefined by the predicted trajectory the payload was not only crossing but also flying next to the individual beam directions of MAARSY, providing information of the radiation patterns main and side lobes.

The trajectory of the sounding rocket (GPS data) is depicted in Figure 5.9(a) with the predefined beam directions of MAARSY, marked with asterisks. The GPS data have been verified by the interferometric analysis of the radar data estimating the position of the individual trajectory points, whenever appropriate radar data was available.¹ Only minor deviations to the GPS trajectory were found, which are likely caused by the imperfect decoding of the radar signal and the given error in the radar phases for the individual antenna and receiver groups.

¹The interferometric analysis of the radar data to derive the WADIS trajectory was performed by Carsten Schult (IAP).

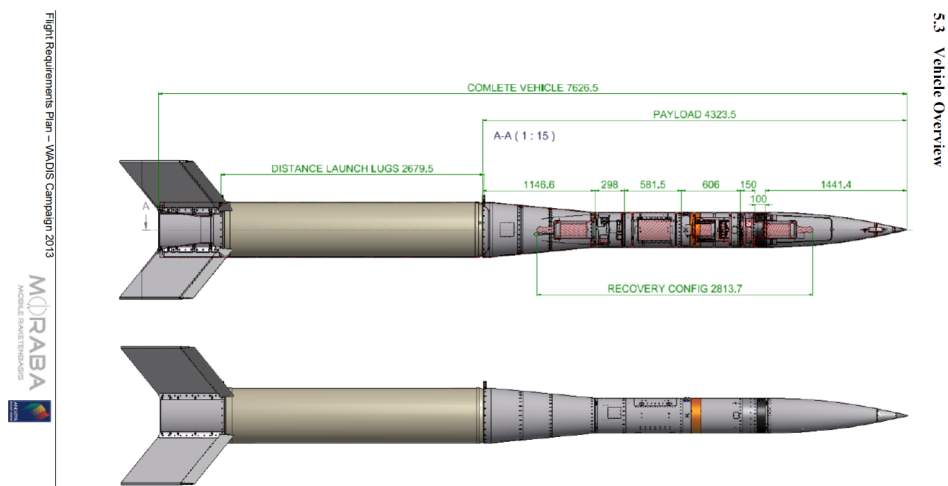


Figure 5.8 Sketch of the WADIS rocket motor and payload. Courtesy of Mobile Rocket Base, German Aerospace Center

5.5 Observations during the WADIS rocket campaign

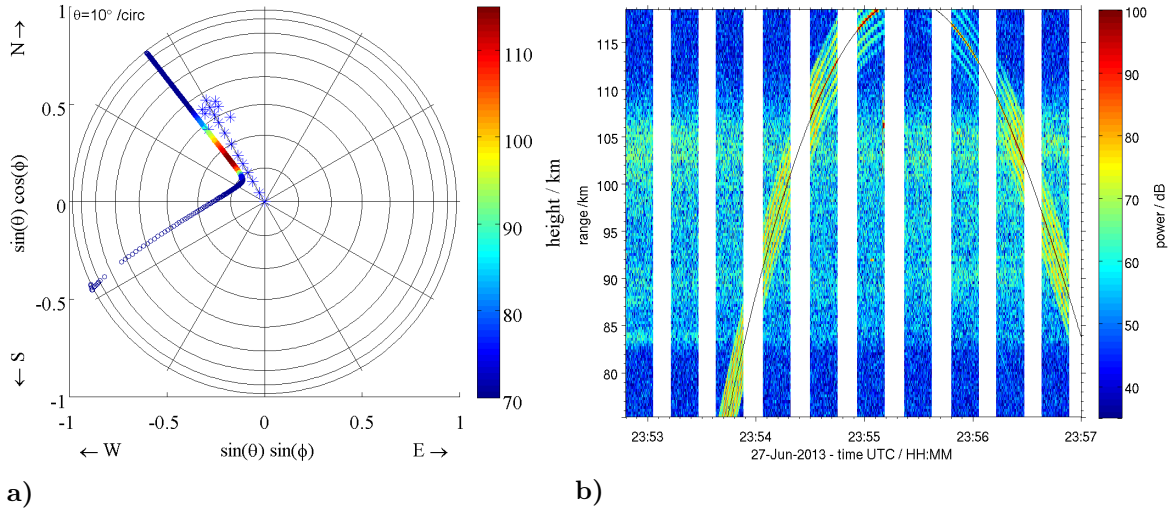


Figure 5.9 a) Trajectory of the WADIS rocket payload in reference to MAARSY, depicted in spherical coordinates, overlaid by the beam positions used in the WADIS scan experiment. b) Integrated power of all beams in the scan (median removed) depicted over range and time. The thin black line marks the range calculated from the GPS coordinates.

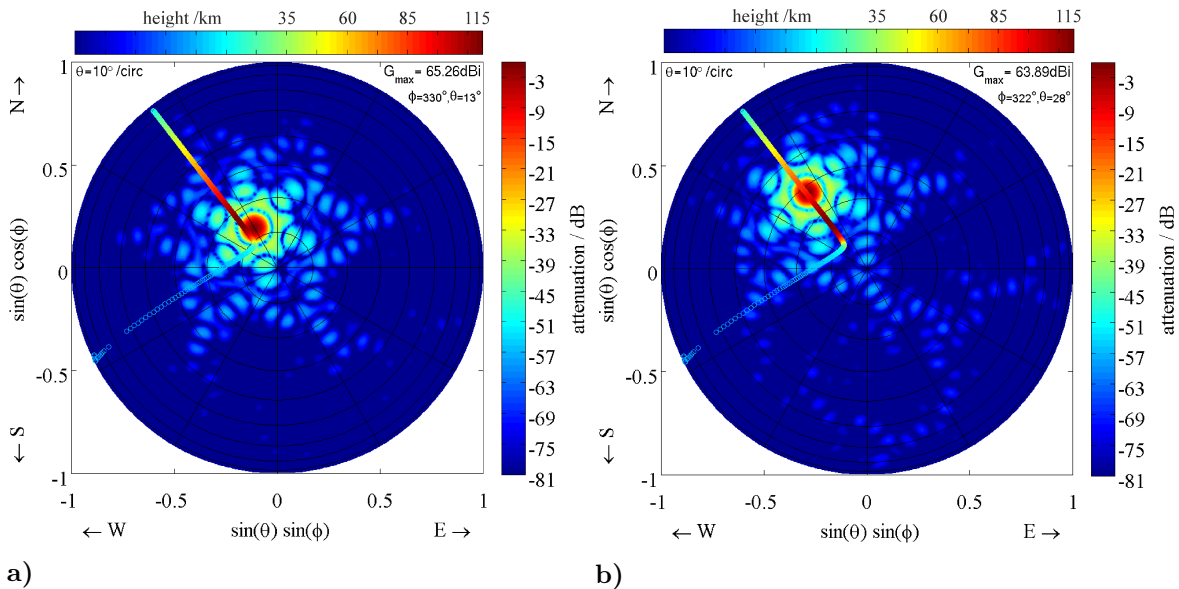


Figure 5.10 a) Two-way radiation pattern of MAARSY overlaid with the trajectory of the WADIS rocket payload for the beam direction $\phi = 330^\circ$ and $\theta = 13^\circ$. b) Same as a) for the beam direction $\phi = 322^\circ$ and $\theta = 28^\circ$. The colorbar above the individual figures denote the height of the WADIS payload for the shown trajectory.

Figure 5.9(b) shows the integrated received power of all (median removed) beam directions representing the trajectory of the payload for the entire flight within MAARSY's observation window. The thin black line marks the range to the payload calculated from the GPS coordinates, which nicely agrees with the mid-range of maximum incident power. This implies a reasonable accuracy of the trajectory and the individual GPS measurements as MAARSY

is range-calibrated with a delay line. Furthermore, within MAARSY's scan at least one direction directly overlaps with the trajectory while in some the payload travels at the rim of the main beam or through side lobes.

The trajectory of the flight is depicted on top of MAARSY's radiation pattern (combined transmission and reception path) in the Figures 5.10(a) and 5.10(b), which underline the highly interesting beam and trajectory combination. The crossing of the WADIS trajectory through the beam position $\phi = 322^\circ$, $\theta = 28^\circ$ is depicted in Figure 5.11 as a 3D surface plot in spherical coordinates. The arrows mark the up- and downleg of the payloads GPS trajectory.

The beams at zenith angles greater than 30° are not reliable for comparisons with the simulated radiation pattern anymore as the pitch angle of the payload changes rapidly with onset of flat spin motion at heights below 75 km during the downleg.

Figures 5.12(a) and 5.12(b) show the height-time-intensity plots in the upper panel for the beam directions $\phi = 330^\circ$, $\theta = 13^\circ$ and $\phi = 322^\circ$, $\theta = 28^\circ$ respectively. The bottom panel represents the interpolation of the simulated radiation pattern to the individual points of the payload's trajectory (marked in blue). For the red curve the free space path loss approximation based on the targets range and the angle of attack and therefore the effective area of the payload are considered. The black dots represent the maximum detected power for the GPS trajectory, which partially is not originating from the payload, but from PMSE or the background noise. The theoretical path loss, assuming free space propagation (Equation 5.4, simplified after Friis, 1946), can be calculated as follows.

$$a_{pl}[dB] = 20 \log_{10}(4 \cdot \pi \cdot r / \lambda) \quad (5.4)$$

In the lower panel of Figure 5.12(a) quite some deviation of the detected power to the simulated radiation pattern can be seen during the upleg. The reason for this is likely the imperfectly decoded radar data where the speed of the target and thus its Doppler shift has been disregarded. This results in a deterioration of the codes side lobe attenuation, which actually can be seen just before 23:54 UTC where the side lobes of the code are more accentuated than the main lobe.

Nevertheless, the shape and intensity of the two presented beam directions appear to be consistent with the simulated radiation pattern. Due to the strength of the backscatter signal the target can also be seen in the side lobes down to -40 dB relative to the beam's maximum intensity. Small deviations in the side lobes can be seen between the detected power and the simulation, which implies either a minor imperfection of the GPS coordinates, but more likely a deviation in MAARSY's beam pointing and shape, or the simulation itself. The simulations have been computed with optimal amplitude and phase distribution including all 433 array elements on transmission and 343 elements on reception. Previously, in Section 4.3 was found that the beam width of MAARSY433 was likely broadened during that time. This was likely accompanied by deteriorated side lobes, which is caused by the existing

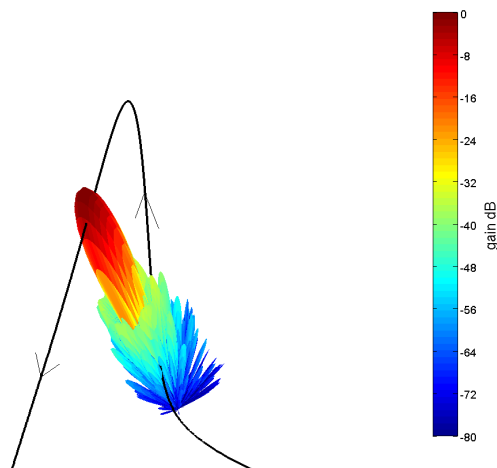


Figure 5.11 Trajectory of WADIS crossing through the simulated radiation pattern of MAARSY pointing to $\phi=322^\circ$, $\theta=28^\circ$.

5.5 Observations during the WADIS rocket campaign

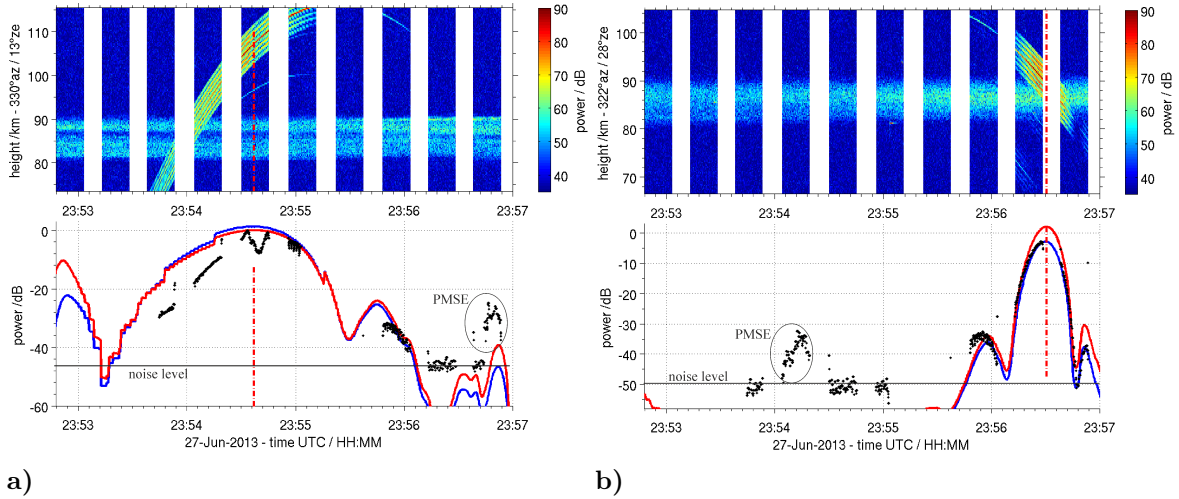


Figure 5.12 a) Top: Detected back scatter from PMSE, the WADIS payload and traces of the rocket nose cone and motor in the beam $\phi = 330^\circ$, $\theta = 13^\circ$. Bottom: Black dots represent the maximum detected power on the GPS trajectory. Blue and red curves depict the interpolation of the simulated radiation pattern as shown in Figure 5.10(a) considering the path loss and payloads geometry and the angle of attack. b) Same as a) for the beam direction $\phi = 322^\circ$, $\theta = 28^\circ$.

polarization mixture. Furthermore, some transmit modules of the array have been non-operational for the specific time and beam pointing, which lead to distortions in the pattern mainly affecting the side lobes intensity. A corresponding simulation and comparison to the ideal pattern is presented in the Appendix in Section A.3, Figures A.1(b) and A.2(a). These simulations show an increase of beam width in one cross-section by 0.2° , while no significant deterioration of the first side lobes is seen. The gain of the antenna array drops according to the amount of failed antennas.

The beam pointing appears to be pretty accurate as the main lobe can be seen at approximately the same instant of time for the individual beam directions and agrees well with the simulated shape. A precise analysis of the beam pointing accuracy is difficult due to the existent radar data gaps, but can be estimated to be in the order of half a degree in both planes. The beam width during the experiment agrees well with the simulations (see bottom panel in Figure 5.12(b)), which is also supported by the position and shape of the side lobes and nulls. A very faint broadening can be guessed, which would support the upper arguments regarding few non-operational transmit elements at the rim of the antenna array. The latter would lead to a reduction of the effective diameter of the array and thus a broadening of the main beam. However, the minor broadening seen in this example is rather negligible. The analysis of this data set obtained during the WADIS campaign proved to be very useful for calibration purpose of MAARSY. Therefore, upcoming rocket campaigns at the Andøya Rocket Range should be analyzed carefully and if possible coordinated with dedicated beam position pattern allowing both the scientific goals of the rocket campaign itself and radar calibration purpose.

5.6 Summary

In this chapter, active experiments were used to verify the radiation pattern of MAARSY. For this purpose the near electric field intensity inside and outside of the antenna array was pointwise measured and a generally good agreement with simulations was found. However, besides this, information for the far field are hard to derive. Thus, airborne measurements were performed, which should allow the direct measurement of MAARSY's transmission pattern. Unfortunately, these measurements did not increase the knowledge of the radiation pattern characteristics as we were not able to measure in the far field. Furthermore, for the specific beam positions the direct signal from the radar was superimposed by clutter, namely scattering off the nearby hills and the sea, spoiling the detected intensities.

In the subsequent experiments the radiation pattern for transmission and reception were used, but with the earlier findings both can still be estimated separately. With the rather early observations of satellite passages and the Earth's moon confidence of satisfying beam pointing accuracy (better than 2°) could be gained. The Earth's moon was successfully detected at the predicted time and beam pointing direction passing through the radar's main beam. The target has been identified by the speed of approach, which was in good agreement with simulations. Even though, the detected signal-to-noise ratio agreed well with the calculations, but it appeared not to be feasible to reliably estimate the antenna array gain due to the detected variability of power.

For the satellite experiments the large targets GRACE and ENVISAT were chosen and successfully observed at the simulated times and in total 18 beam directions. During the experiment observing ENVISAT no backscatter was received for predefined beam directions, which were pointing 4° adjacent to the orbital trajectory. Significant mispointing of the antenna array was thus suspended. Furthermore, the first estimates for the suppression of the first side lobes and the beam width could be derived (better than 10 dB). However, at this time, no absolute phase calibration was yet applied to MAARSY and thus the radiation pattern was presumably distorted.

These findings were substantiated by the observations of meteor head echoes during the Geminids meteor shower 2012 and finally by observing the payload of the WADIS sounding rocket campaign. The superposition of 700 obtained meteor trajectories, which were individually normalized to a simple radiation pattern, facilitated the first 2D view on MAARSY's radiation pattern. However, this specific method does not allow the estimation of the side lobe suppression due to the assumed side lobe free radiation pattern used for the normalization.

The observation of the WADIS' payload allowed the confirmation of the main and first side lobes of MAARSY's radiation pattern in detail for various beam positions. Two of them were examined in detail in this thesis. Thus, the most reliable and accurate agreement with simulations for the beam pointing accuracy ($< 0.5^\circ$), beam width ($+0.1^\circ$) and side lobe attenuation ($> 15\text{ dB}$) was found for the observation of the WADIS' payload.

Chapter 6 Conclusions and outlook

Chapter 6 Conclusions and outlook

The Middle Atmosphere Alomar Radar System (MAARSY) was designed and built for studies of phenomena in the troposphere to the mesosphere region performed with high spatial and temporal resolution. Its large aperture, high output power, flexible beam forming and pointing as well as flexibility in the selection of receiver subarray groups allow highly advanced experiments and new insights into the observed atmospheric phenomena. This includes the investigation on the 3-dimensional structure of the individual radar echoes and their originating processes as well as the dynamics of winds, turbulence and waves in the atmosphere.

The analysis of the radar data and the estimation and comparison of specific parameters of the observed echoes however require detailed knowledge of radar parameters like output power, pulse width and the radiation pattern. The first two points are rather easily measured at the radar and need to be monitored continuously for appropriate use as background parameters for the subsequent data analysis. Simulations of the antenna array radiation pattern with highly advanced models are very helpful for the design process, however the actual radiation pattern considering e.g. imperfections during the building process, active coupling effects of the individual antennas, interaction with the surrounding terrain and aging processes can hardly to be foreseen and simulated.

The radiation pattern of the MAARSY antenna array, however, cannot be measured directly in a laboratory setup due to its size of 90 m diameter. Direct measurements of the radiation pattern of an antenna array of this size and the operating frequency of 53.5 MHz need to be performed in the electric far field, which starts at approximately 3 km altitude. As this method is generally not easily applicable, other methods need to be performed to estimate or derive parameters like beam pointing accuracy, beam shape and width of the main lobe, suppression of the undesired side lobes and the absolute phase distribution for various subarray groups.

The main results of this thesis are

- 1) The phase distribution and stability of the individual receiver subarray groups was derived by observing cosmic radio sources, where reliably stable phases for the individual subarray groups were found (typically $\sigma < 10^\circ$).
- 2) The shape of MAARSY's main lobe agrees with extensive simulations and its pointing accuracy was estimated to be generally better than 0.5° for both, azimuth and zenith angle.
- 3) The beam width of the main lobe was estimated for several beam positions, where the most reliable experiments suggest a broadening of approximately 0.1° relative to the simulations.
- 4) The intensity and influence of the side lobes was found to be in the order of the simulations, which are depending on the specific beam pointing directions approximately 15 dB below the main beam.
- 5) The overall sensitivity of the radar was estimated to be equivalent to a system temperature of 775 – 800 K for the individual polarization periods. Compliant to simulations, the antenna gain of MAARSY343 was estimated to 32.4 dBi for the period of linear polarization. The dynamic range of MAARSY's receivers was measured and subsequently improved from 40 dB to 70 dB at best.

For all of the above points typically various passive and active experiments have been conducted and analyzed to derive or estimate the individual characteristics of MAARSY and its antenna array.

The phase distribution of the individual receiver subarray groups (key result 1) has been derived mainly observing the distinct cosmic radio source Cassiopeia A (Section 4.2). Thus, for all observed subarray groups with a minimum size of a Hexagon (7 antennas) reasonably stable phases have been derived. With these phases, it is now possible to combine the individual subarray groups to form larger groups (e.g. MAARSY343) in software and to use the individual subarrays for interferometric observations. It could be shown, that the radiation pattern is distorted if the appropriate phases are not used. Furthermore in the case of interferometry, the observed targets will be displaced.

For key result 2, at first the drift of cosmic radio sources through MAARSY's main beam was observed and analyzed (see Chapter 4, particularly Section 4.3). These experiments indicated a reasonable shape and good pointing accuracy ($< 1^\circ$) for zenith angles of up to 28.5° . These findings are corroborated by active radar experiments (see Chapter 5), observing the Earth's moon, satellites, meteors and a payload of a sounding rocket. With the observation of satellites 18 different beam directions with maximum 31° zenith angle were verified. Finally, we were able to estimate the pointing accuracy to be in the order of 0.5° for both azimuth and zenith angle, which is equivalent to 1/9th of the beam width. Thus, the potential horizontal displacement at the typical altitude of PMSE is maximum 1 km for a zenith angle of 30° .

The beam width of MAARSY's main lobe (key result 3) was evaluated by passive and active experiments. In the case of passive experiments observing cosmic radio sources, the initially estimated beam width appeared to be significantly larger than simulated. The reason for this is the collection of noise power not only by the main lobe, but with all lobes. The most prominent radio sources Cassiopeia A and Cygnus A, however, are located in the proximity of the Milky Way. While pointing the main beam to the distinct sources, the pointing directions of the first side lobes often match the Milky Way. This leads to increased detected intensities, virtually emanating from the distinct radio sources and broadening of the main beam. The observations have been compared to the Global Sky temperature Model, which led to equivalent results. The same model has been used to derive reference intensity maps, where only the side lobes of MAARSY's radiation pattern are present. This reference was used to "correct" the observations, leading to the appropriate estimation of the beam width. Finally the active experiments, especially the observation of the sounding rocket's payload (Section 5.5), allowed the estimation of the beam width for large off-zenith pointing angles. Here, a marginal broadening of 0.1° was found, which is equivalent to approximately 0.2 km enlarged horizontal width for 85 km height and 30° zenith angle.

The intensity of the side lobes (key result 4) could only indirectly be estimated in the passive experiments. However, the active experiments, especially the observations of satellites and the sounding rocket payload, allowed the reliable detection of the side lobes. For the latter, a one-way side lobe attenuation of 15 dB was found, which is approximately 2 dB below the ideal simulations. This deviation is presumably caused by non-operational transceiver modules at the time of the experiment, which modify the position and intensity of side lobes.

For key result 5, the sensitivity of MAARSY was mainly derived by measurements of the typical receiver noise figure and all existing losses in front of the receivers (Section B.4). The derived system temperature (775-800 K) is also supported by the observations of cosmic radio sources and the estimation of the antenna array gain. For the period of linear polarization of the antenna array the gain of MAARSY343 was estimated to approximately

32.4 dBi, which agrees very good with the simulations. However, for the subsequent periods of mixed linear/circular and circular polarization the estimated gain dropped significantly. This is caused by the decrease of detected power for circular compared to linear polarization, where the polarization of the incident waves emanating from distinct and diffuse radio sources does not match the polarization of MAARSY. The polarization loss was estimated to be approximately 1.5 dB.

Furthermore the dynamic range of MAARSY's receiving system was evaluated. Initially, about 40 dB were found, which was caused by the unfortunate distribution of receiver gain over the individual stages. With this configuration, observations during active experiments were frequently saturated, e.g. for strong PMSE events or observations of meteor head echoes. With the reduction of gain in the Signal Processor Unit the dynamic range was increased up to 70 dB.

During the observations of the distinct cosmic radio sources high fluctuations of ± 4 dB were frequently detected. These are predominantly caused by ionospheric scintillations (irregularities of the electron content in the F-region) and absorption events (increased electron density in the D-region). While ionospheric scintillations only affect the propagating waves from localized coherent sources, absorption events generally damp all incident waves. It has been demonstrated that the detected fluctuations of the detected intensities were not caused by MAARSY, as an independent receiving station simultaneously detected similar events, even though the station is separated by 200 km (Section 4.7.1). The derived composite maps for the individual polarization periods of MAARSY have been compared to single day observations, when intense absorption events were seen (Section 4.7.2). With this method MAARSY has been used as an imaging riometer, which allows the angularly resolved estimation of the D-region ionization. For this specific day, it was possible to analyze the temporal and horizontal extend of D-region patches of significantly increased ionization.

For a better overview and comparison, the findings of the individual experiments are summarized in Table 6.1.

Outlook.

The majority of the passive experiments were conducted during exclusive experiment runs. However, the combination of active and passive experiments would improve the temporal resolution for both significantly. Meanwhile, the phase calibration experiments and cosmic noise intensities for some beam pointing directions are successfully derived from active experiments, using quiet range gates, e.g. from the stratosphere. The latter is of special importance for the continuous quality control of this radar system. Here, the absolute phase distribution of the Hexagon subarrays should be derived, which were not used individually until now. This is particularly interesting as thus the phases of seven adjacent Hexagons could be compared to the phase of the corresponding Anemone they form.

Whenever applicable, MAARSY should be used tracking sounding rockets and their payloads in upcoming campaigns. Optimized experiments including the storage of undecoded raw data may allow significant improvements in the validation of the radiation pattern. This was only partially feasible for the WADIS campaign as it initially was not planned to be used for calibration purpose. At the same time these targets could also be used for absolute phase calibration purpose of the radar if the trajectory is known in detail.

The observed decrease of the incident power emanating from distinct and diffuse radio sources needs to be pursued in the future. This is ideally be done with a special antenna group

	passive experiments		active experiments			
	sky noise	phase calibration	moon	satellite	meteor head echo	rocket payload
MAARSY343						
beam pointing ϕ, θ	180°, 10 – 30°	180°, 10 – 30°	180°, $\approx 48^\circ$	var., 2 – 31°	0°, 0°	322°, 28°
beam pointing accuracy $d\phi$ $d\theta$	< 1°	< 1°	< 2°	< 1°	n/a	$\approx 0.5^\circ$
	< 0.5°	n/a	< 1°	< 1°	< 2°	$\approx 0.5^\circ$
beam width, relative to simulations	4.2 – 4.7°	< 5°	< 6°	< 6°	$\approx 5^\circ$	$\approx 4.6^\circ$
	+0.1°	< +0.5°	< +1°	< +1°	< +1°	< +0.1°
gain relative to simulation	lin. polar.: $\pm 0(\pm 0.5) \text{ dB}$		n/a	n/a	n/a	n/a
	circ. polar.: $-4.45(\pm 0.5) \text{ dB}$		n/a	n/a	n/a	n/a
side lobe attenuation	12 – 15 dB	n/a	> 5 dB	> 10 dB	n/a	15 dB
phase precision						
Anemones σ	n/a	6.6°	n/a	n/a	n/a	n/a
Hexagons σ	n/a	10.7°	n/a	n/a	n/a	n/a

Table 6.1 Overview of the derived parameters characterizing MAARSY’s antenna array radiation pattern. The results of the individual methods are presented, marking the individual focus and their capability for calibration purpose. The abbreviation n/a and the symbol σ denote ”not applicable” and the standard deviation, respectively.

facilitating the use of both orthogonal linear polarizations. This would allow the direct comparison with the intensities detected with the circular MAARSY array and could lighten the antenna array gain estimations for the circular MAARSY array. Additionally, such an antenna group would also be very useful for active atmospheric sounding experiments, as the scattering process may be studied broken down into the individual fractions of detected power into the two orthogonal linear polarization directions.

Concordantly, active scan experiments should be exploited to derive cosmic noise data for various directions allowing the expansion of the already existent cosmic noise map and the regular estimation of absorption intensity. Depending on the amount of beam positions, MAARSY could be used as an imaging narrow beam riometer, which together with the MF-Saura radar could provide reliable electron density profiles.

In terms of continuing quality control, additional experiments observing and tracking satellites should be performed as until now, only the north-south path was thoroughly investigated.

The presented methodology of using the intensities of meteor head echoes is strictly relying on the predetermined simple radiation pattern and only the variations of the trajectories intensities depict potential deviation from the pattern. A purely statistical approach, counting the frequency of detected meteor head echo trajectories per pointing direction appears to be very promising in a first attempt.

Finally, the frequent observations of intense ionospheric scintillation events open a research field of electron density irregularities within the F-region, likely allowing the estimation of the plasma drift.

Appendices

Appendix A The analysis of NEC simulated radiation pattern

A.1 Numerical Electromagnetic Code - Method of Moments

The Numerical Electromagnetic Code has already been used in the M.Sc. thesis *Renkowitz* (2008). Thus the following description is in principle identical as there are no significant changes to the code, which affect the simulations presented in this thesis. The integral equations for electric and magnetic field are solved numerically with the Method of Moments, by point matching of the fields, which is also represented by the Green's-function. The distribution of sources and the evaluation of their fields are the computational core, together with the solution of the matrix equation.

The Method of Moments applies to a general linear-operator equation with a known excitation, a linear operator and the unknown response, which is a sum of basis functions and linear equations, including weighting functions. The choice of basis and weighting functions determines the efficiency and accuracy of the Method of Moment solution. Basis functions are generally chosen as rectangular pulses of linear or sinusoidal functions or polynomials. The intent of NEC is to generate a likely distribution of currents on the modelled wires, subdivided into segments, and thus obtain the evoked fields.

Depending on the distribution of the voltage sources, their resulting currents and the interaction with other sources, the distribution of electric field is calculated. Within NEC electric far field as well as near field can be calculated.

With the aid of an optimized interpolation of pre-computed Sommerfeld integrals NEC2 reduces the necessary computation time, otherwise a double integration over the current distribution of the whole model would be needed. These pre-computed Sommerfeld integrals are used as table look-up in the numerical integral computation.

The Moment Methods resulting matrix equation is solved by factoring the matrix into a product of upper and lower triangular matrices by Gauss elimination. The two matrices are afterwards solved by forward and backward substitution. The computation time for matrix factoring is proportional to the matrix order cubed. In case of symmetry structures decomposing the solution into a sum of eigenmodes, which decrease solution time and needed memory. Solving the smaller eigenmode matrix equations derives the solution of the greater matrix. The matrix furthermore may be solved by the aid of LU-decomposition leading to a partitioned-matrix solution, called Numerical Green's Function (NGF).

For all models simulated during this thesis work the double precision (64 Bit) mode of NEC-4 has been used.

The models have been created and error checked in the GNEC Windows based version of NEC-4 and mainly been calculated on the IAP's computer mainframe consisting of a shared memory and cluster system.

A.2 Quality of a radiation pattern

A typical radiation pattern consists of one main lobe and several generally unwanted side lobes. For such a pattern the quality of the radiation pattern can be expressed in terms of the relative intensities of the wanted main lobe and the undesired side lobes.

For this purpose a figure of merit, the antenna gain-to-noise-temperature (G/T ratio), is frequently used to describe the quality of the radiation pattern and the total receiving system (see e.g. *Dettefsen and Siart*, 2006; *ITU*, 2000). In this expression the gain of an antenna (array) and subsequent amplifying stages are compared to the equivalent noise temperature of the antenna and the receiver. The equivalent antenna noise temperature depends on the

radar	gain	beam width θ_3	min. side lobe atten.	main vs. side lobe	ML vs. SL rel. area
Resolute	23.1 dBi	4.0°	6.4 dB	5.8 dB	34.4 dB
DAVIS	28.2 dBi	6.0°	12.7 dB	15.2 dB	42,5 dB
ALWIN	28.3 dBi	6.0°	13.1 dB	15.8 dB	43.1 dB
ESRAD	31.6 dBi	3.8 - 4.4°	12.7 dB	16.0 dB	46.2 dB
MAARSY343	32.5 dBi	4.0°	16.2 dB	16.3 dB	46.5 dB
MAARSY343AT	31.3 dBi	5.0°	27 dB	28.1 dB	55.4 dB
SvalbardAT	32.1 dBi	3.7°	16.2 dB	23.8 dB	48.9 dB
MAARSY433	33.4 dBi	3.6°	17.4 dB	16.6 dB	47.7 dB
MAARSY433AT	31.9 dBi	4.8°	34.3 dB	34.4 dB	59.5 dB

Table A.1 Comparison of simulated gain for the main lobe (ML) and side lobes (SL) for various radar systems, sorted by their array area. The simulations for the radars ending AT incorporate amplitude taper. ML vs. SL rel. area denotes the relation of the intensities of the main lobe to all side lobes relative to their respective area.

actual radiation pattern and its environment. The better the radiation pattern, illustrated by a good side lobe suppression, the more the antenna temperature is defined by the emitting sources within the main beam. In the microwave frequencies the G/T ratio can be estimated observing two incident power sources of known intensity, e.g. the cold part of the sky and the sun, which dominates at these frequencies.

For atmospheric radars in the lower VHF region, like MAARSY with fairly narrow beam widths, the energy originating from the sky and thus all natural and artificial sources within the receiver band width should dominate. Thus, for arrays with a poor suppression of especially low elevation side lobes, other sources may easily interfere.

For a specific analysis of the amount of incident natural emissions a dedicated catalogue and map of prominent radio sources needs to be evaluated. For MAARSY this evaluation is presented in the dedicated Chapter 4 within this work.

At this point the spatial distribution of natural radio sources is neglected, but a uniformly distributed source is assumed. The integrated gain of the main beam is compared to the integral of all side lobes' intensities depending on their area. The result gives a good indication of the considered antenna arrays pattern quality. The pattern can be modified significantly depending on the actual amplitude and phase distribution applied to the array as have been pointed out in the Section 3.6. Table A.1 presents the calculated relations of the antenna arrays for MAARSY, its predecessor ALWIN¹⁴ and some other radar arrays, simulated with an angular resolution of typically $d\phi = d\theta = 1^\circ$. The antenna arrays of DAVIS¹⁵ and MORRO¹⁶ are almost similar to the former ALWIN array. ESRAD¹⁷ is composed of 284 5-element Yagi antenna array. For equal amplitude feeding, the Resolute Bay radar provides an extremely poor main to side lobe ratio, due to the shape of the antenna array as a mills cross (see e.g. *Hocking et al.*, 2001). With such an array configuration a narrow main beam is achieved on the costs of intense side lobes. In practise, this array incorporates amplitude taper by the use of coaxial feeding cable of different losses, which damps the side lobes, but also widens

¹⁴12x12 4-element Yagi array (see e.g. *Latteck et al.*, 1999)

¹⁵12x12 3-element Yagi array (see e.g. *Morris et al.*, 2011)

¹⁶12x12 4-element Yagi array (see e.g. *University of Tromsø*, 2014)

¹⁷16x18 (-4) 5-element Yagi array(see e.g. *Olsen et al.*, 1997; *Kirkwood et al.*, 1997)

the main beam. The simulation of the SOUSY Svalbard radar¹⁸ considers amplitude taper in form of a discrete step function. For comparison, additional to the uniform amplitude distribution for MAARSY343 and MAARSY433 also amplitude taper can be used to improve the side lobe suppression as it was presented in the Section 3.7.

A.3 Antenna pattern modifications due to variations or component failures

Since the commissioning of MAARSY occasional failures of the power amplifier modules have been encountered. The cause of these failures could not be identified in detail yet, neither on the test bench at Genesis nor at MAARSY directly. However, the failure rate was found to have decreased since the antennas were converted to circular polarization. The current explanation for this is the more uniform radiation pattern of the individual antenna and thus coupling to the surrounding array elements.

These malfunctioning transceiver modules need to be repaired on site, which typically is done twice per year and are thus non-operational for this time on transmit. Therefore, these permanent "missing" antennas are a serious issue to the radiation pattern. Note, these failures only affect the transmit path, the receiver of these transceiver modules are still functional. Depending on the amount and distribution of the malfunctioning modules the effect to the transmission radiation pattern might be significant in terms of deteriorated side lobe attenuation. Figure A.1(b) shows the simulated radiation pattern for MAARSY, when 21 power amplifiers and thus antenna array elements are not operational (state of January 2014). The latter appears a bit patchy with a more diffuse appearance of the side lobes, but still very similar to the reference pattern. The comparison to the ideal pattern is shown in Figure A.2(a). Interestingly, for this specific configuration the first side lobe appears to be less

¹⁸356x 4-element Yagi array (see e.g. *Czechowsky et al.*, 1984)

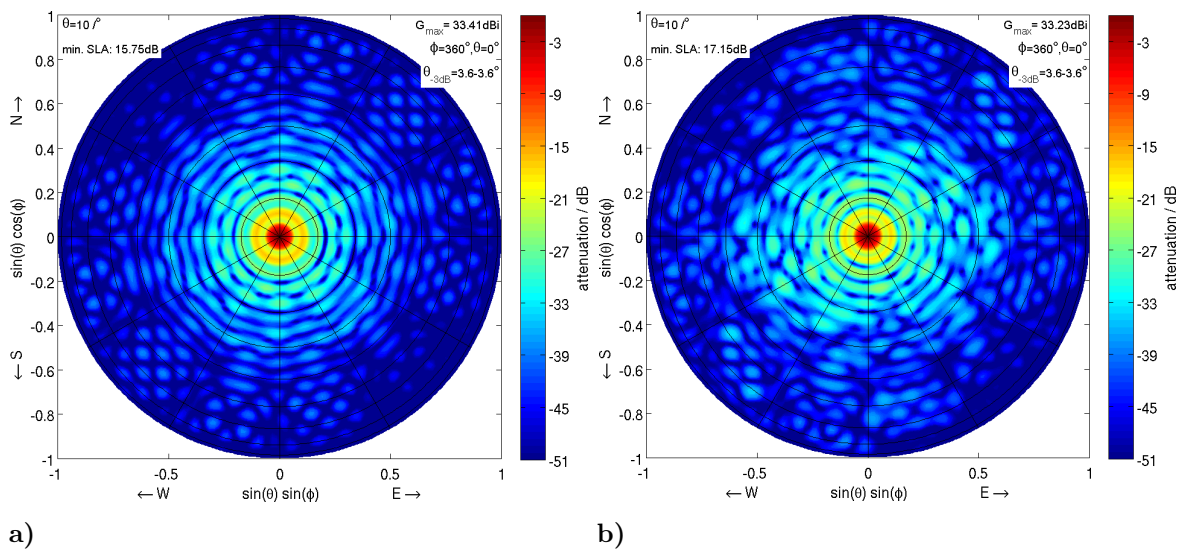


Figure A.1 Simulated radiation pattern of MAARSY433 for **a)** the ideally phased and unity amplitude antenna array and **b)** assuming 21 failed power amplifiers and thus array elements for the transmission case.

A.3 Antenna pattern modifications due to variations or component failures

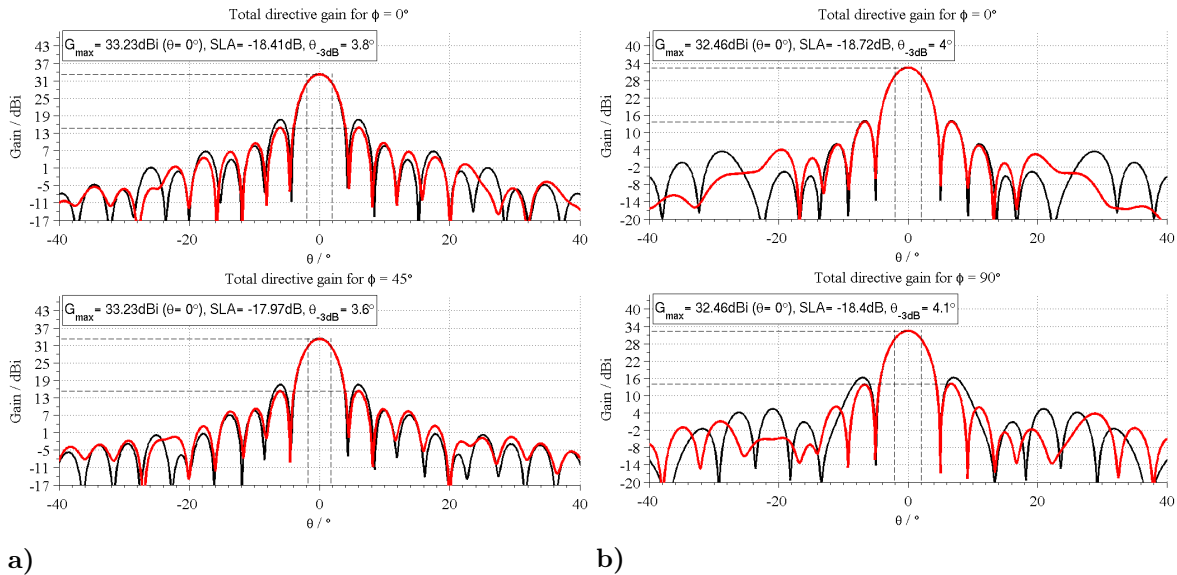


Figure A.2 Comparison of the radiation pattern of the ideally phased and uniform amplitude **a)** MAARSY433 (black) to the case of 21 failed array elements for the cross-sections $\phi = 0^\circ$ (top) and $\phi = 45^\circ$ (bottom). **b)** Comparison of the ideally phased and uniform amplitude MAARSY343 (black) to the case of random fluctuations of every array element of ± 1 dB and $\pm 10^\circ$ for two cross-sections.

intense than for the ideally phased and unity amplitude MAARSY433 pattern. Even though the suppression of higher order side lobes is roughly equivalent to the ideally fed array, but the specific directions of side lobes and the nulls in the pattern are modified. The absolute symmetry of the pattern is lost. Furthermore, the width of the main beam appears to be broadened ($+0.2^\circ$) for the cross-section $\phi=0^\circ$. This is reasoned by three failed modules associated with antennas in the C-08 and D-10 groups which are located at the array circumference and thus the effective maximum array dimension is decreased for this North-South cross-section. The reduction from 433 to 412 array elements corresponds to -0.2 dB, while the integral of the total radiation pattern should only differ exactly by that amount. To see the difference almost similar in the gain of the main beam (33.41 dBi to 33.23 dBi) points out that the integrated intensity of the side lobes is rather unchanged. However, the direction and intensity of the individual side lobes may still differ. This effect may be intensified by the shutdown of amplifier modules caused by safety alarms of the monitoring system provoked by e.g. high temperature of the amplifier modules due to deficient cooling (air condition or fan failure) and detected high reflected power (broken antenna, cable or active impedances), where the latter has recently been improved significantly with the circular polarization. This supports the reasoning of the presence of active impedances caused by mutual coupling of the surrounding array elements and their importance.

Furthermore, in some cases for specific beam pointing directions the impedance of the individual antenna may be modified due to coupling issues. This results in increased impedance mismatch, where the reflected power is not emitted by the antennas. The inherent power loss (reduction of s21 parameter) for typical VSWR of 1.3-1.4 is in the order of maximum 0.2 dB (see Figure A.3). Assuming uniform distribution of this power loss over the entire array, the total intensity of the radiated power should only be affected, but no pattern modification

Appendix A The analysis of NEC simulated radiation pattern

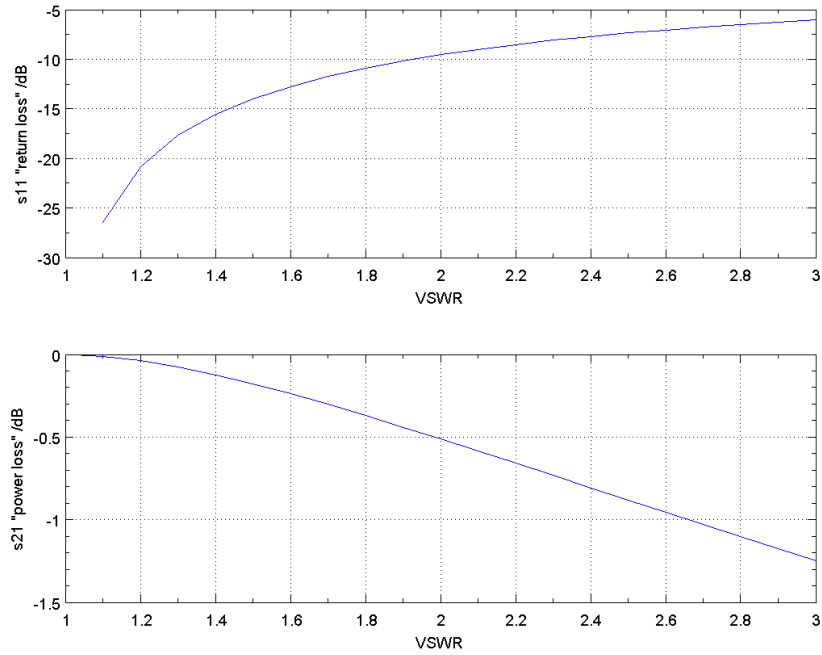


Figure A.3 Insertion and power loss for a given antenna mismatch as voltage standing wave ratio.

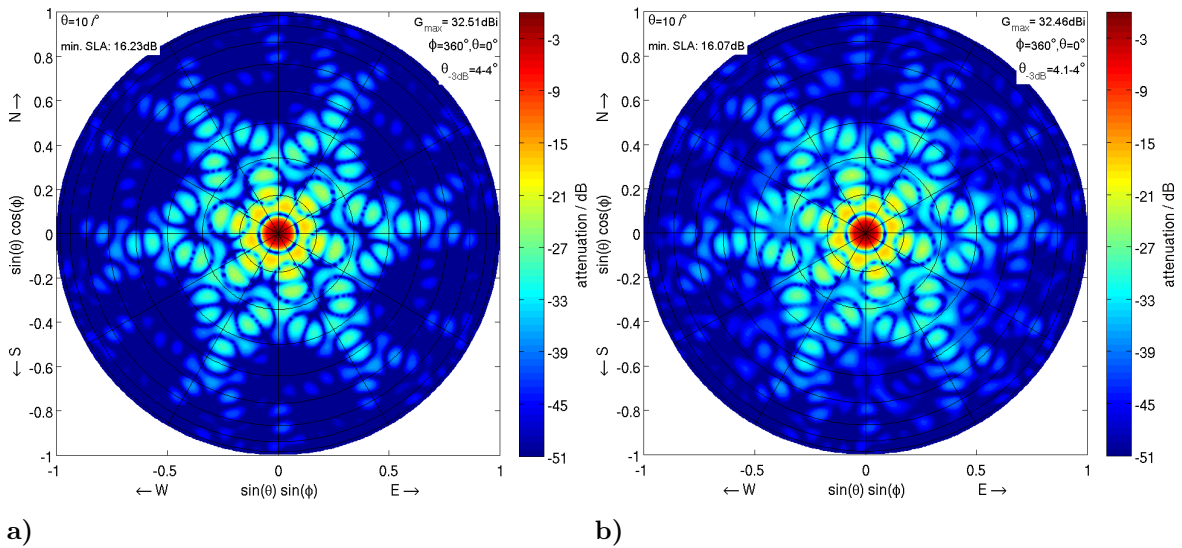


Figure A.4 a) Simulated radiation pattern for the ideally fed MAARSY343 and b) with random fluctuation of every array element of ± 1 dB and $\pm 10^\circ$.

should appear.

Besides these technical failures, random phase and amplitude variations of the emitted signal of each individual antenna affect the radiation pattern. This might be caused by imperfections of the transceiver modules, variations in the antennas or their feeding systems due to e.g. temperature variations. Therefore, simulations with ± 1 dB random fluctuation of amplitude and $\pm 10^\circ$ phase variation for all array elements are simulated and shown in Figure A.4(b), while the comparison to the ideal pattern is depicted in Figure A.2(b).

A.4 Comparison of a simple pattern model to NEC

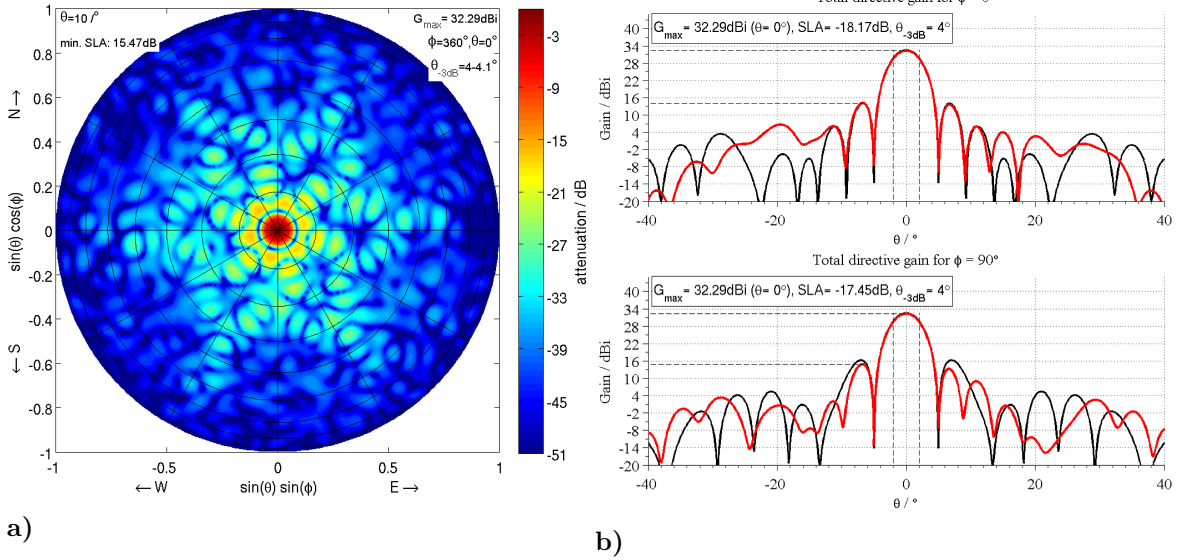


Figure A.5 a) Simulated radiation pattern for MAARSY343 with random fluctuation of every array element of ± 2 dB and $\pm 20^\circ$ and b) the comparison to the ideally fed MAARSY343 pattern (black) for two cross-sections.

Concordantly to the earlier findings variations in the direction and intensity of the side lobes can be found as well as slight broadening of the main beam ($+0.1^\circ$). The simulated pattern for ± 2 dB random fluctuation of amplitude and $\pm 20^\circ$ phase variation for all array elements are shown in Figures A.5(a) and A.5(b).

The model consistency has been verified by comparing the integrated power of all lobes for the individual models to the theoretical loss due to the number of missing antennas. The deviation was below 0.1 dB.

A.4 Comparison of a simple pattern model to NEC

In this section a simple geometric model, computing the array factor for MAARSY, is compared to the dedicated NEC model. The geometry model only considers the array element positions for the array factor. The total antenna array pattern is the product of the array factor and the pattern of the individual array element, which in this comparison is approximated by a gaussian shape of 100° width.

The total array characteristic (pattern) can be derived for a regularly spaced planar antenna array as depicted in Equation A.1, where C_e and C_a are the characteristics of the individual array element and of the total array respectively. The spacing between the array elements is defined by a and b while m and n are the number of available array elements. For off-boresight pointing to azimuth ϕ_0 and zenith angle θ_0 appropriate phase offsets ψ between the array elements need to be included. The beam steering phase offset between the array elements are calculated from the positions of the array elements to each other in respect to the pointing direction to generate a unity phase front.

$$C_a(\phi, \theta) = C_e \left| \frac{\sin n \left(\frac{\psi_c}{2} + \frac{\pi a}{\lambda} \cos \phi \sin \theta \right)}{\sin \frac{\psi_c}{2} + \frac{\pi a}{\lambda} \cos \phi \sin \theta} \right| \left| \frac{\sin m \left(\frac{\psi_r}{2} + \frac{\pi b}{\lambda} \sin \phi \sin \theta \right)}{\sin \frac{\psi_r}{2} + \frac{\pi b}{\lambda} \sin \phi \sin \theta} \right| \quad (\text{A.1})$$

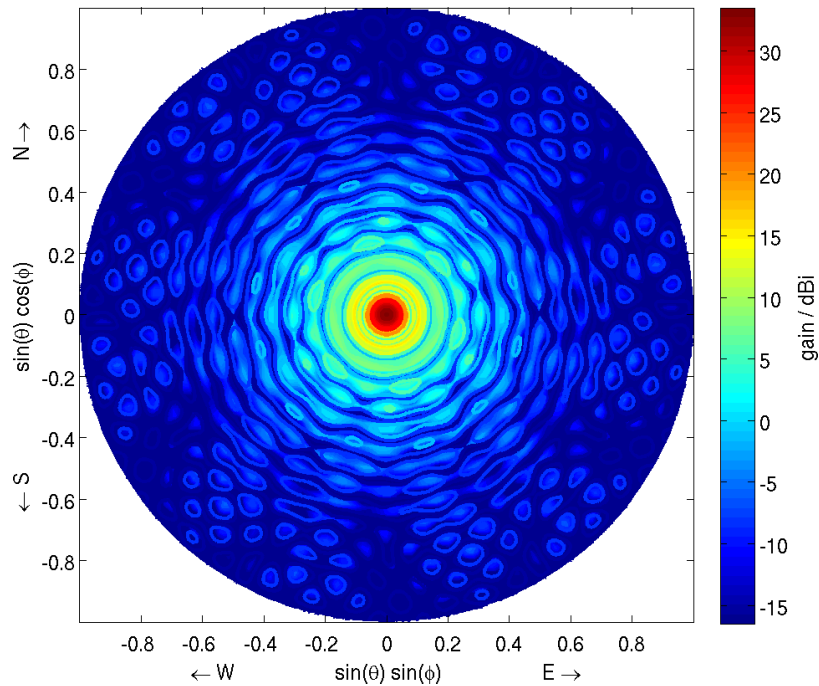


Figure A.6 Comparison of the radiation pattern of MAARSY simulated with NEC (filled contour) and the simple geometry model (contour lines).

For the derivation of this formula see *Renkowitz* (2008) or the references therein like e.g. *Stirner* (1984) and *Balanis* (2005). Furthermore, *Skolnik* (2008), *Mailloux* (1994) and *Johnson* (1993) present thorough information on array theory.

The array factor can also be expressed for non-regular grid structures, the appropriate phases for the individual positions of the array elements are calculated based on the geometry to the desired pointing direction.

The comparison of the NEC simulated (filled contour) and the geometry model (line contour) is depicted in Figure A.6. The structures in the radiation pattern of both simulations are in generally good agreement. The side lobes are located at approximately the same positions, which are defined by the actual distance between the array elements. The intensities of the side lobes are pretty reliable, which are defined by the array factor and the appropriate shape of the individual array element for the specific direction, where the gaussian shape of 100° width is well applicable for the MAARSY individual array element. However, the nulls in the pattern are more pronounced in the geometry model. The deviation between the radiation pattern simulated with NEC and the purely geometric equation are shown in Figure A.7. This analysis implies that the pure geometry model is well applicable for quick simulations (seconds compared to approximately 3 hours). However, for the detailed structures and the evaluation of the pattern dedicated simulations with NEC should be performed. The individual array element is simulated in detail in NEC as well as the mutual coupling and the consideration of ground characteristics. This is especially necessary when the integrated power of the side lobes is important as e.g. in Chapter 4.

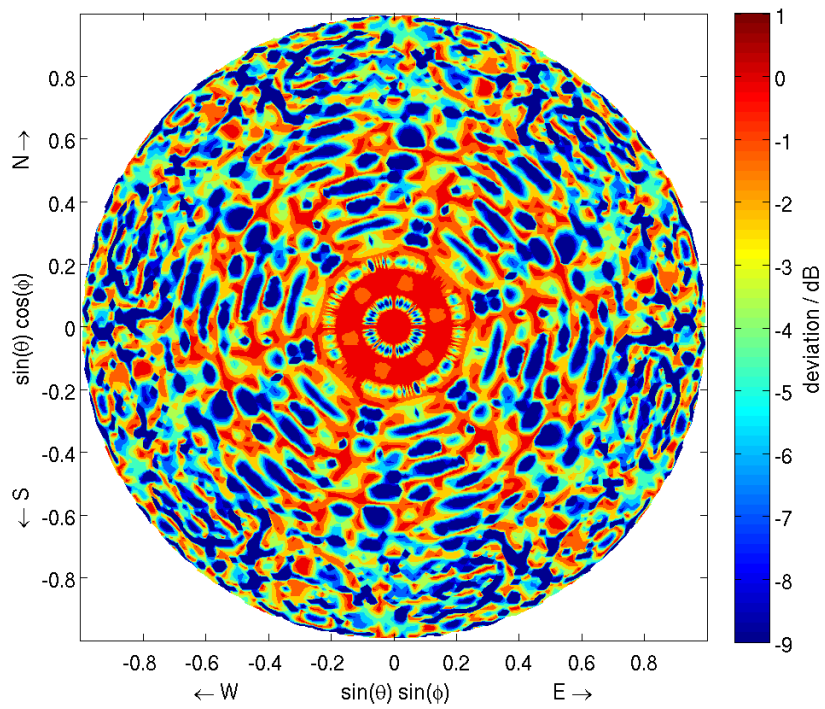


Figure A.7 Deviation of the NEC and geometry model, negative values denotes underestimation of the intensity in the geometry model.

Appendix B Radar hardware performance measurements

B.1 Measurements of MAARSY's array elements

For the determination and verification of the technical specifications of MAARSY, several measurements were conducted during maintenance stays. These technical measurements aimed for e.g. antenna match, phase and amplitude of the feeding coaxial cable, bandwidths, pulse widths, range calibration, linearity and sensitivity. Some of these parameters are evaluated in the subsequent sections.

B.1 Measurements of MAARSY's array elements

The typical impedance of a MAARSY antenna (D-06-1) is shown in Figure B.1(a) as seen by the individual transceiver module. For this purpose the feeding coaxial cable was not included in the calibration process of the measurement setup to maintain the apparent impedance affecting the transceiver module. Therefore, the typical v-shape of the individual antenna as depicted in Figure 3.6(a) (page 19) is modified by the length of the coaxial cable. The apparent return loss and thus the impedance mismatch is shown in Figure B.1(b), representing a well matched antenna for at least 4 MHz bandwidth. The shape is approximately similar to the VSWR curve in Figure 3.5(a), which can be directly calculated by Equation B.1, where a is the return loss and s the VSWR.

$$a = -20 \log \left| \frac{1 - s}{1 + s} \right| \quad (\text{B.1})$$

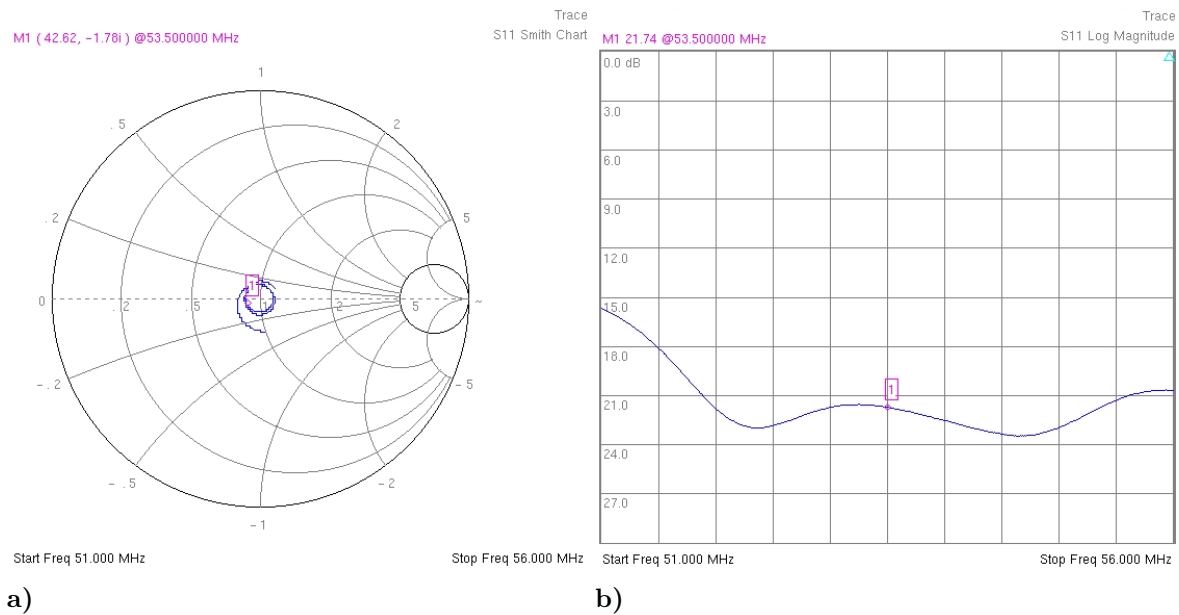


Figure B.1 a) Impedance of a MAARSY antenna as seen by a transceiver module including the coaxial feeding cable illustrated in a Smith-chart with 50Ω reference impedance. b) Same as a), but depicted as return loss log magnitude s11-parameter.

B.2 Measurements of coaxial feeding cables

Even though modern radar receivers and transmitters, based on Direct Digital Synthesis (DDS), are able to compensate amplitude and phase variations, it was decided to use coaxial

Appendix B Radar hardware performance measurements

	s_{21}			s_{11}		
	$\bar{a}/dB, \sigma_a/dB$	$\bar{\phi}, \sigma_\phi$	$\bar{\tau}_{gr}, \sigma_\tau$	$\bar{a}/dB, \sigma_a/dB$	$\bar{\phi}, \sigma_\phi$	$\bar{\tau}_{gr}, \sigma_\tau$
RF	-1.18, 0.04	-3.44, 2.84	224.71, 0.16	-2.36, 0.07	-8.49, 5.69	449.69, 4.03
IF	-3.32, 0.07	106.94, 24.41	812.13, 6.38	-6.69, 0.15	208.19, 49.12	1623.49, 26.49

Table B.1 Measurement results of MAARSY’s coaxial cables that are used on RF and IF during the preparation of the installation. \bar{a} , $\bar{\phi}$ and $\bar{\tau}_{gr}$ are the mean loss, phase and groups delay, while σ denotes their standard deviation respectively.

feeding cables of equal electrical length, instead of only equal phase or even random length and phase. This concept allows the change of every coaxial cable within the array to another if necessary or the fast exchange in case of a failure with equal spares. Furthermore it eases the planning of the cable placement layout and the initial and repetitive perusal of the feeding cables. The same procedure was used for the coaxial cable used on the intermediate frequency (IF), which connects the combined Hexagon signals to the IF switching and combining unit and the baseband receiver. All IF cables were measured for the s_{21} -parameter and s_{11} -parameter for the open and short calibration states at their ends. Because of the amount of the main antenna feeding cable, initially, only some samples have been measured in detail to validate their appropriate characteristics.

The values in Table B.1 clearly show the good quality in terms of loss and phase for the RF coaxial cable, however the phases for the IF cables were widely spread. It was assumed, the manufacturing company rather used the mechanical length of the cables than the electrical length when they prepared and equipped the cable with sockets and plugs. The worst IF cables were either exchanged against spares or electrically too long cables were adjusted. Additionally, for all coaxial cables to the containers there are jumper cables that are connected between the pass-through at the container wall and the receivers, which have been individually adjusted to the outer coaxial cable. Doing so, the phase error has been reduced to a few degrees for both, RF and IF cables. Later measurements of all RF coaxial cables indicate a median phase value of 0.02° with a standard deviation of 0.38° as well as a median loss of 1.35 dB with a standard deviation of 0.23 dB.

Furthermore, these extensive measurements permitted the evaluation of the velocity factor of the used LMR-400 (IF) and LMR-600 (RF) cable. The velocity factors were calculated to be 0.8505 ($\pm 1.5\%$) and 0.8509 ($\pm 0.5\%$) for the LMR-600 and LMR-400 coaxial cable respectively.

B.3 Linearity and dynamic range measurements

In this section the linearity measurements of the MAARSY receiver and the association to the total dynamic range are described and evaluated. The knowledge of the linearity of the total receiver system is crucial for all measurements to ascertain the incident signal in terms of absolute power or temperature. Any non-linearity requires the use of various calibration factors for the apparent detected power levels, which has to be avoided. For this purpose a signal generator is used to feed a continuous wave signal into seven MAARSY receivers, which form the Hexagon IF signal C-06. This signal is split and connected to both IF-to-baseband receivers (of the Hexagon C-06 and Anemone C) to analyze their behavior

B.3 Linearity and dynamic range measurements

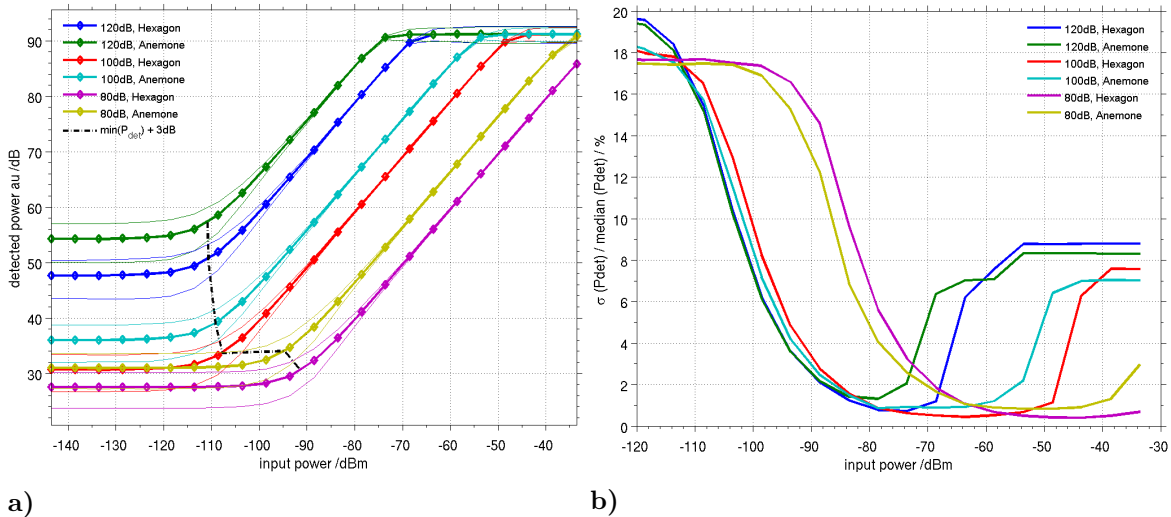


Figure B.3 a) Linearity measurements of input reference power to detected power, indicating the dynamic range for different gain settings for both Anemone and Hexagon antenna groups. The black broken line refers to the 3 dB increase of detected power, what describes the sensitivity. b) Standard deviation of the detected power level divided by the median power level for each input power level. This figure depicts the optimal input power window for minimum uncertainty. The left maxima describes the sensitivity, while the right maxima marks the saturation. The right shift of the 80 dB curves indicates deteriorated overall system noise figure for this gain setting.

in dependence of the incident intensity.

Additionally, the standard deviation of the detected power for a constant input signal describes the gain stability of all receiver stages and quality of the analogue digital converter (ADC).

In Figure B.3(a) are depicted the individual measurements for various gain settings for a Hexagon and an Anemone receiver channel including the observed systematic standard deviation. At low input levels, where the internal noise of the receiver still dominates or interacts, the standard deviation of the detected power related to its median is rather high. The same behavior can be found close to the saturation of the ADC. The total available dynamic range and the apparent reliability of the detected power can be found in the figure for different gain settings for the Hexagon and Anemone channels. The estimated values for the dynamic range are presented in Table B.2. In Figure B.3(b) is depicted the relative standard deviation $\sigma(P_{det})/median(P_{det})$ which highlights the above described dynamic range indications.

The apparent noise figure of the receiver can be seen in both figures, for Figure B.3(a) the horizontal shift of the break of slope indicates the noise figure, marked by the broken black line. The minima of the curves in Figure B.3(b) mark the optimal range of input power. The use of the gain setting 80dB instead of 120 dB or 100 dB results in a horizontal shift of the relative standard deviation curve of about 20dB, what is directly connected to the increase of the noise figure by the same order. The difference for the 120 dB and 100 dB settings at very low input signals arises from the dominating contributor, for 120 dB the RF to IF receivers exceed the noise contribution of the subsequent stages (see Figure B.3(a)). To maintain the maximum sensitivity of MAARSY, the gain needed to be at or above 100 dB, the dynamic range was limited to approximately 45 dB. These unsatisfactory results of limited overall

Appendix B Radar hardware performance measurements

gain /dB	Filter BB/IF /MHz	max. dynamic /dB Anemone	max. dynamic /dB Hexagon
120	0,5/3	48,2	41,3
120	0,5/3	43,6	37
100	0,5/3	60,5	55,1
80	0,5/3	58,3	59,8
63	0,5/3	39,7	42,4

Table B.2 Results of dynamic range measurements for various gain settings for the Anemone and Hexagon receivers.

dynamic range of MAARSY was consecutively subject to improvements. Until this time the receiver gain of MAARSY was distributed on the RF to IF receivers (70 dB) and the IF to baseband receivers (50 dB). As the above findings indicated too high gain at the latter stage it was agreed to evaluate a reduction of gain of the Signal-Processor-Unit (SPU).

Before applying these modifications to MAARSY, one SPU-Channel of the MAARSY test system, located in K uhlungborn, was altered by the manufacturer. This 8-channel transceiver test system is available for dedicated hardware tests, even though it lacks a lot hardware components used at MAARSY. Nevertheless it is a useful test bench for various aspects in the evaluation of MAARSY’s receiver and transmitter components. In Figure B.4(a) the measurements of a modified (red) and unmodified SPU channel are shown. For these measurements a defined signal from a signal generator (on MAARSY’s IF frequency) was injected directly into the SPU. In this modification the gain of the SPU was decreased by approximately 17.5 dB, resulting in an increase in dynamic range of about 11.5 dB due to the accompanied decreased sensitivity of this unit. The latter is not an issue in the final implementation to MAARSY as the previous stages provide enough gain and thus dominate. The total dynamic range of this SPU is now about 71 dB, limiting the overall available dynamic range. In Figure B.4(b) are shown the results of equivalent measurements for the entire MAARSY test system receiver, performed from RF (53.5 MHz) down to the baseband for two different receiver band width settings (0.125 MHz and 3 MHz). Consistently, the modified channel shows about 17 dB less gain, resulting in an increased dynamic range of the same order for both bandwidths.

Additionally, the influence of the receiver bandwidth can be seen clearly for input power levels below -80 dB, where the integrated noise power of the bandwidth supersedes the power level of the injected narrow band signal. This underlines the necessity to limit the receiver bandwidth to a minimum, matching to the experiment settings like pulse width and expected Doppler shift and spread.

Meanwhile, an equivalent SPU modification has been integrated to MAARSY in September 2013 aiming for a 25 dB decrease of gain within the SPU. Additionally, the earlier integrated 20 dB attenuators in the IF path were retained in the system to match the minimum noise floor of the SPU while using maximum gain of the front ends in the RF receivers in the containers. This combination just conserves the minimum noise figure of the total system providing maximum dynamic range.

Subsequent delay line calibrations do not indicate any deterioration of the receivers linearity due to the modification, but increased dynamic range from initially 45 dB to now approximately 70 dB (see Figure B.5(a) and B.5(b)). The total receiver gain of MAARSY has been reduced from initially 120 dB to finally 75 dB, which appears to be an optimal compromise

B.3 Linearity and dynamic range measurements

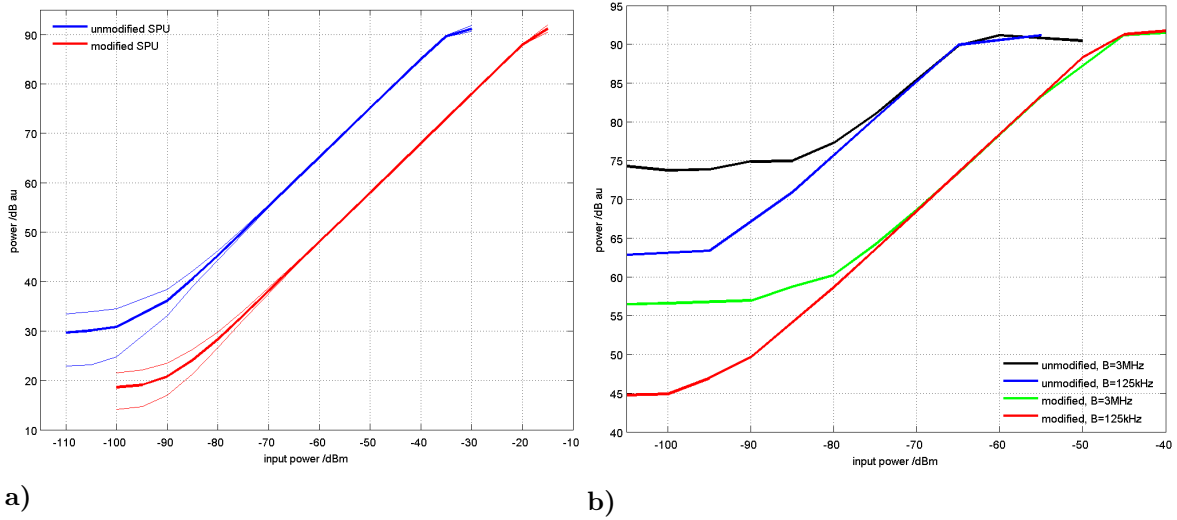


Figure B.4 a) Linearity measurements of MAARSY test systems Signal Processor Unit before (blue) and after the modification (red) accompanied by their standard deviation interval. The reduced gain of the SPU facilitates increased dynamic range. b) Linearity measurements of the complete MAARSY test system receiver, injecting a 53.5 MHz signal for two bandwidth settings into a modified and an unmodified channel.

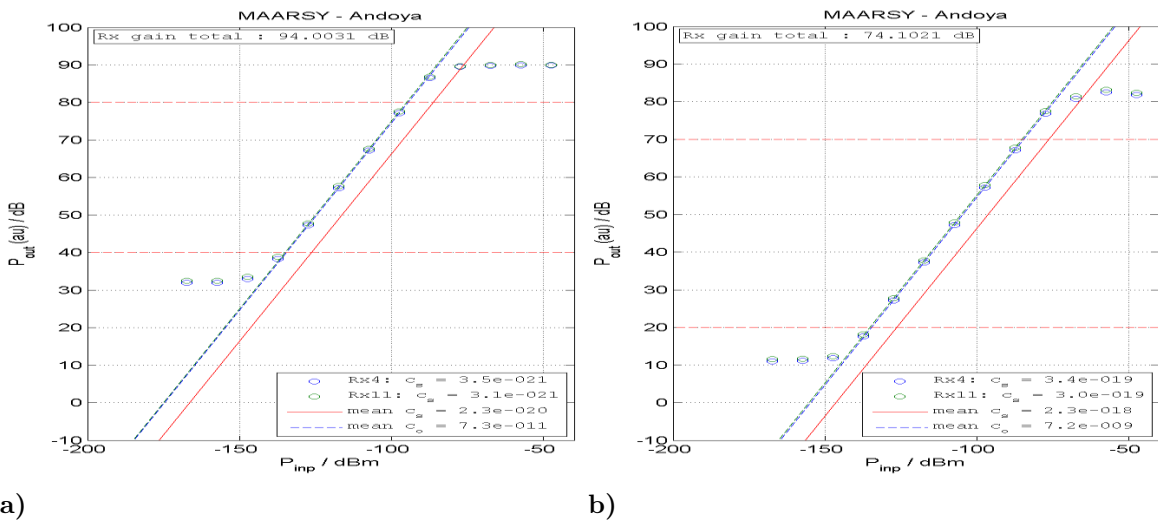


Figure B.5 a) Results of the delay line calibration after SPU modifications. b) Same as a) including additional 20 dB attenuators in the IF path. (courtesy of Dr. R. Latteck, IAP)

for the most experiments. In future upgrades the fixed 20 dB attenuators in the IF path could be exchanged to user selectable attenuators of up to e.g. 30 dB, potentially enhancing the experiments performance.

B.4 Estimation of the receiver noise figure of MAARSY

The noise figure (NF) of the MAARSY receiver system has been evaluated in various measurements and experiments. The first direct measurements of the receiver noise figure were performed in November 2010 by means of an automatic noise figure analyzer HP-8970B and a calibrated solid state noise source HP-346B from 54 MHz down to the IF of approximately 11 MHz for various receiver gain settings. These results are in general in good approximation to the system noise figure as the first stages should dominate. The results of these measurements are presented in Table B.3. However, in subsequent studies and experiments it turned out, the 120 dB gain setting of the receivers was too high for accurate measurements of the noise figure. Nevertheless, these measurements proved to be valuable indicators of guidance, especially the 100 dB setting, which is considered to be very reliable.

gain /dB	measured gain /dB	measured noise figure /dB
50 (+50)	48,8	4,33
70 (+50)	48,6	3,45

Table B.3 Noise figure measurements performed for a MAARSY RF to IF receiver with an automatic noise figure meter.

Another attempt to estimate the internal system noise figure of MAARSY was conducted including all parts of the receiver chain, besides the antennas and their feeding coaxial cable. An electron tube diode noise source (Rohde & Schwarz SKTU) generates a broadband signal with variable intensity, which is connected to a 1:8 splitter and then fed into seven receivers belonging to Hexagon group C-06. The eighth port of the splitter was terminated with $50\ \Omega$ and thus inserting 0.58 dB additional loss of noise power fed into the receivers (see Figure B.6 for a schematic).

Within this experiment the MAARSY receiver system samples the stepwise increase of incident noise from a broad band noise generator on 53.5 MHz. The approximate noise figure of the system can be found when the detected incident noise power is doubled from the $50\ \Omega$ termination level (*Rohde & Schwarz*, 1966). The results of these experiments can be seen in Figure B.7(a). The final value has been interpolated between 1dB-stepwise measurements. The same principle setup of this experiment has been repeated with a calibrated solid state noise source during a later stay at the radar. Divergent to the earlier described setup a step attenuator was used to vary the intensity (excess noise ratio) of the noise source. With these experiments the noise figure of the MAARSY receiver was determined for different gain and bandwidth settings (see Figure B.7(b)). In the earlier described method only 3 points of the individual measurements were used (reference $50\ \Omega$ and the points around the 3 dB increase). Contrary, the Y-factor method (see *Agilent*, 2013) is now used to calculate the noise figure

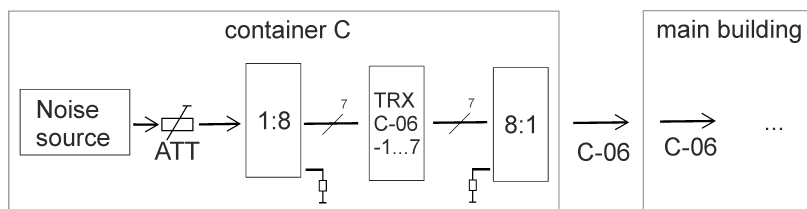


Figure B.6 Schematic of the noise figure measurement setup.

B.4 Estimation of the receiver noise figure of MAARSY

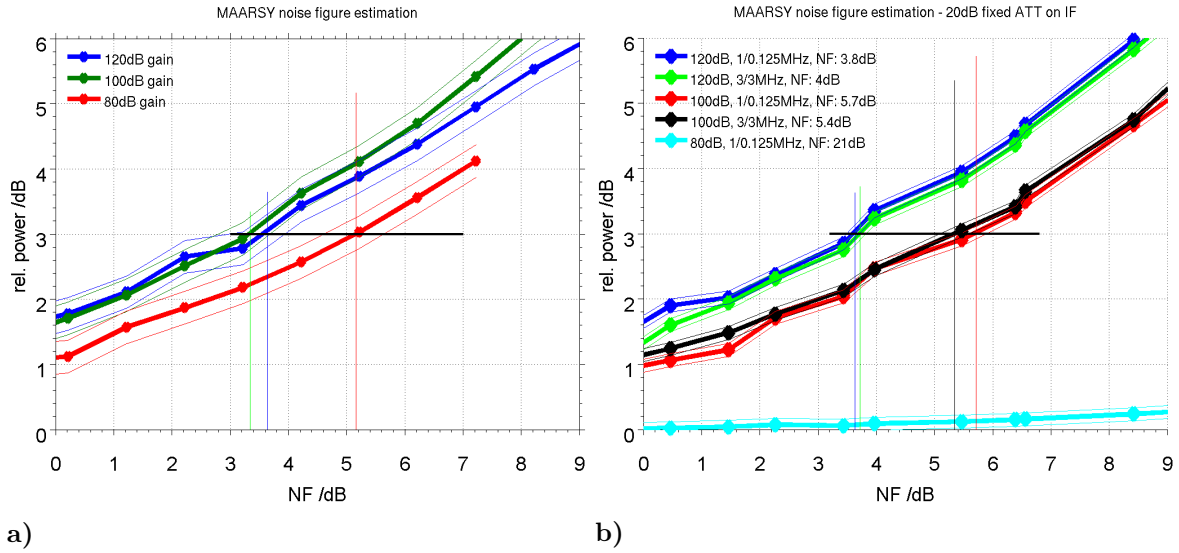


Figure B.7 Results of the first noise figure measurements (NF) (**a**) and the more recent and accurate measurements using a solid state noise source (**b**), accompanied by the respective uncertainty of the used noise sources ± 0.25 dB and ± 0.1 dB. The NF given in the legend of (**b**) is derived with the Y-factor, while the vertical lines represent the single-point NF estimation by a 3 dB increase of the polynomial interpolation.

for every single point of measurement, where the final noise figure results from the median of these.

The noise factor of e.g. an amplifier is expressed as follows:

$$F = (S_{IN}/N_{IN})/(S_{OUT}/N_{OUT}) \quad (\text{B.2})$$

or

$$F = 1 + (T_e/T_0) \quad (\text{B.3})$$

where S and N denote the signal power and the noise power of the input and output signals. T_e describes the equivalent input temperature, while the temperature reference T_0 is defined to 290 K. The noise factor for the concatenation of e.g. two amplifier or loss stages can be calculated by the Friis formula (see *Friis*, 1944),

$$F_{12} = F_1 + ((F_2 - 1)/G_1) \quad (\text{B.4})$$

where F_1 and G_1 are the noise factor and gain of the first stage and F_2 the noise factor of the second stage. With these equations the overall noise figure of the MAARSY transceiver module was estimated, which showed approximately similar results as measured.

The noise figure is the logarithmic noise factor.

$$NF = 10 \log_{10}(F) \quad (\text{B.5})$$

Thermal noise power is defined by Equation B.6, where the P_N is the noise power in W, k_B is the Boltzmann's constant ($1.38 \cdot 10^{-23}$ J/K) and B the bandwidth in Hz.

$$P_N = k_B T B \quad (\text{B.6})$$

Appendix B Radar hardware performance measurements

The excess noise ratio (ENR) is defined as

$$ENR = 10 \log_{10} ((T_S^{ON} - T_S^{OFF})/T_0) \quad (\text{B.7})$$

considering T_S^{OFF} is almost equivalent to T_0

$$T_{on} = T_0 \cdot 10^{(ENR/10)} + T_0. \quad (\text{B.8})$$

The Y-factor is the ratio of the output noise of e.g. an amplifier for the states ON and OFF of the connected noise source, which can be expressed in terms of noise power or temperature

$$Y = N_{ON}/N_{OFF} = T_{ON}/T_{OFF}. \quad (\text{B.9})$$

The noise figure and equivalent receiver temperature is then given by

$$NF = ENR - 10 \log_{10}(Y - 1), \quad (\text{B.10})$$

$$T_{RX} = \frac{T_{ON} - Y \cdot T_{OFF}}{Y - 1}. \quad (\text{B.11})$$

The Y-factor here describes the entire receiving system, including the power detector, which is a valid approximation here as in the prior receiver stages significantly lower noise figure prevail and plenty of gain exist. Thus, the noise of the detector is exceeded easily. If not applicable, a separate measurement of the detector has to be performed for calibration purpose and the total noise figure has to be calculated equivalent to Equation B.4.

The inherent ENR-error due temperature offset to the ENR reference of 290 K can be calculated by

$$ENR_{corr} = ENR_{cal} + ((T_0 - T_{OFF})/T_0). \quad (\text{B.12})$$

Assuming a room temperature of 25° C the resulting error in the calculation of noise figure is in the order of -0.12 dB (see *Agilent*, 2013).

Furthermore, plotting the equivalent temperature of the noise source over detected power, the intersection of the linear fit function with the ordinate roughly describes the negative equivalent noise temperature. This is depicted in Figure B.8 for two band width combinations (1 MHz, 0.125 MHz and 3 MHz, 3 MHz on IF and BB respectively), where the resulting equivalent receiver temperature T_{rec} is depicted in the top of each panel. The larger band width collects more noise power and thus shows an increased equivalent temperature (appropriate to Equation B.6). The derived equivalent receiver temperatures of approximately 435 K and 446 K are equivalent to 3.98 dB and 4.05 dB (see Equation B.3). This result agrees well with the estimations using the Y-factor, see the lower part in Table B.4. Additionally, with these measurements the calibration factor for incident broadband signals for two selected bandwidth settings for a Hexagon channel (see Figure B.8) were derived, which are used in Section 4.6. For narrow band signals alternative calibration measurements with the expected bandwidth of the incident signal have to be performed for selected gain and receiver bandwidth settings. For divergent bandwidths of the incident signal the largest errors have to be assumed close to the sensitivity of the receiver.

B.4 Estimation of the receiver noise figure of MAARSY

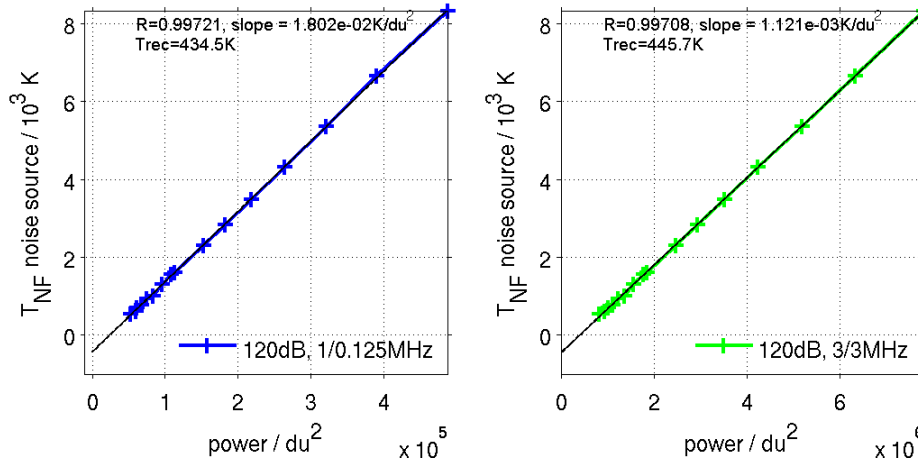


Figure B.8 Calibration factor for an injected broad band signal into a Hexagon receiver group for two bandwidth settings derived with with a calibrated solid state noise source. Additionally, the equivalent receiver temperature is estimated by the intersection of the linear fit with the ordinate and marked as T_{rec} .

gain /dB	bandwidth /MHz	noise figure (NF) /dB
80	3/3	5,8
100	3/3	4,2
120	3/3	4,7
80 -20	0.125/1	21.0
100 -20	0.125/1	5.7
100 -20	3/3	5.4
120 -20	0.125/1	3.8
120 -20	3/3	4.0

Table B.4 Noise figure measurements performed for the complete MAARSY receiver including data acquisition. The noise figure in the upper part is derived with an electron tube noise source for the 3 dB points. The lower part shows measurements with a solid state noise source, applying the Y-factor method.

B.5 MAARSY bandwidth measurements

The knowledge of the effective bandwidth of the radar receiver is crucial to various aspects. Generally, the receiver bandwidth needs to fit the bandwidth of the transmitted signal with additional headroom for the doppler shift due to the targets velocity and the potential spread of the spectrum due to turbulence. However, the bandwidth should be chosen as small as possible to a) limit the incident noise power to the receiver and b) to avoid any potential interference from other transmitters. Generally, in typical systems the receiver filter is set as a matched filter in shape and width to the transmit signal and assumed radio channel characteristics.

For the MAARSY radar the user actually may select between the combination of four different filters for both the intermediate frequency (IF) and the baseband (BB). The widths of all filters are shown in Table B.5, as they are given by the constructing company.

	filter no.				
location	0	1	2	3	4
IF /MHz	-	6	3	1.5	1
BB /MHz	3	1.5	0.5	0.125	-

Table B.5 Available filter settings of the MAARSY receiver independently selectable for intermediate frequency (IF) and baseband (BB).

In the progress of this work the effective bandwidth for some combinations of IF and BB filters had to be determined in order to adjust the calibration factor for the broad band cosmic noise observations and associated calibration. For this purpose, two combinations were directly measured at MAARSY. A signal generator (Rohde&Schwarz, SMY02) has been connected to a 1:8 $53MHz$ splitter, whose outputs were then feeding the seven receiver modules, while the eighth port was terminated with 50Ω . During this measurement the frequency was swept while the radar receiver samples the incident power. The output of the signal generator was set to reach the uppermost end of the linearity range of the receiving system to allow the maximum dynamic and e.g. to see spurious or other suspicious effects. The results of these measurements for two different filter settings are shown in figure B.9(a) and listed in Table B.6.

Additionally to the bandwidths measured directly at the radar, some filter settings were estimated by the use of fast-fourier-transformation (FFT) along the range gates. The data was collected by the radar's data acquisition, sampling atmospheric noise. Figure B.9(b) depicts the derived filter shape and derived bandwidths. The shape of the estimated filter curves appears to be realistic, however the estimated bandwidths seem to be slightly overestimated. A continuing investigation of the broader filter settings and direct measurement injecting a well defined signal for a frequency sweep with a signal generator might complement these measurements.

For both methods no spurious or other suspicious effects were found.

filter IF /MHz	filter BB /MHz	measured /MHz	estimated /MHz
3	3	2.27	2.47
3	1.5	1.24	1.58
1	0.5	-	0.17

Table B.6 Results of the bandwidth determination of the MAARSY receiver for intermediate frequency (IF) and baseband (BB), directly measured and estimated from FFT.

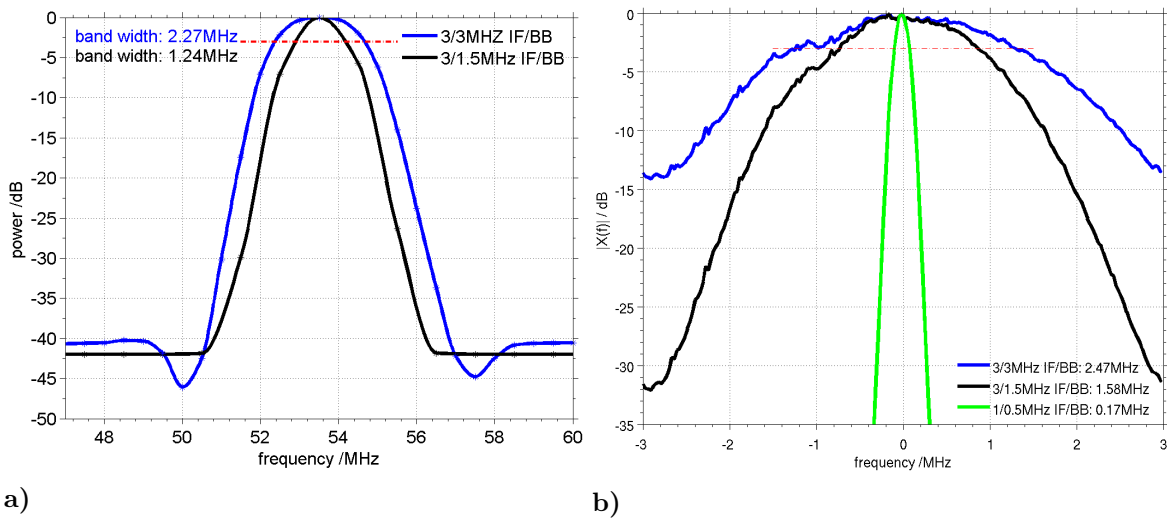


Figure B.9 a) Direct bandwidth measurements of the filter settings 3/3 MHz and 3/1.5 MHz for intermediate frequency (IF) and baseband (BB) respectively. b) Estimated bandwidth derived from the FFT along the range gates.

Appendix C Passive observations with MAARSY

C.1 Results of the Phase calibration attempts

In this section the remaining figures of the phase calibration experiments for the periods of September 2012 to May 2013 (Figure C.1) and May to November 2013 (Figures C.2 and C.3) are shown.

Additionally, an overview table for all receiver subarray groups that were used in the phase calibration experiments is shown for the individual polarization periods of MAARSY (Table C.2).

antenna group no.	antenna group names / identifier							
1-8	433	A	B	C	D	E	F	M
9-16	A-02	A-05	B-02	B-05	B-08	C-04	C-06	C-08
17-24	C-09	D-02	D-04	D-09	E-04	E-05	F-05	F-07

Table C.1 Identifying numbers and names of the groups used in the comparison of phase calibration methods, observing the cosmic radio source CasA and the automatic hardware phase test, Figure 4.9(a).

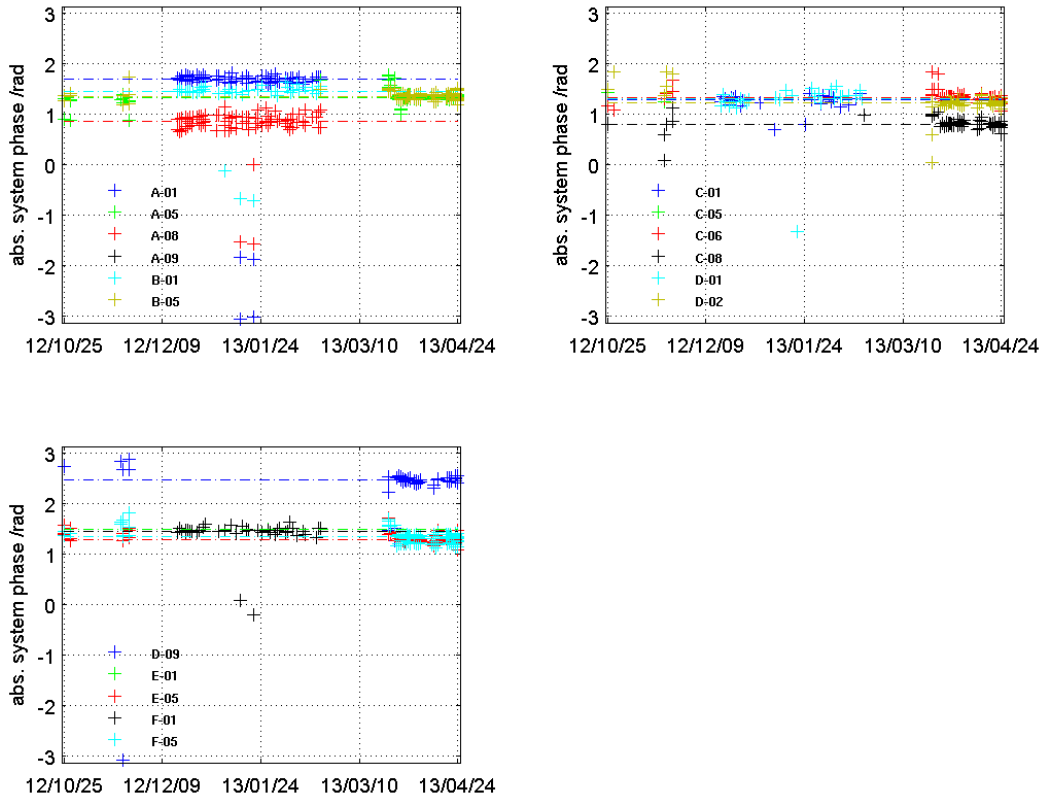


Figure C.1 Phase distribution and variation of the phase measurements observing Cassiopeia A for the connected Hexagon receivers. Period: Sept. 2012 - May 2013.

Appendix C Passive observations with MAARSY

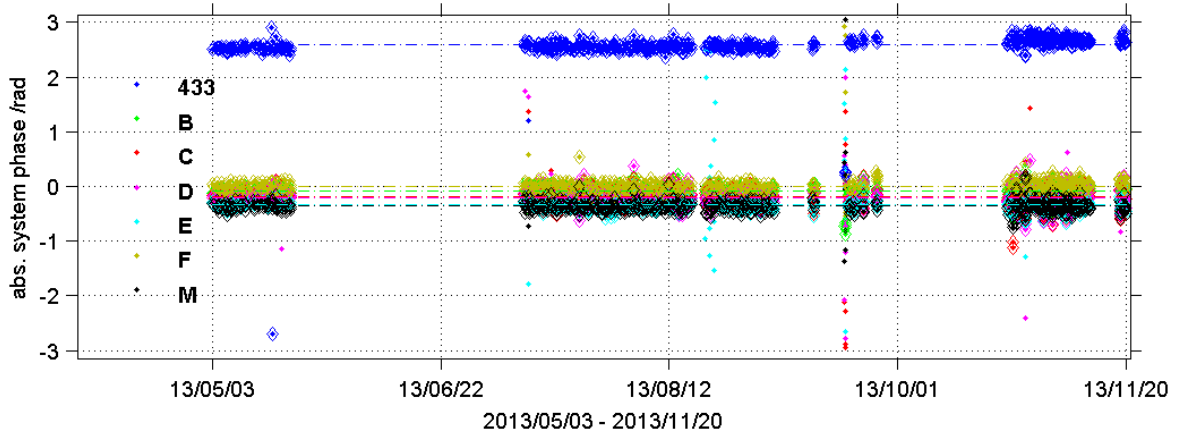


Figure C.2 Phase distribution and variation of the phase measurements observing Cassiopeia A since May 2013 for the 433 and Anemone receivers. The Anemones A-M are completely converted to circular polarization and thus their phases are again close to each other.

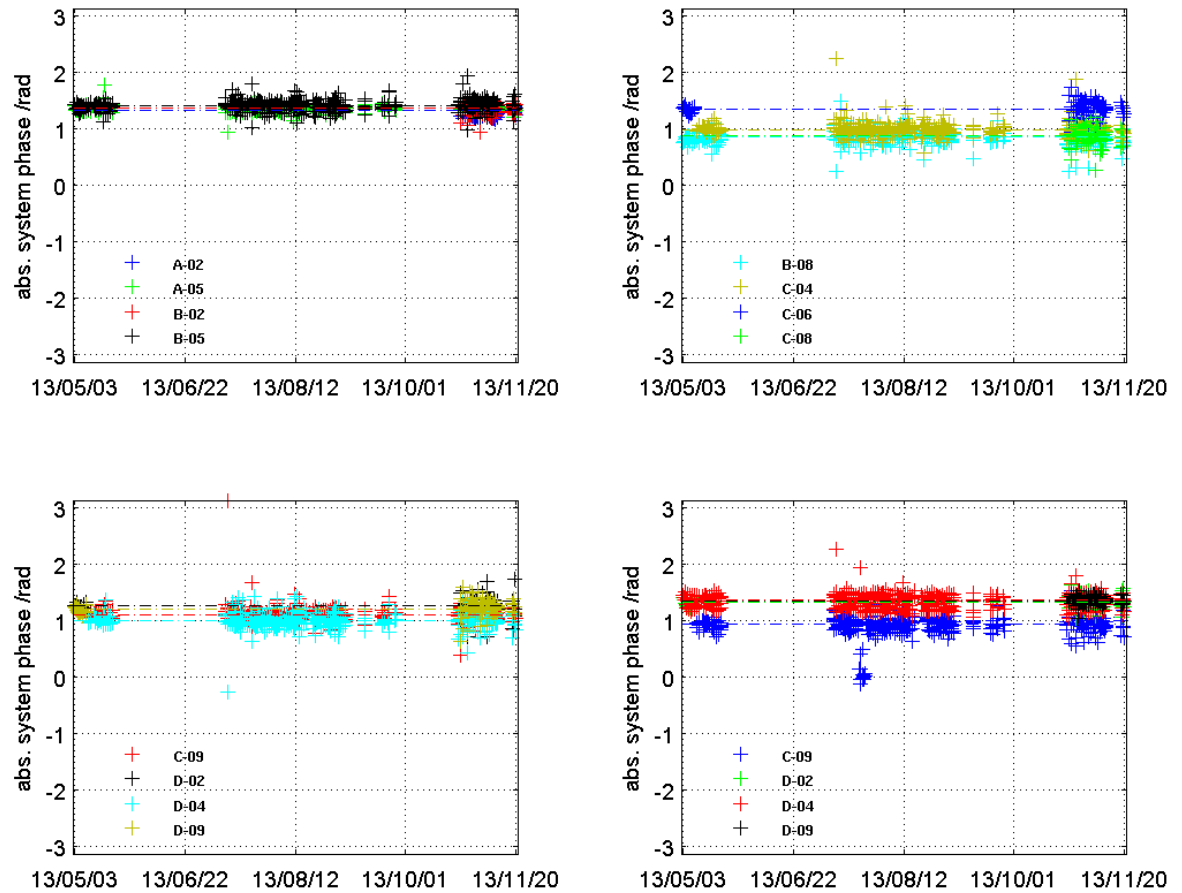


Figure C.3 Phase distribution and variation of the phase measurements observing Cassiopeia A since May 2013 for the Hexagon receivers.

C.1 Results of the Phase calibration attempts

ant. group	no. obs. until Sept.12	$\bar{\psi}/^\circ$	$\sigma_\psi/^\circ$	no. obs. Sept.12- May13	$\bar{\psi}/^\circ$	$\sigma_\psi/^\circ$	no. obs. May13- Nov.13	$\bar{\psi}/^\circ$	$\sigma_\psi/^\circ$
433	47	135.0	7.1	62	153.7	7.7	554	148.7	5.1
B	48	-8.8	6.8	219	-7.2	4.4	555	-4.6	4.8
C	44	-21.9	9.5	185	-11.6	4.9	545	-10.4	6.6
D	40	-18.7	9.9	166	-12.0	4.4	527	-11.4	7.0
E	28	-25.8	7.2	154	-19.5	4.2	532	-18.7	5.5
F	44	-6.3	6.6	213	-0.6	4.3	554	0.3	4.4
M	48	-32.2	8.0	212	53.8	6.8	554	-20.6	5.3
A-01	-	-	-	87	97.1	52.0	-	-	-
A-02	-	-	-	-	-	-	92	75.7	3.8
A-05	44	66.6	1.7	147	76.4	6.8	464	78.2	2.9
A-07	1	72.6	0.0	-	-	-	-	-	-
A-08	-	-	-	81	49.2	23.2	-	-	-
B-01	-	-	-	39	83.7	31.1	-	-	-
B-02	-	-	-	-	-	-	91	78.4	6.0
B-04	1	48.5	0.0	-	-	-	-	-	-
B-05	42	58.7	8.5	115	77.4	4.1	458	80.7	5.4
B-08	-	-	-	-	-	-	438	49.2	6.8
C-01	-	-	-	-	-	-	25	73.6	9.5
C-04	-	-	-	-	-	-	417	56.4	7.0
C-05	42	61.6	13.2	2	76.8	6.9	-	-	-
C-06	-	-	-	79	76.3	6.4	104	78.0	8.0
C-08 (1)	26	25.7	12.4	80	45.7	7.0	6	-35.0	3.5
C-08 (2)	-	-	-	-	-	-	74	51.1	9.1
C-09	-	-	-	-	-	-	427	63.2	8.1
D-01	-	-	-	30	75.3	28.6	-	-	-
D-02	-	-	-	74	70.9	12.1	101	72.7	8.5
D-04	31	38.6	13.6	-	-	-	408	56.9	7.8
D-09	41	52.9	13.0	61	142.3	43.8	112	69.8	7.6
E-01	-	-	-	1	85.5	0.0	-	-	-
E-04	18	39.6	10.3	-	-	-	400	53.4	11.3
E-05	-	-	-	112	73.3	4.9	115	76.1	6.1
E-07	1	62.2	0.0	-	-	-	-	-	-
F-01	-	-	-	38	83.8	20.2	-	-	-
F-04	35	45.8	7.7	-	-	-	-	-	-
F-05	-	-	-	140	76.9	6.3	456	78.1	7.2
F-07	-	-	-	-	-	-	89	77.4	4.0

Table C.2 Results of the phase measurements using Cassiopeia A for the individual periods before Sept. 2012, September 2012 to May 2013 and May 2013 to November 2013. Listed are the group identifier, the amount of individual measurements used, the derived group phases and its standard deviation.

C.2 Detection of radio sources by the use of correlation phases

Another outcome of the phase calibration experiments is the successful detection of the supernova remnant SNR-1572 (Tycho's SNR - 3C10, RA: 0h 25.3m, declination: $+64^\circ 09'$) on various days in October and November 2013. This radio source lies within the plane of the Milky Way and its signature in power is easily masked by the amount of integrated diffuse background radiation for MAARSY's angular resolution. However, it was possible to detect SNR-1572 in the correlation phases of the individual antenna groups (see Figure C.4), as the cross-correlation phases of the received signals and the calculated (predicted) phases are parallel. The resulting almost horizontal offset phases for the individual receivers clearly mark a coherent incident signal.

This radio source is explicitly interesting due to its high declination as it should also be detectable with vertical beam pointing. This would allow the combination of the daily phase calibration within other active experiments like a standard vertical monitoring experiment and thus increase the temporal resolution of these experiments and other experiments in the sequence.

In contrast to the successful detection of Tycho's SNR, the rather nearby W3-nebula (RA: 02h 22.7m, declination $+61^\circ 51'$) could not be found in the correlation phases of any receiver pairs, which were just randomly fluctuating. The likely reason for this is the extent of the source compared to the "point-like" sources CasA, CygA, and Tycho's SNR. The widely spread W3 nebula does not seem to emit uniform radiation, but a sum of individual sources. However the detected power around the position of this source and the indicated flux density suggest a feasible detection.

Both sources, Tycho's supernova remnant and the W3-nebula were already marked in Figure 4.23, representing the detected intensities with MAARSY.

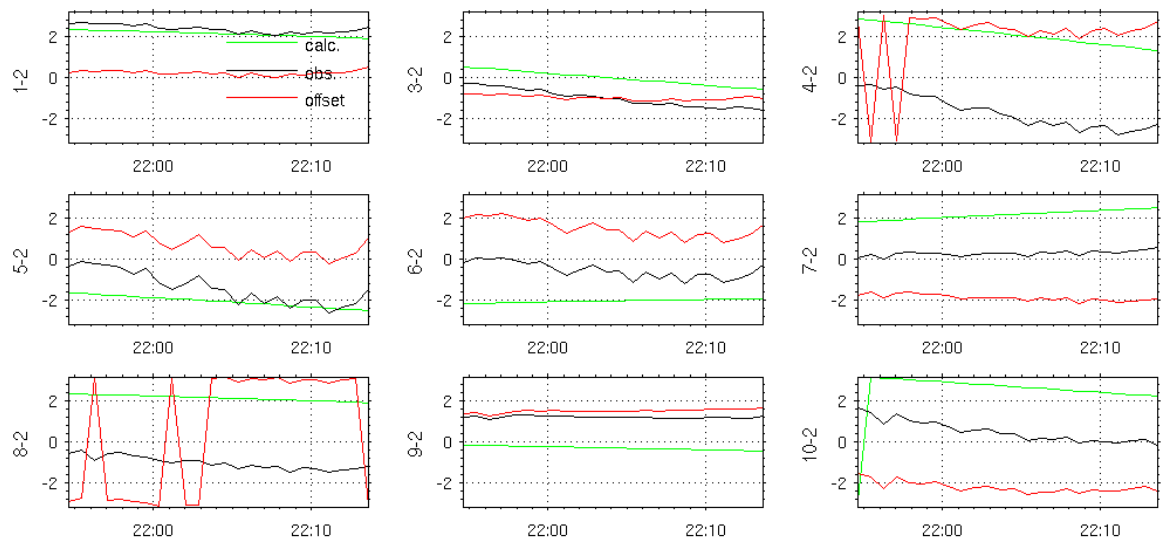


Figure C.4 Correlation phases for the 433, Anemone receivers and 2 Hexagon receivers for the time and coordinates of Tycho's supernova remnant (SNR) observed on 2013/11/19. This was the first radio observation of the Tycho SNR by the IAP.

C.3 Additional tables and figures related to the sky noise observations performed with MAARSY

radio source	type	right ascension	declination
Cassiopeia A, CasA, 3C461	SNR	23:21.1	+58:33
Cygnus A, CygA, 3C405	radio galaxy	19:57.7	+40:36
Taurus A, TauA, 3C144	SNR	05:31.5	+21:59
Tycho SN 1572, 3C10	SNR	00:25.3	+64:09
Virgo A, VirA, M87	radio galaxy	12:28.3	+12:40
3c400, W51	nebula	19:20.8	+14:08
3c157	SNR	06:14.3	+22:36
W3	nebula	02:22.7	+61:51
HB21	nebula	20:43.5	+50:25

Table C.3 Prominent cosmic radio source, which can be observed in the northern hemisphere with a VHF receiving system and an appropriate antenna array (data taken from e.g. *Kuz'min, 1966; Laing et al., 1983; Reich et al., 1997; Green, 2009; VLSS Remote Sensing Division, 2014*). The radio source type abbreviation SNR denotes a supernova remnant.

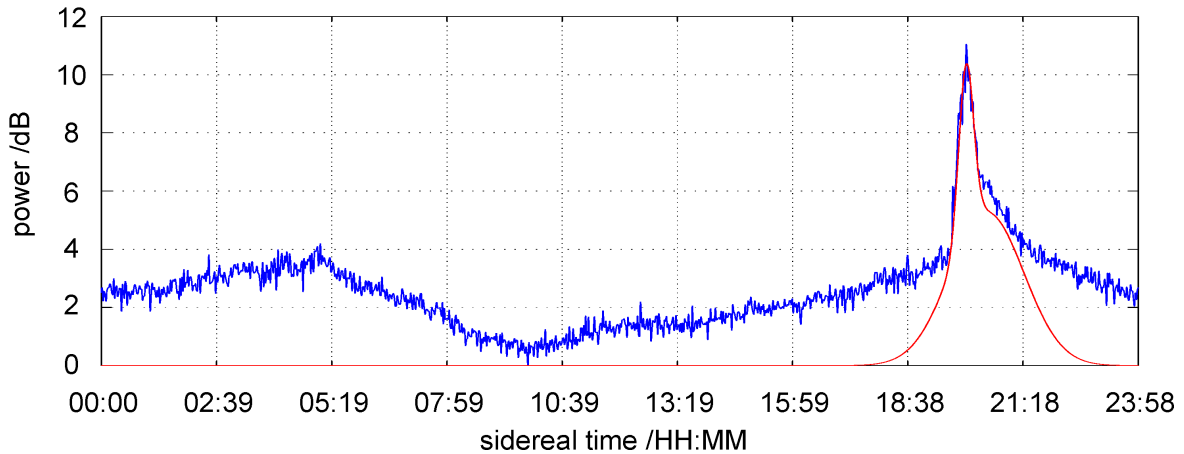


Figure C.5 Example of the Gauss-function fit to the median detected power for the estimation of the time of passage through the antenna main beam. Period: May to September 2013 for MAARSY343.

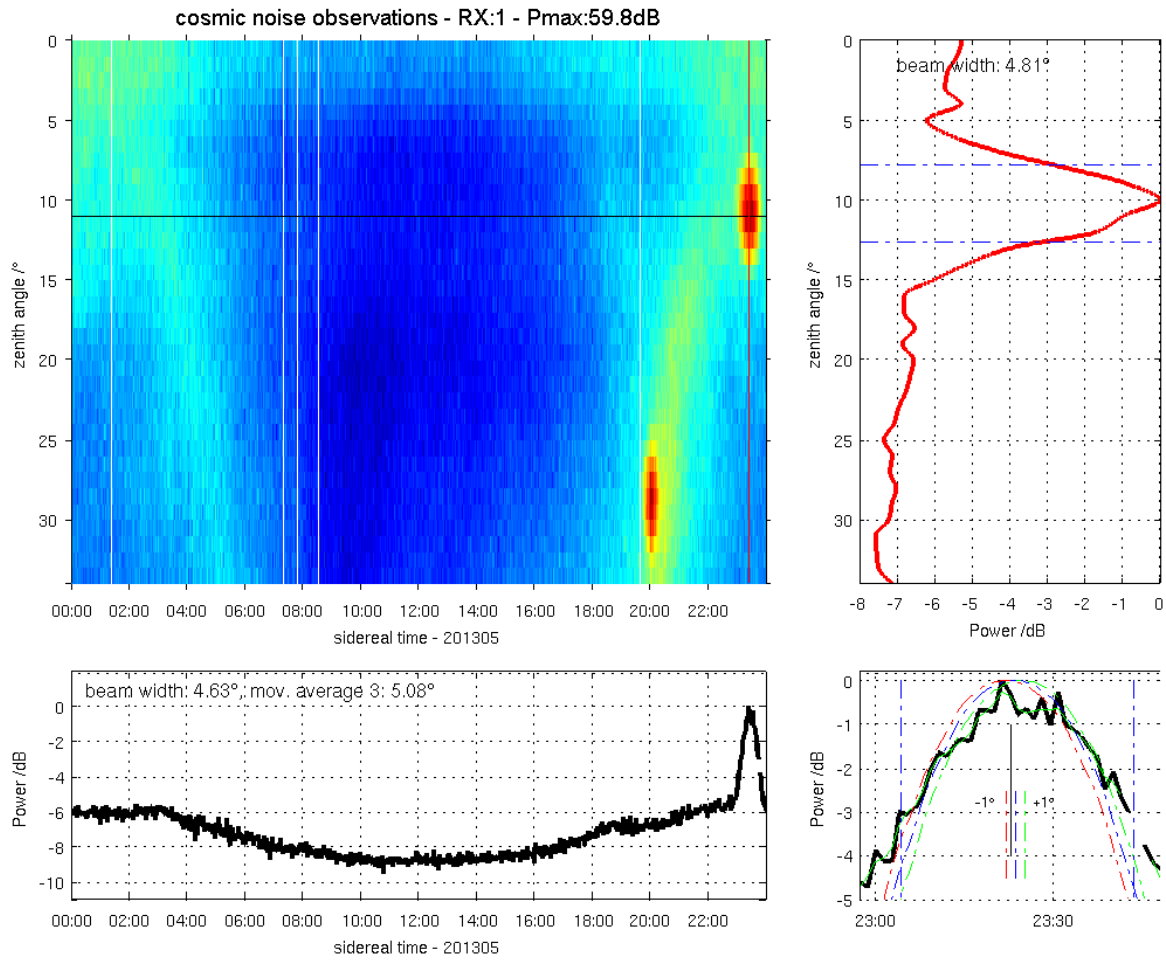


Figure C.6 Analysis of the incident sky noise power for the period of May to September 2013 received with MAARSY433. A detailed description of the individual panels is given in Figure 4.15 and in the accompanied text.

C.3 Additional tables and figures related to the sky noise observations performed with MAARSY

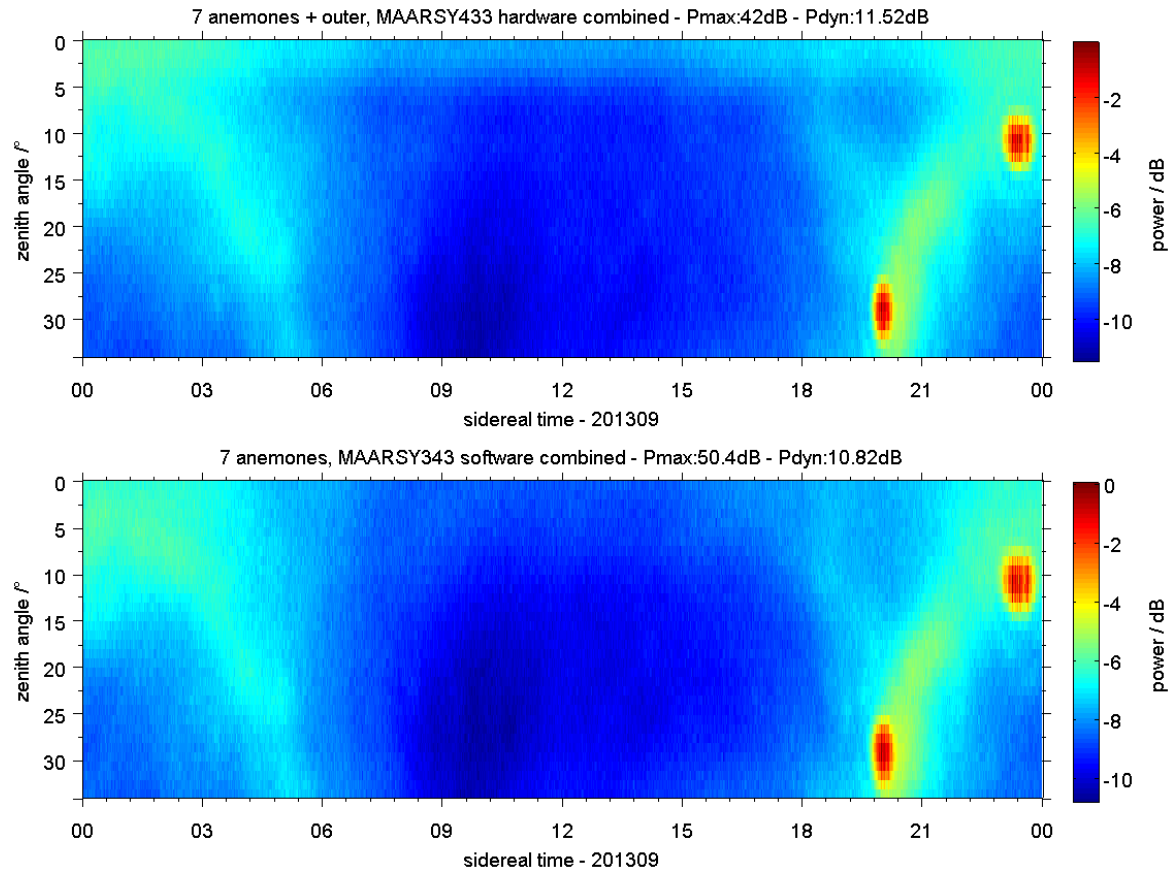


Figure C.7 Detected incident power for the period starting in September 2013 with the circularly polarized MAARSY antenna array. Top: MAARSY433, bottom: MAARSY343.

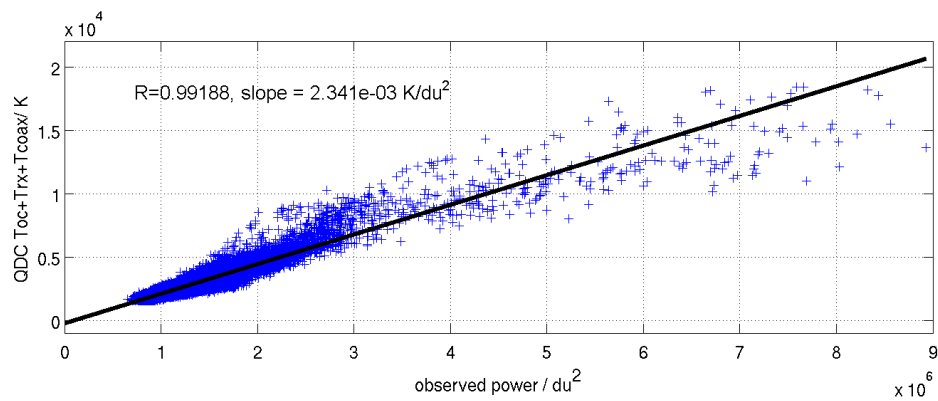


Figure C.8 Correlogram of the MAARSY cosmic noise observations for May to September 2013 with MAARSY343 and the GSM data to derive the calibration factor c_{GSM} .

Appendix D Airborne near field measurements

D.1 Sampling the transmission pattern of MAARSY

In Chapter 4 methods were presented, which allow the estimation of beam pointing accuracy and the beam width to some degree. With the active experiments described in Chapter 5 it was possible to gain confidence of the beam pointing, partially confirming the beam width estimation and side lobe attenuation.

To complement these findings it was planned to build an airborne field probe which should allow the direct in-situ spatial measurement of the field strength while the radar is actively operating. For this purpose a receiver, power detector, sampling unit and acquisition system has been constructed. The schematic setup for this experiment is depicted in Figure D.1.

The aim of this experiment was to measure the total field strength radiated by MAARSY and therefore three ground plane antennas are used and combined to sample all field components at a time. The superheterodyne receiver consists of the following components: input filter and matching circuitry, mixer, 48 MHz local oscillator (LO) and IF output filter for 5.5 MHz. The power detector consists of the logarithmic amplifier (AD8307) with its designated driver (AD603) and input filter allowing up to 120dB dynamic range, succeeded by a buffer amplifier (AD8031). The sampling unit consists of a 18-bit analogue-digital-converter (ADC, MCP3422), operated with 16-bit resolution, placed insulated in the same enclosure as the power detector. The ADC is connected via I²C-bus to the data acquisition system, which is composed of a mini computer ALIX.3D2 and an I²C-USB converter. The latter was needed as the I²C bus types of the ALIX and the ADC were not absolutely compatible (I²C-bus, SM-Bus). To decrease the uncertainty / RMS-error of the sampled intensities the mean of approximately 15 samples were saved every second to the data. The current position was tracked by GPS and stored with the raw data on a memory flash disk and simultaneously transferred via WiFi to the operator's computer, which allowed the instantaneous monitoring of the raw data.

Test bench reference measurements for linearity and selectivity are shown in the Figures D.2(a) and D.3(a). The linearity of the total setup is acceptable, the non-linearity can be corrected in the data. The mid-frequency of the setup is around 53.7 MHz which is defined by the highly selective ceramic filter used in the IF path.

The total setup during a system test, driving around the MAARSY array and sampling its radiated intensity, is shown in Figure D.4(a). Finally, the instrument was placed in a metal transportation box mounted (see Figure D.4(b)) approximately three wavelengths below the helicopter (see Figure 5.1 during lift-off) to minimize its influence. A larger distance was not permitted due to safety aspects.

The radar was configured to transmit a $2 \mu\text{s}$ gaussian shape pulse with 5 kHz pulse repetition frequency for 53 s followed by a 4 s experiment pause. Unfortunately, it was not possible to

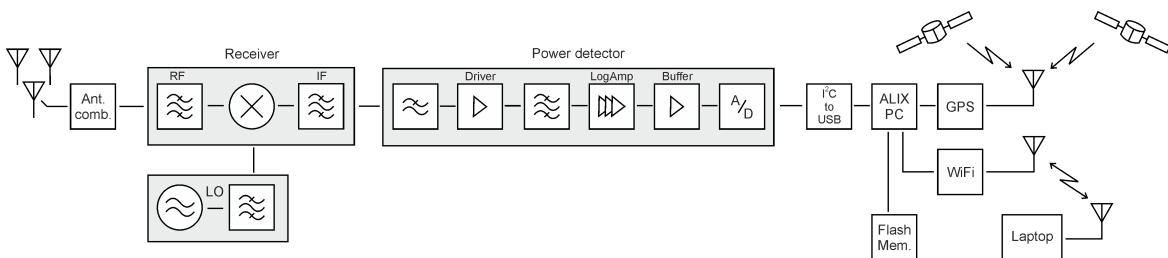


Figure D.1 Sketch of the airborne setup used to sample the intensity radiated by MAARSY.

Appendix D Airborne near field measurements

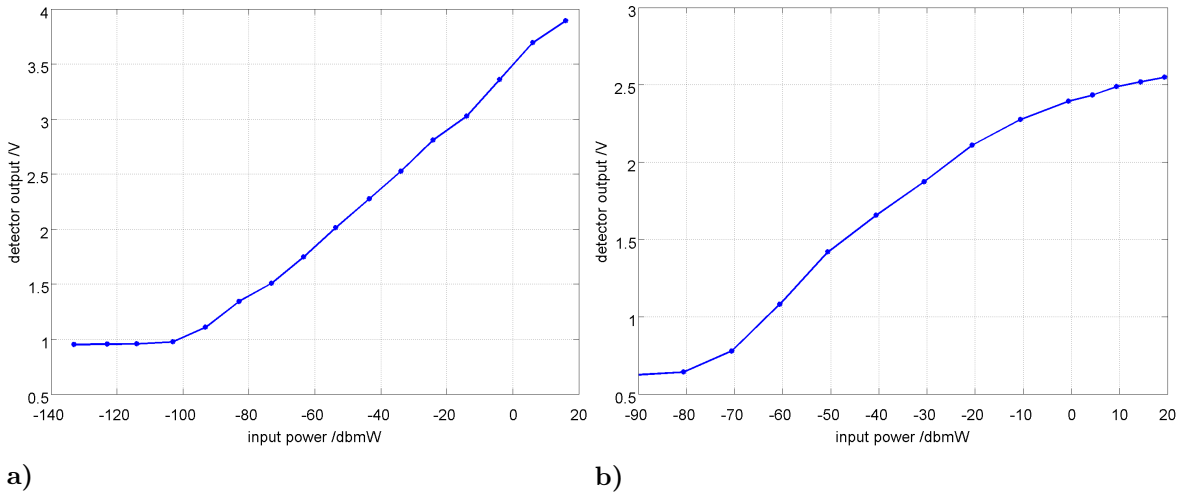


Figure D.2 Laboratory measurements of the linearity of the detector **a)** and of the total setup **b)**, without the antennas.

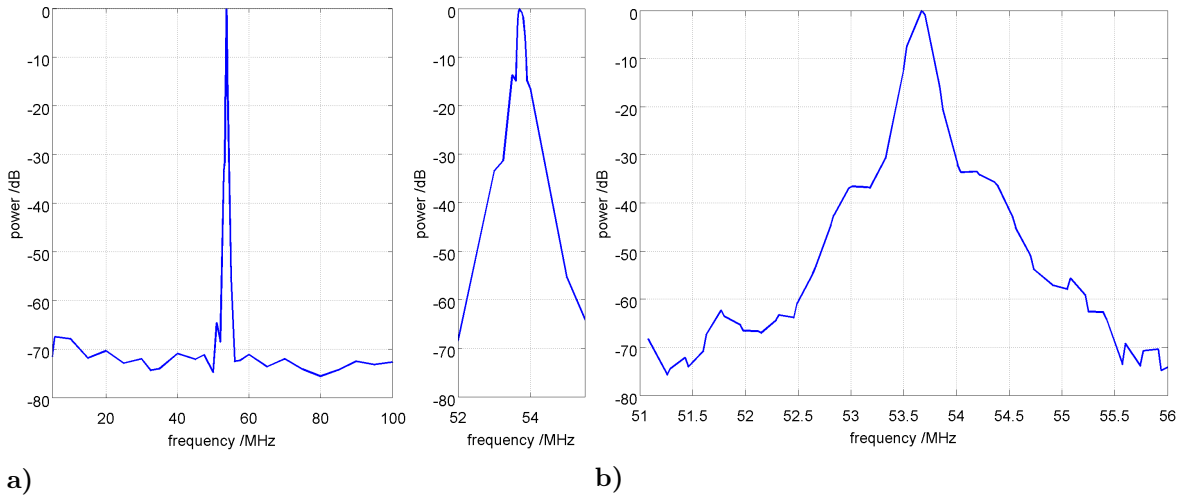


Figure D.3 **a)** Frequency selectivity of the receiver and detector for a board spectrum (left) and zoom around the nominal frequency of 54.7 MHz (right). **b)** Frequency selectivity of the total setup including the A/D-converter, without the antennas.

use MAARSY with the lower most output power settings as a lot of modules were shut down due to low output power alarm. Finally the setting of 55 dBm output power (approximately 300 W each module) was used, where only very few power amplifier modules were non-operational and should not modify the radiation pattern significantly. Initially, the main beam was steered to $\phi = 330^\circ$, $\theta = 25^\circ$ in this experiment, while during the second part of this experiment MAARSY was pointing vertically. The output power was raised to approximately 1 kW each module, where no power amplifier was shut off due to low output power.

Contrary to the original planning we were not allowed to fly high enough to reach the far field and furthermore populated areas were restricted. Therefore the flight trajectory was mainly above the sea, sampling an off-zenith beam of MAARSY. During the first flight a bus failure between the ALIX computer and the ADC was encountered, which forced us to

D.1 Sampling the transmission pattern of MAARSY

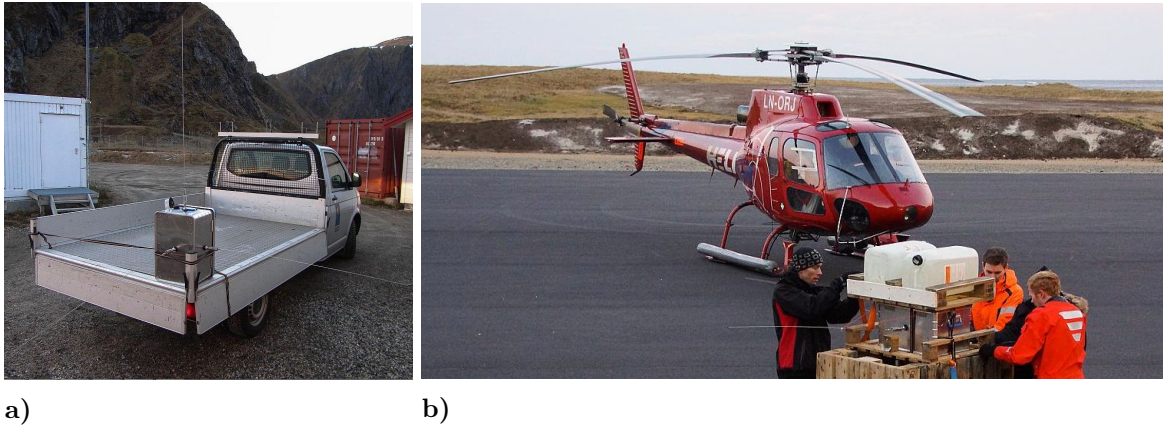


Figure D.4 a) Test setup of the airborne equipment on a car to perform test measurements around the MAARSY antenna array. b) Flight preparations of the equipment, mounting the antennas and stabilizing weights.

stop the experiment.

Unfortunately, this failure could not be reproduced in subsequent tests in an industrial deep freezer (-22°C) in the harbor of Andenes. Thus, it was assumed the failure was subjected to a loss of battery power due to poorly tightened clamps. However, the same failure has been seen during the second flight, but the setup recovered after lowering the altitude. Consequently, the altitude was kept for the rest of the flight at around 1300 m to ensure uninterrupted data.

In the analysis, the data was referenced to 1300 m height for all data points what is associated with range and thus intensity variations from the radar to the helicopter. The detected power was therefore corrected by the free-space path loss assumption. The detected power level during MAARSY's transmission pause was used to derive the background noise and to correct the power level during transmission to remove RF-interferences and potential instrument drifts.

The data of this analysis is depicted in Figures D.5 and D.6 as an overlay on the simulated near electric field computed with NEC for both pointing directions and 1300 m altitude. In both beam pointing directions a large dynamic range of detected power was observed, however a distinct spot of maximum power was not found. The broad appearance around the beam pointing is partially related to the low altitude, where the far field condition is not explicitly fulfilled. Thus, the individual radiations, especially of the most distant antennas, do not superpose perfectly in phase, which results in broadening and less intense maximum. Actually, at least two spots of high intensity can be seen in Figure D.5, where one is in fact related to the direct propagation, while the maximum around $x=y=1\text{km}$ is probably related to the superposition of the direct propagation of side lobes and another path. This seems to be valid also for the region $y=0\text{ km}$, $x=-1.5$ to 0 km . Furthermore, the regions of $y=1\text{ km}$, $x=-1.5$ to 0 km appear to be suspicious due to their absolute power in relation to power at the beam pointing direction. However, the intensity variation seen there (up to 20dB) indicates the presence of side lobes and nulls between them. The agreement to the near electric field contour at this specific region is rather good.

The source of the indirect component of the superposition is presumably caused by scattering off the close-by hills Andhue ($\approx 0.5\text{ km}$ south of MAARSY) and Røyken ($\approx 1.5\text{ km}$ southwest of MAARSY), which is schematically shown in Figure D.7. Even though the side

Appendix D Airborne near field measurements

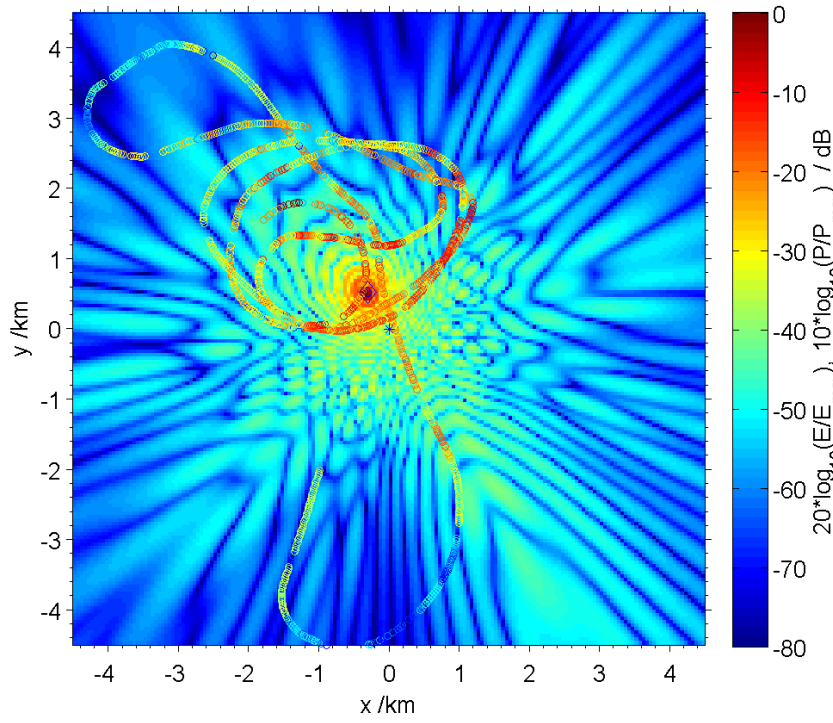


Figure D.5 Simulated near electric field and the corresponding detected intensities of the airborne equipment for a beam pointing to $\phi = 330^\circ, \theta = 25^\circ$.

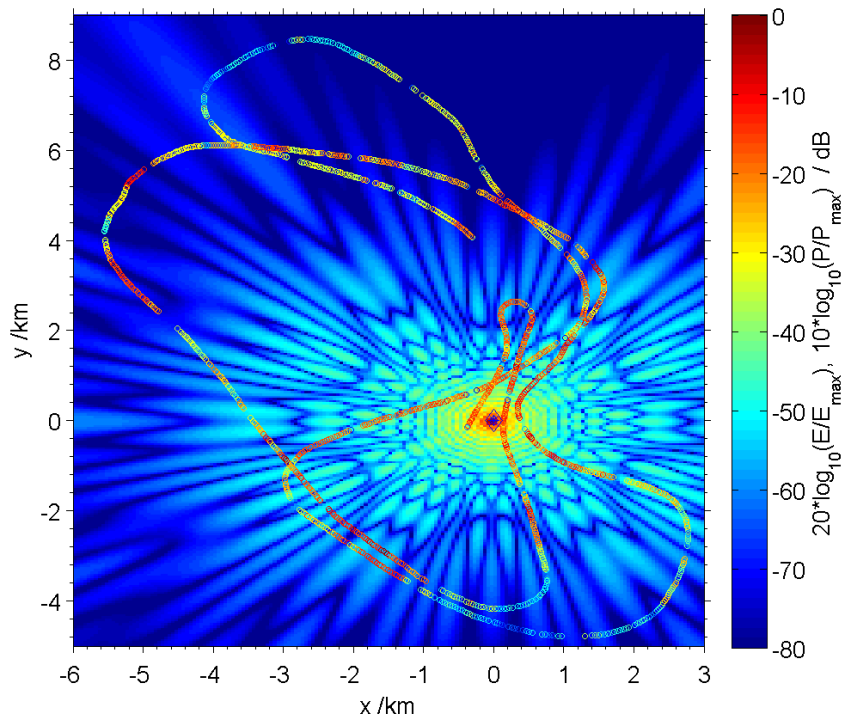


Figure D.6 Simulated near electric field and the corresponding detected intensities of the airborne equipment for a beam pointing to $\phi = 0^\circ, \theta = 0^\circ$.

D.1 Sampling the transmission pattern of MAARSY

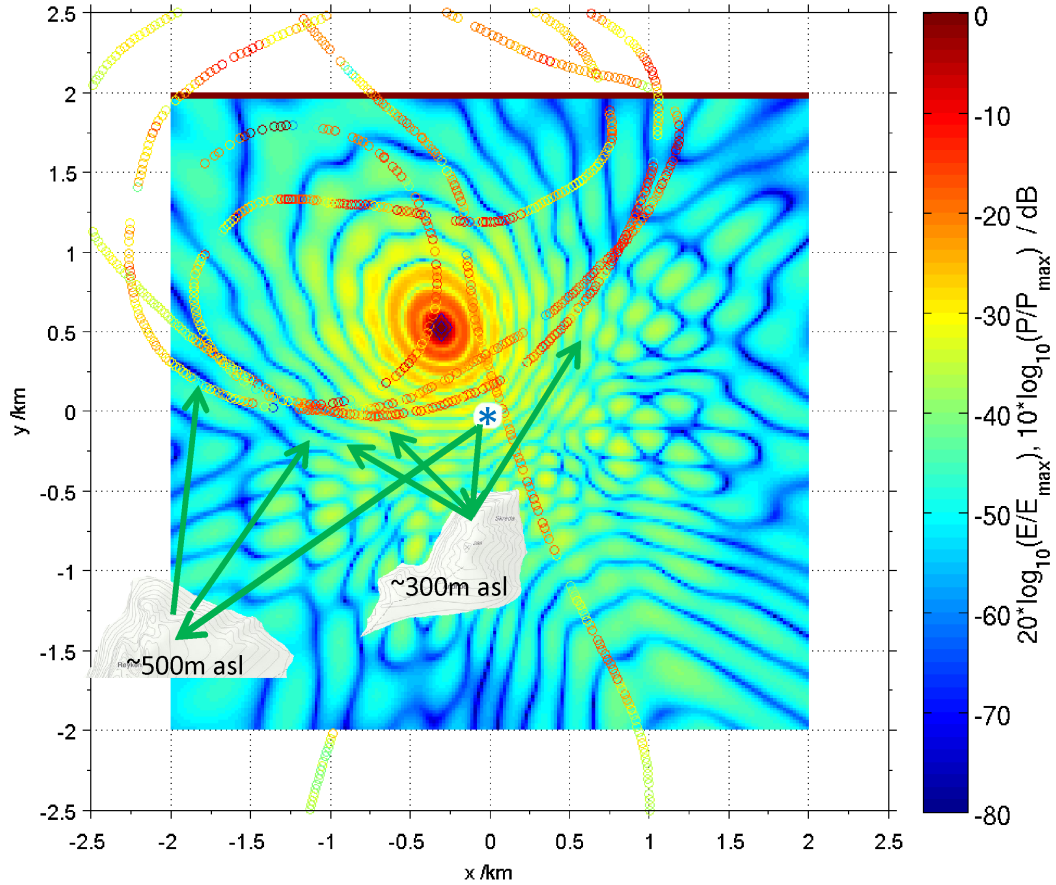


Figure D.7 Sketch of the likely source spoiling the sampled radiation pattern for the beam pointing to $\phi = 330^\circ, \theta = 25^\circ$, reflection and scattering off the nearby hills. The asterisk mark the position of the radar, while the arrows indicate the likely path of the clutter signals. Map sections taken from http://webhotel2.gisline.no/gislinewebinnsyn_vesteralen/.

lobes pointing to these hills are in the order of -30 dB and less, the integral of all side lobes facing the hills represents a significant amount of power. Additionally, clutter from the sea and other ground targets may have compromised the measurements as well, which is likely the cause for the increase in detected power at large distances (e.g. in Figure D.6 at $x=-5, y=4$ and nearby spots).

Besides the mentioned difficulties and challenges during the two flights, the project proved to be able to sample the radiation pattern of a radar like MAARSY. Performing the same experiment at higher altitudes, at least 3 km height, the measurements would be explicitly in the far field and also the clutter from the hills should be significantly decreased. One option to reach these demands is to place the device in an airplane, which would provide valuable information about the radars radiation pattern during transmission.

Bibliography

- Aarons, J. (1973), Total electron content and scintillation studies of the ionosphere, *NATO - Advisory Group for Aerospace Research & Development*, 166.
- Aarons, J. (1997), 50 years of radio scintillation observations, *IEEE Antennas and Propagation Magazine*, 39(6), 7–12, doi:10.1109/74.646785.
- Agafonov, M. I. (1996), Cassiopeia a flux density secular decrease and variations at metre wavelengths., *Astronomy and Astrophysics*, 306, 578–580.
- Agilent (2013), Noise figure measurement accuracy - the Y-factor method - application note 57-2, *Tech. rep.*, Agilent Technologies.
- Baars, J. W. M., R. Genzel, I. I. K. Pauliny-Toth, and A. Witzel (1977), The absolute spectrum of cas a; an accurate flux density scale and a set of secondary calibrators, *Astronomy and Astrophysics*, 61, 99–106.
- Balanis, C. A. (2005), *Antenna Theory*, 3. ed., John Wiley & Sons.
- Balsley, B. B., and K. S. Gage (1980), The MST radar technique - potential for middle atmospheric studies, *Pure and Applied Geophysics*, 118, 452–493, doi:10.1007/BF01586464.
- Banola, S., B. M. Pathan, D. R. K. Rao, and H. Chandra (2005), Spectral characteristics of scintillations producing ionospheric irregularities in the indian region, *Earth, Planets and Space*, 57, 47–59.
- Bartels, J., N. H. Heck, and H. F. Johnston (1939), The three-hour-range index measuring geomagnetic activity, *Journal of Geophysical Research*, 44(4), 411–454.
- Basu, S., E. MacKenzie, and S. Basu (1988), Ionospheric constraints on VHF/UHF communications links during solar maximum and minimum periods, *Radio Science*, 23, 363–378, doi:10.1029/RS023i003p00363.
- Basu, S., E. Kudeki, C. E. Valladares, E. J. Weber, H. P. Zengingonul, S. Bhattacharyya, R. Sheehan, M. A. Biondi, H. Kuenzler, and J. Espinoza (1996), Scintillations, plasma drifts, and neutral winds in the equatorial ionosphere after sunset, *Journal of Geophysical Research*, 101(A12), 26,795 – 26,809, doi:10.1029/96JA00760.
- Basu, S., E. J. Weber, T. W. Bullet, M. J. Keskinen, E. MacKenzie, P. Doherty, R. Sheehan, H. Kuenzler, P. Ning, and J. Bongiolatti (1998), Characteristics of plasma structuring in the cusp/cleft region at Svalbard, *Radio Science*, 33(6), 1885–1899, doi:10.1029/98RS01597.

- Baumgarten, G., J. Fiedler, F.-J. Lübken, and G. von Cossart (2008), Particle properties and water content of noctilucent clouds and their interannual variation, *Journal of Geophysical Research*, *113*, D06,203.
- Becker, E. (2004), Direct heating rates associated with gravity wave saturation, *Journal of Atmospheric and Solar-Terrestrial Physics*, *66*, 683–696, doi:10.1016/j.jastp.2004.01.019.
- Béniguel, Y., V. Romano, L. Alfonsi, M. Aquino, A. Bourdillon, P. Cannon, G. De Franceschi, S. Dubey, B. Forte, V. Gherm, N. Jakowski, M. Materassi, T. Noack, M. Pozoga, N. Rogers, P. Spalla, H. J. Strangeways, E. M. Warrington, A. Wernik, V. Wilken, and N. Zernov (2009), Ionospheric scintillation monitoring and modelling, *Annals of Geophysics*, *52*, 391–416, doi:10.4401/ag-4595.
- Bilitza, D. (2001), International reference ionosphere 2000, *Radio Science*, *36*(2), 261–275, doi:10.1029/2000RS002432.
- Boland, J. W., J. P. Hollinger, C. H. Mayer, and T. P. McCullough (1966), Polarization of Cygnus A, Taurus A and Cassiopeia A at 2.07 centimeters, *Astrophysical Journal*, *144*, 437–439.
- Bridle, A. H. (1967), Flux densities of Cassiopeia A and Cygnus A at 10.05 MHz, *The Observatory*, *87*, 60–63.
- Briggs, B. H. (1984), The analysis of spaced sensor records by correlation techniques, *MAP Handbook*, *13*, 166–186.
- Budden, K. G. (1961), *Radio Waves in the Ionosphere: the mathematical theory of the reflection of radio waves from the stratified ionised layers*, Cambridge University Press.
- Cane, H. (1978), A 30MHz map of the whole sky, *Australian Journal of Physics*, *31*, 561–565.
- Chau, J. L., and R. F. Woodman (2004), Observations of meteor-head echoes using the Jicamarca 50 MHz radar in interferometer mode, *Atmospheric Chemistry and Physics*, *4*(2), 511–521, doi:10.5194/acp-4-511-2004.
- Chau, J. L., D. L. Hysell, K. M. Kuyeng, and F. R. Galindo (2008), Phase calibration approaches for radar interferometry and imaging configurations: Equatorial spread f results, *Annales Geophysicae*, *26*, 2333–2343.
- Chau, J. L., F. R. Galindo, C. J. Heinselman, and M. J. Nicolls (2009), Meteor-head echo observations using an antenna compression approach with the 450 MHz Poker Flat Incoherent Scatter Radar, *Journal of Atmospheric and Solar-Terrestrial Physics*, *71*, 636–643, doi:10.1016/j.jastp.2008.08.007.
- Chau, J. L., J. Röttger, and M. Rapp (2013a), Pmse strength during enhanced D-region electron densities: Faraday rotation and absorption effects at VHF frequencies, *Journal of Atmospheric and Solar-Terrestrial Physics*, doi:http://dx.doi.org/10.1016/j.jastp.2013.06.015.
- Chau, J. L., T. Renkowitz, G. Stober, and R. Latteck (2013b), MAARSY multiple receiver phase calibration using radio sources, *Journal of Atmospheric and Solar-Terrestrial Physics*, doi:10.1016/j.jastp.2013.04.004.

Bibliography

- Cohen, A. S., W. M. Lane, W. D. Cotton, N. E. Kassim, L. T. J. W., R. A. Perley, J. J. Condon, and W. C. Erickson (2007), The VLA Low-frequency Sky Survey, *Astrophysics*, *134*, 1245–1262.
- Crane, R. (1974), Morphology of ionospheric scintillation, *12th Aerospace Sciences Meeting*, doi:10.2514/6.1974-52.
- Czechowsky, P., R. Rüster, and G. Schmidt (1979), Variations of mesospheric structures in different seasons, *Geophysical Research Letters*, *6*, 459–462, doi:10.1029/GL006i006p00459.
- Czechowsky, P., G. Schmidt, and R. Rüster (1984), The mobile soussy doppler radar: Technical design and first results, *Radio Science*, *19*, 441–450.
- Czechowsky, P., I. M. Reid, R. Rüster, and G. Schmidt (1989), VHF radar echoes observed in the summer and winter polar mesosphere over Andoya, *Journal of Geophysical Research*, *94*, 5199–5217, doi:10.1029/JD094iD04p05199.
- de Oliveira-Costa, A., M. Tegmark, B. M. Gaensler, J. Jonas, T. L. Landecker, and P. Reich (2008), A model of diffuse galactic radio emission from 10 MHz to 100 GHz, *Monthly Notices of the Royal Astronomical Society*, *338*, 247–260, doi:10.1111/j.1365-2966.2008.13376.x.
- de Vos, M., A. W. Gunst, and R. Nijboer (2009), The LOFAR Telescope: System Architecture and Signal Processing, *Proceedings of the IEEE*, *97*, 1431–1437, doi:10.1109/JPROC.2009.2020509.
- del Pozo, C. F., F. Honary, N. Stamatiou, and M. Kosch (2002), Study of auroral forms and electron precipitation with the iris, dasi and eiscat systems, *Annales Geophysicae*, *20*, 1361–1375, doi:10.5194/angeo-20-1361-2002.
- Detlefsen, J., and U. Siart (2006), *Grundlagen der Hochfrequenztechnik*, 2nd ed., R. Oldenbourg Verlag, München.
- Doviak, R. J., R. J. Lateaitis, and C. L. Holloway (1996), Cross correlations and cross spectra for spaced antenna wind profilers - 1. Theoretical Analysis, *Radio Science*, *31*, 157–180.
- Downs, G. S., and A. R. Thomson (1972), The distribution of linear polarization in Casiopeia A at wavelengths of 9.8 and 11.1 cm, *The Astronomical Journal*, *77*, 120–133.
- Dyrud, L., and D. Janches (2008), Modeling the meteor head echo using Arecibo radar observations, *Journal of Atmospheric and Solar-Terrestrial Physics*, *70(13)*, 1621–1632, doi:10.1016/j.jastp.2008.06.016.
- Ecklund, W. L., and B. B. Balsley (1981), Long-term observations of the Arctic mesosphere with the MST radar at Poker Flat, Alaska, *Journal of Geophysical Research*, *86*, 7775–7780, doi:10.1029/JA086iA09p07775.
- Ellingson, S. W., G. Taylor, J. Craig, J. Hartman, J. Dowell, C. Wolfe, T. E. Clarke, B. C. Hicks, N. E. Kassim, P. S. Ray, L. J. Rickard, F. K. Schinzel, and K. Weiler (2013), The LWA1 Radio Telescope, *IEEE Transactions on Antennas and Propagation*, *61*, 2540–2549.
- European Space Agency (2012), ENVISAT mission website, ESA EO Missions, web access, <https://earth.esa.int/web/guest/missions/esa-operational-eo-missions/envisat>.

- Evans, J. V., and G. H. Pettengill (1963a), The scattering properties of the lunar surface at radio wave lengths, in *The Moon, Meteorites and Comets*, edited by G. P. Kuiper and B. Middlehurts, p. 129, Chicago: The University of Chicago Press.
- Evans, J. V., and G. H. Pettengill (1963b), The scattering behavior of the Moon at wavelengths of 3.6, 68, and 784 centimeters, *Journal of Geophysical Research*, *68*(2), 423–447, doi:10.1029/JZ068i002p00423.
- Franke, S. J., J. Röttger, and C. LaHoz (1992), Frequency domain interferometry of polar mesosphere summer echoes with the EISCAT VHF radar: A case study, *Radio Science*, *27*, 417–428.
- Friedrich, M., M. Harrich, K. Torkar, and P. Stauning (2002), Quantitative measurements with wide-beam riometers, *Journal of Atmospheric and Solar-Terrestrial Physics*, *64*, 359–365.
- Friis, H. T. (1944), Noise figures of radio receivers, *Proceedings of the Institute of Radio Engineers*, *32*, 419–422.
- Friis, H. T. (1946), A note on a simple transmission formula, *Proceedings of the Institute of Radio Engineers*, *34*(5), 254–256.
- Fukao, S., S. Kato, T. Aso, M. Sasada, and T. Makihira (1980), Middle and upper atmosphere radar (mur) under design in japan, *Radio Science*, *20*(6), 225–231.
- Fukao, S., T. Sato, T. Tsuda, S. Kato, K. Wakasugi, and T. Makihira (1985a), The MU radar with an active phased array system: 1. Antenna and power amplifiers, *Radio Science*, *20*(6), 1155–1168, doi:doi:10.1029/RS020i006p01155.
- Fukao, S., T. Tsuda, T. Sato, S. Kato, K. Wakasugi, and T. Makihira (1985b), The MU radar with an active phased array system: 2. In-house equipment, *Radio Science*, *20*(6), 1169–1176, doi:doi:10.1029/RS020i006p01169.
- Fukao, S., H. Hashiguchi, M. Yamamoto, T. Tsuda, T. Nakamura, and M. K. Yamamoto (2003), Equatorial Atmosphere Radar (EAR): System description and first results, *Radio Science*, *3*, 19/1–19/17, doi:10.1029/2002RS002767.
- Gancarz, R. (2010), Development of radar beam configurations for meteor experiments with the atmospheric sounding radar MAARSY, Master’s thesis, University of applied sciences Wismar.
- Garcia, R. R., and S. Solomon (1985), The effect of breaking gravity waves on the dynamics and chemical composition of the mesosphere and lower thermosphere, *Journal of Geophysical Research*, *20*, 3850–3868.
- GFZ Helmholtz Centre Potsdam (2014), Indices of global geomagnetic activity, web/FTP access, http://www-app3.gfz-potsdam.de/kp_index/ftppreferences.html.
- Giraud, A. (1965), A Note on the Radio Reflectivity of the Lunar Surface, in *Symposium on Planetary Atmospheres and Surfaces*, vol. 69D(12), edited by S. D. R. S. Journal of Research of the National Bureau of Standards, pp. 1677–1681, National Bureau of Standards.

Bibliography

- Green, D. A. (2009), A Catalogue of Galactic Supernova Remnants (2009 March version), *Bulletin of the Astronomical Society of India*, 37.
- Haldoupis, C. (2011), A Tutorial Review on Sporadic E Layers, *Aeronomy of the Earth's Atmosphere and Ionosphere IAGA Special Sopron Book Series*, 2, 381–394, doi:10.1007/978-94-007-0326-1_29.
- Hall, P. J., R. T. Schilizzi, P. E. F. Dewdney, and T. J. W. Lazio (2008), The Square Kilometer Array (SKA) Radio Telescope: Progress and Technical Directions, *Radio Science Bulletin*, 326, 4–19.
- Harrich, M., M. Friedrich, S. Marple, and K. Torkar (2003), The background absorption at high latitudes, *Advances in Radio Science*, 1, 325–327.
- Haslam, C. G. T., W. E. Wilson, D. A. Graham, and G. C. Hunt (1974), A further 408 MHz survey of the northern sky, *Astronomy and Astrophysics Supplement Series*, 13, 359–394.
- Haslam, C. G. T., U. Klein, C. J. Salter, H. Stoffel, W. E. Wilson, M. N. Cleary, D. J. Cooke, and P. Thomasson (1981), A 408 MHz all-sky continuum survey. I - Observations at southern declinations and for the North Polar region, *Astronomy and Astrophysics*, 100-2, 209–219.
- Haslam, C. G. T., C. J. Salter, H. Stoffel, and W. E. Wilson (1982), A 408 MHz all-sky continuum survey. II - The atlas of contour maps, *Astronomy and Astrophysics Supplement Series*, 47, 1–143.
- Helmboldt, J., and N. Kassim (2009), The evolution of Cassiopeia A at low radio frequencies, *The Astronomical Journal*, 138, 838–844.
- Helmboldt, J. F., N. E. Kassim, A. S. Cohen, W. M. Lane, and L. T. J. (2008), Radio frequency spectra of 388 bright 74 MHz sources, *The Astrophysical Journal Supplement Series*, 174, 313–336.
- Hocking, W. K. (1985), Measurement of turbulent energy dissipation rates in the middle atmosphere by radar techniques: A review, *Radio Science*, 20(6), 1403–1422, doi:10.1029/RS020i006p01403.
- Hocking, W. K., and J. Röttger (1997), Studies of polar mesosphere summer echoes over EISCAT using calibrated signal strengths and statistical parameters, *Radio Science*, 32(4), 1425–1444, doi:10.1029/97RS00716.
- Hocking, W. K., M. Kelley, R. Rogers, W. O. J. Brown, D. Moorcroft, and J.-P. S. Maurice (2001), Resolute Bay VHF radar: A multipurpose tool for studies of tropospheric motions, middle atmosphere dynamics, meteor physics, and ionospheric physics, *Radio Science*, 36(6), 1839–1857, doi:10.1029/2000RS001005.
- Holloway, C. L., R. J. Doviak, S. A. Cohn, E. Lataitis, and J. S. van Baelen (1997), Cross correlations and cross spectra for spaced antenna wind profilers: 2. Algorithms to estimate wind and turbulence, *Radio Science*, 32, 967–982, doi:10.1029/96RS03885.
- IAGA, International Association of Geomagnetism and Aeronomy, Working Group V-MOD. Participating members, C. C. Finlay, S. Maus, C. D. Beggan, T. N. Bondar, A. Chambodut, T. A. Chernova, A. Chulliat, V. P. Golovkov, B. Hamilton, M. Hamoudi, R. Holme,

- G. Hulot, W. Kuang, B. Langlais, V. Lesur, F. J. Lowes, H. Lühr, S. Macmillan, M. Manda, S. McLean, C. Manoj, M. Menvielle, I. Michaelis, N. Olsen, J. Rauberg, M. Rother, T. J. Sabaka, A. Tangborn, L. Tøffner-Clausen, E. Thébaud, A. W. P. Thomson, I. Wardinski, Z. Wei, and T. I. Zvereva (2010), International Geomagnetic Reference Field: the eleventh generation, *Geophysical Journal International*, *183*(3), 1216–1230, doi:10.1111/j.1365-246X.2010.04804.x.
- ITU (2000), Determination of the G/T ratio for earth stations operating in the fixed-satellite service - Recommendation ITU-R S.733-2, *Tech. rep.*, International Telecommunication Union.
- ITU (2012), The radio refractive index: its formula and refractivity data - Recommendation ITU-R P.453-10, *Tech. rep.*, International Telecommunication Union.
- Janches, D., J. D. Mathews, D. D. Meisel, and Q. H. Zhou (2000), Micrometeor observations using the Arecibo 430MHz radar I. Determination of ballistic parameter from measured Doppler velocity and deceleration results, *Icarus*, *145* (2), 53–63, doi:10.1006/icar.1999.6330.
- Jansky, K. G. (1933), Radio waves from outside the solar system, *Nature*, *132*, 66.
- Jiao, Y., Y. T. Morton, S. Taylor, and W. Pelgrum (2013), Characterization of high-latitude ionospheric scintillation of GPS signals, *Radio Science*, *48*, 698–708, doi:10.1002/2013RS005259.
- Johnson, R. C. (1993), *Antenna engineering handbook*, third ed., Mc Graw-Hill.
- Jones, J., A. R. Webster, and W. K. Hocking (1998), An improved interferometer design for use with meteor radars, *Radio Science*, *33*, 55–65.
- Kassim, N. E., T. Joseph, W. Lazio, W. Erickson, R. A. Perley, W. D. Cotton, E. W. Greisen, A. S. Cohen, B. Hicks, H. R. Schmitt, and D. Katz (2007), The 74 MHz System on the Very Large Array, *The Astrophysical Journal Supplement Series*, *172*, 686–719, doi:doi:10.1086/519022.
- Kato, S., T. Ogawa, T. Tsuda, I. Kimura, and S. Fukao (1984), The middle and upper atmosphere radar: First results using a partial system, *Radio Science*, *19*(6), 1475–1484, doi:10.1029/RS019i006p01475.
- Kero, J., C. Szasz, T. Nakamura, T. Terasawa, H. Miyamoto, and K. Nishimura (2012), A meteor head echo analysis algorithm for the lower VHF band, *Annales Geophysicae*, *30*(4), 639–659, doi:10.5194/angeo-30-639-2012.
- Kirkwood, S., A. Rechou, K. Stebel, V. Barabash, P. Chilson, L. Marcus, and P. Olsen (1997), Wind profiling with ESRAD, the ESRAD MST radar, in *proceedings of the COST-76 workshop*.
- Kraus, J. D. (1986), *Radio Astronomy*, 2nd ed., Cygnus-Quasar.
- Kraus, J. D. (1997), *Antennas*, 2nd ed., Tata McGraw-Hill.
- Kudeki, E., and G. R. Stitt (1987), Frequency domain interferometry: A high-resolution radar technique for studies of atmospheric turbulence, *Geophysical Research Letters*, *14*, 198–201.

Bibliography

- Kühr, H., A. Witzel, I. I. K. Pauliny-Toth, and U. Nauber (1981), A catalogue of extragalactic radio sources having flux densities greater than 1 Jy at 5 GHz, *Astronomy and Astrophysics, Supplement Series*, 45, 367–430.
- Kuz'min, A. (1966), *Radioastronomical Methods of Antenna Measurements*, Academic Press.
- Laing, R. A., J. M. Riley, and M. S. Longair (1983), Bright radio sources at 178 MHz - Flux densities, optical identifications and the cosmological evolution of powerful radio galaxies, *Monthly Notices of the Royal Astronomical Society*, 204, 151 – 187.
- Latteck, R., and J. Bremer (2013), Occurrence frequencies of polar mesosphere summer echoes observed at 69° N during a full solar cycle, *Advances in Radio Science*, 11, 327–332, doi:10.5194/ars-11-327-2013.
- Latteck, R., W. Singer, and H. Bardey (1999), The ALWIN MST radar - Technical design and performances, *Proceedings of the 14th ESA Symposium on European Rocket and Balloon Programmes and Related Research*.
- Latteck, R., W. Singer, S. Kirkwood, R. J. Morris, D. Holdsworth, and N. Swarnalingam (2007), Absolute calibration of VHF radars using a calibrated noise source and an ultrasonic delay line, *Proceedings of the 11th International Workshop on technical and Scientific Aspects of MST radars*.
- Latteck, R., W. Singer, R. J. Morris, W. K. Hocking, D. J. Murphy, D. A. Holdsworth, and N. Swarnalingam (2008), Similarities and differences in polar mesosphere summer echoes observed in the Arctic and Antarctica, *Annales Geophysicae*, 26, 2795–2806.
- Latteck, R., W. Singer, M. Rapp, B. Vandeppeer, T. Renkwitz, M. Zecha, and G. Stober (2012), The new MST radar on Andøya: System description and first results, *Radio Science*, 47, doi:10.1029/2011RS004775.
- Lazio, T. J. W., A. S. Cohen, N. E. Kassim, R. A. Perley, W. C. Erickson, C. L. Carilli, and P. C. Crane (2006), Cygnus A: A Long Wavelength Resolution of the Hot Spots, *Astrophysics Journal*, pp. 1–7, doi:10.1086/504408.
- Li, Q. (2011), Multi-frequency radar observations of polar mesosphere summer echoes: Statistical properties and microphysical results, Ph.D. thesis, University of Rostock.
- Li, Q., M. Rapp, J. Röttger, R. Latteck, M. Zecha, I. Strelnikova, G. Baumgarten, M. Hervig, C. Hall, and M. Tsutsumi (2010), Microphysical parameters of mesospheric ice clouds derived from calibrated observations of polar mesosphere summer echoes at Bragg wavelengths of 2.8 m and 30 cm, *Journal of Geophysical Research*, 115, D00I13, doi:10.1029/2009JD012271.
- Lübken, F.-J. (1999), Thermal structure of the Arctic summer mesosphere, *Journal of Geophysical Research*, 104, 9135–9149, doi:10.1029/1999JD900076.
- Lübken, F.-J., M. Rapp, and P. Hoffmann (2002), Neutral air turbulence and temperatures in the vicinity of polar mesosphere summer echoes, *Journal of Geophysical Research*, 107(D15).

- Lübken, F.-J., B. Strelnikov, M. Rapp, W. Singer, R. Latteck, A. Brattli, U.-P. Hoppe, and M. Friedrich (2006), The thermal and dynamical state of the atmosphere during polar mesosphere winter echoes, *Atmospheric Chemistry and Physics*, *6*, 13–24.
- Lübken, F.-J., W. Singer, R. Latteck, and I. Strelnikova (2007), Radar measurements of turbulence, electron densities, and absolute reflectivities during polar mesosphere winter echoes (PMWE), *Advances in Space Research*, *40*(6), 758–764, doi:10.1016/j.asr.2007.01.015.
- Maeda, K., H. Alvarez, J. Aparic, J. May, and P. Reich (1999), A 45-MHz continuum survey of the northern hemisphere, *Astronomy and Astrophysics Supplement Series*, *140*, 145–154.
- Mailloux, R. J. (1994), *Phased Array Antenna Handbook*, vol. 1, 1. ed., Artech House London.
- Mayer, C. H., and J. P. Hollinger (1968), Polarized brightness distribution over Cassiopeia A, the Crab Nebula, and Cygnus A at 1.55-cm wavelength, *Astrophysical Journal*, *151*, 53–63.
- McKean, J. (2011), Multi-frequency imaging of Cygnus A with LOFAR, in *LOFAR Workshop*.
- McKean, J. (2013), estimated flux density of Cygnus A, private communication.
- McKean, J., L. Ker, R. J. van Weeren, F. Batejat, L. Birzan, A. Bonafede, J. Conway, F. De Gasperin, C. Ferrari, G. Heald, N. Jackson, G. Macario, E. Orr, R. Pizzo, D. Rafferty, H. Rottgering, A. Shulevski, C. Tasse, S. van der Tol, I. van Bemmelen, G. van Diepen, and J. E. van Zwieten (2011), LOFAR: Early imaging results from commissioning for Cygnus A, *Proceedings - 10th European VLBI Network Symposium and EVN Users Meeting: VLBI and the new generation of radio arrays*.
- Morris, R. J., A. R. Klekociuk, and D. A. Holdsworth (2011), First observations of southern hemisphere polar mesosphere winter echoes including conjugate occurrences at $\approx 69^\circ\text{S}$ latitude, *Geophysical Research Letters*, *38*, L03811, doi:10.1029/2010GL046298.
- Olsen, P.-E., L. Marcus, and S. Kirkwood (1997), ESRAD, Esrange MST radar, in *Proceedings of the 13th ESA Symposium, Öland, Sweden*, vol. ESA SP-397, pp. 267–270.
- Otsuka, Y., K. Shiokawa, M. Nishioka, and Effendy (2012), VHF radar observations of post-midnight F-region field-aligned irregularities over Indonesia during solar minimum, *Indian Journal of Radio & Space Physics*, *41*, 199–207.
- Palmer, R. D., R. F. Woodman, S. Fukao, M. F. Larsen, M. Yamamoto, T. Tsuda, and S. Kato (1990), Frequency domain interferometry observations of tropo/stratospheric scattering layers using the MU radar: Description and first results, *Geophysical Research Letters*, *17*, 2189–2192.
- Palmer, R. D., S. Vangal, M. F. Larsen, S. Fukao, T. Nakamura, and M. Yamamoto (1996), Phase calibration of VHF spatial interferometry radars using stellar sources, *Radio Science*, *31*, 147–156, doi:DOI:10.1029/95RS02319.
- Pellinen-Wannberg, A. (2005), Meteor head echoes - observations and models, *Annales Geophysicae*, *23*(1), 201–205, doi:10.5194/angeo-23-201-2005.

Bibliography

- Pellinen-Wannberg, A., and G. Wannberg (1994), Meteor observations with the European Incoherent Scatter UHF Radar, *J. Geophys. Res.*, *99(A6)*, 11,379–11,390, doi:10.1029/94JA00274.
- Priese, J. (1964), Über die Ermittlung der Antenneneigenschaften des Adlershofer 36-m-Radioteleskopes bei einer Wellenlänge von 53,67 cm, *Hochfrequenztechnik und Elektrotechnik*, *73*, 79–90.
- Rao, A. P. (2003), Ionospheric effects in radio astronomy, web access, chapter 16 of the Giant Metrewave Radio Telescope (GMRT) of the Tata Institute of Fundamental Research , India, User Observing Help <http://www.ncra.tifr.res.in/ncra/gmrt/gmrt-users/observing-help-for-gmrt-users/low-frequency-radio-astronomy/ch16.pdf>.
- Rapp, M., and F.-J. Lübken (2004), Polar mesosphere summer echoes (PMSE): review of observations and current understanding, *Atmospheric Chemistry and Physics*, *4*, 2601–2633, doi:10.5194/acp-4-2601-2004.
- Rapp, M., L. Leitert, R. Latteck, M. Zecha, P. Hoffmann, J. Höffner, U.-P. Hoppe, C. La Hoz, and E. V. Thrane (2011a), Localized mesosphere-stratosphere-troposphere radar echoes from the E-region at 69° N: Properties and physical mechanism, *J. Geophys. Res.*, *116*, A02320, doi:10.1029/2010JA016167.
- Rapp, M., R. Latteck, G. Stober, P. Hoffmann, W. Singer, and M. Zecha (2011b), First three-dimensional observations of polar mesosphere winter echoes: Resolving space-time ambiguity, *Journal of Geophysical Research*, *116*, A11307, doi:10.1029/2011JA016858.
- Rapp, M., I. Strelnikova, Q. Li, N. Engler, and G. Teiser (2012), Charged aerosol effects on the scattering of radar waves from the D-region, in *Climate And Weather of the Sun-Earth System (CAWSES): Highlights from a priority program*, edited by F.-J. Lübken, Springer, Dordrecht, The Netherlands, doi:10.1007/978-94-007-4348-9.
- Reber, G. (1940), Cosmic static, *Astrophysical Journal*, *91*, 621.
- Reich, P., W. Reich, and E. Fürst (1997), The Effelsberg 21cm radio continuum survey of the Galactic plane between $l=95.5^\circ$ and $l=240^\circ$, *Astronomy and Astrophysics Supplement Series*, *126*, 413–435.
- Renkowitz, T. (2008), Analysis and Optimisation of Medium Gain X-Yagi Antennas for the EISCAT_3D 237.5 MHz Incoherent Scatter Radar Active Array, Master's thesis, University Rostock.
- Renkowitz, T., W. Singer, R. Latteck, and M. Rapp (2011), Multi beam observations of cosmic radio noise using a VHF radar with beam forming by a Butler matrix, *Advances in Radio Science*, *9*, 1–9, doi:10.5194/ars-9-349-2011.
- Renkowitz, T., W. Singer, R. Latteck, G. Stober, and M. Rapp (2012), Validation of the radiation pattern of the Middle Atmosphere Alomar Radar System (MAARSY), *Advances in Radio Science*, *10*, 245–253, doi:10.5194/ars-10-245-2012.
- Renkowitz, T., G. Stober, R. Latteck, W. Singer, and Rapp (2013a), New experiments to validate the radiation pattern of the Middle Atmosphere Alomar Radar System (MAARSY), *Advances in Radio Science*, *11*, 283–289, doi:10.5194/ars-11-283-2013.

- Renkwitz, T., R. Latteck, W. Singer, and G. Stober (2013b), Validation of the receiving pattern of the MAARSY phased antenna array, *Proceedings of the 13th International Workshop on technical and Scientific Aspects of MST radars*.
- Riahi, N. (2002), Cassiopeia A Flux Density Measured with APRAXOS, *Tech. rep.*, Institute of Astronomy, ETH Zürich.
- Rickett, B. J., and W. A. Coles (2000), Scattering in the Solar Wind at Long Wavelength, in *Radio Astronomy at Long Wavelength*, pp. 97–104, Stone, Weiler, Goldstein, Bougeret.
- Roger, R. S., C. H. Costain, T. L. Landecker, and C. M. Swerdlyk (1999), The radio emission from the Galaxy at 22 MHz, *Astronomy and Astrophysics Supplement Series*, 137, 7–19.
- Rohde & Schwarz (1966), *Instruction Book, Noise Generator, Type SKTU*, Rohde & Schwarz, r 8508/663 ed.
- Röttger, J. (1980), Reflection and scattering of VHF radar signals from atmospheric refractivity structures, *Radio Science*, 15(2), 259–276.
- Sato, K., M. Tsutsumi, T. Sato, T. Nakamura, A. Saito, Y. Tomikawa, K. Nishimura, H. Yamagishi, and T. Yamanouchi (2011), Program of the Antarctic Syowa MST/IS Radar (PANSY), *Stratospheric Processes and Their Role in Climate*, 36, 23–26.
- Sato, T., T. Nakamura, and K. Nishimura (2000), Orbit Determination of Meteors Using the MU Radar, *IEICE Trans. Commun.*, E83-B, 1990–1995.
- Schult, C., G. Stober, J. L. Chau, and R. Latteck (2013), Determination of meteor-head echo trajectories using the interferometric capabilities of MAARSY, *Ann. Geophys.*, 31, 1843–1851, doi:10.5194/angeo-31-1843-2013.
- Senior, T. B. A., K. M. Siegel, and A. Giraud (1962), Some physical constants of the lunar surface, as indicated by its radar scattering and thermal emission properties, in *The Moon*, edited by Z. Kopal and Z. K. Mikhailov, IAU SYMPOSIUM 14, pp. 533–544.
- Singer, W., R. Latteck, M. Friedrich, P. Dalin, S. Kirkwood, N. Engler, and D. Holdsworth (2005), D-region electron densities obtained by differential absorption and phase measurements with a 3-MHz Doppler radar, *17th ESA Symposium on European Rocket and Balloon Programmes and Related Research*, pp. 233–238.
- Singer, W., R. Latteck, M. Friedrich, M. Wakabayashi, and M. Rapp (2011), Seasonal and solar activity variability of D-region electron density at 69°N, *Journal of Atmospheric and Solar-Terrestrial Physics*, 73(9), 925–935, doi:http://dx.doi.org/10.1016/j.jastp.2010.09.012.
- Skolnik, M. I. (2008), *Radar handbook*, 3 ed., McGraw-Hill, iISBN 978-0-07-148547-0.
- Stirner, E. (1984), *Antennen, Grundlagen*, vol. 1, 2. ed., Hüthig.
- Stober, G., W. Singer, and C. Jacobi (2011), Cosmic radio noise observations using a mid-latitude meteor radar, *Journal of Atmospheric and Solar-Terrestrial Physics*, 73, 1069–1076, doi:10.1016/j.jastp.2010.07.018.

Bibliography

- Stober, G., S. Sommer, M. Rapp, and R. Latteck (2013a), Investigation of gravity waves using horizontally resolved radial velocity measurements, *Atmospheric Measurement Techniques*, *6*, 2893–2905, doi:10.5194/amt-6-2893--2013.
- Stober, G., C. Schuldt, C. Baumann, R. Latteck, and M. Rapp (2013b), The Geminid meteor shower during the ECOMA sounding rocket campaign: specular and head echo radar observations, *Annales Geophysicae*, *31*, 473–487, doi:10.5194/angeo-31-473-2013.
- Strelnikova, I., and M. Rapp (2013), Statistical characteristics of PMWE observations by the EISCAT VHF radar, *Annales Geophysicae*, *31*, 359–375, doi:10.5194/angeo-31-359-2013.
- Taylor, G., S. W. Ellingson, N. Kassim, J. Craig, J. Dowell, C. N. Wolfe, J. Hartman, G. Bernardi, T. Clarke, A. Cohen, N. P. Dalal, W. C. Erickson, B. Hicks, L. J. Greenhill, B. Jacoby, W. Lane, J. Lazio, D. Mitchell, R. Navarro, S. M. Ord, Y. Pihlstrom, E. Polisensky, P. S. Ray, L. J. Rickard, F. K. Schinzel, H. Schmitt, M. Sigman, E. Soriano, K. P. Stewart, K. Stovall, S. Tremblay, D. Wang, K. W. Weiler, S. White, and D. L. Wood (2012), First light for the first station of the long wavelength array, *Astrophysics*, pp. 1–29.
- Tiwari, S., A. Jain, S. Sarkar, S. Jain, and A. K. Gwal (2012), Ionospheric irregularities at Antarctic using GPS measurements, *Journal of Earth System Science*, *121*(2), 345–353, doi:10.1007/s12040-012-0168-8.
- Tromsø Geophysical Observatory (2014), Geomagnetic data, magnetometer online access, K-indices and means' values, web access, <http://flux.phys.uit.no/geomag.html>.
- University of Tromsø (2014), MORRO radar, department of physics and technology, website, <http://tupac.phys.uit.no/cesar/MORROradarSite/MORROradar.html>.
- Viezbicke, P. P. (1976), Yagi antenna design, *Tech. rep.*, U.S. Department of Commerce, National Bureau of Standards.
- Vincent, R. A., P. T. May, W. K. Hocking, W. G. Elford, B. H. Candy, and B. H. Briggs (1987), First results with the Adelaide VHF radar: Spaced antenna studies of tropospheric winds, *Journal of Atmospheric and Solar-Terrestrial Physics*, *49*, 353–366.
- Vinyajkin, E., and V. Razin (2004), Secular Decrease and Random Variations of Cassiopeia A at 151.5 and 927 MHz, *Astrophysics*, arXiv:astro-ph/0412593v1.
- Visessiri, K., V. Torchakul, N. Leelaruij, and N. Hemmakorn (2004), Observation of VHF Ionospheric Scintillation and Impact on Satellite Communication, *International Conference on Electrical Engineering/Electronics, Computer, Telecommunications and Information*.
- VLSS Remote Sensing Division (2014), The VLSS Bright Source Spectral Calculator, web access, <http://www.nrl.navy.mil/rsd/vlss/calspec/>; referring to the VLSS Bright Source Spectral Catalog (VBSSC), Helmboldt et. al (2008).
- Weiler, W., K. (2000), The Promise of Long Wavelength Radio Astronomy, in *Radio Astronomy at Long Wavelength*, pp. 243–255, Stone, Weiler, Goldstein, Bougeret.
- Whitney, H. E., and S. Basu (1977), The effect of ionospheric scintillation on VHF/UHF satellite communications, *Radio Science*, *12*, 123–133, doi:10.1029/RS012i001p00123.

- Woodman, R. F. (1971), Inclination of the geomagnetic field measured by an incoherent scatter technique, *Journal of Geophysical Research*, *76*, 178–184.
- Woodman, R. F., and A. Guillen (1974), Radar observations of winds and turbulence in the stratosphere and mesosphere, *Journal of the Atmospheric Sciences*, *31*, 493–505.
- Xu, L., J.-S. Xu, Y.-H. Zhu, and S.-M. Li (2009), Gps measurements of ionospheric irregularity drifts and their initial results, *Chinese Journal of Geophysics*, *52(1)*, 1–12.
- Yamamoto, M., S. Fukao, R. F. Woodman, T. Ogawa, T. Tsuda, and S. Kato (1991), Mid-latitude E region field-aligned irregularities observed with the MU radar, *Journal of Geophysical Research*, *96(A9)*, 15,943–15,949.
- Yatawatta, S. (2008), LOFAR calibration and imaging results, online available presentation.
- Zeller, O., M. Zecha, J. Bremer, R. Latteck, and W. Singer (2006), Mean characteristics of mesosphere winter echoes at mid- and high-latitudes, *J. Atmos. Solar Terr. Phys.*, *68(10)*, 1087–1104, doi:10.1016/j.jastp.2006.02.015.

List of Acronyms, Abbreviations, and Symbols

Acronyms

ADC	analogue-digital converter
ALOMAR	Arctic Lidar Observatory for Middle Atmosphere Research
ALWIN	ALomar WINd radar
ALWIN64	remainder of the ALWIN antenna array of 64 Yagi antennas
AMISR	Advanced Modular Incoherent Scatter Radar
ARR	Andøya Rocket Range
BB	baseband position
CasA	Cassiopeia A
CygA	Cygnus A
DBS	Doppler Beam Swinging
DDS	direct digital synthesis
DRAO	Dominion Radio Astrophysical Observatory
EAR	Equatorial Atmospheric Radar
EISCAT	European Incoherent SCATter, Scientific Association
EISCAT_3D	Project name of a planned radar system, successor of the existing EISCAT VHF mainland system
ENR	excess noise ratio of a noise source
FCA	Full Correlation Analysis
FDI	Frequency Domain Interferometry
GNEC	Windows based NEC software package
GPS	Global Positioning System, a satellite navigation system
GSM	Global Sky temperature Model by (<i>de Oliveira-Costa et al.</i> , 2008)
I/Q	in-phase and quadrature component of a complex signal
IAP	Leibniz-Institute of Atmospheric Physics e.V. at University of Rostock
IF	intermediate frequency
IFSCU	intermediate frequency switching and combining unit of MAARSY
ITU	International Telecommunication Union

List of Acronyms, Abbreviations, and Symbols

LOFAR	LOw Frequency ARray for Radio astronomy, built by ASTRON, Netherlands
LST	local sidereal time
LWA	Long Wavelength Array, New Mexico/USA
MAARSY	Middle Atmosphere Alomar Radar SYstem
MAARSY343	MAARSY antenna array, 343 elements
MAARSY433	MAARSY full antenna array, 433 elements
MF	Medium frequency; 0.3–3 MHz
MHE	meteor head echo
MoM	method of moments (NEC)
MST	Mesosphere Stratosphere Troposphere
MU	Middle-Upper atmosphere radar, Japan
NEC	Numerical Electromagnetic Code
NF	noise figure
OSWIN	OStsee WINd radar
PMSE	Polar Mesosphere Summer Echoes
PMWE	Polar Mesosphere Winter Echoes
QDC	quiet day curve
RA	right ascension, celestial coordinate
radar	radio detection and ranging
RF	radio frequency
SA	Spaced Antenna, wind estimation method
SkiYmet	All-Sky Interferometric Meteor Radar
SLA	side lobe attenuation
SNR	signal-to-noise ratio, supernova remnant
SOUSY	SOUNding SYstem
SPU	signal processor unit
UHF	Ultra High Frequency, typ. 300-3000 MHz
UTC	coordinated universal time
VHF	Very High Frequency, typ. 30-300 MHz
VLA	Very Large Array, New Mexico/USA
VLSS	Very Large Array Low frequency Sky Survey
VSWR	Voltage Standing Wave Ratio
WADIS	Sounding rocket campaign, WAVE propagation and DISSipation in the middle at- mosphere

List of Acronyms, Abbreviations, and Symbols

Symbols

A_{eff}	effective antenna area
a_p	planetary a-index
c	speed of light
c_{GSM}	calibration factor for power conversion, arbitrary units to K
c_{RX}	calibration factor for power conversion, arbitrary units to W
D	maximum diameter of an antenna array
e	partial pressure of water vapor
G	antenna gain
k_B	Boltzmann constant
K_p	3-hourly planetary K-index
L	largest distance between antennas in an array
l_{geo}	geographic latitude
m_e	mass of an electron
n	radio refractive index
N_{CI}	number of coherent integrations
n_e	electron density
NF	noise figure
P_a	total atmospheric pressure
P_r	received power
P_t	transmit power
r	range from the radar to the target, radius
S_ν	flux density of a cosmic radio source
T	temperature
t_{er}	time of 1° rotation of Earth
δ	celestial coordinate, declination
η	radar volume reflectivity
λ	wavelength
ω_o	observed wave frequency
ω_p	plasma frequency
ϵ	permittivity
ϕ	azimuth angle
Ψ	antenna phase
σ	radar cross-section, standard deviation
τ	effective radar pulse width
θ	zenith angle
$\theta_{-3\text{dB}}$	half-power full-width of the antenna main beam
v	velocity of a electromagnetic wave

List of Tables

3.1	Individual periods of MAARSY’s conversion from linear to circular polarization.	22
3.2	Simulated gain, beam width, the position and suppression of the 1st and 2nd side lobe and position of the 1st null in MAARSY’s radiation pattern for unity amplitude distribution and boresight pointing.	25
3.3	Examples of amplitude taper for a circular-aperture antenna array (<i>Balanis</i> , 2005; <i>Mailloux</i> , 1994). θ_{-3dB} and θ_{FN} are the half-power beam width and the position of the first null in the pattern.	31
4.1	Parameters of the absolute phase calibration experiment for MAARSY. . . .	38
4.2	Comparison of hardware phase test and cosmic radio source calibration for the period Sept. 2012 to May 2013.	43
4.3	Characteristics of the simulated radiation pattern of MAARSY for the individual periods. Listed are the gain, the beam width, minimum side lobe attenuation	52
4.4	Results of the analysis of the galactic radio emissions estimating the beam width for beam pointing to Cassiopeia A and Cygnus A with MAARSY433, MAARSY343 and the side lobe cleaned MAARSY343 sorted for the observation periods with and without ionospheric scintillations.	59
4.5	Calibration factor c_{RX} and c_{GSM} for MAARSY343 (including the observational bandwidth), the system temperature for the individual periods and the flux density of the individual sources used for the gain estimation for Cassiopeia A and Cygnus A. For the calibration factors du represents the detected power in digitizer units, the absolute value of the digitized in-phase and quadrature components.	65
4.6	Gain estimation for MAARSY343 by observing cosmic radio sources for the three periods a) Sept. 2012 to May 2013, b) May 2013 to Sept. 2013 and the preliminary results for c) the time since Sept. 2013. The columns CasA and CygA refer to observations of the radio sources Cassiopeia A and Cygnus A, respectively. Δg depicts the deviation to the simulated gain of the antenna array.	66
5.1	Radar and geometry parameters of the moon experiment.	80
6.1	Overview of the derived parameters characterizing MAARSY’s antenna array radiation pattern. The results of the individual methods are presented, marking the individual focus and their capability for calibration purpose. The abbreviation n/a and the symbol σ denote ”not applicable” and the standard deviation, respectively.	95

List of Tables

A.1	Comparison of simulated gain for the main lobe (ML) and side lobes (SL) for various radar systems, sorted by their array area. The simulations for the radars ending AT incorporate amplitude taper. ML vs. SL rel. area denotes the relation of the intensities of the main lobe to all side lobes relative to their respective area.	99
B.1	Measurement results of MAARSY's coaxial cables that are used on RF and IF during the preparation of the installation. \bar{a} , $\bar{\phi}$ and $\bar{\tau}_{gr}$ are the mean loss, phase and groups delay, while σ denotes their standard deviation respectively.	108
B.2	Results of dynamic range measurements for various gain settings for the Anemone and Hexagon receivers.	110
B.3	Noise figure measurements performed for a MAARSY RF to IF receiver with an automatic noise figure meter.	112
B.4	Noise figure measurements performed for the complete MAARSY receiver including data acquisition. The noise figure in the upper part is derived with an electron tube noise source for the 3 dB points. The lower part shows measurements with a solid state noise source, applying the Y-factor method.	115
B.5	Available filter settings of the MAARSY receiver independently selectable for intermediate frequency (IF) and baseband (BB).	116
B.6	Results of the bandwidth determination of the MAARSY receiver for intermediate frequency (IF) and baseband (BB), directly measured and estimated from FFT.	117
C.1	Identifying numbers and names of the groups used in the comparison of phase calibration methods, observing the cosmic radio source CasA and the automatic hardware phase test, Figure 4.9(a).	119
C.2	Results of the phase measurements using Cassiopeia A for the individual periods before Sept. 2012, September 2012 to May 2013 and May 2013 to November 2013. Listed are the group identifier, the amount of individual measurements used, the derived group phases and its standard deviation. . .	121
C.3	Prominent cosmic radio source, which can be observed in the northern hemisphere with a VHF receiving system and an appropriate antenna array (data taken from e.g. <i>Kuz'min</i> , 1966; <i>Laing et al.</i> , 1983; <i>Reich et al.</i> , 1997; <i>Green</i> , 2009; <i>VLSS Remote Sensing Division</i> , 2014). The radio source type abbreviation SNR denotes a supernova remnant.	123

List of Figures

1.1	Photograph of the MAARSY site, showing on the left the MAARSY antenna array, accompanied by the ALWIN64 antenna array on the right.	2
2.1	Temperature profiles (upper left) and electron density profiles (lower right) for high latitudes (69°N) derived from IRI model (see <i>Bilitza, 2001</i>) for summer (red) and winter (blue) conditions. Taken from <i>Li (2011)</i>	6
2.2	Left: Individual terms of the radio refractive index (Equation 2.4) for 53 MHz (red) and 3 MHz (black) and the corresponding total refractive index for both frequencies in respect to their individual colored abscissa (right panel).	8
2.3	Sketch of typical height coverage of atmospheric radars using coherent scattering. The shaded areas mark the altitude range, from where the specific radars do not continuously receive backscatter.	8
2.4	Range-Time-Intensity plots of a) Polar Mesospheric Summer Echoes and b) Polar Mesospheric Winter Echoes observed with MAARSY, zenith beam. Note the differing range interval of approximately 78 to 92 km in a) and 57 to 86 km in b)	11
2.5	a) Sketch of the 97 beam positions used in the PMSE campaign 2011, projected for 84 km altitude. b) Signal to noise ratio for an observation of PMSE on 2011/07/22 depicted for 1 km altitude resolution, derived from 97 quasi-simultaneous beam direction. Taken from <i>Latteck et al. (2012)</i>	11
3.1	Photograph of the former ALWIN radar. The container in the left housed the radar equipment, while a part of the 144 4-element Yagi array is shown on the right.	14
3.2	a) Sketch of the VHF radar site MAARSY, left the 433 element MAARSY array, accompanied by the ALWIN64 array, three individual ALWIN64 transmit antennas and the main building. b) Drawing of the total antenna array MAARSY, colored groups form seven Anemones named MAARSY343, the entire antenna array is called MAARSY433 in this work. Taken from <i>Latteck et al. (2012)</i>	15

List of Figures

3.3	Block diagram of the MAARSY system, taken from <i>Latteck et al. (2012)</i> . The left column shows the antenna array with magnified Hexagon subgroup, connected to its dedicated transceiver modules and subsequent Hexagon combiner, placed in the containers surrounding the array (middle column). In total 61 individual IF signals are connected to the combining and switching units in the main building, where the user selected groups are finally feeding the baseband receivers. For transmission, the individual signals are generated in the transceivers, triggered and disciplined by appropriate trigger and reference signals from the main building.	16
3.4	a) Sketch of MAARSY's IF switching and combining unit (IFSCU), taken from <i>Latteck et al. (2012)</i> . b) Selection of different array subgroups, RX-01 for the total MAARSY433 array, RX-02 to RX-08 seven Anemones, RX-09 to RX-16 eight Hexagons.	17
3.5	a) Shape and frequency width of a $0.33\mu s$ pulse accompanied by the simulated band width of the MAARSY antenna in form of a voltage standing wave ratio (VSWR). b) Drawing of the MAARSY array element. Taken from <i>Latteck et al. (2012)</i>	19
3.6	a) Simulated impedance of the MAARSY antenna depicted in a Smith-chart and b) measured impedance of the prototype antenna.	19
3.7	The left panel depicts the angular dependency of an incident linearly polarized wave received with a linearly polarized antenna. The right panel shows the inherent loss of an elliptically polarized wave received with a circularly polarized antenna.	21
3.8	Coordinate system used for the NEC simulations.	23
3.9	a) Computed radiation pattern of MAARSY343, formed by seven Anemone subarray groups, pointing vertical in top-view overlaid by colored lines indicating the cross-sections depicted in b) along $\phi = 0^\circ$ and 45°	23
3.10	Computed radiation pattern of a) MAARSY433 and b) MAARSY343 pointing to $\phi = 180^\circ$, $\theta = 10.5^\circ$, depicted in top-view.	24
3.11	a) Computed radiation pattern of the hardware combined MAARSY433 (red) and the software combined MAARSY343 (black) pointing vertical for two cross-sections $\phi = 0^\circ$ and 45° . b) Comparison of MAARSY433 (red) and MAARSY343 (black) pointing to $\phi = 180^\circ$, $\theta = 10.5^\circ$ and $\theta = 28^\circ$	25
3.12	a) Sketch of the maximum zenith beam pointing angle for the linearly polarized MAARSY avoiding the generation of grating lobes derived from simulations. b) Exemplary radiation pattern in top-view of the total MAARSY array pointing to $\phi = 11^\circ$, $\theta = 40^\circ$. For this large off-vertical pointing no direct grating lobes are seen, however their side lobes are already generated into south-eastern and south-western directions.	27
3.13	Schematic of a classical All-Sky Interferometric Meteor Radar (SkiYmet) configuration.	28
3.14	a) Sketch of the MAARSY antenna array, divided into 12 approximately equal slices, of which the colored antennas are used to form individual beams at $\theta = 25^\circ$, taken from <i>Gancarz (2010)</i> . b) Simulation of the radiation pattern generated by the configuration marked in a)	29

3.15 **a)** Simulated radiation pattern of MAARSY using 6 Anemones A-F, each forming an individual beam. **b)** Angular distribution of observed meteors for the six simultaneous beam directions. The orientation of the axes are identical to **a)**. Consistent with earlier figures, each ring overlaying both plots denotes a zenith angle distance of 10° 30

3.16 **a)** Simulated radiation pattern in top view of MAARSY343 applying amplitude taper. **b)** Radiation pattern of MAARSY343 for unity illumination (black), amplitude taper with a $(1-r)$ taper function (green) and $(1-r)^2$ (red) as used in **a)**. 31

3.17 Comparison of MAARSY343 with uniform phase and amplitude (left) and incorporating amplitude taper to reduce the side lobe level by additional 10 dB (right). 32

4.1 **a)** Linearity and dynamic range of the MAARSY receiver for the gain setting used in the sky noise and phase calibration observations. **b)** Celestial coordinate system, zenith is marked for an observation position of $\approx 69^\circ\text{N}$. ¹ 35

4.2 **a)** Radiation pattern in top-view of the software combined MAARSY343 pointing to $\phi = 180^\circ, \theta = 10.5^\circ$ and **b)** to $\phi = 180^\circ, \theta = 28.5^\circ$. Both figures are overlaid with the trajectory of Cassiopeia A (in **a)**) and Cygnus A (in **b)**), respectively, as well as a red arrow indicating the typically performed scan from $\theta = 0 - 34^\circ$ 36

4.3 Example of a phase calibration experiment for one passage of Cassiopeia A through MAARSY's main beam on 2013/04/29. Shown are the calculated (green), the observed (black) and their difference (red) phases for the antenna groups 433 (1), Anemones B (3) to F (7) in reference to Anemone A (2). . . . 39

4.4 Results of the phase measurements using Cassiopeia A for the 433 and the Anemone receivers A to F in reference to Anemone A for the period before September 2012. The broken horizontal lines mark the median phase of the respective receiver. Phases marked with a diamond symbol are used for the further analysis. 39

4.5 Results of the phase measurements using Cassiopeia A for 11 Hexagons for the period before September 2012. Both panels show the derived phases of the individual receivers in reference to Anemone A. The broken horizontal lines mark the median phase of the respective receiver. 40

4.6 Phase distribution and variation of the phase measurements observing Cassiopeia A for the 433 and Anemone receiver. Period: Sept. 2012 - May 2013. Phases marked by a diamond are used in the subsequent analysis. Note, the Anemone M is approximately 75° separated from the Anemones A-F due to its circular polarization. 40

4.7 Observed phases for MAARSY433 and the Anemone receiver including data from active mesospheric experiments in June and July. Increased variability and spurious phases for the hardware combined MAARSY433 channel are found, the Anemones remain reliable. 41

4.8 **a)** Phase and amplitude deviation from the median for 63 antenna group and receiver combinations, derived from the hardware phase test. **b)** Standard deviation of the amplitude and phase measurements in **a)**. 42

List of Figures

4.9	a) Deviation of the antenna and receiver phases determined by radio source observations and the hardware phase tests since May 2013 (left) and the median of all common day observations (right). b) Median phases of all existent radio source phase calibration and hardware phase test data since May 2013, regardless of the specific day of the observations (left). The resulting phase deviations between the two methods (right). All phases are referenced to Anemone A (antenna group 2).	44
4.10	a) Simulated radiation pattern of MAARSY343 in top view without phase correction. b) Comparison of the ideally combined MAARSY343 (black) and without phase correction (red) for two cross-sections $\phi = -45^\circ$ and 0°	45
4.11	Magnitude of cross-correlation of all 16 receiver channels for times of a Cassiopeia A passage (a) and for beam pointing to "quiet" regions (b). 1: MAARSY433, 2-8: Anemones A-M, 9-16: Hexagons A-05, B-05, C-04, D-04, E-04, F-05, C-09, B-08.	46
4.12	Detected incident relative power (P_{max} is depicted in the title) in arbitrary units for a sky noise scan on 28th-29th of November 2012 for the software combined MAARSY343. The highlighted individual sources are Cygnus A (1), the Milky Way (2) and Cassiopeia A (3).	47
4.13	Zoom of the detected incident relative power for a sky noise scan performed on 28th of November 2012 for MAARSY433 and the software combined MAARSY343. The black ellipses and hexagons mark the visible side lobes in the detected intensities.	48
4.14	a) Incident power for five individual beam pointing directions intended to observe the passage of Cassiopeia A between May and November 2013. Bold lines depict the median enclosed by the absolute minima and maxima. b) Standard deviation for the same observations.	49
4.15	Analysis of the incident sky noise power for the period of Sept. 2012 to April 2013 received with MAARSY343. The left upper panel depicts the total incident noise power of the composite for a complete sidereal day for beam pointing directions zenith to 34° off-zenith. The upper right and lower left panel depict the cross-sections through CasA. The distribution of power for both planes is analyzed for beam pointing accuracy and beam width, where the latter is denoted in the panels. The lower right panel presents a zoom to the temporal cross-section through CasA. Overlaid are the simulated intensities of CasA for beam pointings in red, blue and green for $\Delta\phi = -1^\circ, 0^\circ$ and $+1^\circ$ in reference to its culmination point. The black vertical line indicates the estimated time of passage from the observation. The broken vertical blue lines mark the estimated 3 dB points.	51
4.16	Analysis of the incident sky noise power for the period of May to September 2013 received with MAARSY343. A detailed description of the individual panels is given in Figure 4.15 and in the accompanied text.	53
4.17	Analysis of the incident power of Cygnus A for the period starting in September 2013 received with the circularly polarized MAARSY343. Descriptions of the individual panels are given in Figure 4.15 and in the accompanied text.	54

4.18	GSM simulated intensities emanating from distinct and diffuse cosmic radio sources for 1° resolution at the frequency of 53.5 MHz transformed to Mollweide projection in celestial coordinates. The red line indicates the Milky Way, the horizontal lines mark the MAARSY zenith position and the typical (30°) and the extended (60°) scan range. Modified after <i>Renkowitz et al.</i> (2012).	56
4.19	Left: Comparison of the observed intensities during December 2011 with the GSM temperature model for two beam directions pointing to Cassiopeia A and Cygnus A. Right: Correlograms of both comparisons highlight the similarity of observations and the model data. Modified after <i>Renkowitz et al.</i> (2012).	57
4.20	Top: Incident power originating from distinct and diffuse cosmic radio sources from modeled GSM data convolved with the simulated complete MAARSY343 radiation pattern. Bottom: Deviation of the observations (composite May to September 2013, previously depicted in Figure 4.16) and GSM model data.	58
4.21	Top: Modeled GSM sky noise data convolved with the simulated side-lobe-only MAARSY343 radiation pattern. Bottom: Observation data (composite May to Sept. 2013) subtracted by the above shown side lobe pick up.	59
4.22	Analysis of the data from Sept. 2012 to April 2013 (shown in Figure 4.15), but subtracted by the simulated side lobe pick up. The estimated beam width of this side-lobe-free pattern is now in good agreement with the simulations (4° to 4.2° for both planes).	60
4.23	Composite of cosmic noise scans ($\phi = 180^\circ$, $\theta = 0 - 60^\circ$) covering a declination range of $9.3 - 69.3^\circ$. The individual radio sources dominating on the observation frequency are marked according their position and can be found in the Appendix in Table C.3. The increased intensity extending along most of the individual radio sources marked by (1) originate from the Milky Way, as well as (2) which is the North Polar Spur.	61
4.24	Deviation of observation with MAARSY343 for September to November 2013 for the zenith scan range of $0^\circ - 60^\circ$ (see Figure 4.23) and GSM reference model data.	62
4.25	Detected intensities for the scan range $\theta = 0^\circ$ to 60° with subtracted side lobes pick up (similar to Figure 4.22) for the period September to November 2013. Compare to Figure 4.23.	62
4.26	Incident noise power for the standard sky noise zenith scan from 0° to 34° on 2013/10/14. The individual sources CasA ($\approx 20:40$ UTC) and CygA ($\approx 17:20$ UTC) show extremely high fluctuations in power (ellipses), while the intensity originating from CasA also seems to change its angle of arrival by about 3° during the passage trough the beam (red arrow). See Figure 4.23 on page 61 as reference for rather undisturbed conditions.	68
4.27	All-sky snapshots of the angular distribution of incident cosmic radio emissions received by KAIRA on a) 2013/12/27 for quiet conditions with CasA close to zenith ($\phi = 185^\circ$, $\theta = 11^\circ$) and CygA ($\phi = 250^\circ$, $\theta = 40^\circ$) at an equivalent sidereal time as in the subsequent figures. b) shows the onset of a scintillation event, where CasA's intensity is damped, for 2013/12/25 at 16:01:05 UTC. The green contour intensity originates from the Milky Way. Courtesy of Dr. McKay-Bukowski, SGO.	69

List of Figures

4.28	All-sky snapshots of the angular distribution of incident cosmic radio emissions received by KAIRA on 2013/12/25 at a) 16:01:07 UTC and b) 16:01:09 UTC. Note, Figures 4.27(b) to 4.28(b) are separated by 2 s each. Courtesy of Dr. McKay-Bukowski, SGO.	70
4.29	a) Incident power of Cassiopeia A observed with KAIRA (blue, left axis) and MAARSY (black, right axis) on 2013/06/08 at \approx 05:12 UTC. The red broken vertical line marks the time of the culmination of CasA. The detected power emanating from CasA vary significantly for both stations, indicating disturbed ionospheric conditions, while b) depicts mainly quiet conditions for both stations as detected on 2013/06/11 at \approx 05:01 UTC. Note, KAIRA tracks CasA and thus, a flat line is assumed for quiet conditions, while for the MAARSY observations CasA drifts through the main beam.	70
4.30	Ionograms derived from observations of the ionosonde in Tromsø, show in a) distortion events called Spread-F on 2013/06/08, while the profiles in b) describe a quiet F-region on 2013/06/11.	71
4.31	Incident noise power detected on 2013/06/07, marked by intense fluctuations of the individual sources (black ellipses) and damping events of the diffuse background (red arrows). See Figure 4.23 on page 61 as reference for rather undisturbed conditions.	72
4.32	The upper panel depicts the angularly and temporally resolved deviation of the observations from 2013/06/07 to the appropriate QDC of the same period. The lower panel represents the median of all beam pointing direction for one sampling period of time. The arrows and ellipses mark the major absorption events.	73
4.33	Estimated electron densities for 2013/06/07 derived with the Saura-MF radar accompanied by two profiles from 2013/06/11 as reference for quiet night/day conditions and the variability during these hours marked by thin lines of according color. The magenta profile depicts the median for the 2013/06/07 2, 6, 8, 12 UTC hourly profiles. The black profile for 20 UTC underlines the ongoing reversion to the quiet profile.	74
5.1	Experimental setup during lift-off aiming for the direct sampling of the MAARSY radiation pattern in Dec. 2012.	77
5.2	a) Simulated two-dimensional intensity of the electric near field in the proximity of MAARSY. The red asterisks above yellow circles mark the individual measurement positions used for the comparison to the model. b) Comparison of the simulated intensities to the measured field strengths including least-squares fit for all values (blue) and measured intensities above 1 V/m (black).	78
5.3	a) Simulated, scaled near electric field strength of MAARSY for $z=1.8$ m and 1 kW peak power per transceiver module. The green line marks the path of the measurements. b) Comparison of simulated and measured near electric field strength accompanied by an analytical radial decrease of the intensity.	79
5.4	Received backscatter from the moon during an experiment on 2012/02/04. The approach of the moon, its calculated time of passage (black vertical line) and high fluctuation of incident power can be seen. The depicted range is aliased due to the high pulse repetition frequency to provide sufficient duty cycle and thus integrated radiated power for this experiment. Modified after <i>Renkwitz et al.</i> (2012).	81

5.5	Observations of the GRACE satellites for three selected beam directions. The beam positions according to the orbital trajectory of the satellites are depicted in the lower right panel. The yellow lines mark the orbital trajectory of the satellites. Modified after <i>Renkwitz et al. (2012)</i>	82
5.6	Observations of the ENVISAT satellite for three selected beam directions. The beam positions according to the trajectory of the satellites are depicted in the lower right panel. Taken from <i>Renkwitz et al. (2012)</i>	83
5.7	a) Overlay of 700 meteor head echo trajectories observed during the Geminids meteor shower 2012, b) smoothed and interpolated from a) . The colored circles represent the pattern approximation which was used to normalize the individual trajectories.	85
5.8	Sketch of the WADIS rocket motor and payload. Courtesy of Mobile Rocket Base, German Aerospace Center	86
5.9	a) Trajectory of the WADIS rocket payload in reference to MAARSY, depicted in spherical coordinates, overlaid by the beam positions used in the WADIS scan experiment. b) Integrated power of all beams in the scan (median removed) depicted over range and time. The thin black line marks the range calculated from the GPS coordinates.	87
5.10	a) Two-way radiation pattern of MAARSY overlaid with the trajectory of the WADIS rocket payload for the beam direction $\phi = 330^\circ$ and $\theta = 13^\circ$. b) Same as a) for the beam direction $\phi = 322^\circ$ and $\theta = 28^\circ$. The colorbar above the individual figures denote the height of the WADIS payload for the shown trajectory.	87
5.11	Trajectory of WADIS crossing through the simulated radiation pattern of MAARSY pointing to $\phi=322^\circ$, $\theta=28^\circ$	88
5.12	a) Top: Detected back scatter from PMSE, the WADIS payload and traces of the rocket nose cone and motor in the beam $\phi = 330^\circ$, $\theta = 13^\circ$. Bottom: Black dots represent the maximum detected power on the GPS trajectory. Blue and red curves depict the interpolation of the simulated radiation pattern as shown in Figure 5.10(a) considering the path loss and payloads geometry and the angle of attack. b) Same as a) for the beam direction $\phi = 322^\circ$, $\theta = 28^\circ$	89
A.1	Simulated radiation pattern of MAARSY433 for a) the ideally phased and unity amplitude antenna array and b) assuming 21 failed power amplifiers and thus array elements for the transmission case.	100
A.2	Comparison of the radiation pattern of the ideally phased and uniform amplitude a) MAARSY433 (black) to the case of 21 failed array elements for the cross-sections $\phi = 0^\circ$ (top) and $\phi = 45^\circ$ (bottom). b) Comparison of the ideally phased and uniform amplitude MAARSY343 (black) to the case of random fluctuations of every array element of ± 1 dB and $\pm 10^\circ$ for two cross-sections.	101
A.3	Insertion and power loss for a given antenna mismatch as voltage standing wave ratio.	102
A.4	a) Simulated radiation pattern for the ideally fed MAARSY343 and b) with random fluctuation of every array element of ± 1 dB and $\pm 10^\circ$	102

List of Figures

A.5	a) Simulated radiation pattern for MAARSY343 with random fluctuation of every array element of ± 2 dB and $\pm 20^\circ$ and b) the comparison to the ideally fed MAARSY343 pattern (black) for two cross-sections.	103
A.6	Comparison of the radiation pattern of MAARSY simulated with NEC (filled contour) and the simple geometry model (contour lines).	104
A.7	Deviation of the NEC and geometry model, negative values denotes underestimation of the intensity in the geometry model.	105
B.1	a) Impedance of a MAARSY antenna as seen by a transceiver module including the coaxial feeding cable illustrated in a Smith-chart with 50Ω reference impedance. b) Same as a) , but depicted as return loss log magnitude s11-parameter.	107
B.3	a) Linearity measurements of input reference power to detected power, indicating the dynamic range for different gain settings for both Anemone and Hexagon antenna groups. The black broken line refers to the 3 dB increase of detected power, what describes the sensitivity. b) Standard deviation of the detected power level divided by the median power level for each input power level. This figure depicts the optimal input power window for minimum uncertainty. The left maxima describes the sensitivity, while the right maxima marks the saturation. The right shift of the 80 dB curves indicates deteriorated overall system noise figure for this gain setting.	109
B.4	a) Linearity measurements of MAARSY test systems Signal Processor Unit before (blue) and after the modification (red) accompanied by their standard deviation interval. The reduced gain of the SPU facilitates increased dynamic range. b) Linearity measurements of the complete MAARSY test system receiver, injecting a 53.5 MHz signal for two bandwidth settings into a modified and an unmodified channel.	111
B.5	a) Results of the delay line calibration after SPU modifications. b) Same as a) including additional 20 dB attenuators in the IF path. (courtesy of Dr. R. Latteck, IAP)	111
B.6	Schematic of the noise figure measurement setup.	112
B.7	Results of the first noise figure measurements (NF) (a)) and the more recent and accurate measurements using a solid state noise source (b)), accompanied by the respective uncertainty of the used noise sources ± 0.25 dB and ± 0.1 dB. The NF given in the legend of (b)) is derived with the Y-factor, while the vertical lines represent the single-point NF estimation by a 3 dB increase of the polynomial interpolation.	113
B.8	Calibration factor for an injected broad band signal into a Hexagon receiver group for two bandwidth settings derived with with a calibrated solid state noise source. Additionally, the equivalent receiver temperature is estimated by the intersection of the linear fit with the ordinate and marked as T_{rec} . . .	115
B.9	a) Direct bandwidth measurements of the filter settings 3/3 MHz and 3/1.5 MHz for intermediate frequency (IF) and baseband (BB) respectively. b) Estimated bandwidth derived from the FFT along the range gates.	117
C.1	Phase distribution and variation of the phase measurements observing Cassiopeia A for the connected Hexagon receivers. Period: Sept. 2012 - May 2013.	119

C.2	Phase distribution and variation of the phase measurements observing Cassiopeia A since May 2013 for the 433 and Anemone receivers. The Anemones A-M are completely converted to circular polarization and thus their phases are again close to each other.	120
C.3	Phase distribution and variation of the phase measurements observing Cassiopeia A since May 2013 for the Hexagon receivers.	120
C.4	Correlation phases for the 433, Anemone receivers and 2 Hexagon receivers for the time and coordinates of Tycho's supernova remnant (SNR) observed on 2013/11/19. This was the first radio observation of the Tycho SNR by the IAP.	122
C.5	Example of the Gauss-function fit to the median detected power for the estimation of the time of passage through the antenna main beam. Period: May to September 2013 for MAARSY343.	123
C.6	Analysis of the incident sky noise power for the period of May to September 2013 received with MAARSY433. A detailed description of the individual panels is given in Figure 4.15 and in the accompanied text.	124
C.7	Detected incident power for the period starting in September 2013 with the circularly polarized MAARSY antenna array. Top: MAARSY433, bottom: MAARSY343.	125
C.8	Correlogram of the MAARSY cosmic noise observations for May to September 2013 with MAARSY343 and the GSM data to derive the calibration factor c_{GSM}	125
D.1	Sketch of the airborne setup used to sample the intensity radiated by MAARSY.	127
D.2	Laboratory measurements of the linearity of the detector a) and of the total setup b) , without the antennas.	128
D.3	a) Frequency selectivity of the receiver and detector for a board spectrum (left) and zoom around the nominal frequency of 54.7 MHz (right). b) Frequency selectivity of the total setup including the A/D-converter, without the antennas.	128
D.4	a) Test setup of the airborne equipment on a car to perform test measurements around the MAARSY antenna array. b) Flight preparations of the equipment, mounting the antennas and stabilizing weights.	129
D.5	Simulated near electric field and the corresponding detected intensities of the airborne equipment for a beam pointing to $\phi = 330^\circ, \theta = 25^\circ$	130
D.6	Simulated near electric field and the corresponding detected intensities of the airborne equipment for a beam pointing to $\phi = 0^\circ, \theta = 0^\circ$	130
D.7	Sketch of the likely source spoiling the sampled radiation pattern for the beam pointing to $\phi = 330^\circ, \theta = 25^\circ$, reflection and scattering off the nearby hills. The asterisk mark the position of the radar, while the arrows indicate the likely path of the clutter signals.	131

Acknowledgements

First of all I like to thank Dr. Werner Singer and Dr. Ralph Latteck, who initially offered me and luckily convinced me to stay at the IAP and to work on this interesting topic. Concomitantly, I owe Dr. Jürgen Bremer and Prof. Markus Rapp special thanks for believing in and supporting me since the very beginning as well as the director of the IAP Prof. Franz-Josef Lübken for giving me this opportunity. Not less, I am deeply grateful to Prof. Hartmut Ewald, my university supervisor of this thesis.

After being involved in the planning of MAARSY, the thrill was not only to be a part of the team that built the radar, but also to squeeze and raise the radar and to find new scientific possibilities and objectives for it. Here especially, I like to thank Prof. Jorge Chau, who brought and gave new ideas with his insights, which significantly contributed to this thesis. This is in particular true as due to his initiative, we unintentionally found the first own incoherent scatter signals with MAARSY, which definitely pushed me.

I like to thank again Dr. Werner Singer and Dr. Ralph Latteck for all their help, the discussions, thoughts and ideas over the years, which clearly helped and guided me during this thesis work as well as giving me MAARSY observation time, whenever feasible. Additionally, my thanks go to Dr. Gunter Stober, who contributed to publications and this thesis work by computing the GSM model data as well as Carsten Schult for the interferometric analysis of radar data deriving meteor head echo trajectories. I also like to thank Dr. Marius Zecha and Dr. Irina Strelnikova for not only sharing the office with me lately, but being amenable and helpful for several wishes, ideas, questions and discussions.

I'm very thankful for the support by Dr. Derek McKay-Bukowski from SGO, who was immediately willing to share data from KAIRA. Furthermore, I thank Dr. John McKean and Dr. Frank Schinzel providing latest information about LOFAR and LWA observations of cosmic radio sources.

I wish to thank all people that were involved in building and keeping MAARSY operational, especially from IAP, the Andøya rocket range, Genesis Software and involved students. Without your contribution MAARSY wouldn't be the same that it is today and likely would have changed the scope and focus of this thesis.

My thanks go also to Jens Hildebrand, who helped a lot with L^AT_EX issues as well as to Christoph Kottke, who was very helpful in Linux issues of the data acquisition system of the airborne probe. Moreover, I have to thank the IAP's IT department, providing support in several aspects as well as access to IAP's mainframe allowing hundreds and hundreds of hours running my simulations. I also give thanks to the IAP colleagues in general, for the working atmosphere and plenty of unforgettable impressions and insights to countless aspects of atmospheric research.

I also need to thank Prof. Andreas Ahrens, who initially pointed me towards the IAP during my B.Sc. study. This opened an amazingly interesting field to explore and to grow.

Furthermore, I wish to express my gratitude to the proofreaders of this thesis and all who contributed, even though they might not be aware of it.

Last but definitely not the least I'm deeply indebted to my family, my parents who always supported and encouraged me and of course to Ulli and Markus ! Even though, I could not always spend the time as it maybe would have been needed, but you always remember me what is really important.

THANK YOU !

List of own publications

Peer reviewed publications:

Latteck, R., W. Singer, M. Rapp, and T. Renkwitz, MAARSY - the new MST Radar on Andøya / Norway, *Advances in Radio Science*, 8, 219–224, doi:10.5194/ars-8-219-2010, 2010.

Renkwitz, T., W. Singer, R. Latteck, and M. Rapp, Multi beam observations of cosmic radio noise using a VHF radar with beam forming by a Butler matrix, *Advances in Radio Science*, 9, 1–9, doi:10.5194/ars-9-349-2011, 2011.

Renkwitz, T., W. Singer, R. Latteck, G. Stober, and M. Rapp, Validation of the radiation pattern of the Middle Atmosphere Alomar Radar System (MAARSY), *Advances in Radio Science*, 10, 245–253, doi:10.5194/ars-10-245-2012, 2012.

Latteck, R., W. Singer, M. Rapp, B. Vandepier, T. Renkwitz, M. Zecha, and G. Stober, The new MST radar on Andøya: System description and first results, *Radio Science*, 47, doi:10.1029/2011RS004775, 2012.

Renkwitz, T., G. Stober, R. Latteck, W. Singer, and Rapp, New experiments to validate the radiation pattern of the Middle Atmosphere Alomar Radar System (MAARSY), *Advances in Radio Science*, 11, 283–289, doi:10.5194/ars-11-283-2013, 2013b.

Chau, J., T. Renkwitz, G. Stober, and R. Latteck, MAARSY multiple receiver phase calibration using radio sources, *Journal of Atmospheric and Solar-Terrestrial Physics*, doi:10.1016/j.jastp.2013.04.004, 2013.

Non-peer reviewed publications:

Renkwitz, T., W. Singer, and R. Latteck, Study of multibeam ability for the VHF MST ALWIN radar system, *Proceedings of the 12th International Workshop on technical and Scientific Aspects of MST radars*, pp. 127–130, editors: N. Swarnalingam and W.K. Hocking, Canadian Association of Physicists, Ottawa, Ontario, Canada, ISBN 978-0-9867285-0-1, 2010.

Renkwitz, T., R. Latteck, W. Singer, and G. Stober, Validation of the receiving pattern of the MAARSY phased antenna array, *Proceedings of the 13th International Workshop on technical and Scientific Aspects of MST radars*, 2013a.

List of presentations

Renkwitz, T., W. Singer, R. Latteck, Study of multibeam ability for the VHF MST ALWIN radar system. *12th International Workshop on technical and Scientific Aspects of MST radars, London/Ontario, Canada, 2009*

Renkwitz, T., R. Latteck, W. Singer, The active phased array antenna of the Middle Atmosphere Alomar Radar System (MAARSY). *U.R.S.I. Landesausschuss in der Bundesrepublik Deutschland e.V. Kleinheubacher Tagung, Miltenberg, Germany, 2010*

Renkwitz, T., R. Latteck, W. Singer, Validation of the radiation pattern of the Middle Atmosphere Alomar Radar System (MAARSY). *U.R.S.I. Landesausschuss in der Bundesrepublik Deutschland e.V. Kleinheubacher Tagung, Miltenberg, Germany, 2011*

Renkwitz, T., R. Latteck, W. Singer, G. Stober, Validation of the receiving pattern of the MAARSY phased antenna array, *13th International Workshop on technical and Scientific Aspects of MST radars, Kühlungsborn, Germany, 2012*

Renkwitz, T., R. Latteck, G. Stober, W. Singer, New experiments to validate the radiation pattern of the Middle Atmosphere Alomar Radar System (MAARSY). *U.R.S.I. Landesausschuss in der Bundesrepublik Deutschland e.V. Kleinheubacher Tagung, Miltenberg, Germany, 2012*

Renkwitz, T., G. Stober, R. Latteck, W. Singer, M. Rapp, Validation of the radiation pattern of the Middle Atmosphere Alomar Radar System (MAARSY) *IEEE 2013 Phased Array Symposium, Boston, USA, 2013*

Thesen zur Dissertation

Evaluation and validation of a novel MST-Radar for studying atmospheric 3D structures

1. Räumlich und zeitlich aufgelöste Sondierungen der Erdatmosphäre werden vorzugsweise mit Phased Array Systemen im VHF-Bereich vorgenommen, da hier Irregularitäten des Neutralgases sowie des ionosphärischen Plasmas starke Radarechos erzeugen. Sondierungen der Troposphäre und unteren Stratosphäre (1 - 16 km) sowie der Mesosphäre (60 - 90 km) wurden bis 2008 mit dem ALWIN Radar (53,5 MHz) durchgeführt. Das aus 144 Yagi-Antennen bestehende Phased Array ermöglichte Sondierungen mit einer Strahlbreite von 6° vom Erdboden bis in 100 km Höhe mit einem Durchmesser der Beobachtungsfläche von etwa 500 m in der Troposphäre und 9 km in 85 km.
2. Die elektronische Schwenkbarkeit des ALWIN-Radarstrahls war technisch bedingt auf lediglich 9 Positionen begrenzt, vertikal und jeweils 7° und 13° aus dem Zenit geschwenkt entlang der Haupthimmelsrichtungen. Das Strahlungsdiagramm war für die 13° Position bereits deutlich verschlechtert und erlaubte nur eingeschränkte Studien zur räumlichen Verteilung der beobachteten Streuer.
3. Das neue MAARSY-VHF-Radar übertrifft die Eigenschaften von ALWIN entscheidend mit einer minimalen Winkelauflösung von $3,6^\circ$ gegenüber 6° und einer freien Schwenkbarkeit des Radarstrahls bis zu einer Zenitwinkelablage von 40° . Eine verbesserte zeitliche und räumliche Auflösung (Datendurchsatz und Pulsformung), eine höhere effektiv abgestrahlte Pulsausgangsleistung (600 kW statt 25 kW) und die flexible Auswahl unterschiedlicher Subarrays im Empfangsfall (aktuell maximal 2x16 I/Q Kanäle) ermöglichen jetzt auch interferometrische Anwendungen.
4. Auf Grund des verfügbaren Platzes wurde für MAARSY eine Phased Array Antenne aus 433 Yagi-Antennen entworfen. Die Antennen sind in einer gleichseitigen Dreiecksgitterstruktur angeordnet, wobei jede Antenne ein eigenes Sende-Empfangsmodul besitzt. Dies verbessert die Schwenkbarkeit und ermöglicht als kleinstes Subarray eine Gruppe von 7 Antennen, die auch zu Gruppen von je 49 Antennen abgetastet werden können.
5. Das komplette MAARSY-Antennenarray, die verschiedenen Subarray-Anordnungen und der Einzelstrahler (3-Element Yagi) wurden unter Berücksichtigung realistischer Randbedingungen (Erdboden, Antennenmaterial) simuliert. Die so erhaltenen Parameter, wie Antennengewinn, Strahlbreite und Unterdrückung der Nebenzipfel, konnten in nachfolgenden Messungen am System sowie mit passiven und aktiven Experimenten verifiziert werden.
6. Die Kenntnis der Positionierungsgenauigkeit und der Breite des Radarstrahls ist von entscheidender Bedeutung für die Durchführung, Auswertung und Vergleichbarkeit der Radarexperimente. Für MAARSY bedeutet eine Fehlpositionierung von 1° in Richtung Zenit bereits eine horizontale Verschiebung der Radarziele von 1,5 km in einer Höhe von 85 km und eine Strahlverbreiterung von 1° in dieser Höhe eine Vergrößerung des Messvolumens um 62%.

7. Der Dynamikbereich eines Atmosphärenradars sollte ausreichend groß sein, um sowohl die variable Hintergrundstrahlung der kosmischen Radioquellen, als auch die eigentlichen Radarechos zu erfassen. Dies wurde anfangs nur bedingt erfüllt mit einem Dynamikbereich von 40 dB, der jedoch im Ergebnis dieser Untersuchung auf etwa 70 dB erweitert werden konnte.
8. Die Systemtemperatur eines Atmosphärenradars sollte unterhalb der minimalen Rauschtemperatur der kosmischen Radioquellen liegen (bezogen auf den jeweiligen Frequenzbereich und die Winkelauflösung des Antennenarrays). Für MAARSY konnte eine äquivalente Systemtemperatur von maximal 800 K bestimmt werden, wobei die für MAARSY sichtbaren ruhigsten Himmelsbereiche etwa 1200 K entsprechen.
9. Die Beobachtung bekannter kosmischer Radioquellen im VHF-Bereich ermöglicht die Verifizierung der Richtcharakteristik eines Antennenarrays (Positionierungsgenauigkeit und Strahlbreite) sowie die Abschätzung des Antennengewinns.
10. Die Beobachtung einer für die Winkelauflösung annähernd punktförmigen kohärenten kosmischen Radioquelle im VHF-Bereich ermöglicht die Phasenkalibrierung der vorhandenen Antennengruppen eines Antennenarrays. Für MAARSY konnten die Phasen bis zu den Subarrays von 7 Antennen mit typischen Standardabweichungen besser als 15° bestimmt werden.
11. Die Signale kosmischer Radioquellen unterliegen beim Durchdringen der Ionosphäre Dämpfungs- und Szintillationseffekten, die zu einer deutlichen Variation der erfassten Signale führen können und bei der Kalibrierung des Systems berücksichtigt werden müssen. Für MAARSY konnten zeitlich und räumlich begrenzte Absorptionseffekte von über 1,5 dB sowie Szintillationen von ± 4 dB (vom Medianwert) beobachtet werden.
12. Für räumlich aufgelöste Beobachtungen ist die Strahlbreite von entscheidender Bedeutung, da sie das Beobachtungsvolumen begrenzt. Die 4° -Strahlbreite des größten synthetisch kombinierten Arrays von MAARSY (343 Antennen) konnte mittels der Beobachtung von kosmischen Radioquellen, sowie durch aktive Radarexperimente an künstlichen Zielen in der Erdatmosphäre verifiziert werden.
13. Die mit MAARSY bestimmten Rauschtemperaturen kosmischer Radioquellen befinden sich in guter Übereinstimmung mit radioastronomischen Referenzkarten, was die Richtigkeit des simulierten Strahlungsdiagramms bestätigt. Bei sorgfältiger Berücksichtigung der Nebenzipfel im Strahlungsdiagramm von MAARSY konnte mittels der Beobachtung kosmischer Radioquellen der Antennengewinn zu 32.4 dBi abgeschätzt werden.
14. Um Signalverluste auf Grund von Faraday-Rotation bei starker Hintergrundionisation zu vermeiden, wurde das Antennenarray von linearer auf zirkulare Polarisierung umgebaut.
15. Mit Hilfe von aktiven Radarexperimenten konnten detaillierte Informationen über das Strahlungsdiagramm gewonnen werden. Die Rückstreuung von Satelliten und Raketen-nutzlasten ermöglichte die Verifizierung der Positionierungsgenauigkeit und der Breite des Hauptstrahls mit einem Positionierungsfehler besser als $0,5^\circ$ und einer Ungenauigkeit der Strahlbreite von $0,1^\circ$. Position und Intensität der ersten Nebenzipfel mit einer Nebenzipfeldämpfung von 15 dB konnten ebenso ermittelt werden.